On Introducing Imperfection in the Non-Linear Analysis of Buckling of Thin Shell Structures

Version of June 13, 2014

Tian Chen

On Introducing Imperfection in the Non-Linear Analysis of Buckling of Thin Shell Structures

THESIS

submitted in partial fulfillment of the
requirements for the degree of

MASTER OF SCIENCE

in

CIVIL ENGINEERING

by

Tian Chen

TU Delft Delft University of Technology
Department of Structural Mechanics
Faculty CEG, Delft University of Technology
Delft, the Netherlands
www.ceg.tudelft.nl

ETH Eidgenössische Technische Hochschule Zürich
Swiss Federal Institute of Technology Zurich
Swiss Federal Institute of Technology
Wolfgang-Pauli-Strasse 15, Hönggerberg
8093, Zurich, Switzerland
www.ethz.ch

On Introducing Imperfection in the Non-Linear Analysis of Buckling of Thin Shell Structures

Author: Tian Chen
Student id: 4240642
Email: t.chen-3@student.tudelft.nl

Abstract

This master thesis details the investigation of the effect of geometrical imperfection on thin shell structures using general FEM software packages. The author proposes a finite element based method for the analysis and design of thin shell structures, and describes the implementation of such a procedure on four FEM packages. The procedure involves assessing structural imperfection sensitivity, and imposing geometrical imperfection prior to a physical and geometrical non-linear analysis.

Starting with thin metallic cylinders, by incorporating imperfection to the surface, the author shows that ANSYS is capable of reproducing Koiter's asymptotic theory as well as experimental data. The author further demonstrates the robustness of the procedure by implementing it on four simple yet realistic structures with both symmetric and asymmetric load cases.

For extremely imperfection sensitive structures such as an axially loaded cylinder, the author introduces four different types of imperfection that could be imposed instead of the first buckling mode, and gauges the effectiveness of each with a modified knock-down factor. By varying the vertical curvature, it is discovered that an axisymmetric imperfection shape governs the ultimate buckling capacity of any near-cylindrical shells. Change in Gaussian curvature is calculated as the end of every load step in the FEM analysis. By plotting the change in Gaussian curvature, the onset of buckling can be readily defined.

Finally, physical non-linearities are introduced to the FEM models to gauge the effect of yielding and cracking. It is found that metallic shells buckle within the elastic range, though yielding eliminates post-buckling capacity. With concrete cracking, instability occurs soon after cracks develop at the buckles of the imperfection shape, therefore reducing the capacity by as much as 8 times from that of the elastic model.

Thesis Committee

Committee chair:	Prof. Dr. Ir. Jan G. Rots, Faculty CEG, TU Delft
Committee member and supervisor:	Dr. Ir. Pierre C.J. Hoogenboom, Faculty CEG, TU Delft
Committee member:	Dr. Ir. Frans P. van der Meer, Faculty CEG, TU Delft
Committee member (External):	Prof. Dr. Eleni Chatzi, D-BAUG, ETHZ

Preface

First and foremost, I would like to express my sincere gratitude to my advisor Pierre Hoogenboom for chatting with me about research and life as an academic, and of course, for guiding me through this thesis. I would like to thank my thesis committee, Jan, Frans, and Eleni for their encouragement, insightful comments, and hard questions.

While challenging at times, the past $^5/_7$ of seven months had been fun and exciting, and deeply rewarding. Though writing thesis is never about the writer as much as it is about the fruit of his or her research. I hope that this thesis paves way for future investigations in the field of thin shell buckling; let's face facts, there are many questions waiting to be answered.

For the remaining $^2/_7$ of the time, I would like to thank Arup Amsterdam and the colleagues within for indulging me with interesting and challenging projects.

As I will be leaving this place and embarking on the next phase of my journey, I would like to leave this with you for your reading pleasure.

Tian Chen
Delft, the Netherlands
June 13, 2014

Contents

Chapter 1

Introduction

1.1 Objective

Thin shells are often the structure of choice when the design is weight critical. They inherently have excellent strength to weight ratio; this attribute allows for much thinner designs than that of other types of structures. Experienced designers realize that the rigidity of shells prevents them from giving ample warning before catastrophic failures. Unlike traditional constructions where the structure would deform visibly a long time prior to collapse, shells typically exhibit no such behaviour. These failures are often attributed to buckling instabilities [16]. Despite this blemish, shell structures have been widely adopted in aerospace, civil and offshore industries. Consequently, many experiments have been performed (especially on stiffened and un-stiffened cylindrical shells) in an attempt to formulate theories that can be used by designers. The experimental results, however, displayed a wide scatter (See Fig. 1.1), the average of which was significantly less than that of the established linear buckling theory. It has been agreed that initial geometric imperfections is the main cause for this scatter and deviation [10].

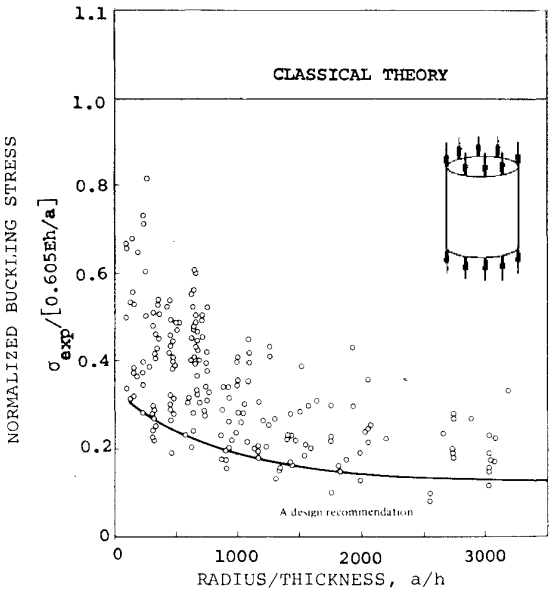

Figure 1.1: Test results of axially compressed cylinders (From *Buckling of Bars, Plates and Shells* by D. O. Brush and B. O. Almroth).

The current design approach to account for this deviation follows the "Lower Bound Design Philosophy", where the critical buckling load is multiplied by an empirical knock-down factor to

ensure that the resultant is a "lower bound" of all experimental data obtained. Driven by the need to reduce weight and cost of developing buckling-resistant aeronautical structures, most research done on this subject have been focusing a few narrowly defined subjects (e.g. axially compressed cylindrical shells), where experimental data is abundant and the knock-down factor can be confidently calculated.

However, from a civil engineer's point of view where shell structures may take on any form, the author noted a general lack in progress in the following areas,

1. Axially loaded cylinders were almost always the only structure studied, scant attention has been paid to other elementary shapes, or more complex structures.
2. Aside from cylinders, design codes offer little guideline aside from the "lower Bound Design Philosophy". The onerous tasks of experimentation are at the hands of the designers as past data were obtained almost exclusively from cylindrical shells.
3. The Lower Bound design method penalizes efficient and well designed shells by enforcing an uniform, and conservative "knock-down" factor.
4. Updated correlation between modern software packages, theories, and practice. Computational capability and performance increases daily; yet designers have not been able to take full advantage of these increasingly powerful tools.
5. For thin shells, physical non-linearity is usually neglected since the onset of buckling is in the elastic range. However, it is necessary for the simulation of post-buckling behaviour.
6. There is no attempt in classifying structures beyond the applied load and support conditions. Curvature may be a useful quantity when estimating the imperfection sensitivity of a structure.

Koiter in his doctoral dissertation proposed the Imperfection Sensitivity Design Philosophy where initial periodic imperfection is incorporated into the problem formulation. Using the basics of his theory and many that builds on it, this thesis plans to address these challenges and introduce to engineers an easy-to-implement method to standardize the analysis of thin-shell structures that are imperfection sensitive.

1.2 Procedure

There has been a resurgence in thin-shells in the recent decade as architects become more and more interested in designing free-formed structures. It is the hope of the author that this thesis can provide design engineers with a relatively simple method to evaluate the robustness of their shell structure. To expand on the procedure flowchart (Fig 1.2), each item is discussed in detail here.

Step 1 Construct the Finite Element Method model

Method Build the model consisting of elements and nodes from either a CAD model, a macro script, and so on.

Step 1a Input physical non-linearity parameters

Method If the design may yield / crack prior to buckling then material data must be supplied (e.g. stress-strain curve, concrete cracking, etc).

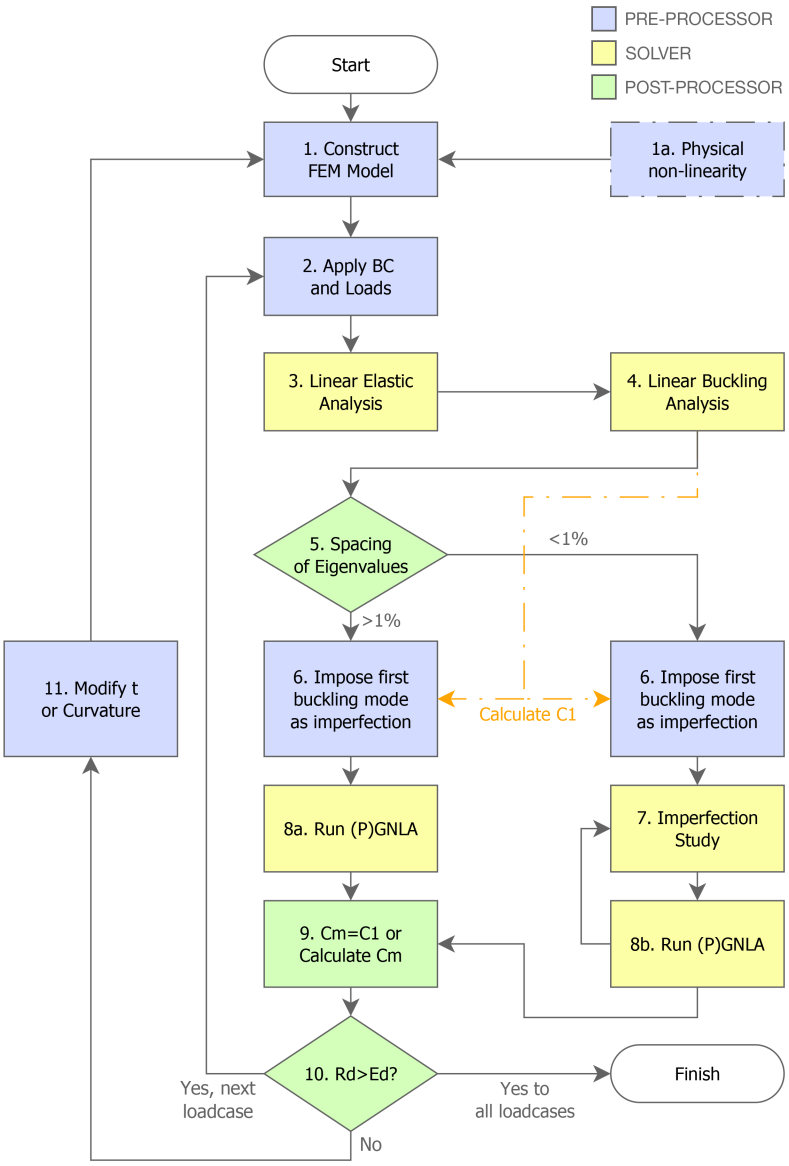

Figure 1.2: Proposed procedure for identifying and analysing imperfection sensitive thin-shell structures, every step is addressed in this thesis

Step 2 Apply boundary conditions and loads

Method Apply boundary conditions and one load case, be it self-weight, wind, snow, seismicity, and so on. Note that each load combination must be applied separately as non-linear analysis does not allow superposition of resultants (e.g. stresses, strains).

Step 3 Perform linear elastic analysis on the perfect structure.

Method This is a standard analysis that can be performed easily with all FEM packages. Check the support reaction force against hand-calculation to ensure the loads are applied correctly.

Step 4 Perform linear buckling analysis on the perfect structure.

Method This is a standard analysis that can be performed easily with all FEM packages. Request at least 20 buckling modes, record the modal shape and the

load factor of each mode.

Step 5 Imperfection sensitivity - spacing of eigenvalues

Method Determine whether or not the structure is imperfection sensitive by calculating the difference in eigenvalue between the first and the 20th buckling mode.

Step 6 Impose imperfection in the shape of the first buckling mode

Method This is done based on the capability of the software.

Step 7 Imperfection study

Method Should the eigenvalues be closely spaced, a detailed imperfection study should be done to extract the largest reduction factor.

Step 8a Run Geometric Non-linear Analysis on the imperfect model

Method Obtain the ultimate buckling capacity and compare it with the critical eigenvalue from Step 4.

Step 8b Run Geometric Non-linear Analysis on the imperfect model for each imperfection shape

Method Obtain the lowest ultimate buckling capacity and compare it with the ultimate buckling capacity from Step 8a.

Step 9 Calculate the largest reduction factor

Method This reduction factor should be calculated in reference to the ultimate capacity resulting from Step 8a.

Step 10 Unity check

Method Whether structural resistance is greater than load. If true then move back to Step 2 and apply the next set of loads. If not, move to Step 11.

Step 11 If the unity check fails

Method Then either the thickness should be increased, or if possible, the geometry of the design should be changed.

1.3 Thesis Summary

Each step of the procedure above is discussed in this thesis. The thesis is divided roughly in two parts, the first part focuses the practicality of imperfection imposition on thin-shell structures. It discusses software capability, validity of the proposed procedure, and then provides several case studies of real design problems. It also includes, as the last step, an discussion on the influence of physical non-linearities. The second part is more abstract in its topics. Focusing on variations of the cylindrical structure, different shapes of imperfections are discussed and implemented, influence of initial curvature, and the change in Gaussian curvature behaviour are analysed in-depth.

1.3.1 Chapter Descriptions

Following this introduction, this thesis starts by giving a concise and easy-to-understand background on shell structures, shell buckling and imperfection sensitivity in Chapter 2. As this thesis focuses on the FEM implementation of imperfection sensitivity analyses, Chapter 3 surveys four popular FEM packages and addresses their strengths and short-comings. The four packages are ANSYS, Abaqus, Diana, and GSA.

As cylinder buckling under axial load is one of the most widely studied problem, Chapter 4 compares FEM results against both experimental and theoretical results and finds common ground with both, thereby giving confidence in the proposed procedure for future analyses. Following this validation, the purposed method of imperfection imposition is applied to four simple yet realistic engineering problems, a hyperboloid cooling tower, a liquid containing silo, a monolithic dome, and an airplane fuselage in Chapter 5. In Chapter 8, a multi-linear stress strain model and a reinforced concrete model is applied to the cylinder and the hyperboloid respectively to assess the influence of plasticity or cracking on the buckling behaviour. This ends the first portion of the thesis.

Thus far in this thesis, imperfection in the shape of the first buckling mode has been the only shape applied, Chapter 6 studies imperfection in other modes, and other shapes in general. Like Chapter 8, the cylinder, and the hyperboloid are used as trial structures. In this case, they are chosen for their markedly different imperfection sensitivity levels. Lastly, to understand difference between the two shapes, a range of different geometries each with a different curvature are studied in Chapter 7. In addition to the differences in initial curvature, incremental changes in Gaussian curvature are also studied.

Chapter 2

Existing Knowledge

2.1 Shell structures

Shells, a derivative of the Latin *scalus*, describes a broad spectrum of natural objects ranging from the shell of a nautilus to the carapace of a turtle. The word has been adapted to describe human made structures commonly associated with a finite curvature and vanishing thickness, e.g. aircraft fuselages, gas and water pipes, hull of ships, and also many civil constructions.

When designed properly, shell structures exhibit incredible strength. As they carry a large portion of the load through membrane action, their thickness can be much less than that of plate structures spanning the same area. Nature has utilized the inherent strength of shells through evolution and produced strong and beautiful structures such as egg shells, sea shells, blood cells and other shapes that surround us.

When the thickness of a shell structure is reduced to a certain level, given by the ratio a/t, we call it a thin shell. The radius, a, is defined in Eq. (2.1), and t is the thickness of the shell. Figure 2.1 gives definitions to the geometrical variables.

$$a = \frac{1}{2}s + \frac{1}{8}\frac{l^2}{s} \tag{2.1}$$

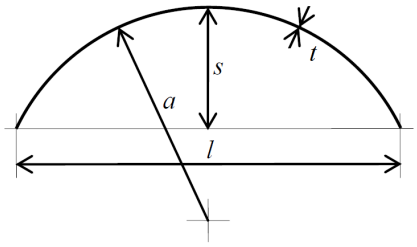

Figure 2.1: Geometry of a shell [24]

Traditionally, civil shell structures were designed through the hands of masters (Felix Candela, Frei Otto, Vladimir Shukhov, and Heinz Isler to name a few) using the empirical method of form finding. Form finding can be seen as an extension of the famous revelation of Robert Hooke "As hangs a flexible cable, so inverted, stand the touching pieces of an arch"; a shell structure can be formed by inverting a piece of hanging cloth, see Figure 2.2 for such a model. These physical models can then be loaded to find their real capacities.

[1] Heinz Isler, Wikipedia, `http://en.wikipedia.org/wiki/File:Gartencenter_Wyss_Zuchwil_01_09.jpg`

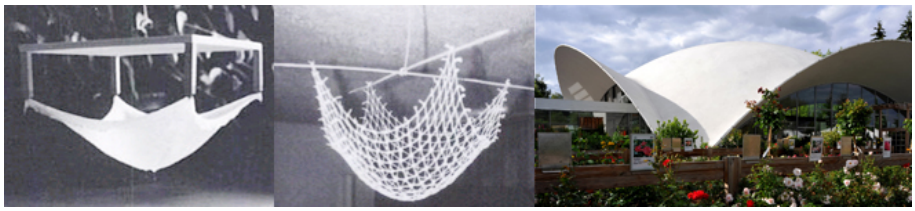

Figure 2.2: Shell structure, and its hanging models[1]

Structural designers and architects favour these thin shells due to their inherent elegant and their ability to span a large roof area efficiently. Figure 2.3 shows one example of a successfully executed shell structure. In search for ever lighter and stronger shapes, aerospace engineers have been utilizing shell structures almost exclusively.

Figure 2.3: TWA Terminal at J.F.K. International Airport[2]

2.2 Failure

Designers realize that the rigidity of shells prevents them from giving ample warning before catastrophic failures. Unlike traditional constructions where the structure would deform visibly a long time prior to collapse, thin shells typically exhibit no such behaviour. These failures are usually attributed to bifurcation buckling [16]. Buckling is a structural instability and is caused by a bifurcation in equilibrium. Buckling happens when the strain energy initially absorbed in-plane convert to bending. Due to the higher stiffness of membrane action, the corresponding amount of energy causes a large non-linear bending deformation. To complicate the matter, the capacity of many thin shell structures are imperfection sensitive.

Table 2.1 summarizes the critical load p_C, the critical membrane force n_{cr} of simple shell structures. Note that these are the analytical solutions of linear buckling.

2.3 Nothing is perfect

A chicken's egg is on average 60 mm long and 40 mm wide. The thickness is on average 0.31 mm. This gives an a/t ratio of approximately $1/100$, placing it in the category of thin shells. Shells such as eggs are extremely strong as anyone who tried to squeeze crack an egg will agree. An egg that is nicked (even imperceptibly) however, would crack at a much lower force. This significant

[2]Evan P. Cordes, TWA Flight Center, Wikipedia, `http://en.wikipedia.org/wiki/TWA_Flight_Center`

	p_C N/m^2	n_C $N\,m^{-1}$
Cylinder, axially loaded	-	$\frac{-1}{\sqrt{3(1-\nu^2)}}\frac{Et^2}{a}$
Hyperboloid, axially loaded	-	$\frac{1}{\sqrt{3(1-\nu^2)}}\frac{Et^2}{a}$
Cylinder, external pressure	$\frac{2}{\sqrt{3(1-\nu^2)}}\frac{Et^2}{a^2}$	$\frac{1}{\sqrt{3(1-\nu^2)}}\frac{Et^2}{a}$
Dome base radius $> 3.8\sqrt{at}$	$\frac{2}{\sqrt{3(1-\nu^2)}}\frac{Et^2}{a^2}$	$\frac{-1}{\sqrt{3(1-\nu^2)}}\frac{Et^2}{a}$

Table 2.1: Critical loading and membrane force of shells

reduction in capacity suggests that eggs (with positive Gaussian curvatures) under hydrostatic pressure (from the hand squeezing) are susceptible to imperfections.

2.3.1 imperfection sensitivity

Some man-made thin shells exhibit similar reduction in load carrying capacity, while others do not. Calladine in his 1995 paper on "Understanding Imperfection-Sensitivity in the Buckling of Thin-Walled Shells" [17] gave an introductory account on the various advances made in this field since the 1940s. He stated that imperfection sensitivity in a structure is usually categorized by three characteristics,

1. buckling capacity is much less than what is predicted by the classical theory. For the case of an axially compressed cylinder, the predicted bifurcation value is as much as six times higher than the actual buckling load [16].
2. experimental buckling capacity is unpredictable and scatters over a wide range, see Fig 1.1.
3. catastrophic failure occurs at on set of buckling.

Graphically speaking, the structure is imperfection sensitive if λ_S in Fig 2.4 is less than λ_C and there is limited post-buckling strength (i.e. point F is always lower than point E).

Kármán was the first scientist to formally attempt an theory trying to predict the buckling capacity of imperfection sensitive shells. He proposed that unlike real columns, shells behave similarly to columns transversely supported by non-linear spring supports, i.e. these springs have a much stiffer tensile response than compressive. Crookedness in these fictitious columns resulted in the three above behaviours that characterize shells.

Around the same time, Koiter investigated the same problem in his PhD thesis [28]. He concluded that this discrepancy is predominately due to *geometrical sensitivity* of these thin shell structures, meaning imperfection in the shape of a shell is the main reason why it may buckle at a lower than predicted load. He further showed that square root of the amplitude of geometrical imperfections is approximately the reduction factor of the buckling capacity of a shell. Eq. (2.2) shows the general equation of post-buckling load displacement relation,

$$P/P_C = 1 + b(\delta/t)^2 \tag{2.2}$$

where P_C is the classical critical buckling load from LBA; δ is the normal-to-surface amplitude of buckling displacement, and t is the thickness. b is a geometrical constant that describes the rate of change of load after buckling.

Using perturbation analysis, Koiter expanded equation (2.2) and described the calculation of load factors in equation (2.3), where λ is the load factor, λ_C is the critical load factor calculated

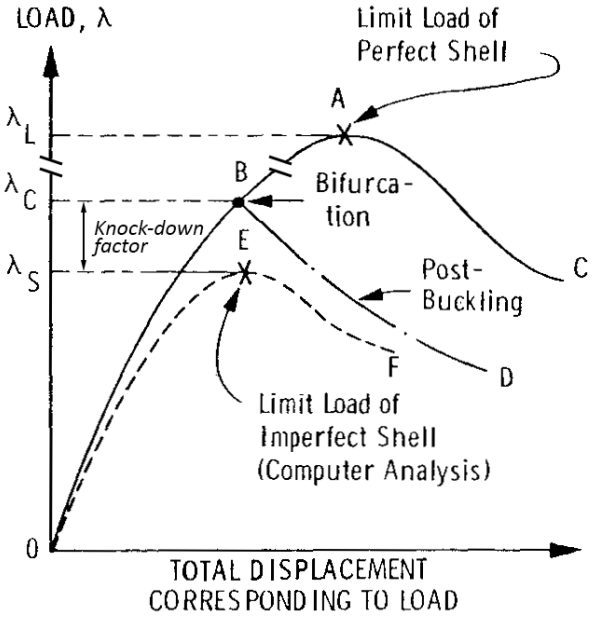

Figure 2.4: Load-deflection curve showing points of interest, path 0AB presents axisymetric deformation, 0BD non axisymmetric deformation, 0EF for a real structure (or GNLA with imperfection). Snap through occurs at point E. [16]

using LBA, w is the normalized bifurcation buckling modal amplitude, and a and b are related to the geometrical and load characteristics of a given structure.

$$\lambda = \lambda_C(1 + aw + bw^2 + ...) \tag{2.3}$$

Depending on the constants a and b, Koiter identified three categories of buckling behaviour (Fig. 2.5).

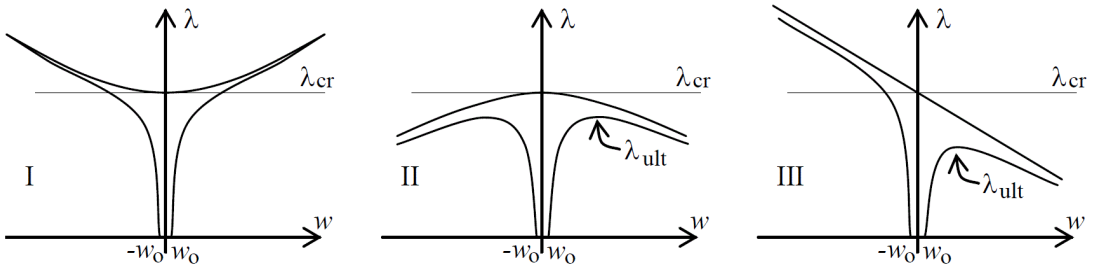

Figure 2.5: Buckling behaviour, left: not susceptible, susceptible, one-sided susceptibility [24]

This classification also defines imperfection insensitive structures as $b > 0$. Bars, plates and other typical structural elements belong to this first category in 2.5 where there exists a stable post-buckling path to prevent the structure from progressively collapsing into a heap of broken pieces.

This is not the case for many shell structures. When the initial part of the post-buckling path has a negative slope, buckling occurs violently and the magnitude of the critical load factor depends on the degrading influence of initial imperfection as in the categories II, and III in Figure 2.5. λ_S is the load factor that an imperfect structure would buckle at, and for categories II and III λ_S is smaller than λ_C, and structures in those categories are imperfection sensitive. The reduction from λ_C is indicated in Table 2.2.

Category	a	b	λ_s/λ_c
I	$= 0$	> 0	Not susceptible to imperfections
II	$= 0$	< 0	$= 1 - 3(-b/4)^{1/3}(\rho w_{imp})^{2/3}$
III	> 0	-	$= 1 - 2(-\rho a w_{imp})^{1/2}$

Table 2.2: Koiter's knock-down factor equations for the different geometries

Note that the above equations assume there exists a unique buckling mode at the critical load. Koiter hypothesized that this is not the cause for axially loaded cylinders where the lowest mode is associated with several buckling loads, or for hydrostatically pressured domes where the critical load is followed immediately by a group of bifurcation loads. For these cases, due to modal interaction, extreme sensitivity is expected and equation (2.3) turns into N asymptotic equations. Note that in equation (2.4) the repeated indices represent summations from one to N.

$$[\lambda/\lambda_c - 1]w_i = A_{ijk}w_{bj}w_{bk} + B_{ijkl}w_{bj}w_{bk}w_{bl} + ... \tag{2.4}$$

This thesis is concerned with shells in the second category where $a = 0$ as the geometry is axisymmetric. It is shown that the most negative b is, the greater sensitivity of the critical load to initial geometric imperfections [15].

2.3.2 Implementation of imperfection

Due to the size and production size and scale (often unique) of shell structures, they are subjected to lenient quality control and large construction tolerances. It is impossible to completely eliminate all imperfections; consequently various methods have been proposed to account for the effect of imperfections in the finite element calculation of the load capacity of shells.

When designing a shell structure, it is almost never the case that the shape is simple enough (e.g. constant curvature) for there to exist an analytical solution. For complex structures where there is no analytical solution, finite element analysis is usually the only viable method forward (aside from physical modelling, for example, by Heinz Isler [19]). To perturb the model geometry with some imperfection, that imperfection must be made known.

While imperfections are random by nature, there has been efforts to investigate and classify geometrical imperfections. Koiter in his initial theory imposes imperfection solely in the shape of buckling modes. The argument was that any imperfection shape may be decomposed into a series of periodic pattern with Fourier series. In a later paper, he applied his method to a more localised, albeit still periodic, imperfection and found the same type of imperfection-sensitivity.

Cederbaum and Arbocz took a probabilistic approach to Koiter's theory by varying two critical parameters, initial imperfection amplitude and the allowable load, in an attempt to construct a reliability design theory [18]. The idea of constructing an imperfection data bank was proposed by Arbocz [11] in 1979. Majority of the data were gathered from electro-plated stiffened and un-stiffened cylinders. However, this pursuit has not produced an actual accessible database in today's definition (i.e. on the internet), rather, the measurements were published in a collection of research articles.

In the aerospace industry, due to the limited number of contractors, contractor-manufacturing-process specific tolerances and imperfection shapes are recognized by the engineers and utilized as the first-estimate of imperfection [23]. A similar method has been in use in structural engineering, where imperfections are classified by the fabrication method [11]. Unfortunately, most advances in this field have been done with axially loaded cylindrical shells as they are easy to test both

experimentally and numerically, and more importantly, they are the most relevant shape for the aerospace industry.

It is clear that when the imperfection cannot be measured or otherwise be made known (e.g. the structure has not been built and the contractor does not have accurate tolerance data), the "worst" imperfection should be assumed and an appropriate knock-down factor be applied. This method may penalize the design unduly and increase the weight and cost enough to overshadow the benefit of a shell structure all together. To obtain a more accurate imperfection representation associated with certain geometries, several methods were proposed.

2.3.3 Finite Element Analysis

In Finite Element Method, the software discretizes a structural continuum into finite elements. Governing differential equations are then solved numerically for each element. Different strategies are implemented to account for both geometrical and physical non-linearities. In the academic context, a shell is a structure whose structural behaviour can be mathematically described by shell elements. A generalized shell element is a 2 dimensional element that describe both in-plane and out-of-plane forces and moments.

Using the previously defined ratio a/t, shell structures can be divided into the following categories [24].

Very thick shells ($a/t \leq 5$)
3-D effects - use 3-D solid elements

Thick shells ($5 \leq a/t \leq 15$)
In-plane membrane forces, out of plane bending and higher order transverse shear included

Moderate shells ($15 \leq a/t \leq 30$)
In-plane membrane forces, out of plane bending and linear transverse shear included

Thin shells ($30 \leq a/t \leq 4000$)
In-plane membrane forces, out of plane bending moments and shear included, though transverse shear deformation neglected

Membrane ($4000 \leq a/t$)
In-plane membrane forces only

Element Formulation

This thesis focuses on the structural behaviour of thin shells where $30 \leq a/t \leq 1000$. There are typically three approaches to analyse such problems. First is to assume that the geometry of individual elements resemble flat plates, and therefore can be solved with plate equations. The issue with such an approach is that the size of each element must be sufficiently small to not misrepresent the overall curvature of the surface. The second is to use Sanders-Koiter equation which incorporates the curvature of each element into its formulation. For simple geometries with constant curvatures (k_x, k_y, k_{xy}), the differential equation can be simplified to Eq. (2.5). While the Sanders-Koiter equation should be able to converge at the correct solution with much less DOFs, no surveyed software packages provide such elements.

$$\frac{Et^3}{12(1-\nu^2)} \bigtriangledown^2 \bigtriangledown^2 \bigtriangledown^2 \bigtriangledown^2 u_z + Et\Gamma\Gamma u_z = \bigtriangledown^2 \bigtriangledown^2 p_z \tag{2.5}$$

The last and the most popular approach is to degenerate a 3-D solid element into a 2-D surface element (Fig. 2.6) [20]. This approach is most commonly implemented in modern FEA software packages and is the one used for this thesis [7]. In Chapter 3, the strategies implemented by various popular FEM packages are compared and contrasted.

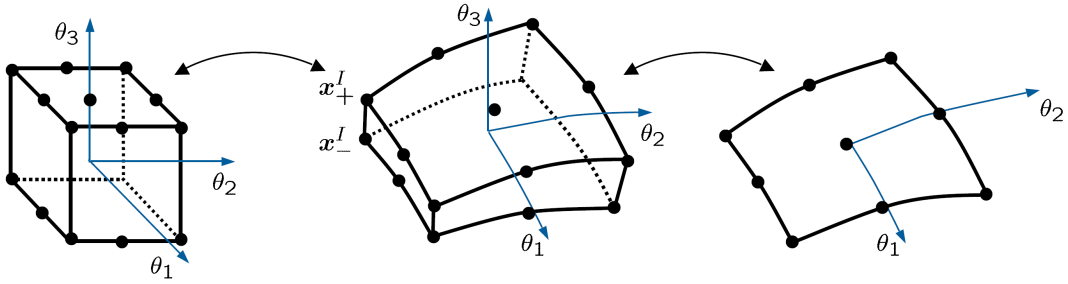

Figure 2.6: Degenerate of 3-D Solid elements [20]

2.3.4 Analysis of buckling behaviour

Linear buckling analysis (LBA) is typically used to find the critical buckling load of a structure. This type of analysis solves the Eigenvalue problem and produces a set of Eigenvalues and their associated vectors. In practical terms, this analysis produces a set of buckling modes each containing a buckling shape, and a load factor. The lowest of these theoretical load factors should cause the structure to fail in buckling.

The Lower bound approach is based on this type of analysis. Eurocode 1993-1-6 (2007) provides detailed and theoretical procedure for the design of thin-shell structures with the focus on the design of cylindrical silos and tanks. The code provides several methods to designers. The first and most often applied method compares resistance stresses from LBA of a perfect shell with the design stresses. LBA calculates the buckling modes of a structure along with their associated load factors λ_{cr}. During design, reduction factors, Eq. (2.6), are then applied to the lowest load factor λ_{cr} to account for geometric imperfections and other non-linear behaviours [12]. It was noted that the Eurocode treats the issue of thin shell buckling with more academic rigour and based on more theoretical ground than other guides (e.g. AISC / ACI) [36].

$$\lambda_{\mathrm{a}} \leq C \frac{\lambda_{\mathrm{cr}}}{\gamma_{\mathrm{m}}} \tag{2.6}$$

where λ_{a} is the allowable applied load factor, λ_{cr} is the lowest buckling load of the perfect structure, C is the empirical 'knockdown' factor, γ_{m} is the traditional partial factor of safety. λ_{cr} can be obtained from Table 2.1 for simple shells of revolution.

This approach is appealing to designers as it is similar to the calculation procedure of other types of structure, and can be easily performed without special training. It is however up to designer's judgement as to what the reduction factors C should be applied for different loading and support conditions. Many experts in the field of shell structures suggest that to design against catastrophic failure, the designer must possess knowledge of the failure mode of the design through either experience or experiment. Without those, reduction factors must be set sufficiently low as to negate many advantages of a shell structure [16]. Furthermore, Von Kármán and Tsien [27] stated that the classical small deflection theory does not produce the realistic buckling shapes, and that the deformed structure may produce buckling shapes with lower associated eigenvalues.

The second approach and the one used in this thesis involves the evaluation of the structure using a geometrically non-linear analysis that includes imperfections. This procedure was used

by numerous scientists in more recent studies of imperfection sensitive problems [35]. A shell is considered imperfection sensitive if the load capacity resulting from a geometrically non-linear analysis (GNLA) with imperfection is less than that from a LBA, as this means the load carrying capacity is reduced by the imperfection. Values for the magnitude and patterns of imperfections of the most basic shapes (e.g. cylinders, spheres) may be found in *Imperfection Databanks* [11], but the Eurocode states that various imperfection patterns be studied if the most detrimental pattern cannot be easily identified. The buckling resistance is calibrated by comparisons between it and the known resistances of other real shells or experimental ones [36].

The last approach is applicable only for the simplest of structures, in which analytical equations based on Koiter's asymptotic theory can be applied directly.

2.3.5 Imposition of Modal Shape

Ramm stated that FEM is suited to geometric imperfections of any shape. He suggested that the geometrical perturbation of a perfect shell is equivalent to a new independent model that can be analysed separately. He further recommended that the imperfection can be based on buckling modes, post-buckling mode, combination of several modes, or realistic deviations.

Performing non-linear analysis directly on a symmetric structure with a symmetric load may produce unrealistic result as buckling is a second order effect that results from either out of balance load or displacement, neither of which existed in a perfect structure. Several studies recommend either to apply a small out of balance load or displacement to the structure to obtain more accurate results. (Note that in the Chapter 6, the effects of combinations and higher buckling modes are investigated.)

Chapter 3

Software Comparison

3.1 Introduction

Bushnell summarized the technical advances in buckling failure analysis up until 1981 in his lecture on *"Buckling of Shells - Pitfall for Designers"*. The aim is always to determine the maximum load-carrying capacity of a structure, and to that end three main approaches were described, one is to adapt Koiter's asymptotic theories to different classes of structures (plates, shells, etc), two is to simulate these behaviours in general purpose computer programs, and three is to develop special purpose programs (e.g. BOSOR5) for the analysis of axisymmetric structures [16]. Both method one and three remain applicable only to a limited class of structures, and are used mainly for academic research. This chapter explores the second method and shows that general purpose programs are capable of accomplishing the eventual goal as the specialized programs but requires far less specialized training.

The first task of this study is to understand the capability of the different software packages to impose geometrical imperfection, and to perform GNLA on the imperfect geometry; and the second is to compare the accuracy, performance, and user-friendliness of the different packages, and to select one package to use for all future studies in this thesis. The packages in question are GSA (General Structural Analysis), ANSYS, and Diana. Abaqus is included as a fourth package when it was discovered that GSA cannot perform GNLA with 2-D elements. The author uses a hyperboloid shaped wet cooling tower as the benchmark model to perform these analyses on with all of the above software packages.

The author spent much time in familiarizing himself with the software packages. This report details the findings and observations made as the author progressed. Note that since it is the author's first time using most of these packages, errors are invariably made. Also note that these software packages are being actively developed, and thin shell buckling is one of the areas where developers are focusing their efforts on. This report only reflects the reality of the time it is being written, and may contain false information when read at a future time. The author aims to perform these analyses with the most time-saving methods possible. As a result, most of these are done with the geometry being generated by a script or a spreadsheet, and the analyses done with the GUI of the packages.

3.1.1 Computer System

All analyses in this section are performed on a notebook PC with the specifications listed in Table 3.1. The versions of the different software packages are also listed for reference.

Computer Model	ASUS K56CA
Operating System	Windows 8.1 Enterprise 64-bit OS
Processor	Intel Core i5-3317U @ 1.70GHz, x64-based
GPU	Intel(R) HD Graphics 4000
RAM	4.00 GB
# of Cores	2

Software packages	**Version**
Oasys General Structural Analysis (GSA)	8.6
Mechanical ANSYS	14.5
TNO Diana	9.44
Simulia Abaqus	6.13

Table 3.1: Computer Specifications

3.2 Hyperboloid Model

Cooling towers dissipate waste heat from processes to the atmosphere. Hyperboloid concrete towers are the largest type of cooling towers. They operate on the principle of evaporative cooling, the warm water circulates to the base of the tower and the temperature lowers as water evaporates. The warm moist air rises to the top of the tower as it is less dense than its surrounding cold air. Hyperboloid cooling towers are often used for their high structural strength verses material ratio. The hyperbolic shape also accelerates the upward convective air flow, increasing the cooling efficiency.

3.2.1 Shape

The geometry of a typical cooling tower is shown in Figure 3.1 [5]. To simplify the geometry and to assist in mesh generation, a single hyperbolic curve is defined using the following parameters obtained from an existing tower,

$$r_{\text{Throat}} = 25.1\,\text{m}\ ;\ r_{\text{Bottom}} = 39.3\,\text{m}\ ;\ h_{\text{Bottom}} = 76.8\,\text{m} \tag{3.1}$$

The equation of a hyperbolic curve is defined in equation (3.2) by constants a and b. By placing the center of the coordinate system at the red circle in Figure 3.1, we could solve for a by setting $x = r_{\text{Throat}}$ and $z = 0$. After a is obtained, b is solved by setting $x = r_{\text{Bottom}}$ and $z = \pm h_{\text{Bottom}}$.

$$\frac{x^2}{a^2} - \frac{z^2}{b^2} = 1\ ;\ a = 25.1\,\text{m}\ ;\ b = 63.7\,\text{m} \tag{3.2}$$

Rearranging the equation, the varying radius x could be found by incrementing the height z. Note that the coordinate system had been shifted to the base of the hyperboloid in equation (3.3).

$$x = r(z) = \sqrt{(z - h_{\text{Bottom}})^2 \frac{a^2}{b^2 + 1}}\ ;\ z = 0 \rightarrow 108 \tag{3.3}$$

The points above $h_{\text{Total}} = 108\,\text{m}$ are discarded since 108 m is the height of the cooling tower, see Figure 3.1. The surface of a cooling tower is formed by revolving this hyperbolic curve around the vertical axis. The shell is assumed to have a uniform thickness of 0.190 m. To find the radius to thickness ratio, or the slenderness ratio, the radius is first calculated,

$$c^2 = a^2 + b^2\ ;\ c = 68.5\text{m} \tag{3.4}$$

Therefore the ratio is,

$$\frac{c - a}{t} = \frac{43.4}{0.19} = 228.5 \tag{3.5}$$

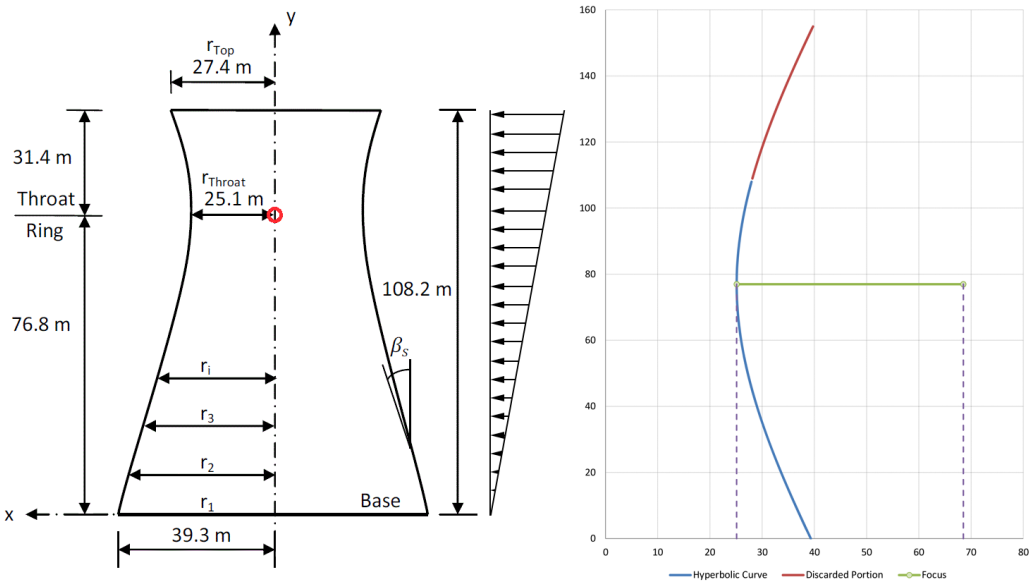

Figure 3.1: Geometry of a typical cooling tower

3.2.2 Mesh

To perform a finite element analysis, one must divide the geometrical shape into a grid of elements. Each element is defined by a set of points and their associated coordinates. A grid of points is generated by assuming a constant increment of 1 m long the z axis, and a constant angle of variation of 2° at odd elevation steps and 4° at even ones (see Figure 3.2). This differences in angular division allows for 8 node elements to be created. Following this grid arrangement, 180 elements are generated per 2 meters.

8 node curved shell elements are used to accurately represent the doubly curved surface. There is no danger of irregular elements in this model as the model could be thought of as a cylinder with a wider top and bottom. The element aspect ratio is kept as 1 at the neck of the tower, and the maximum ratio of 2 occurred at the base.

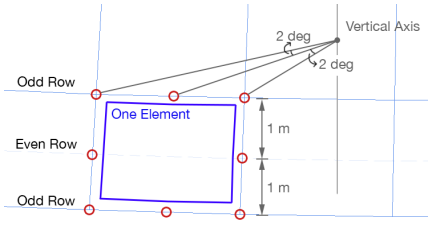

Figure 3.2: Geometry of the mesh, and size of a typical shell element

There are 6 degrees of freedom (DOFs) at each of the nodes, three translational, and three rotational. The drilling rotations can be eliminated to reduce the number of equations. Note that the mesh density is not refined at this stage since all results are relative between the packages. This mesh results in 4860 elements, 14760 nodes and 88560 DOFs.

3.2.3 Material

A generic reinforced concrete material is defined. Since this thesis is more interested in the relative effect of imperfection, and not the failure modes, the material properties are crudely

defined as a weighted average between steel reinforcement and concrete.

$$E_{equiv} = 22 \times 10^9 \,\text{Pa} \; ; \; \nu = 0.2 \tag{3.6}$$

3.2.4 Loads

For the purpose of this study, only the self-weight of the structure is applied. The initial load factor is set as 1.

$$g = 9.81 \,\text{m/s}^2 \; ; \; \rho = 2400 \,\text{kg/m}^3 \tag{3.7}$$

During GNLA, the gravitational acceleration, g, is linearly incremented.

3.2.5 Supports

The base ring of the shell is pinned against translation in the three axes but allowed to freely rotate. This simulates the real structure where the shell is supported by a ring beam and a series of diagonal ($\wedge$) shaped struts. In the real structure, there is a ring beam at the base and the top of the structure. These are summarily neglected.

3.3 GSA - General Structural Analysis

Below is a detailed report on the performance of each FEM packages. GSA is a Structural Analysis and Design package produced by Oasys, the software house of Arup. Its aim is to provide engineers with efficient, reliable and capable FEA tools. Comparing to the other two packages, GSA is arguably more user friendly and intuitive, though this comes at a cost as it lacks many of the features that are essential to this project. Its incremental non-linear performance when analysing larger models is found lacking when compared with Diana or ANSYS.

3.3.1 Model

GSA allows data to be directly copied and pasted from Excel. This greatly simplifies the nodal coordinate, and element connectivity inputs. The resulting structure is immediately visible on the graphical display, and sections can be extracted by dragging a window across. Figure 3.3 shows an example of such an interface.

GSA is currently incapable of performing analyses with 8 node curved elements; such an element does exist in the element library, though it is used exclusively for pre-processing at the moment. Therefore 8 node flat elements are implemented by modifying the coordinate of the middle nodes to be the average of their neighbours. Self-weight is added to the structure, and pinned connections are assigned to the nodes on the bottom ring through the graphical interface as well.

3.3.2 Linear Elastic Analysis

A maximum deflection occurs at the top of the structure as expected. The magnitude of the Z-directional deflection is $-4.5\,\text{mm}$. The sum of the reaction forces R_z is $89.76 \times 10^6\,\text{N}$, similar to what is calculated in the theoretical section with a difference of $1.8\,\%$.

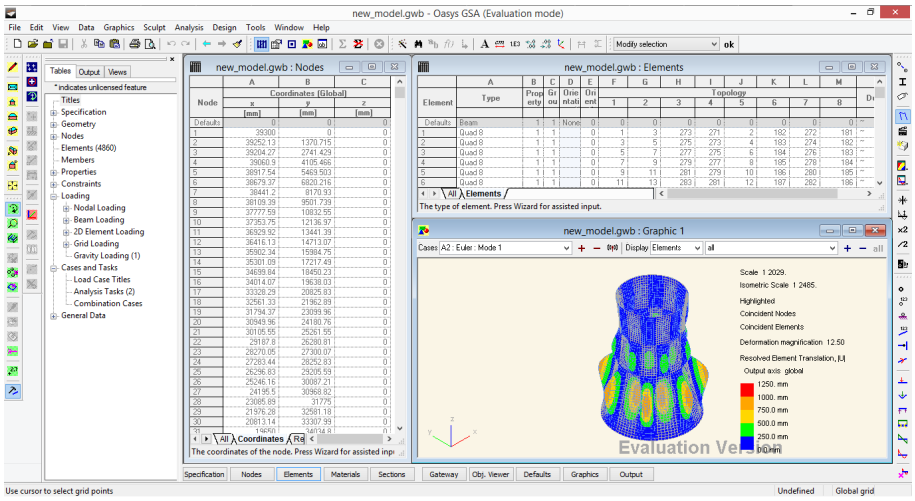

Figure 3.3: GSA user interface showing node and element input windows, and a graphical display

3.3.3 Linear Buckling Analysis

GSA's Euler modal buckling analysis produces modal shapes similar to those produced by the other packages as shown in Figure 3.4. The lowest load factor resulted is 19.98. This LF is significantly higher than what is produced by the other packages. This is attributed to the use of flat shell elements as oppose to curved elements, as an equivalent model in ANSYS using SOLID181 elements resulted in the same LF as GSA.

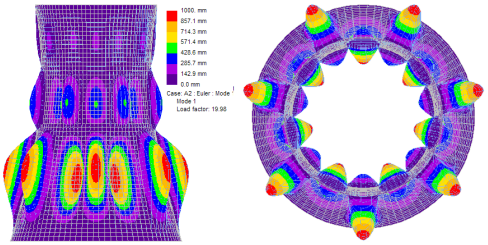

Figure 3.4: GSA LBA mode 1

The resulting mode 1, 2, 3 and 4 consists of three layers of buckles with each layer containing 14 buckles, 7 outward, and 7 inward. The deflection distribution of mode 1 and 2 are as follows (scaled to a maximum of 1000 mm); top layer: $\pm$ 150 mm; middle layer: $\pm$ 450 mm; base layer: $\pm$ 1000 mm.

Similar FEM analysis on a cooling tower was done by Krätzig, et al. to show the functionality of his proposed finite element [30]. The resulting linear buckling shape is presented in figure 3.5. His model is significantly more complex, and also geometrically much larger, though some comparisons can be made between his un-stiffened model and Figure 3.4. There are only two layers of buckles in the vertical direction of his model as its height to width ratio is smaller. The bottom buckles emerge higher up in elevation in his model, suggesting that the boundary layer is stiffer than the model in this study (his boundary conditions possibly included rotational stiffness). In the tangential direction, the number of buckles (bow-in and bow-out) however remain identical to the model in this study (7 buckles in the half shell). The inclusion of stiffeners also offer some insights to the buckling behaviour. When lateral deformation is constricted, largest buckles occur intra-stiffener.

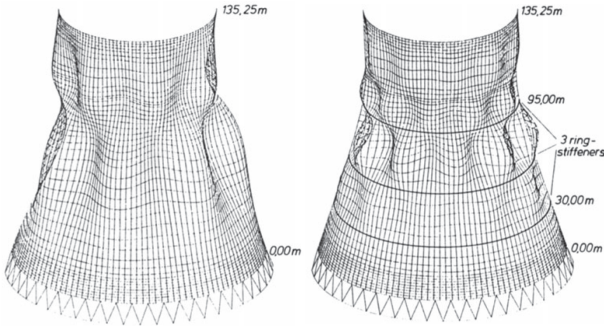

Figure 3.5: Buckling modal shape resulting from Kratzig's analysis

3.3.4 Imperfection

GSA can rather easily impose initial deformations in the shape of buckling modes with user defined magnitude. 100 mm is imposed as the maximum magnitude of imperfection. 100 mm is on the same magnitude as the thickness of the shell, and is a sufficiently accurate estimate since we are more interested in the relative effect of imperfections.

GSA 8.6 Tools ▼ Manipulate Model ▶ Create New Model from Deformed Geometry ...

From the prompt window, the user can select from which case (Load, or combination) the deformation originates. The user can also choose between applying a scale factor or using a maximum displacement (with automatic scaling). Rotation can also be accounted for.

Note that since the 8 node flat elements are usually wrapped out of plane by the modal deformation, the usage of flat shell elements is necessary but not the most suitable. This becomes a moot point however since no further analyses can be done with GSA.

3.3.5 Geometrically Non-linear Analysis

GSA does not have the ability to perform non-linear buckling analysis on 2-D elements. This restricts the usage of GSA to serve as a checker of the buckling modes and load factors.

3.4 ANSYS

ANSYS is one of the most popular finite element analysis and computer aided engineering software. It markets two suite of products, Simulation Technology (Structural Mechanics, Multiphysics, etc) and Workflow Technology (Workbench Platform, High-Performance Computing, etc). The Workflow Technology compliments the Simulation Technology by improving productivity, and usability [8].

The author wrote an APDL (ANSYS Parametric Design Language) script to generate the model, the mesh, and the input parameters such as density, thickness, and load. In the interest of saving time, the model is imported into Workbench for the subsequent analyses. See Figure 3.6 for a detailed sequence description.

3.4.1 Element Type

SHELL281 is an 8-Node Structural Shell element with quadratic interpolation functions, Eq. (3.8) [4]. The element has eight nodes with six degrees of freedom at each node: translations in the x, y, and z axes, and rotations about the x, y, and z-axes. It is most accurate for linear, large

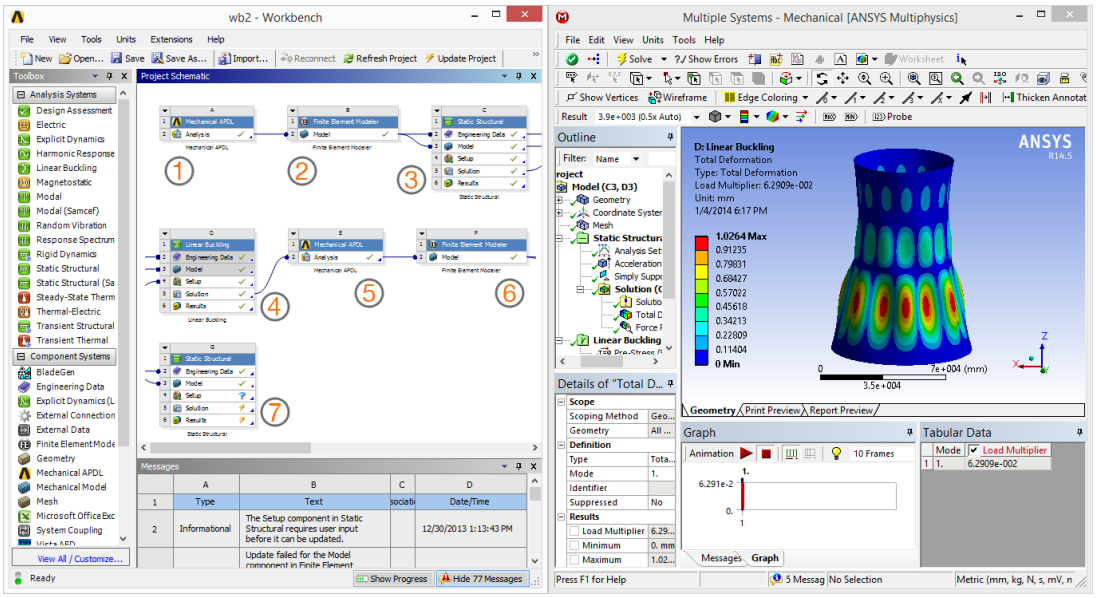

Figure 3.6: ANSYS Workbench interface; 1. APDL module to run the script, 2. importing the resultant geometry, 3. Static Structural module to run the linear elastic analysis, 4. Using the load from 3, and running the linear buckling analysis, 5. Application of imperfection through a APDL script, 6. importing the resultant geometry again, 7. Non-linear Analysis

rotation, and large strain non-linear analyses. Initial shell thickness can be specified at each node, and change in shell thickness is also accounted for in non-linear analyses. The formulation is based on logarithmic strain and true stress measures. The element kinematics allow for finite membrane strains (stretching). However, the curvature changes within a time increment are assumed to be small.

$$\begin{aligned} u =& \frac{1}{4}(u_I(1-s)(1-t)(-s-t-1) + u_J(1+s)(1-t)(s-t-1) + u_K(1+s)(1+t)(s+t-1) \\ &+ u_L(1-s)(1+t)(-s+t-1)) + \frac{1}{2}(u_M(1-s^2)(1-t) + u_N(1+s)(1-t^2) \\ &+ u_O(1-s^2)(1+t) + u_P(1-s)(1-t^2)) \end{aligned} \tag{3.8}$$

3.4.2 Linear Elastic Analysis

ANSYS does not differentiate between linear and non-linear analyses, rather, non-linearity and large deformation are provided as options within the static structural analysis.

The geometry is imported as an APDL script, and linked to the static structural module within Workbench. A downward acceleration of $9.81\,\mathrm{m/s^2}$ is applied to the structure. As a result, a maximum deflection occurs at the top of the structure as expected. The magnitude of the Z-directional deflection is $-5.73\,\mathrm{mm}$. The sum of the reaction forces R_z is $89.78 \times 10^6\,\mathrm{N}$, similar to what is calculated in the theoretical section with an percentage difference of $1.8\,\%$.

3.4.3 Linear Buckling Analysis

The geometry and load is linked from the static linear module to the buckling module. 20 modal shapes are requested. The block Lanczos solver is used as it is currently the only option available. Lanczos alogrithm is an iterative energy method to find eigenvalues and eignvectors

of a square matrix. It is particularly useful when dealing with very large sparse matrices. The symmetric pairs are observed as expected, and the load factors are similar to that of Diana and Abaqus.

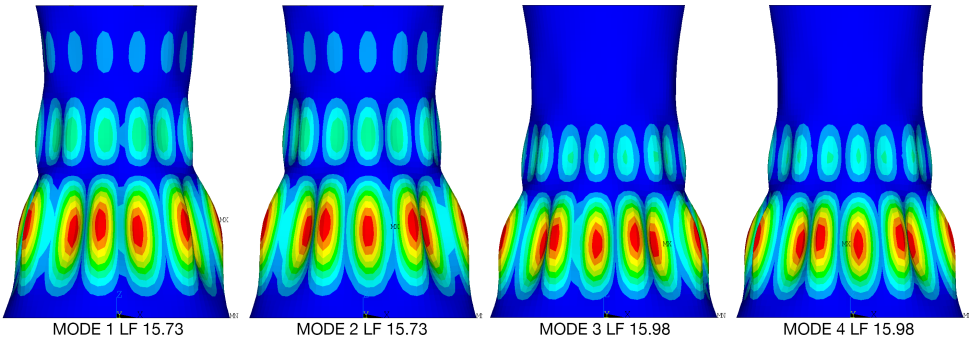

Figure 3.7: First four buckling mode shapes resulted from LBA

3.4.4 Imperfection

As instructed by an ANSYS publication [26], a short APDL script is executed to impose the modal shape onto the existing geometry. This script can be executed for as many times as necessary to impose multiple deformations to the geometry.

```
/prep7
   UPGEOM, 100, 1,1,file,rst   ! UPGEOM, maximum deflection, Load step, Sub step,
    File name
FINISH
```

3.4.5 Geometric Non-linear Analysis

Geometric non-linear analysis is performed in Workbench's static module with large deflection (NLGEOM [6]) toggle switched on. Since post-buckling behaviour is not of interest at the moment, stabilization is not implemented, nor is the arc-length convergence method.

It is not discovered until a later stage that ANSYS is capable of automatically determining load steps (AUTOTS [6]), or that it can bisect when convergence doesn't occur. Therefore during this study, the load steps are entered manually. Table 3.2 shows the load factors. The first trial increments the load factor by one at every load step until 16, 16 being one higher than the load factor given in the linear buckling analysis. The analysis fails to converge at step 11. In the second trial, starting at step 11, the load factor is changed to an increment of 0.05 or 5 % instead.

The second trial results in a load factor verses deflection curve plotted in Figure 3.8. It is assumed that when divergence occurs at the on-set of buckling. Since we are not interested in the actual failure of the structure, the on-set of buckling at a load factor of $\lambda_{\text{ult}} = 11.92$ is deemed to be the capacity of the structure. This value is smaller than the load factor from the linear buckling analysis. This fits the expectation as from the closely spaced load factors, the structure appears to be slightly sensitive to imperfections.

This value is consistent with what is given by the other software packages, and the differences between the different packages may lay in their convergence criteria.

LF	Trial 1 m/s^2	LF	Trial 2 m/s^2
1	9806.6	1	9806.6
2	19613.2	2	19613.2
3	29419.8	3	29419.8
		⋮	
8	78452.8	8	78452.8
9	88259.4	9	88259.4
10	98066.0	10	98066.0
11	107872.6	11.000	107872.6
12	117679.2	11.005	107921.6
13	127485.8	11.010	107970.7
14	137292.4	11.015	108019.7
			⋮
		12.185	119493.4
		12.190	119542.5
		12.195	119591.5
		13.000	127485.8

Table 3.2: Load Factor Steps

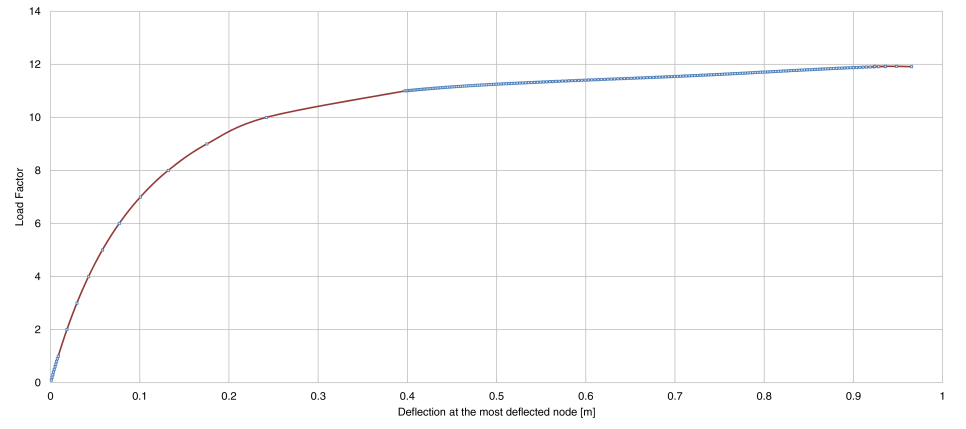

Figure 3.8: ANSYS load factor vs. deflection curve

3.5 Diana

3.5.1 Model

Diana itself is a finite element solver, and it relegates pre- and post-processing duties to other packages. Either iDiana or FX+ can be used for those purposes. Since the trial model (the hyperboloid) can be easily described analytically, the pre-processing is done via a vba macro that generates a file in the format of Diana's input files. This also allows for smaller tolerance errors, and greater user control. The analyses are done within Diana through its GUI. Diana provides 8 node curved shell elements both with (CQ48S) and without (CQ40S) drilling rotation DOFs. Input files can be imported by the following procedure.

DIANA Analysis setup ▼ Input data file ▼ Add .dat file

3.5.2 Linear Elastic Analysis

The following procedure in Diana starts the linear elastic analysis.

DIANA ▼ Select analysis type ▼ Structural linear static

Diana produces similar results in both deflection and support reaction as the other packages.

3.5.3 Linear Buckling Analysis

The modal buckling analysis is called Structural Stability analysis in Diana. The number of modes to be solved is set by the user, so is the output format. The user can request Diana to output the result in a table or as a model for the post-processor. Both are requested since both the load factors and the shapes are of interest.

The Diana solver package itself is relatively easy to use and understand. The documentation and the examples are tremendously useful in aiding novices. The iDiana pre- and post-processor however proves to be user unfriendly. So far the only commands used are the ones offered by the examples, in particular, the cylindrical shell example in the stability category. The following is a post-processing script that displays the displacement contour.

```
# To obtain load factors
UTILITY TABULATE LOADCASES

# To obtain modal shapes
RESULTS LOADCASE MO1
# MO1 for mode one, MO2 for mode two, etc.
RESULTS NODAL DTX....G RESDTX
!Displacement
PRESENT SHAPE

# To obtain modal displacements
CONSTRUCT COORDSYS CYLINDRIC CS1 Z
RESULTS TRANSFORM LOCAL CYLINDRIC CS1 RR
PRESENT CONTOUR LEVELS
```

3.5.4 Imperfection

Within the buckling analysis, Diana allows for the user to apply imperfections in geometry to the structure. The imperfections could take one of three shapes: a buckling mode, user defined, and random. Each accepted a maximum deflection as an input. For this study, the first buckling mode is selected, with a maximum deflection of 100 mm. This imperfection is carried through into the subsequent analyses. The feature of including imperfection of a random shape is of value when trying to show that modal shaped deformation always cause the largest reduction in capacity.

```
Structural stability
   Structural stability Settings
     Eigen Setup
       No - Incorporate initial displacements
       Yes  - Imperfection
         Pattern  ->  Buckling mode
         Mode number  1
         Maximum value of imperfection 100 mm or 0.1 m
```

3.5.5 Geometric Non-linear Analysis

The second type of analysis done in Diana is GNLA. Updated Lagrange is selected as oppose to Total Lagrange to ensure that the geometry from the previous step's equilibrium state is used as the reference geometry for the next iteration. Load steps are then defined. The method of iteration governs the speed of convergence but not the result. The convergence norm has the same effect. These are left to their default values.

```
Structural Non-linear
  Structural non-linear Settings
    Type
      Geometrically non-linear
        Geometrical Settings
          Type of geometrical non-linearity -> Updated Lagrange
    Execute
      Load steps -> Settings
        Execute load steps
          Steps
            Iteration based step sizes
            Maximum step size -> Set this low enough to ensure divergence does
   not occur at near failure
             (resulting in ill-conditioned matrix error)
            Others can be adjust by trial and error
```

To prove that without imperfection, the model would behave completely linear elastically, both models (perfect and perturbed) are run through the same analysis with the same load steps. From the above deflection plot, we observe that the structure behave linearly until the very last load step. The last load step shows a structure failing in the modal shape. I hypothesize that this is due to a precision issue within the software itself as all other parameters are perfectly symmetric and no out-of-plane components are observed. Note that the plot would indicate that the structure behaves non-linearly from the start despite the material being linear elastic. The analysis diverges at a load factor of 11.20. This result follows a very similar load deflection curve as ANSYS despite appearing numerically different.

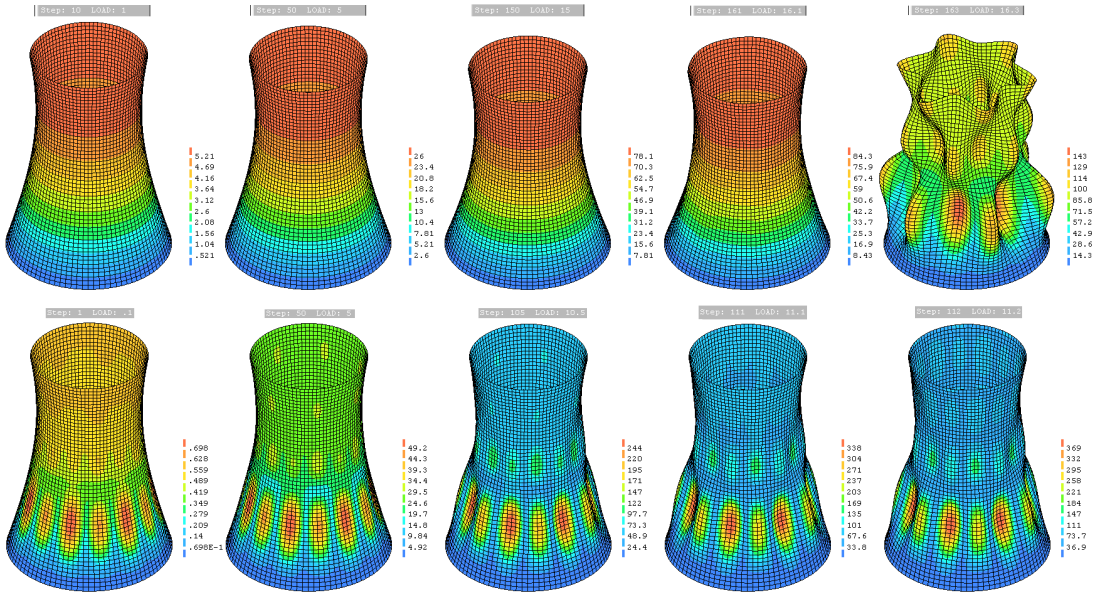

Figure 3.9: Diana - displaced shapes, comparison between perfect and imperfection model

3.6 Abaqus

Abaqus is another popular FEA package widely used in academia and industry. It was initially designed to analyse very non-linear behaviours (e.g. deformation of rubber) and that is still its advantage over other packages. Its operation sequence is similar to that of the other packages. A model is generated in the pre-processor, analyzed, and displayed in the post-processor. Its utilization of Object Oriented Python as a scripting language presents a large advantage over other packages that have limited scripting ability.

The author has discovered that the documentation is difficult to navigate through. Though since all actions within the GUI are recorded as input commands in the command file, it is easy to replicate them in the overall input. As with the other packages, the author chose the fastest method to generate and analyze this structure. In this case, it was a input file including all load steps ran directly through the command interface.

3.6.1 Linear Elastic Analysis

Abaqus produced similar results as the other packages using the following input.

```
# STEP: SW
#*Step, name=SW, nlgeom=NO
#*Static
1., 1., 1e-05, 1.

# *Dload
, GRAV, 9.806, 0., 0., -1.
*End Step
```

3.6.2 Linear Buckling Analysis

Abaqus recommends the use of 9-node elements when analysing the buckling behaviour of doubly curved shell structures. It states that if the middle node is not specified (as in 8-node elements),

the internally calculated middle node may not actually be on the curved surface, thus leading to inaccurate solution. This advise is not heeded since the written script does not generate such nodes. As the calculated buckling capacity is similar to ANSYS, the geometry generating script is not changed.

```
*Step, name=Euler, nlgeom=NO, perturbation
*Buckle
20, , 28, 100
#** BOUNDARY CONDITIONS
*Boundary, op=NEW, load case=1
_M3, PINNED
#** LOADS
*Dload
, GRAV, 9.81, 0., 0., -1.
*End Step
```

The resulting first 2 pairs of eigenvalues are 14.72 and 14.97. Note that Abaqus indicated that the buckling load estimate equals to dead loads plus the eigenvalue multiplied by any live loads. Therefore one should be added to the eigenvalues, giving 15.72, and 14.97, which is identical to that of the other packages.

```
BUCKLING LOAD ESTIMATE = ("DEAD" LOADS) + EIGENVALUE * ("LIVE" LOADS).
    "DEAD" LOADS = TOTAL LOAD BEFORE *BUCKLE STEP.
    "LIVE" LOADS = INCREMENTAL LOAD IN *BUCKLE STEP
```

3.6.3 Imperfection

Following the documentation and the sample file called "Buckling of an imperfection-sensitive cylindrical shell" in the following directory,

ABAQUS Example Problems Guide ▼ 1. Static Stress/Displacement Analyses ▼ 1.2 Buckling and Collapse Analyses▼ 1.2.6 Buckling of an imperfection-sensitive cylindrical shell

The **IMPERFECTION* command is used to impose the first modal shape to the model.

```
#**File name, and load step
*IMPERFECTION, FILE=buckling,STEP=1
#**Modal number, and scale factor
1,0.1
```

It is noted that additional lines can be appended to the end of the above code to impose additional buckling modes onto the structure.

3.6.4 Geometrically Non-linear Analysis

Abaqus provides the option to allow large deformation (NLGEOM), to create automatic or manual load stepping (*STEP), and arc-length step control.

```
#**This is step one of the non-linear analysis. The load is set to increment by a
    load factor of one. Actual substep increments are determined by Abaqus.
#** STEP: NL1        # Step 2 would look NL2
*STEP, name=NL1, nlgeom=YES, solver=ITERATIVE,AMPLITUDE=RAMP
*STATIC
```

```
1., 1., 1e-05, 1.      # Step 2 would look 1., 2., 1e-05, 1.
*DLOAD
, GRAV, 9.81, 0., 0., -1. # Step 2 would look , GRAV, 19,62, 0., 0., -1.
#** OUTPUT REQUESTS
#** Get reaction force from node set _M3, ie. the bottom nodes
*RESTART, write, frequency=0
*NODE PRINT,NSET=_M3,SUMMARY=YES
RF
#** Get displacements from node set _M5, ie. the top nodes
*NODE PRINT,NSET=_M5,SUMMARY=YES
U
*End Step
```

The resulting load deflection curve compares well with the other packages, so no further investigation is done.

3.7 Comparison with theoretical Solution

3.7.1 Linear Static

Linear static analysis is performed mainly to ensure that the geometry is properly connected, and that there is no unit inconsistency. The check is done by summing the reaction forces in the vertical direction, and equating that to the theoretical weight of the structure. The theoretical weight of the structure is calculated as follows,

$$R_z = \sum_{z=0}^{108} 2\pi r(z) \cdot \rho g h; h = 1000\text{mm} \tag{3.9a}$$

$$= \sum_{z=0}^{108} 2\pi \sqrt{(z - h_{Bottom})^2 \frac{a^2}{b^2 + 1}} \cdot \rho g h \tag{3.9b}$$

$$= 88.16 \times 10^5 \,\text{N} \tag{3.9c}$$

This load will be increased until the structure fails in buckling. Note that buckling will never happen in theory in a perfect structure as the material is linear elastic and the load, the boundary conditions and the geometry are all axisymmetric. The linear elastic results is in Table 3.3. While

		GSA	ANSYS	DIANA	ABAQUS
Reaction Force	MN	89.76	89.78	89.81	89.77
Deflection	mm	-4.5	-5.723	-5.723	-5.721

Table 3.3: Linear elastic reaction forces and deflection

all the packages results in similar reaction forces, they are slightly different from the calculation. This is due to the fact that summation is used in the calculation as oppose to integration. The discretization resulted in slight difference in the volume of each height layer.

3.7.2 Geometrically Non-linear Analysis

The highest load factors reached in Figure 3.10 are assumed to be where the buckling bifurcations start. The values are listed in Table 3.4.

Table 3.5 shows the first twenty load factors generated from each of the packages. Note that GSA produces results significantly different from the other packages.

Package	Load Factor	C mm
GSA	-	-
ANSYS	11.92	1.32
Diana	11.20	1.40
Abaqus	11.70	1.34

Table 3.4: Load factors from non-linear analyses

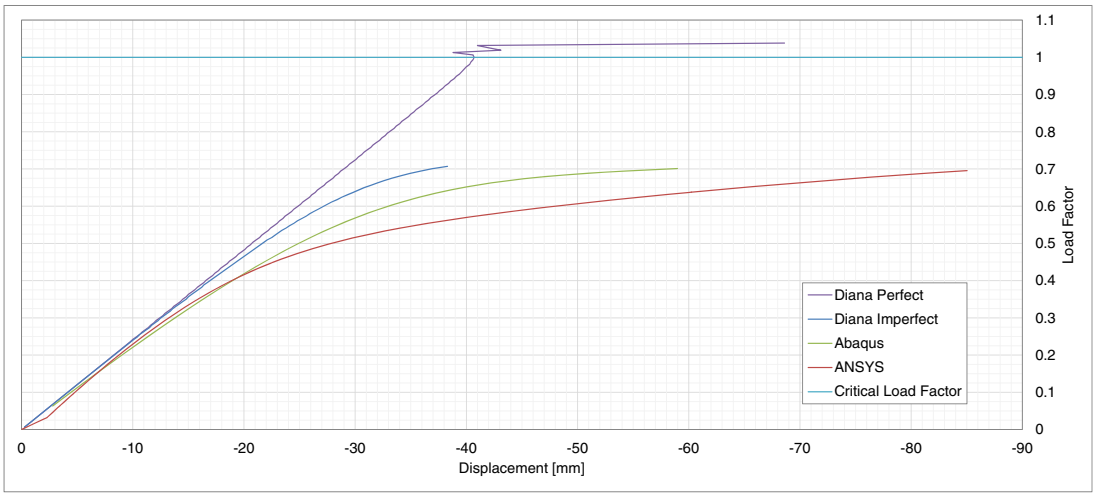

Figure 3.10: Force-deflection curves of the different software packages

3.7.3 Computation performance

Several measurements are used to compare the software packages. Table 3.6 lists the computer performance data generated by the output files of each package. Note that since the majority of resources are spent on the non-linear portion, GSA data is not realistically comparable and are excluded.

3.8 Conclusion

4 FEA packages are tested for their capability in analysing thin shell structures. A hyperboloid shaped cooling tower is used as a reference structure, with the self-weight as the sole load case. The sequence of analyses performed are as follows. Linear elastic analysis is done to verify the geometry, linear buckling analysis calculates the load factors and the modal shapes, imperfection is applied to the structure in the shape of the first buckling mode, and geometrically non-linear analysis is performed to obtain the realistic capacity. Memory usage, file size and CPU-time are recorded and compared. The user interfaces are assessed for their intuitiveness.

GSA is a structural analysis program developed by and for engineers. It is concluded that GSA lacks critical capabilities that forces it to be excluded from the selection. The reasons being: it cannot utilize meshes of non-flat shell elements; and it cannot perform non-linear buckling analysis on 2-D elements. Though it is worth noting that GSA serves as an excellent geometry viewer and validator, and buckling modal shape checker. Abaqus is substituted in as the third viable package for comparison as a result.

With Diana, ANSYS, and Abaqus, it is a general observation that the pre-processor included are difficult to use and impractical for all but the simplest geometries (GSA does not contain a

Mode #	Load Factor			
	GSA	ANSYS	DIANA	ABAQUS
1	19.98	15.73	15.70	15.72
1	19.98	15.73	15.70	15.72
3	20.29	15.98	15.94	15.98
4	20.29	15.98	15.94	15.98
5	20.73	16.32	16.28	16.31
6	20.73	16.32	16.28	16.31
7	21.40	16.86	16.83	16.86
8	21.40	16.86	16.83	16.86
9	23.00	18.12	18.10	18.12
10	23.00	18.12	18.10	18.12
11	23.60	18.58	18.53	18.56
12	23.60	18.58	18.53	18.56
13	24.90	19.62	19.58	19.61
14	24.90	19.62	19.58	19.61
15	24.92	19.63	19.60	19.63
16	24.92	19.63	19.60	19.64
17	25.34	19.97	19.93	19.67
18	25.34	19.97	19.93	19.67
19	25.55	20.12	20.09	20.11
20	25.55	20.12	20.09	20.12

Table 3.5: Buckling modes and associated load factors

		GSA	ANSYS	DIANA	ABAQUS
Total CPU Time	s	-	1004	2892	4205
Max. total memory	MB	-	926	2560	486
Folder Size	GB	-	1.56	9.23	0.493
Cost of a License [1]	€	1,750	13,000	10,000 to 40,000	?

[1]With the exception of GSA, all have refused to provide an official general quote

Table 3.6: Analyses performance data of geometrical non-Linear analyses

full pre-processor). This is especially true should the user want to create a model from scratch. It is frequently easier to either generate the model through a script, or import the surface from a CAD program and utilize only the meshing ability of the pre-processor (which can be advanced and excellent).

With the exception of GSA, the three remaining packages successfully performed all the tasks with relative ease. Specifically, all fours packages have the capability of adding geometric imperfection in the shape of one buckling mode to shell finite element models.

The FEA solvers in the three packages offered similar results from the linear elastic and linear buckling analyses. Results from the geometrically non-linear analyses gave not insignificant differences, especially in the stiffness behaviour. This is due to the difference in element formulation and other solver parameters, as well as numerical loss-of-precision. The final capacities obtained are comparable. This shows that the procedure outlined in Chapter 1 can and should be used when designing thin shell structures in place of the Lower Bound Design method. This is particularly true since the mesh geometry needed by the linear buckling analysis can be reused

for subsequent non-linear analyses, the additional amount of effort in generating the model is negligible. The computation time in GNLA is significant though it does not require man-hour input.

Each package also has its own advantages and disadvantages. DIANA offers a relatively gentle learning curve; one is able to construct the model, perform the analyses, and obtain reasonable results without wasting time. Though this comes with a cost; Diana is not as flexible, and its performance lags behind the other two packages. At the time of writing, DIANA does not have a scripting language, thus forcing the user to either use its graphical pre-processors (iDIANA or FX+) or to generate the input file externally. The imposition of more than one buckling mode is a challenge as this task is associated with the Structural Stability analysis and not separately as its own task. Lastly, DIANA's result files at ˜10GB are one magnitude larger than that of ANSYS'. This presents a challenge should a sensitivity analysis be required and many models must be analysed.

ANSYS provides a friendlier and more robust user interface, both through Workbench (and the pre-processor within), and through APDL, the scripting language that underlines all of ANSYS. Its imperfection imposition is a separate function, and can be performed at any stage of the analysis to impose imperfection of any shape. In addition, nodal coordinate change is a separate function that can be utilized to achieve the same task. Its disadvantages lie in its complexity. As ANSYS can be used for all types of FEM analyses (e.g. CFD, electromagnetism, thermal-mechanics, etc), its terminology is extremely general, thus leading to confusion when attempting to find the relevant information. While well documented, ANSYS' manual is broken into several books, each containing thousands of pages and is difficult to parse through. Through all the available commands in APDL, it is difficult to discern the effect of each.

Abaqus is similar to Diana in that an input file can be generated externally and directly imported. However, it also provides the scripting option should the user be familiar with Python. While its documentation is also difficult to use, the graphical interface records all user actions and save them as a input file so trial and error works fairly well. Its capabilities to impose imperfection and its non-linear solver function similarly to those of ANSYS'. It is noted that the Riks analysis (called arc-length method in ANSYS) is more robust and user-friendlier than ANSYS.

ANSYS is chosen to be used for the remainder of this thesis for its capability and performance, despite being difficult to use initially. From my impression at several design firms, ANSYS is more well known in the industry. The license fee is potentially cheaper. It has a good balance between file size, calculation speed and memory usage. Though the selection is dependent on personal preference, availability of licenses, and other facts that are not related to the packages' capabilities.

Chapter 4

Study of cylinders

4.1 Introduction

Thin cylindrical shells are widely used in the aerospace industry, most satellites have extremely thin shells as their casing, airplane fuselage is essentially a stiffened cylindrical shell, and so on. The boom in space exploration led to a surge of research initiatives at NASA in the 1960s and onward. Cylinders were widely studied also due to a large discrepancy between the experimental and the theoretical results. In this thesis, in hindsight, an axially compressed cylinder would have been a better candidate for the software assessment as well, as it is an extensively studied imperfection sensitive buckling problem.

Civil engineers have long been utilizing the cylindrical shape for storage silos and tanks, though since these structures usually loaded by their content inside, imperfection sensitivity is not an issue. Only in cases when there is a heavy wind load on a near empty tank, or when there is ground acceleration do these shells buckle. The investigation of real silo structures is described in chapter 5.

This chapter is devoted to showing that the general purpose FE program ANSYS is capable of delivering realistic results to the axially compressed cylinder. This is done by comparing the results from ANSYS to both experimental data, and to Koiter's theoretical formulation, Eq. (2.3).

4.2 Geometry

The length and width of the cylinder model are chosen to resemble a typical test setup. The a/t ratio is set at 500. The applied load also simulates a typical compression test condition where the test apparatus press downward onto the top ring of the cylinder. To prevent in-extensional deformation, the same ring is restrained laterally. The bottom ring is pin supported.

While appearing simple, many factors influence the behaviour of the cylinder and the analysis. In particular, depending on the mesh size, nonuniformity near the edges may not be present in the LBA, increasing the predicted critical load by 8-20% [16]. Therefore the surface must have sufficient mesh density to trigger the buckling modes along the top and bottom edge. The resulting mesh contains 4860 elements, and 88560 DOFs.

4.2.1 Loading

The compression load is applied first as a uniform downward edge pressure. This force controlled load application resulted in asymmetrical buckling modes along the xy plane, and edge warping

as shown in Figure 4.1. Warping of the loaded edge can be eliminated by applying the load through displacement as suggested by Ramm [38]. Therefore to obtain perfectly symmetrical buckling modes, and thus better simulate the test set-up, displacement controlled method is used where the top ring is simultaneously moved downward by a fixed magnitude of 0.025 m. This loading was referred to as "end-shortening" by Kroplin in his study of cylinders ($a/h = 200$) with imperfection, his results are used for comparison in Chapter 6 [31]. The magnitude is set sufficiently small to improve convergence.

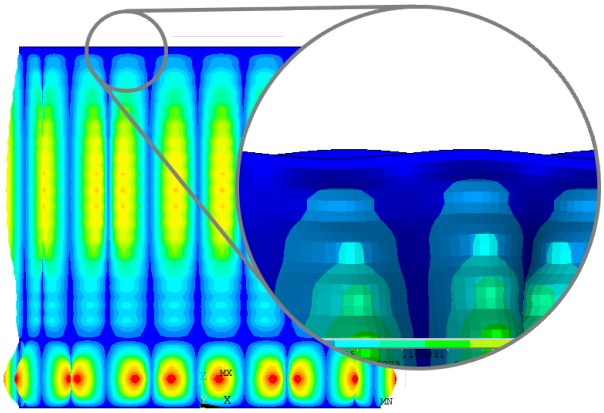

Figure 4.1: Asymmetric modes with force control

4.2.2 Comparison between load application methods

Since displacement controlled loading is impossible to apply in almost all real structures, the difference between force and displacement control is compared here. The procedure remains identical in all other respects; first LBA is performed to obtain the critical load factor, then imperfection is applied to the structure in the shape of the first buckling mode with a maximum amplitude of $t/2$. GNLA with large deformation enabled then calculates the load displacement behaviour of the structure. The only difference is in the application of the load. In the first model, uniform edge pressure is incremented at every load step, whereas in the second model, the increments are applied as uniform edge displacements.

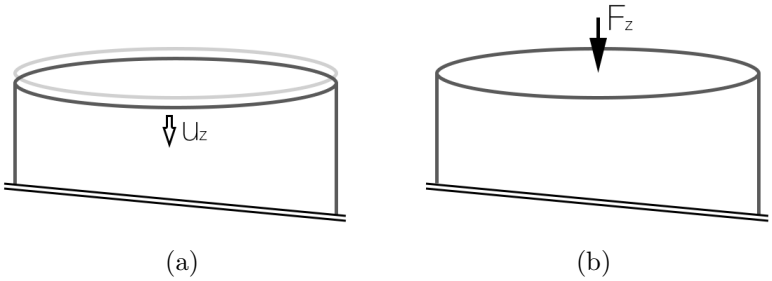

Figure 4.2: (a) Displacement controlled loading (b) Force controlled loading

The eigenvalues resulting from a LBA is calculated from either of the two conditions in Figure 4.2.

$$u_{\text{cr}} = \lambda_{\text{cr}}^{\text{D}} \cdot u_z \tag{4.1}$$

$$F_{\text{cr}} = \lambda_{\text{cr}}^{\text{F}} \cdot F_z \tag{4.2}$$

To show that the critical load factor from displacement controlled loading $\lambda_{\text{cr}}^{\text{D}}$ can be applied equally to the force controlled situation, we assume the structure has the stiffness K, and that the system is linear elastic. Then the following relationships must be true,

$$F_{\text{cr}} = K u_{\text{cr}} \tag{4.3}$$

$$F_{\text{z}} = K u_{\text{z}} \tag{4.4}$$

Re-arranging Eq (4.1), and substituting it into Eq (4.4),

$$F_{\text{z}} = K \cdot \frac{u_{\text{cr}}}{\lambda_{\text{cr}}^{\text{D}}} \tag{4.5}$$

Moving $\lambda_{\text{cr}}^{\text{D}}$ to the LHS,

$$\lambda_{\text{cr}}^{\text{D}} \cdot F_{\text{z}} = K \cdot u_{\text{cr}} \tag{4.6}$$

Using Eq (4.2) and we get,

$$\lambda_{\text{cr}}^{\text{D}} \cdot F_{\text{z}} = F_{\text{cr}} \tag{4.7}$$

Figure 4.3 shows two load-displacement curves extracted from the same node. While there is slight difference in the displacement, the final load factor obtained is similar. Displacement control allows the post-buckling behaviour to be observed (albeit only in the immediate vicinity of onset of buckling), whereas one can never be certain that the point of divergence in a force controlled simulation is actually the on-set of instability. In a paper on FEM application to thin-walled members [39], Sarawit recommends implementing displacement control to bypass limiting points when there is no snap back behaviour.

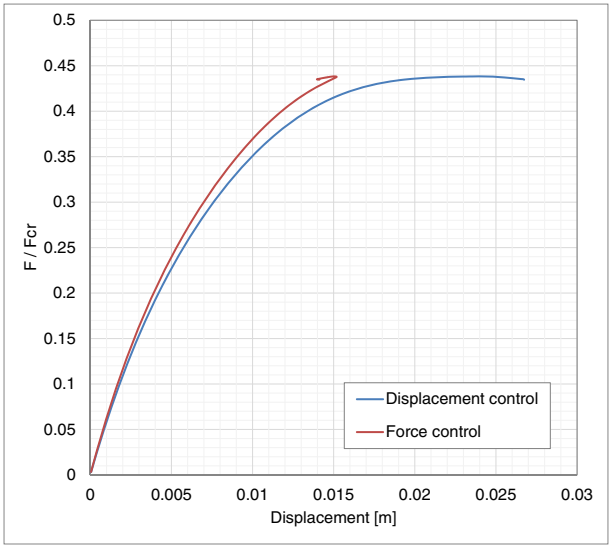

Figure 4.3: Comparison of force verses displacement controlled loading

4.2.3 Post-buckling

The above would suggest that displacement control should be used whenever possible on structures prone to instability. In reality, displacement control is seldom applied since most natural and human actions are imposed as forces, and it is next to impossible to apply the equivalent displacement field at each load step. Other techniques are developed as a result to adequately address this issue. Nonlinear stabilization, arc-length method, and slow-dynamic analysis are studied in an attempt to extract more information about the post-buckling path. These three methods are proposed by ANSYS Structural Analysis Guide to converge unstable structures.

Nonlinear stabilization is a new ANSYS technique that adds an artificial damper or dashpot element to every node. When there is a large displacement at a node, a large damping force is generated to reduce that displacement. Since the dashpot force is proportional to velocity and not displacement, a fictitious velocity is calculated as the change in displacement over the duration of the current time-step. When there is no instability, ANSYS claims that small deflection generates negligible restoring force. With many trials, the user should be able to specify a damping coefficient that is sufficiently large to circumvent divergence but that is not so large as to introduce excessive stiffness. Because the dashpot elements are attached to every node, this technique is able to circumvent both local and global instability. The disadvantage of this technique is that the slope of the load displacement curve must still remain positive for Newton-Raphson to function, therefore it is not applicable in cases where stiffness drops suddenly.

"However, nonlinear stabilization cannot detect the negative-slope portion of a load vs. displacement curve problem with global instability." - ANSYS manual

In the Newton-Raphson (NP) Approach, the solution is found by linear increments of positive slopes, the arc-length method attempts to converge the Newton-Raphson equilibrium along an arc instead of a line. This allows convergence to occur even when the slope of the load deflection curve becomes zero or negative. The figure on the left in Fig. 4.4 shows a situation where convergence is impossible with NP irrespective of the size of the increments since decrements are necessary. This method is only able to circumvent global instability and only when loads are applied as forces. As shown in the figure on the right, the radius of the arc is an important parameter, and may be determined through a large number of trial runs. The implementation in ANSYS is an improvement on the Riks method based on the theoretical work by Forde and Stiemer [21].

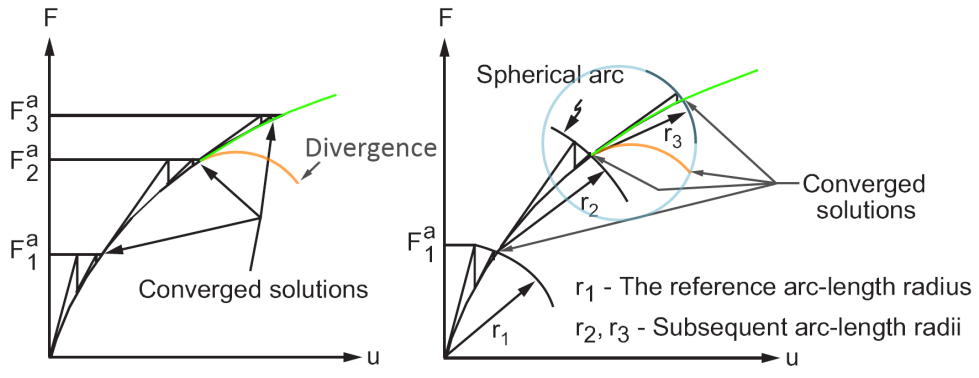

Figure 4.4: Scheme of the arc-length method

Slow dynamic analysis attempts to solve the same structural problem but in a time-dependent manner. The initial condition is set so that both displacement and velocity start at zero. This method take considerably more effort than the above two as the user must supply the time-integration parameters and the damping factor.

Abaqus in its documentation suggested similar methods when dealing with unstable responses. Slow dynamic analysis, dash-pot stabilization, displacement method, and Ritz method were listed as the possible solutions. Two noticeable differences were mentioned, one, it appears as though dynamic analysis can be used at the onset of divergence thus speeding up the analysis considerably, and two, Ritz method can be used only when the load can be controlled by a single scalar parameter.

Stabilization did not resulted in better convergence. ANSYS' arc-length implementation attempts to restart the analysis every time divergences occurs, resulting in an infinite loop. It is the author's suspicion that the post-buckling behaviour of an axially compressed cylinder is too unstable to be captured unless the arc-length radius is set extremely small, though then drift back may occur. It is noted that many researchers and analysts have experienced difficulty in using ANSYS arc-length method when analysing unstable structures (even for 1-D elements) [33]. As a result, ANSYS Inc. appeared to have reformulated the algorithm in its newest release [44]. The slow dynamic method show promising signs of convergence. However the results are difficult to interpret as there exist significant discrepancies from the static analyses. Much more time must be invested to obtain a functional model, therefore in all subsequent analyses in this thesis where force control is used, the author assumes the peak force represents the onset of buckling. This assumption was used by Wunderlich, et al. in the simplified analysis of Elastic-Plastic Buckling of shells where post-peak behaviour is discarded. It was stated that since the interest is in finding the buckling capacity of a structure, it is sufficient to obtain pre-buckling behaviour [46]. It was suggested that incremental and iterative procedure combined with convergence acceleration was sufficient for this purpose. Convergence acceleration was necessary due to the geometrical softening of the structure, and such accelerator is implemented in ANSYS.

4.3 Linear Buckling Analysis

For the thin cylinder modeled in this chapter, LBA produced extremely closely spaced distinct buckling modes. In fact, the sequence of buckling modes becomes sensitive to many modeling parameters such as mesh density, support loading condition, and so on. This shows that the order of buckling modes has no real significance. 1 % difference in load factor is observed only after 200 modes. Figure 4.5 shows that these modes are not merely rotations of the first mode but are rather distinct modes.

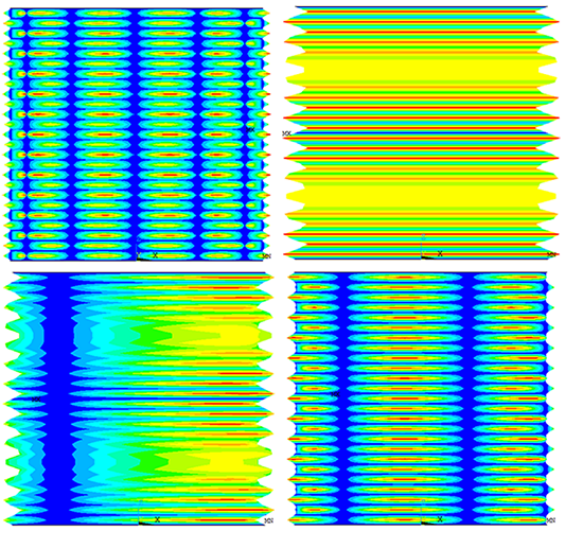

Buckling Mode	Load Factor	% Diff
1	4.8309	0.00%
10	4.8322	0.03%
20	4.8350	0.08%
30	4.8363	0.11%
40	4.8389	0.17%
50	4.8413	0.22%

Figure 4.5: The first four buckling modes, and sample load factors up to the 50th mode

4.4 Comparison to experimental data

In the 60s and the 70s, a large number of tests were performed on thin-shell cylinders which varying slenderness ratio, a/h. The aggregated result is plotted against the critical buckling load, Eq. (4.8), and one such plot is shown in Figure 4.6b where the test results are shown as black circles. Figure 4.6a shows a buckled cylinder with fully developed elastic buckling pattern, the interior of the cylinder is fitted with a mandrel.

$$\sigma_{\text{cr}} = [3(1-\nu^2)]^{-1/2}\frac{Eh}{a} \simeq 0.605\frac{Eh}{a} \tag{4.8}$$

If Koiter's assertion that geometrical imperfection is the cause of the discrepancy is correct, then ANSYS should produce results similar to the experiments if a reasonable geometrical imperfection is assumed. GNLA is performed on cylinders with varying slenderness ratio, but the same first mode imperfection with a maximum amplitude of $t/2$. The failure stress is normalized to σ_{cr} and superimposed onto Figure 4.6b as blue circles.

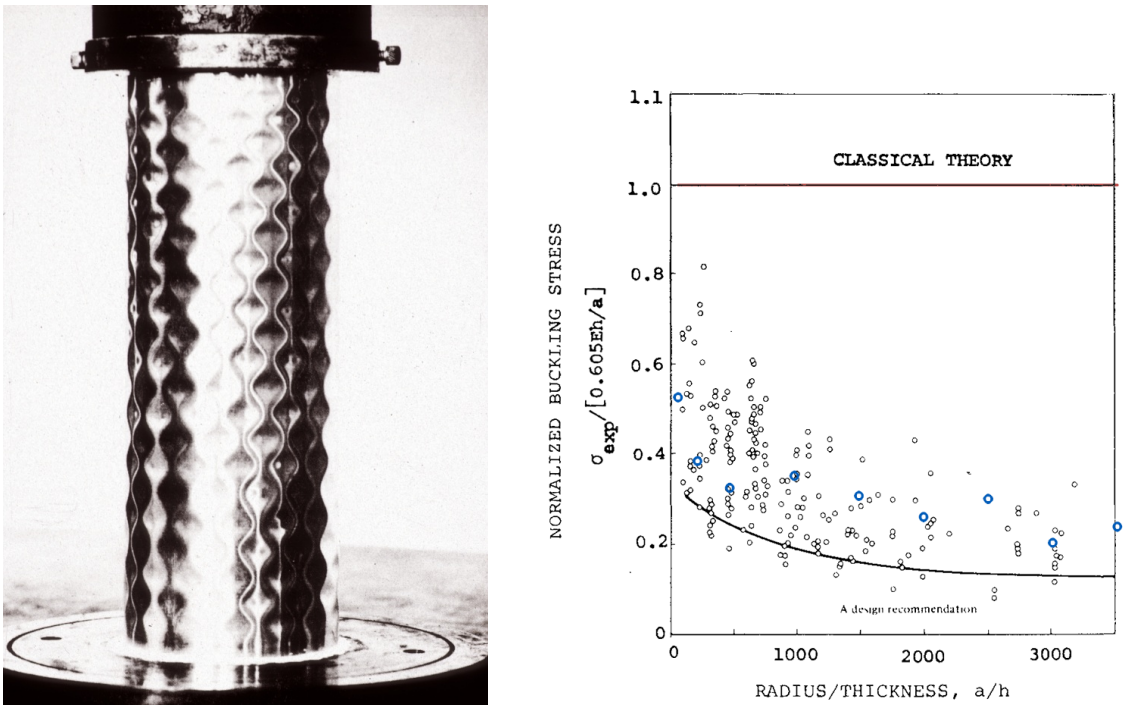

(a) Cylinder with completely developed elastic buckle pattern [25]

(b) Experimental data of axially compressed cylinder with FEM results [14]

Figure 4.6: Experimental normalized buckling stress of compressed cylinder of different geometry

This shows that ANSYS is capable of simulating experiments of geometrically imperfect cylinders. It further shows that a theoretically governing imperfection shape (first mode with amplitude of $t/2$) results in average capacity reduction in real specimens. The fact that the FE models calculated higher buckling stress capacity than experiments suggest that either the magnitude of real imperfection is greater than the assumed $t/2$ or that real imperfection shape reduces capacity more than the first modal shape. It is likely that the reason is a combination of both.

4.5 Comparison to Koiter's Law

The load displacement plots in Figure 4.7b are obtained by varying the values of $\bar{\delta}/t$ in Koiter's equation, Eq. (4.9).

$$\left(1 - \frac{P_S}{P_C}^{3/2}\right) = \frac{3(3)^{1/2}}{2}(-b)^{1/2}\left|\frac{\bar{\delta}}{t}\right|\left(\frac{P_S}{P_C}\right) \tag{4.9}$$

In this section, the first mode with various maximum amplitude from $\bar{\delta}/t = 0.001$ to $\bar{\delta}/t = 1$ is used as the geometrical imperfection. This is done to show that there exists an correlation between ANSYS model and the theoretical formulation (Figure 4.7a), and that ANSYS is able to reproduce the theoretical results if imperfection is included in the model.

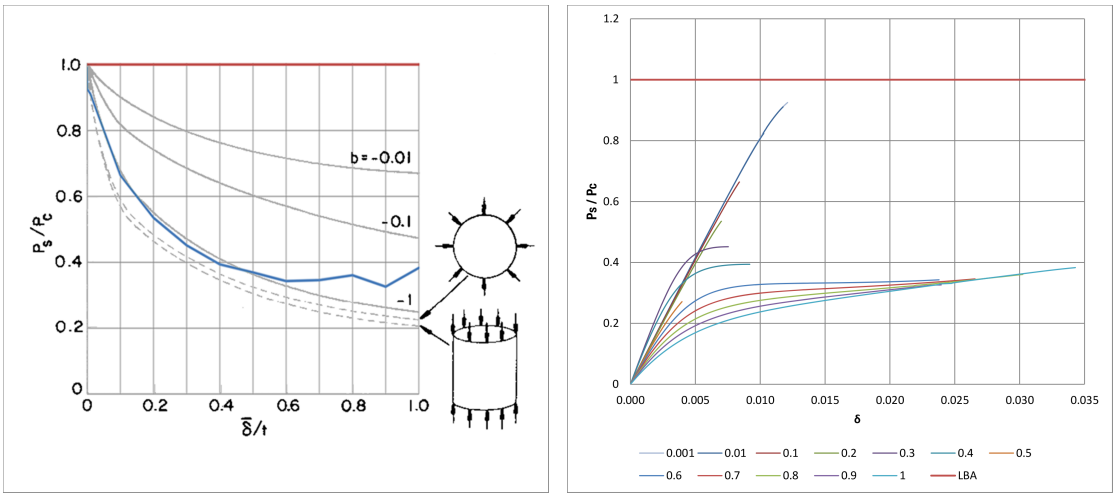

(a) (b)

Figure 4.7: (a) Theoretical curved compared with ANSYS GNLA [15] (b) Load displacement curves for all thickness ratios, force controlled increments

Figure 4.7b shows that using the first mode, ANSYS produced results very close to the curve $b = -1$ for $\bar{\delta}/t$ up to 0.6. The close correlation to the $b = -1$ curve is expected since no modal combination is imposed. Budiansky stated that $b = -1$ imply an imperfection-sensitivity level as severe as that of a cylinder under axial compression, this statement is proved by ANSYS here. This is a important finding as it shows that ANSYS, a general FE program, without implementing any buckling formulations (such as the ones used in LBA) is able to produce accurate results. The divergence between the theoretical and ANSYS results past $\bar{\delta}/t$ up to 0.6 maybe investigated further. Results from ABAQUS also showed similar divergence in higher imperfection range [47].

Figure 4.7a shows the load displacement curves as well as the upper bound resulting from GNLA of cylinders of different $\bar{\delta}/t$. It's evident that passing a certain threshold, the magnitude of imperfection reduces only the stiffness of the structure, but not the buckling capacity. As stated above, this contradicts Koiter's prediction that capacity continuously decrease, even as the rate of decrease declines.

Referring to the dotted line in Figure 4.7(a), Koiter's Law suggests that for the cases of extremely sensitive shells such as an axially loaded cylinder, a combination of buckling modes may interact to produce a lower buckling factor, with the governing equation (2.4). In the next chapter, modal combinations are studied to investigate Koiter's modal interaction suggestion.

4.6 Conclusion

A number of parameters including slenderness, and imperfection magnitude, and the loading method are studied to assess their effects on the buckling capacity of a axially compressed thin cylinder. It is first observed that the order of buckling modes is meaningless as they are extremely closely spaced, and is sensitive to variations of the FE model (in particular mesh density, and loading method). Furthermore, given the large difference between the load factor resulting from LBA and from any of the performed GNLA, it is extremely un-conservative to use the critical buckling load for design.

Force and displacement controlled loading is compared and found to be equally adequate in predicting the buckling capacity of the cylinder. However, displacement controlled analysis provides the assurance that the peak has actually been reached, and calculates post-buckling behaviour.

Comparing the results from GNLA and aggregated experimental data, it is shown that by imposing geometrical imperfection, GNLA can adequately simulate real test conditions and specimen using only one maximum amplitude ($t/2$) and only the first mode as imperfection. GNLA with single modal imperfection results corroborates well with Koiter's asymptotic theory for single modal imperfection up to a certain maximum imperfection magnitude. These results demonstrate the viability of the purposed procedure of imperfection imposition, and the capability of FEM in analysing such problems despite the various simplifications made on the boundary and loading conditions.

Chapter 5

Simple Applications

5.1 Introduction

This study analyses four simple yet realistic structures with the proposed procedure. The structures studied are a hyperboloid concrete wet cooling tower, a concrete dome, a steel liquid storage silo and an airplane fuselage. The dimensions, loads, and support conditions are set to simulate reality. This study demonstrates the capability of ANSYS Mechanics in analysing imperfect structures with multitude of load types and support conditions.

5.2 Hyperboloid

5.2.1 Geometry

The structural model used in chapter two is reused in this study, however the geometry generation script is changed to polar coordinate (θ and ϕ) to obtain better element aspect ratios. A full-length model is used to account for both symmetric and anti-symmetric buckling modes. Figure 5.1 defines the variables used in the following equations. Using the calculated constants a and b,Eq. (3.2), the focal point (and the distance from it to the z axis) of the hyperbola is calculated as follows,

$$c = \sqrt{a^2 + b^2} \tag{5.1}$$

The eccentricity of the hyperbola is then,

$$e = \frac{c}{a} \tag{5.2}$$

From the focal point, R_2 is calculated based on ϕ_1. Note that ϕ_1 ranges from ϕ_{base} to ϕ_{top}. The angles beneath the focal line are negative.

$$R_2 = \frac{a(e^2 - 1)}{1 + e \cdot cos(\phi)} \tag{5.3}$$

From there, the radius of the hyperboloid R_1 is calculated using simple trigonometry.

$$R_1 = c - R_2 cos(\phi_1) \tag{5.4}$$

The volume of the hyperboloid is calculated in equation (5.5).

$$V = \int_{\phi_{\text{base}}}^{\phi_{\text{top}}} \int_0^{2\pi} tr^2 cos(\phi)\, \mathrm{d}\theta\, \mathrm{d}\phi \tag{5.5}$$

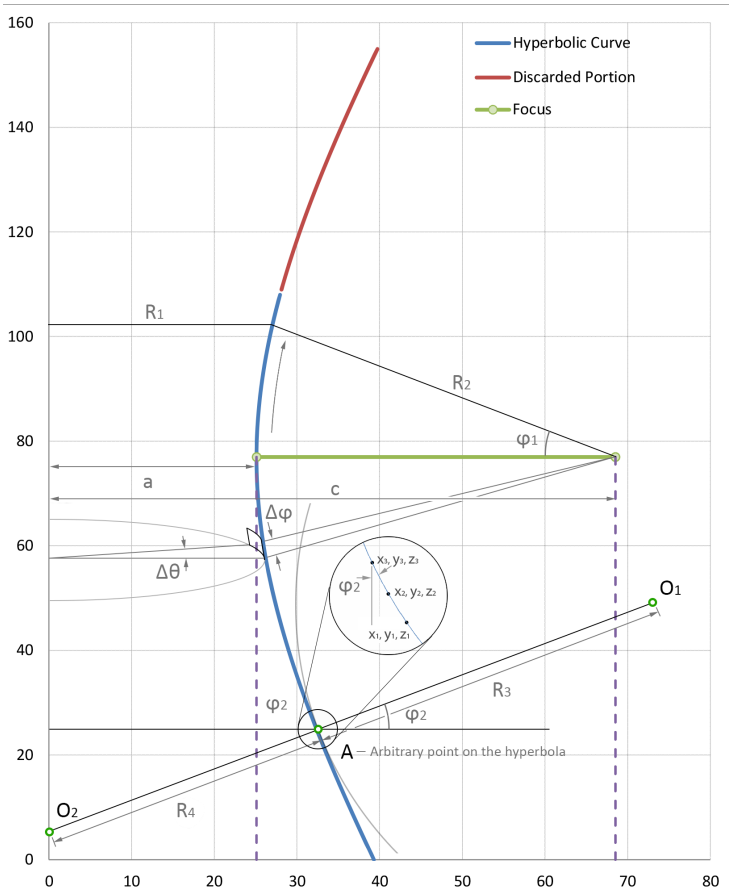

Figure 5.1: Geometry of the hyperboloid

Finite element mesh

As with all structures in this study, single layered curved 8 node elements (SHELL281 [9]) is used to mesh the surface. Curved elements are able to incorporate initial curvature effects. SHELL281 is suited for large strain nonlinear applications. The thickness can vary over individual elements (nodal thickness definitions). It can be layered to simulate composite sandwich materials. The local coordinate system is set so the z axis is normal to the plane.

As oppose to assuming a mesh density as was done in the second Chapter, a mesh sensitivity study of the linear eigenvalue problem is done. The mesh density is continuously halved until the relative change of the eigenvalues converges. The second requirement is for the mesh to have several elements along each spatial deformation wave.

The three different models shown in Figure 5.2 are generated by initial variations of 50 % and 150 % on Δz and $\Delta\theta$ from the model in the centre. Variables Δz and $\Delta\theta$ are defined in Figure 5.1. The lowest four resulting buckling modes of each model are compared. From the results listed in Table 5.1, it is observed that the coarse mesh exceeds the threshold of 1 % difference. Therefore the next finest mesh ($\Delta z = 1.0\,\mathrm{m}$; $\Delta\theta = 4°$) is used.

Load cases

In addition to self-weight as was done in Chapter 3, wind pressure is applied as a second load case. The wind pressure is assumed to increase linearly in the vertical direction, and varies sinusoidally along the tangential direction. The peak pressure is set at 10 000 Pa, and the

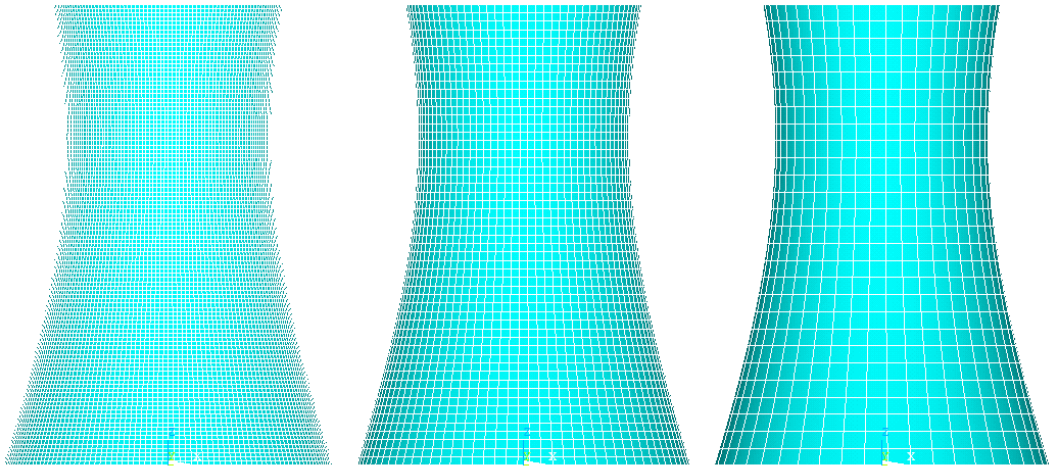

Figure 5.2: Different mesh density of the hyperboloid

Δz m	$\Delta\theta$ °	# Elements	# DOFs	Mode 1	δ %	Mode 2	δ %	Mode 3	δ %	Mode 4	δ %
0.5	1	19440	352080	15.7237	-0.022	15.9705	-0.037	16.3143	-0.010	16.8462	-0.061
1.0	2	4860	88560	15.7272	0.000	15.9764	0.000	16.3160	0.000	16.8565	0.000
2.0	4	1215	22410	15.7941	0.426	16.1024	0.789	16.3463	0.186	17.0975	1.430

Table 5.1: Hyperboloid Mesh Density Comparison

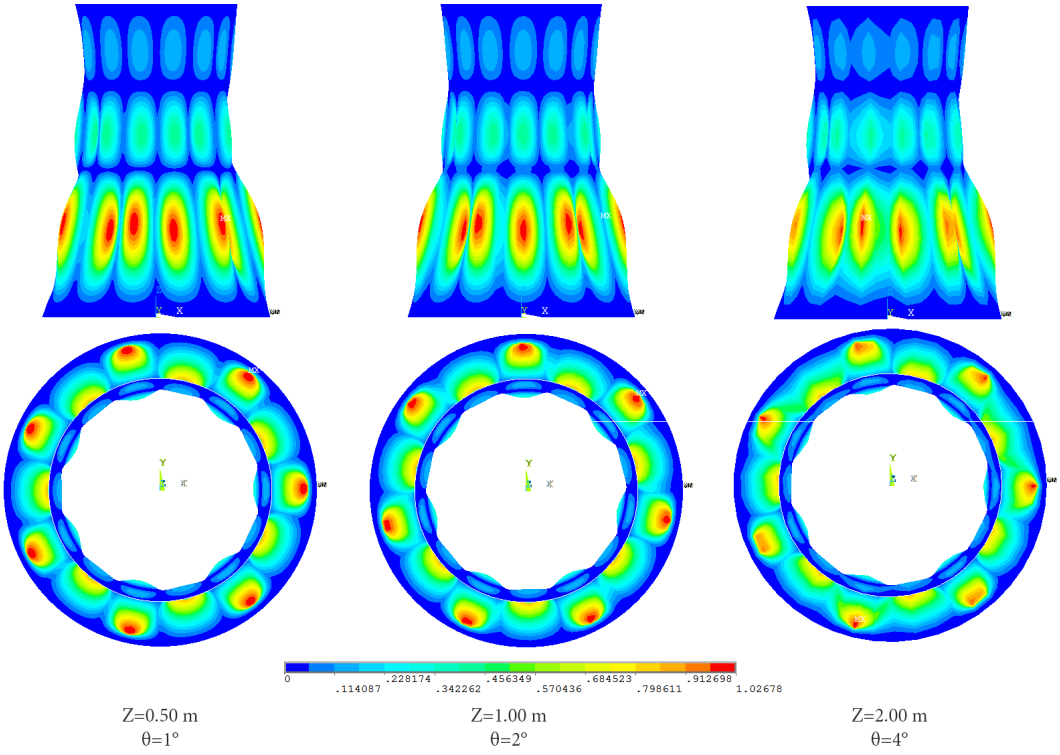

Figure 5.3: The first buckling modal shape comparison

distribution is described by equation (5.6).

$$p_{\text{wind}}(z,\theta) = \frac{p_{\text{wind,max}}}{h} z \cdot sin(\theta) \tag{5.6}$$

The combination of the first two loads is considered as the third load case. The intent is to simulate a simple load combination of $G + \psi Q$.

Load case	Description	$p_{\text{wind,max}}$
1	Self-weight of the structure	-
2	Wind pressure	10 000 Pa
3	Self-weight with wind pressure	10 000 Pa

Table 5.2: Hyperboloid load cases

5.2.2 Analysis

Buckling, yielding, crushing

The proposed method is only valid when the shell buckles elastically since the material is assumed to be linear elastic (see Chapter 8 for discussion on non-linear material behaviour). Therefore, a check is made to ensure that the relative slenderness is greater than one.

$$\lambda = \sqrt{\frac{n_{\text{cr}}}{n_{\text{p}}}} > 1 \tag{5.7}$$

The critical membrane force is taken from Table 2.1

$$n_{\text{cr}} = \frac{1}{\sqrt{3(1-\nu^2)}} \frac{Et^2}{a} \tag{5.8}$$

and the crushing force is simply,

$$n_{\text{p}} = f \cdot t \tag{5.9}$$

Where f is the compressive yield stress of concrete and t is the thickness of the shell. Using C35 as the typical concrete quality, $f_{\text{c}} = 35\,\text{MPa}$. Therefore equation (5.7) gives the following slenderness ratio, and shows that the hyperboloid would buckle before yielding.

$$\lambda = 1.62 > 1 \tag{5.10}$$

Linear elastic, linear buckling analyses, and imperfection imposition

The linear elastic analysis gives a reaction force and a deformation that can be checked against theoretical values to ensure that the geometry is proper. This is done in Chapter 3 and though the mesh density of the model is adjusted, the results remain similar. Load factors and buckling shapes remain similar as well. An imperfection of $t/2 = 95\,\text{mm}$ is imposed on the geometry in the shape of the first positive buckling mode in preparation for the next analysis.

The resulting load factors are listed in Table 5.3. Note that the factors are spaced close together with the first and the third mode differing by 1.5 % in the first load case. The negative values associated with LC2 and LC3 are due to the suction force of the wind. Since the eigenvalue solver starts at 0, half of the eigenvalues of a symmetrically laterally loaded structure would always be negative. In the third case, positive LFs dominate due to the presence of self-weight.

Mode number	LC1	LC2	LC3
1	15.727	-9.830	-8.076
2	15.727	-9.830	-8.076
3	15.976	-9.085	-6.737
4	15.976	-9.085	-6.737
5	16.316	-8.242	5.760
6	16.316	-8.242	5.760
7	16.856	-7.248	5.968
8	16.856	-7.248	5.968
9	18.123	-6.602	6.458
10	18.123	-6.602	6.458
11	18.575	6.602	6.763
12	18.575	6.602	6.763
13	19.621	7.248	7.324
14	19.621	7.248	7.324
15	19.634	8.242	7.799
16	19.634	8.242	7.799
17	19.971	9.085	8.282
18	19.971	9.085	8.282
19	20.124	9.830	8.756
20	20.124	9.830	8.756

Table 5.3: Hyperboloid load factors

Non-linear Analysis

Two different non-linear analyses are run for each load case, one with and the other without imperfection. The load displacement curves are shown in Figure 5.4. The imperfect GNLA curves results in a less stiff structure than that from the Linear Buckling Analysis (LBA) as expected. However the perfect GNLA curves follow an almost linear curve that attain a much higher maximum load factor. For the first load case, this is due to the fact that the given structure and its load condition are both axi-symmetric. Therefore without physical non-linearity, a fictional stiffness is introduced by the geometry much in the same way as column crushing. The divergence in these linear curves are caused by an accumulation of loss of precision, leading to a type of computational imperfection.

In the second and the third load cases however, the load is asymmetric and the fictitious stiffness theory does not explain the excessive capacity. The stepwise GNLA somehow avoids the lower buckling modes, and buckles at a buckling mode does not resemble any of the modes generated by the LBA. Further investigation is necessary to explain this anomaly.

Note that in the third load case, the load factor given by the LBA is lower than that from the imperfect GNLA. This is due to the fact that in the case of GNLA, the load increment is applied only to the wind load, where as in LBA the load factor is calculated considering both the self-weight and the wind load. This issue is documented in APDL command manual 7.5.2. [7]. The resulting knock-down factor is listed in Table 5.4.

It is evident that using GNLA without imperfection can be dangerously under-conservative, over-estimation of stiffness and strength is evident even when the load is asymmetrical. With the perturbation however, the strength is brought to a level that is lower than the result from LBA. The reductions of 0.76 and 0 84 are in line with the traditional factor of safety applied to all structure indicating that hyperboloids are not overly imperfection sensitive. This prediction

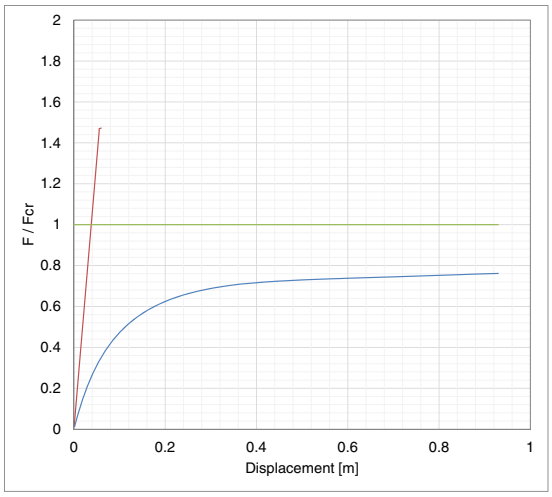

(a) LC1 - Self-weight

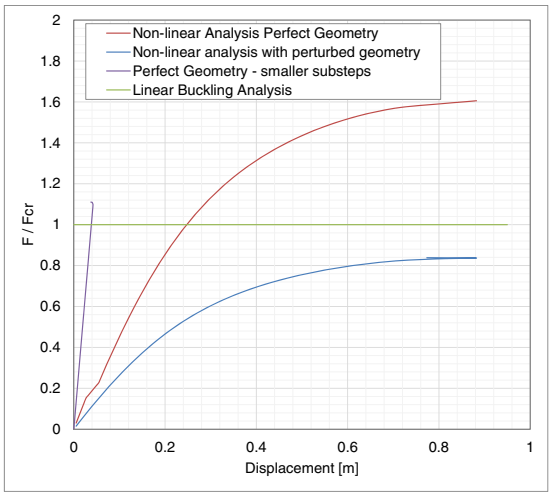

(b) LC2 - Wind Pressure

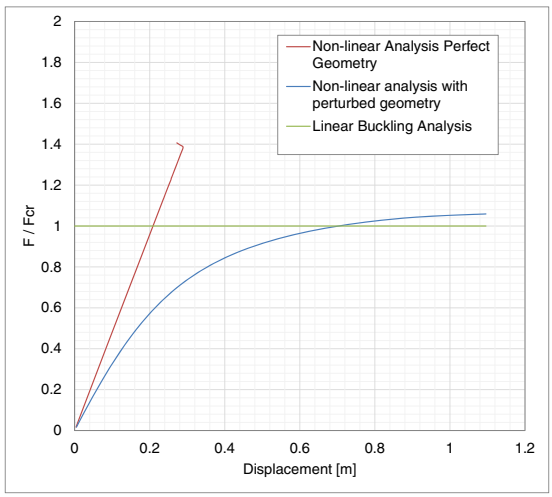

(c) LC3 - Self-weight + wind pressure

Figure 5.4: Cooling tower load factor verses deflection curves

Load Case	Imperfection	Maximum deviation	LBA LF	GNLA LF	C
1	None	-	15.727	23.15	1.47
	Mode 1	95 mm		11.98	0.76
2	None	-	6.602	7.33	1.11
	Mode 11	95 mm		5.535	0.84
3	None	-	5.760	8.1	1.41
	Mode 5	95 mm		6.098	1.06*

*This is lower than one due to self-weight not being scaled during GNLA

Table 5.4: Hyperboloid cooling tower knock-down factor

is reported by Zerna who stated that shells with negative Gaussian curvature exhibit small imperfection sensitivity [48].

5.3 Dome

Domes and spheres are structures with a positive Gaussian curvature. Monolithic domes are concrete domes constructed by first casting a ring beam as the foundation, inflating a PVC-coated nylon or polyester fabric, and then casting Shotcrete with the fabric as the formwork.

5.3.1 Geometry

A typical dome situated in a region with heavy wind load is selected for this study [40]. The base radius of the dome is $R_{\mathrm{D}} = 55'$ or approximately 16.75 m. The height from the base to the tip of the dome is $H_{\mathrm{D}} = 37'$ or approximately 11.25 m. The thickness of the dome varies from $8''$ (203 mm) at the base to $3''$ (76 mm) at the tip. See Figure 5.5 for a graphical representation of the variables. The actual radius of the dome is found with equation (5.11). Note that this is

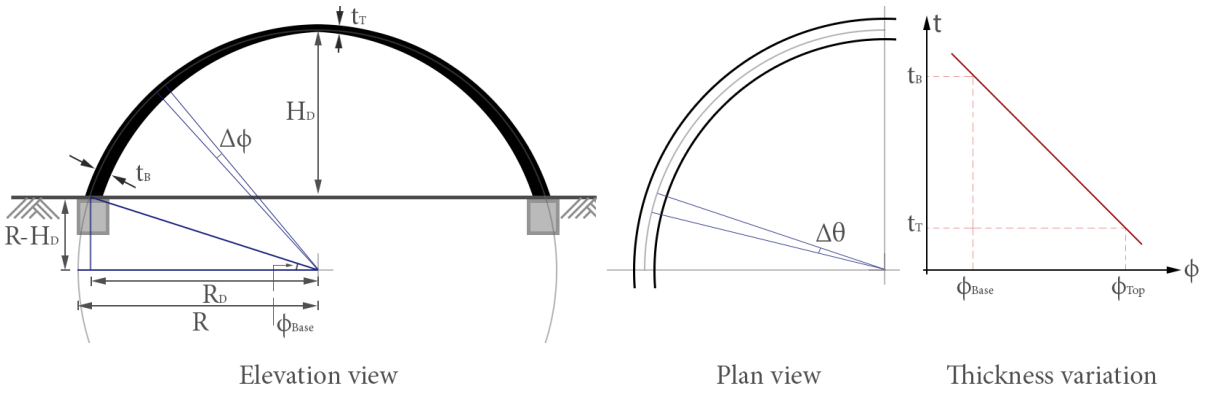

Figure 5.5: Geometry of a typical dome

a rearrangement of the calculation for sagitta in Eq. (2.1).

$$R = \frac{H_{\mathrm{D}}^2 + R_{\mathrm{D}}^2}{2H_{\mathrm{D}}} = \frac{(11.25^2 + 16.75^2)}{2 \cdot 11.25} = 18.09\,\mathrm{m} \tag{5.11}$$

The variable thickness is implemented as a function of the vertical angle as shown in equation (5.12).

$$t(\phi) = \frac{t_{\mathrm{T}} - t_{\mathrm{B}}}{\pi/2}\phi + t_{\mathrm{B}}; \forall \phi \in [\phi_{\mathrm{base}}, \pi/2] \tag{5.12}$$

The slenderness ratio of the dome varies proportionally to its thickness. At the base, $a/t_{\mathrm{bottom}} = 89$, where as at the top, $a/t_{\mathrm{top}} = 237$. The Gaussian curvature of the dome is assumed constant over its surface.

$$\kappa_1 = \kappa_2 = \frac{1}{R} = 0.055 \;;\; K = \kappa_1\kappa_2 = 0.00305 \tag{5.13}$$

Material

Again, a generic reinforced concrete is used to represent the mixture of Shotcrete and the reinforcement grid.

$$\rho = 2400\,\mathrm{kg/m^3} \;;\; E = 35\,\mathrm{GPa} \tag{5.14}$$

Loads

Under normal operating conditions, the self-weight would be the dominate load on the structure. However, since these domes are built in areas of heavy wind, it is expected that wind load would become the principle load condition in extreme circumstances. To simulate a variety of wind load conditions, different pressures are applied to the surface of the dome shell. The relationship between wind speed and pressure can be estimated using Equation (5.15) [37].

$$p = {}^1\!/_2 \rho w^2 \xi \tag{5.15}$$

Literature [40] suggests that the most critical wind load occurs when half of the dome is subjected to positive pressure, and the other half to negative pressure (suction). This load combination is implemented by assuming a wind pressure profile of two sine waves, one circumferential and the other vertical. The peak wind speed is taken from the FEMA specification for the "Design and Construction Guidance for Community Safe Rooms" as these structures are frequently used as safe rooms in the event of a hurricane or tornado [1].

The second load case is a uniformly applied external pressure. This is a well studied buckling imperfection problem and is included as a reference [16]. Table 5.5 lists the three load cases tested.

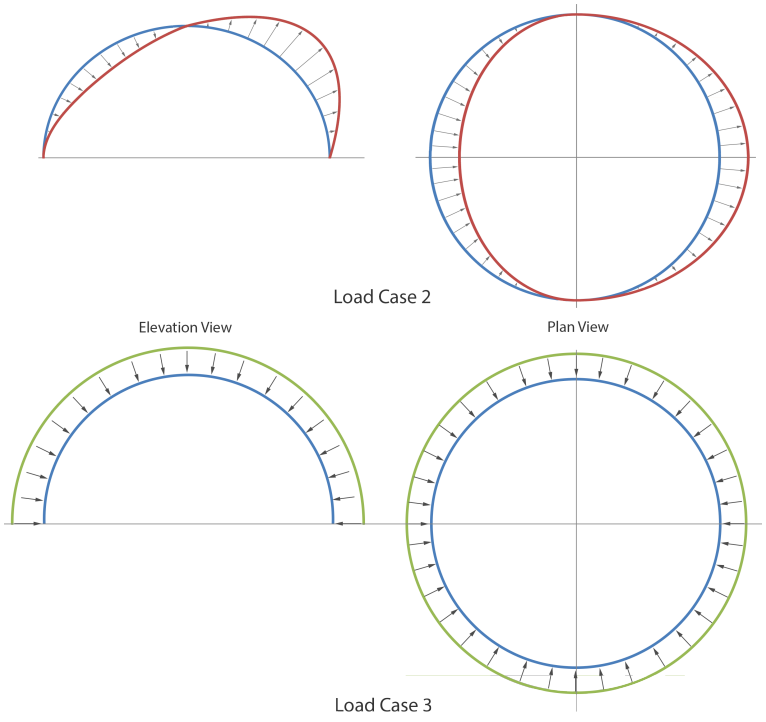

Figure 5.6: Load profiles of dome in elevation and plan view (not to scale)

Load Case	Description	Wind pressure Pa
1	Self-weight	-
2	Wind pressure and suction	10000
3	Uniform external pressure	10000

Table 5.5: Dome Load Cases

Mesh Comparison

Two different algorithms are used to mesh the dome. The first attempt used a constant height increment Δz along the z axis. However this resulted in very flat elements near the base of the dome, and very elongated ones at the tip. Changing to a spherical coordinate, the author is able to increment with $\Delta\phi$ and eliminate the element aspect ratio issue.

The two variables determining the size of a mesh are shown in Figure 5.5, namely the change in the Zenith $\Delta\phi$ and in the Azimuth $\Delta\theta$. These are varied in the same manner, by 50 % and 150 %, to assess the relative changes in the buckling load factors of the structure.

ϕ m	θ °	Mode 1 %	Δ	Mode 3 %	Δ	Mode 5 %	Δ	Mode 7 %	Δ
0.0625	1	9.60144	0.974	10.8384	0.866	11.4960	1.212	12.195	0.736
0.1250	2	9.50886	0.000	10.7453	0.000	11.3583	0.000	12.1058	0.000
0.2500	4	9.43707	-0.755	10.7912	0.427	11.3761	0.156	12.3431	1.960

Table 5.6: Dome Mesh Density Comparison

As observed in Table 5.6 and Figure 5.8 there are significant differences in both the load factors and buckling modes between the finer and the coarser meshes, and therefore the model with the finest mesh is used for future analyses. Note that the mesh can theoretically be made more refined, however a further refined mesh is computationally not feasible.

It is hypothesised that smaller elements are needed due the load being more concentrated, and therefore the buckling is more of a local behaviour.

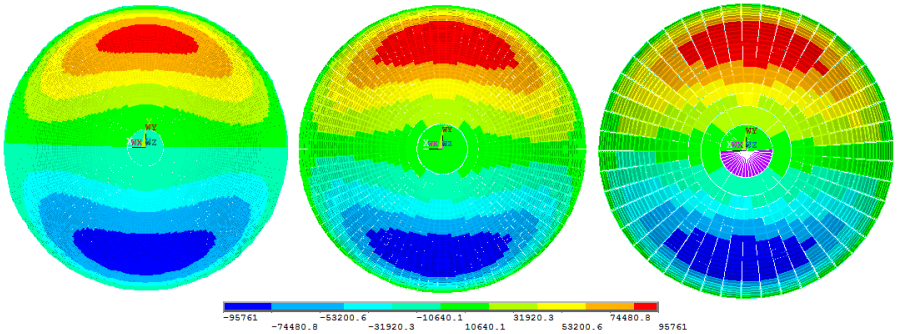

Figure 5.7: Load profile of domes with different mesh density

5.3.2 Analyses

Buckling, yielding and crushing

This section verifies that the dome buckles prior to crushing.

$$\lambda = \sqrt{\frac{n_{\text{cr}}}{n_{\text{p}}}} > 1 \tag{5.16}$$

The critical membrane force is taken from Table. 2.1

$$n_{\text{cr}} = \frac{1}{\sqrt{3(1-\nu^2)}} \frac{Et^2}{a} \tag{5.17}$$

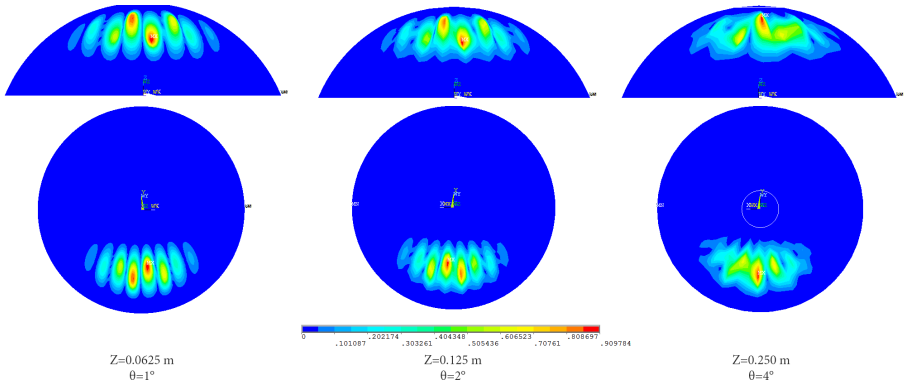

Figure 5.8: Comparison of buckling shapes of models with different mesh density, using wind load as the test load case

and the crushing force is simply,

$$n_{\mathrm{p}} = f \cdot t \tag{5.18}$$

Where f is the compressive yield stress of concrete and t is the thickness of the shell. Using C35 as the typical concrete quality, $f = 35\,\mathrm{MPa}$. Therefore equation (5.16) gives the following slenderness ratio, and shows that the hyperboloid would buckle before yielding.

$$\lambda = 2.152 > 1 \tag{5.19}$$

Linear elastic analysis

This analysis is to verify the mass of the structure is indeed correct. Equation (5.20) calculates the volume of the dome using the variable thickness equation derived in equation (5.12).

$$V_{\mathrm{dome}} = \int_0^{2\pi} \int_{\phi_{\mathrm{base}}}^{\frac{\pi}{2}} t(\phi) r^2 cos(\phi)\, \mathrm{d}\theta\, \mathrm{d}\phi \tag{5.20}$$

This volume is multiplied with the density of typical concrete in equation (5.14).

$$m_{\mathrm{dome}} = V\rho \;;\; m_{\mathrm{dome}} = 4.874\,21 \times 10^5\,\mathrm{kg} \tag{5.21}$$

The resulting mass compares well with the mass calculated by ANSYS at $4.874\,29 \times 10^5\,\mathrm{kg}$.

Linear buckling analysis

LBA is performed on the dome model with each load case. The resulting load factors are listed in Table 5.7. The closely spaced LFs are observed especially for the second load case, where uniform pressure is applied. The resulting buckling shapes are shown in figure 5.9. The first mode is an axisymmetric mode with buckles observed at the top of the dome. Higher modes show progressively lowering of buckles until the whole surface is covered. Each axisymmetric mode is followed by a series of asymmetric ones with buckles starting at the same height.

Imperfection

Assuming the fabric is manufactured with greater precision than the concrete casting procedure, the inner surface must be more uneven than the outer. Therefore, the imperfection is more of a change in thickness than a change in geometry. However, for ease of comparison, the same

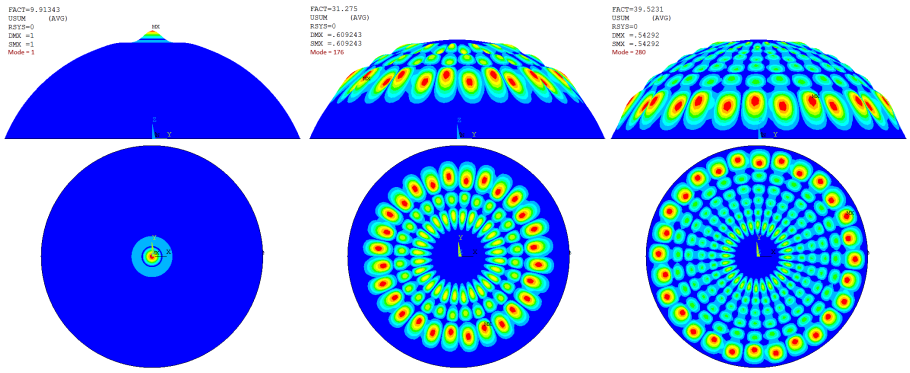

Figure 5.9: Sample buckling modes of the uniform pressure load case

Mode	LC1	LC2	LC3
1	N/A	-19.307	9.9134
2		-19.307	10.119
3		-18.019	10.119
4		-18.019	10.512
5		-17.108	10.512
6		-17.108	11.185
7		-15.957	11.185
8		-15.957	12.007
9		-14.074	12.007
10		-14.074	12.939
11		14.074	12.939
12		14.074	13.054
13		15.957	13.191
14		15.957	13.191
15		17.108	13.544
16		17.108	13.544
17		18.019	13.967
18		18.019	13.967
19		19.307	14.102
20		19.307	14.102

Table 5.7: Dome LBA load factors of the different load cases

imperfection imposition method is used. The thickness of the dome averages to 5′ or 130 mm. A maximum imperfection of 65 mm or $t/2$ is imposed on the structure. Bauer states that the axisymmetric local (and also regular and random) thickness deviations affect critical load much less than the corresponding initial imperfections of the surface [13]. The first mode is used as the imperfection shape, though it is unclear that a higher mode won't govern.

Non-Linear Analysis

With the same procedure as the above two structures, the dome is analysed taking geometrical non-linearity into account. It can be seen in figure 5.4 that without imperfection, capacity resulting from GNLA is similar to that from LBA, even though some of the load cases are asymmetric.

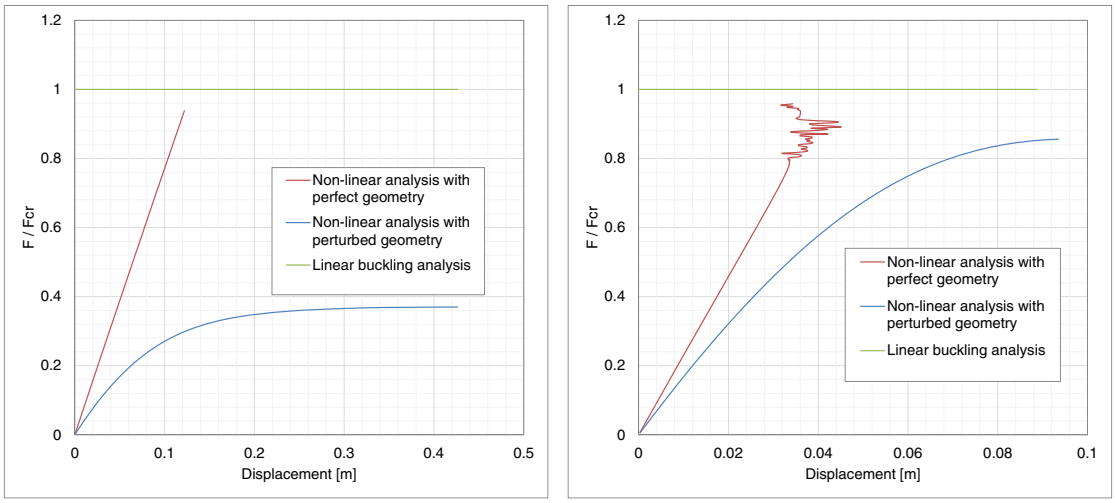

(a) LC2 - Wind

(b) LC3 - Uniform pressure

Figure 5.10: Dome load factor verses deflection curves

Theory predicts the buckling thickness of a dome with either a geometry that allows for full stresses to develop, and also with a geometry that is optimized for material usage. With a given geometry, the membrane stress can be calculated using equation taken from Table 2.1 for spherical shells.

$$n_{\text{cr}} = \frac{-1}{\sqrt{3(1-\nu^2)}}\frac{Et^2}{a} = \frac{-1}{\sqrt{3(1-0.2^2)}}\frac{35000 \cdot 139.7^2}{18094} = -156 \cdot 10^6 \text{ MPa} \tag{5.22}$$

This is similar to the membrane stress n_{a} resulted from the GNLA.

Figure 5.10a exhibits a linear behaviour for the perfect geometry and a non-linear one for the imperfection geometry with significant capacity reduction. In figure 5.10b, the solution converges badly for the perfect geometry, suggesting possible bifurcation behaviour. It can be seen from Table 5.8 that significant knock down factor is needed in the case of wind load, but not for the case of uniform pressure. This disagrees with research findings [15]. Two possible explanations for this include the fact that the imperfection in the shape of the first buckling shape may not govern, and that the support condition is pinned as opposed to clamped. The effects of higher modes are investigated in the Chapter 6.

Load Case	Imperfection	Maximum deviation	LBA LF	GNLA LF	C
LC1		N/A			
LC2	None	-	22.390	21.200	0.943
LC3	Mode 11	130 mm	22.390	8.285	0.370
LC4	None	-	15.771	15.118	0.962
LC5	Mode 1	130 mm	15.771	13.750	0.870

Table 5.8: Dome knock down factors

5.4 Liquid Containment Silo

Storage silos typically resemble cylinders or spheres due to the need to contain heavy liquids that exerts radial pressure outward. A cylindrical silo is studied in this thesis. One of the

principle curvatures of a cylinder is zero, and therefore the Gaussian curvature is also zero. As the material properties improve, ever thinner and bigger silos are constructed. Therefore instabilities due to various load conditions have become a practical issue.

5.4.1 Geometry

A typical liquid storage silo is used as the test structure (Meridian Manufacturing Inc. 304 Stainless Steel Flat Bottom Liquid Fertilizer Tanks Model SS1840) [3]. Its geometry is shown in Figure 5.11. Its height from base to top of the cylinder is $h = 42'9''$ or $\sim 13\,\text{m}$. Its radius is $r = 8'$ or $\sim 4.25\,\text{m}$ throughout its height. The thickness is assumed to be $t = 25\,\text{mm}$, through in reality it may vary along the height of the silo. There is a lid atop the silo with a pitch of $10°$ resulting in a lid height of $\sim 0.825\,\text{m}$. Any ring-shaped stiffeners are ignored. Ring-stiffened cylinders are tested as the next case study.

$$\frac{a}{t} = \frac{8.5}{0.025} = 340 \tag{5.23}$$

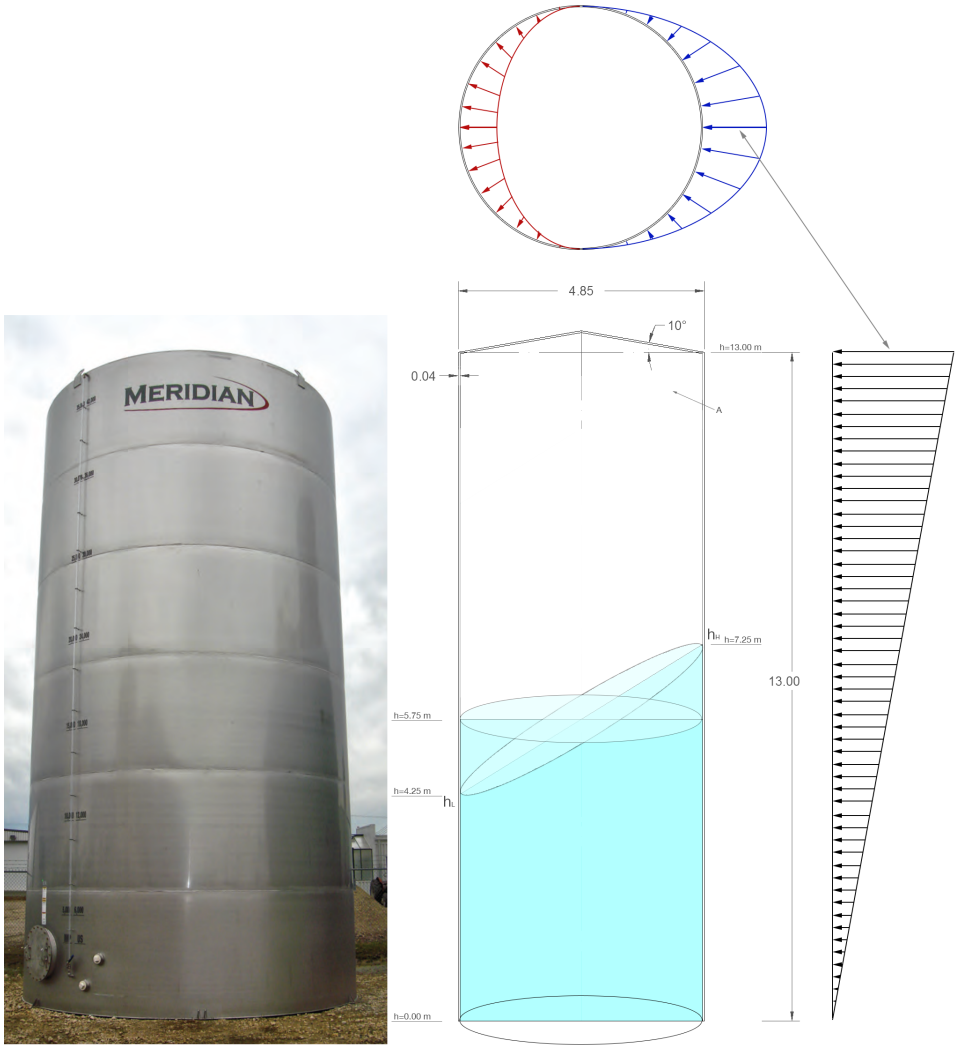

Figure 5.11: A Meridian Storage Silo, its geometry, and the different water levels, sloshing angles and wind pressure

The silo is made with welded stainless steel to prevent rust. Grade 304L stainless steel (Table 5.9) is used to handle corrosive substances and to reduce cost associated with annealing (the L indicates that the material has low carbon content).

0.2% Yield Strength MPa	Ultimate Strength MPa	Density kg/m^3	Modulus of Elasticity GPa
241	586	8030	193

Table 5.9: 304L Stainless Steel Properties

Loads

The self-weight of the structure can be easily calculated. This self-weight is checked against the first load case. The volume of the structure comprises of the cylinderical and the conical part.

$$V_{\text{cylinder}} = \int_0^{h_{\text{cylinder}}} \int_0^{2\pi} rt\, d\theta dz + \int_{h_{\text{cylinder}}}^{h_{\text{total}}} \int_0^{2\pi} r\theta tz \,\mathrm{d}\theta \,\mathrm{d}z \tag{5.24}$$

In addition to self-weight, several different load conditions are applied to the structure to assess their impact on its buckling capacity. Since the function of the silo is to contain liquid, it is sensible to apply different water pressure on the circumference of the structure. It is also interesting to simulate the effect of sloshing of liquid to create an asymmetrical loading situation. While the cases with the silo loaded to capacity is a necessary design load case, it has been shown that such loading does not buckle a cylinder. It is included (load case 2) for the mesh density study. Teng [41] stated that empty and partially filled silos subjected to wind pressure are susceptible to buckling and these were the loads applied. Resinger and Greiner contradictorily stated that wind load along does not cause collapse of the silo, this is tested in this study. The list of load cases are shown in Table 5.10.

Additional load cases have been tested and analyzed by Resinger and Greiner, including under-pressure (internal vacuum) and axial load (snow load on lid), and therefore not included here.

Liquid pressure applied to the cylindrical surface is calculated based on the relative height between the liquid surface and position in the shell, and the angle of sloshing. Equation (5.25) shows the relationship between height, and the hydrostatic pressure applied to each element.

$$p_{\text{circumferential}} = \frac{1}{2}\rho g h(z,\theta) \;;\; \forall z = 1 \rightarrow h \text{ and } \forall \theta = 1 \rightarrow 360 \tag{5.25}$$

where

$$h(z,\theta) = \begin{cases} S \cdot \theta + h_L - z & \text{if } \theta \leq 180 \\ -S \cdot (\theta - 180) + h_L - z & \text{if } \theta \geq 180 \end{cases}$$

The slope of the sloshing liquid surface is defined by the low and the high points of the water surface, and can be calculated with equation (5.26). The surface assumes a flat profile in between the two elevations at least along the elliptical intersection between the liquid and the cylindrical shell, see curve A in 5.11. The actual water surface may not be flat, but the impact should not be felt by the edge.

$$S = \frac{h_H - h_L}{1/2 \cdot 360} \tag{5.26}$$

The wind pressure is defined as a linearly increasing function with respect to the silo height. In the circumferential direction, the wind distributes in the shape of a sine wave, i.e. half of the silo

is subjected to over-pressure, and the other half to under-pressure or suction (see Figure 5.11). Wind pressure acts perpendicularly to the element surface. The maximum amplitude is set to $p_{\max} = 10\,000\,\text{Pa}$.

$$p_{\text{wind}} = sin(\theta)p(z) \ ; \ \forall z = 1 \rightarrow h \text{ and } \forall \theta = 1 \rightarrow 360 \tag{5.27}$$

where

$$p(z) = \frac{p_{\max}}{h} z \tag{5.28}$$

Load Case	Description	Height L m	Height H m	Wind pressure Pa
1	Self-weight	0	0	0
2	Empty silo	0	0	50000
3	Half capacity with sloshing	4.25	7.25	50000
4	Half capacity no sloshing	5.75	5.75	50000

Table 5.10: Silo Load Cases

Mesh Density

A mesh refinement study is performed to determine the size of each element. The relative change of the eigenvalues in the buckling analysis is recorded as the element size decreases. In addition to the relative change in eigenvalues, each spatial deformation wave must contain several elements, [2].Once both conditions are satisfied, then the mesh size is found.

The two same variables (as the hyperboloid mesh) determine the mesh density in this model, namely the length of each element in the height direction z and the change in angle in the radial direction θ. Using the first load case as the reference case, here are the results obtained by varying z and θ by 50% and 150%. The lowest four buckling modes are used for comparison. Load case two (wind load with no hydrostatic pressure) is used as the test load case.

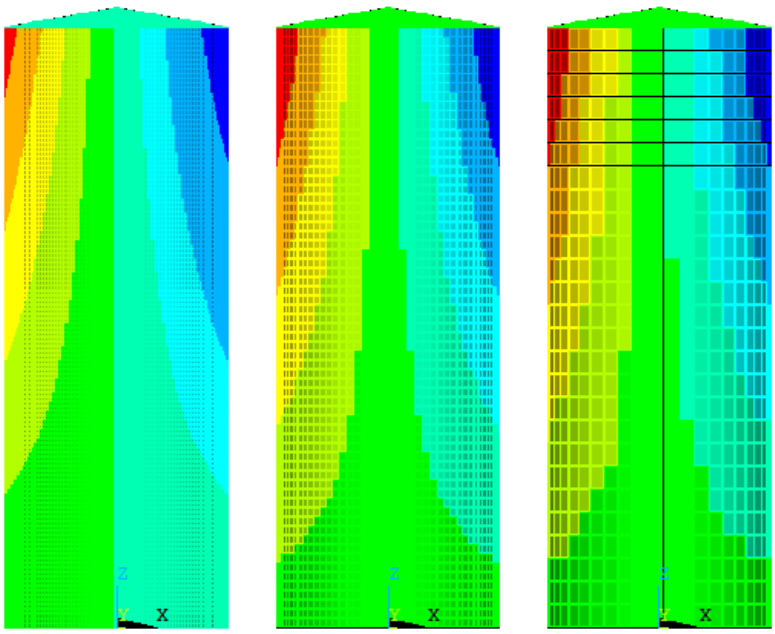

Figure 5.12: Comparison of mesh density

z m	θ °	# Elements	# DOFs	Mode 1	Δ 10^{-3} %	Mode 2	Δ 10^{-3} %	Mode 3	Δ 10^{-3} %	Mode 4	Δ 10^{-3} %
0.05	1	25200	453606	22.527	-	25.885	-	26.288	-	27.018	-
0.1	2	6750	121506	22.532	0.211	25.898	0.500	26.307	0.718	27.058	1.487
0.25	4	1620	29166	22.562	1.543	26.096	8.149	26.725	16.62	27.970	35.24

Table 5.11: Silo Mesh Density Comparison using wind load as reference

The buckling shapes of the different meshes are shown in Figure 5.13. Note that in the coarse mesh the elements do not have sufficient resolution to capture the peak of the buckle wave. This may introduce additional stiffness to the structure, and therefore the next finest mesh is chosen.

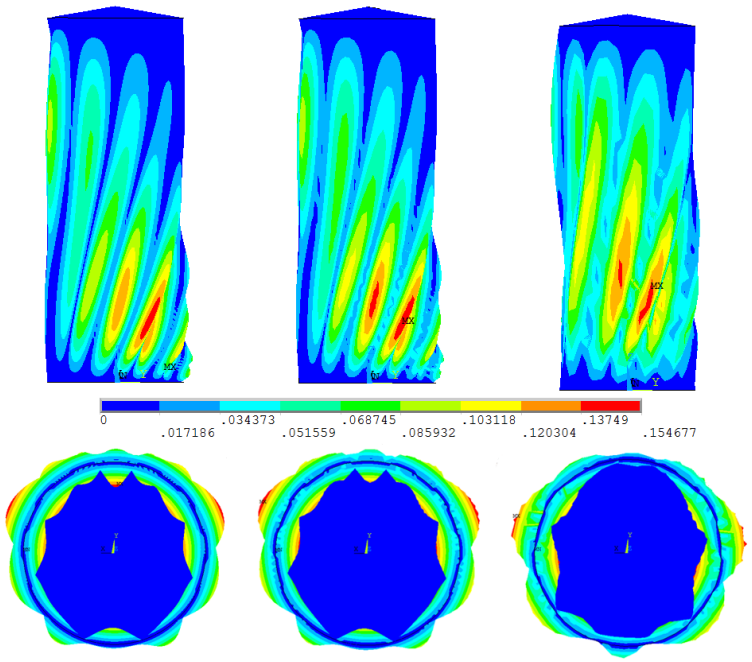

Figure 5.13: Mesh density comparison - buckling shape

5.4.2 Analysis

Linear Elastic

The self-weight of the structure calculated in Eq. (5.29) is compared with the ANSYS model load case one.

$$V_{\text{cylinder}} \cdot \rho = 43\,527.35\,\text{kg} \tag{5.29}$$

This is similar to the ANSYS result of 43 529 kg.

Linear Buckling

Similar to what was done previously, a linear buckling analysis is performed with each load case individually to obtain the associated load factors. It is worth noting that the asymmetrical load causes the load factor to decrease, even though the total pressure applied onto the structure remains constant.

Load Case	1	2	3	4
Capacity	-	0%	50%	50%
Sloshing	-	-	Yes	No
Wind	-	No	Yes	Yes
Height 1 m	-	-	4.25	5.75
Height 2 m	-	-	7.25	5.75
1	-	22.532	22.89	23.31
2	-	22.532	22.891	23.31
3	-	25.898	26.218	27.743
4	-	25.898	26.616	28.048
5	-	26.307	27.671	28.519
6	-	26.307	27.676	28.52
7	-	27.058	27.82	29.149
8	-	27.083	28.21	29.612
9	-	27.596	28.227	29.622
10	-	27.705	28.624	29.897

Table 5.12: Silo Linear Buckling Load Factor

Imperfection

An geometrical imperfection in the shape of the first buckling mode is applied to the structure. The maximum amplitude of the imperfection is 12.5 mm, half of the thickness of the shell.

Non Linear Buckling

It is observed that unlike the hyperboloid, the results from GNLA of the perfect silo does not overestimate the capacity. This is due to the fact that all load cases have an asymmetrical (i.e. wind load) component. The load displacement plots show linear elastic behaviour until bifuration for the perfect geometry. With an imperfect geometry however, the behaviour is non-linear from the start and the tangent stiffness decreases as load increases. Table 5.13 lists the resulting load factors and knock-down factors from both LBA and GNLA. It is observed that with imperfection, a knock-down factor of $^3/_4$ can be conservatively applied.

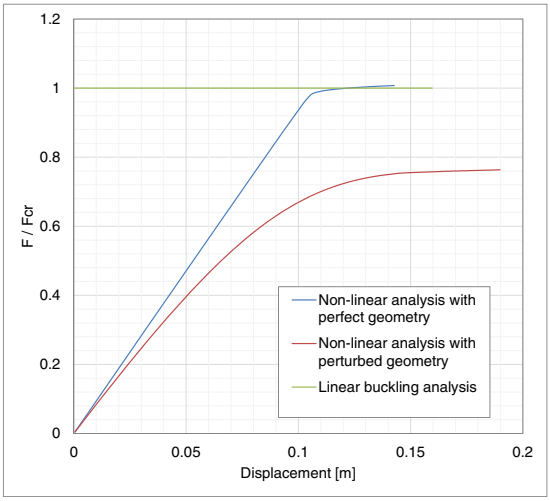

(a) LC2 - wind pressure, empty silo

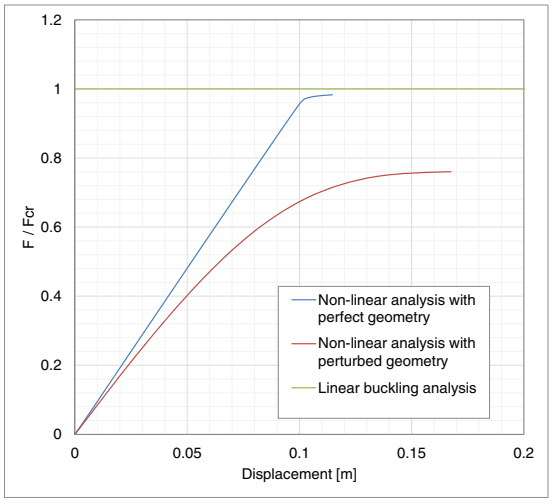

(b) LC3 - wind pressure, silo with sloshing water table

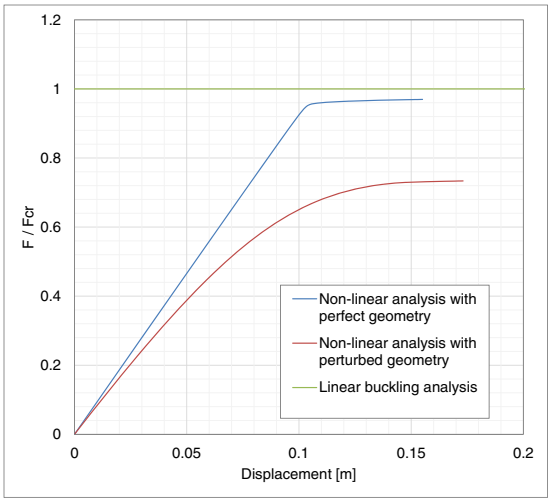

(c) LC4 - wind pressure, silo with flat water table

Figure 5.14: Silo load factor verses displacement curves

Load Case	Imperfection	Maximum deviation	LBA LF	GNLA LF	C
LC1		-			
LC2	None	-	22.532	22.700	1.010
	Mode 11	12.5 mm	22.532	17.200	0.763
LC3	None	-	22.890	22.500	0.980
	Mode 1	12.5 mm	22.890	17.400	0.757
LC4	None	-	23.31	22.6	0.971
	Mode 1	12.5 mm	23.31	17.304	0.741

Table 5.13: Summary of silo knock-down factors and other results

5.5 Aircraft fuselage

Using a grossly over-simplified model of an aircraft, the author intends to analyse the aircraft fuselage air-frame modelled by ring- and stringer- stiffened cylindrical shell. The model of the silo is recycled here to represent the fuselage thin of the aircraft.

5.5.1 Geometry

The fuselage is a major component of the air-frame of an aircraft. It extends from the nose to the empennage and holds crews, passengers and cargo. Traditionally, a fuselage is composed of a cylindrical skin supported longitudinally by stringers and radially by stiffening rings. The stiffening rings (formers or frames) set the shape of the fuselage and reduce the column length of stringers to prevent instability. The rings typically have a cross section of a I-beam. Stringers (longerons) are thin strips of material which are connected to the skin of the fuselage. In some aircraft designs, the stringers are also fastened to the stiffening rings, while in others, the stringers run the whole length of the fuselage uninterrupted.

Width of the fuselage is 5.77 m and height is 5.97 m. For simplicity, an average radius of 6 m is used. The ring stiffeners are 200 mm wide and are spaced 560 mm apart. The trapezoidal stringers are spaced 4° apart in the tangential direction. They are 50 mm, 80 mm and 40 mm in height, larger width (adjacent to the skin), and smaller width respectively. The thicknesses of the skin, the stiffeners, and the stringers are 5 mm,7.5 mm, and 5 mm respectively.

Mesh

The mesh generation is done parametrically to ensure all the above variables can be changed to adapt to different air crafts and possibly to ship hulls as well. In addition to the length and the width of the fuselage itself, the number of elements along each ring, the spacing of the rings, the spacing of the stringers are all parametric variables.

To address the fact that the stringers run through the ringed stiffeners without being physically attached to them in some aircraft designs, the rings do not share the node with the stringers and the skin at points of intersection. The stringers are modelled as quadratic Timoshenko beams (BEAM189) that allows for large deformation.

In the refined mesh model, there exists 148 680 elements in total, and 2 548 800 degrees of freedom. This study considers the situation where the aircraft is airborne at cruising altitude with a constant velocity. As a rigid object, the aircraft has six degrees of freedom. This study is concerned mainly with the equilibrium in the longitudinal direction, or the direction of flight and the vertical axis z. In the direction of flight (x), the two forces acting are thrust and drag. Drag is felt by all surface area perpendicular to the flow of wind, and thrust is produced by the turbo engines mounted to the wings. Assuming the wind is composed entirely of headwind, its effect can be calculated from calculating the surface area of the cockpit. In the earth-referenced vertical z direction. A stiff continuous cross-beam span the entire wingspan of the aircraft. This is used to transfer the lift generated by the wings to the fuselage and the tail to equilibrate with the weight of the aircraft.

Loads and Supports

To further simplify the analysis, one segment of the fuselage is considered as an axially loaded cylinder. The load is applied as uniform displacement along one end of the segment, and the other end is pinned.

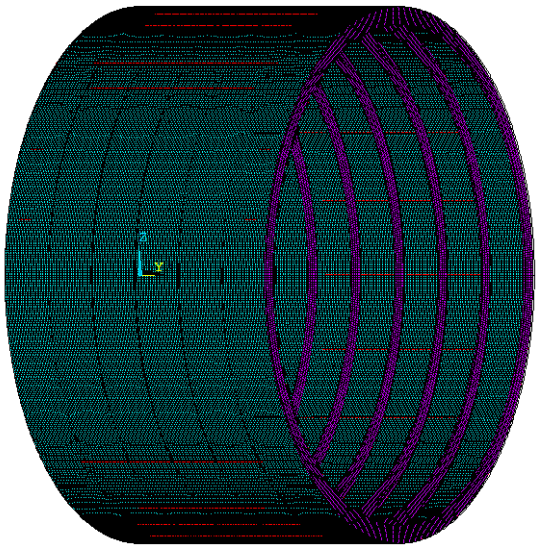

Figure 5.15: Fuselage mesh

Material

Traditionally, the whole fuselage is made entirely of aluminum. It is used due to its excellent strength to weight ratio and its ability to be extruded into any shape.

$$E = 205 \times 10^9 \,\text{MPa} \; ; \; \nu = 0.3 \tag{5.30}$$

Computational Cost

With this large model, the computational performance becomes a significant factor in the method of analysis. The standard procedure is applied to the fuselage, and the computation times of the different analyses are listed in Table 5.14. It is evident that LBA is an expensive analysis to run. This can be attributed to using zero as the starting point of eigenvalue search. By generating the imperfection shape without the use of LBA, the computation time can be decreased by $\sim 40\,\%$.

Analyses Type	Computation Cost s
Linear Elastic	294
Linear Buckling	11406
Imperfection	60
Non-Linear (average of 6 steps)	3082

Table 5.14: Computation cost of the different analyses

Linear Buckling Analysis

From LBA, the critical load factor calculated is $\lambda_{\text{cr}} = 3.96$. The buckling shape calculated is not symmetrical(Figure 5.16b); the asymmetry is attributed to the placement of longitudinal stringers, leading to different stiffnesses around the ring. It is seen that buckles occur in between the stiffeners and stringers, and closer to the supports (due to the pinned boundary layer). This type of local buckling is shown not to produce large reduction in capacity in Chapter 6. Therefore

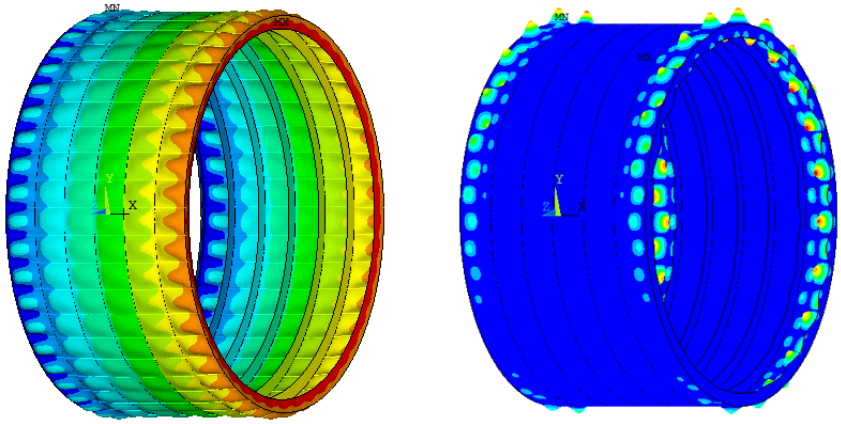

(a) Linear Elastic Analysis (b) Linear Buckling Analysis

Figure 5.16: Behaviour of the fuselage

one must obtain sufficient number of buckling modes until the first global buckle occur. The linear increase in computation cost makes this infeasible.

5.5.2 Imperfection

The first mode is imposed as the imperfection for the subsequent non-linear analysis. However, as stated above, a global buckling mode would be more desirable as the imperfection shape. This shape can be generated without the use of LBA, but by using the "superimposed wave" imperfection shape as described in Chapter 6. It remains to be seen whether global imperfection results in a larger reduction factor.

Non-Linear

Two non-linear analyses are run, one with imperfection and the other without. The resulting force verses displacement diagrams are plotted in Figure 5.17. Result of the analysis of the perfect structure vastly over-estimates the critical buckling capacity as is the case with other axisymmetric structures and loads. The model with imperfection however results in an ultimate capacity that is very similar to the critical one, $C \sim 1$. This suggests that using the first mode as imperfection, it would appear that the structure is not imperfection sensitive at all. While it is reassuring to know that the issue of over estimation is eliminated, it remains to be seen whether a higher mode or other imperfection shapes would render the structure imperfection sensitive.

The progressive displacement diagrams are shown in figure 5.18. Note that the buckles are localized to boxes bounded by stringers and stiffeners. The amplitude decreases as the buckles move toward the middle. This confirms the expectation that local buckling is not imperfection sensitive as the knock-down factor is 1. One may also observe the buckling of radial stiffeners. As the edge is restrained laterally, the stiffeners buckle inward uniformly.

5.6 Conclusion

Four simple yet realistic structures are studied using the proposed method of imperfection imposition. The cooling tower is used as an example of a hyperbolic structure. Self-weight and wind

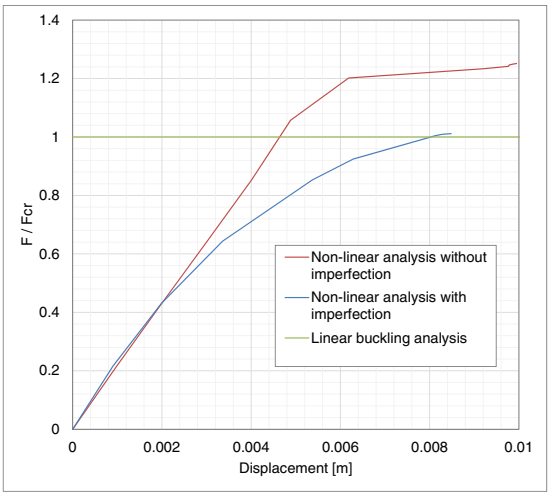

Figure 5.17: Force displacement plot of the fuselage segment

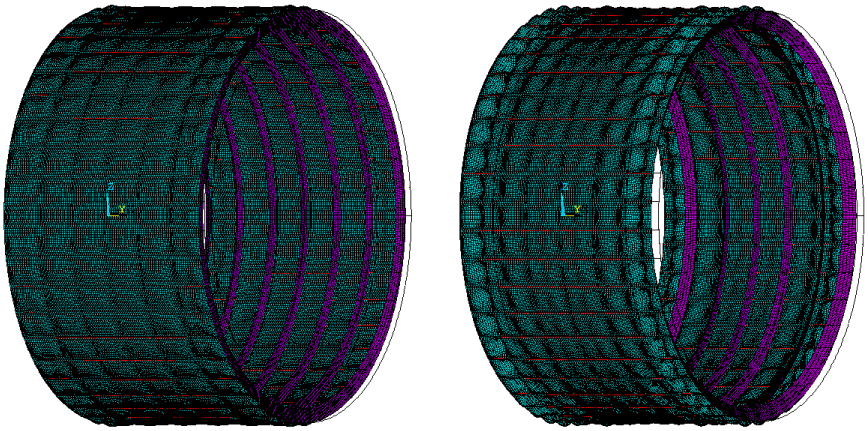

(a) Initial State (b) Final State

Figure 5.18: Initial and final displacement of the fuselage segment showing local buckles in between stringers and stiffeners

load are applied separately and in concert, both with and without geometrical imperfection, to assess the effect of imperfection on symmetric and asymmetric loading conditions. It is found that in both load cases, the model without imperfection follows a linear load-deflection curve that diverges at or above the critical load as calculated with the linear buckling analysis. The divergence is attributed to the sudden failure due to bifurcation buckling caused by excessive numerical imprecision. With geometrical imperfection, a knock-down factor of 0.75 can be applied to the critical load factor. The next structure tested is a monolithic concrete dome. Three loads are applied, namely the self-weight, wind load, and uniform external pressure. The same observation is made when the model is not perturbed by imperfection. When it is however, the knock-down factor is necessary to account for geometrical imperfection. For wind load, a factor of 0.37 is needed, and for the case of uniform pressure, $C = 0.87$. The spacing of the LBA load factors suggest higher modes may govern the behaviour.

The third model studied is the liquid containing silo. The structure is modelled after a commercially available aluminum silo. Wind load is applied to both an empty and a half filled silo with flat or sloshing water surface. The largest knock-down factor, $C = 0.74$, is associated with a half filled silo with flat water surface.

The fourth is also a cylindrical structure. A typical aircraft fuselage is modelled with stiffeners

and stringers. From LBA, it is observed that local buckling governs the behaviour. However, it may be the case that imperfection in the shape of a (much) higher mode with global buckling governs the GNLA result. Due to the computational cost of LBA, it becomes infeasible to calculate more than a few modes. Therefore, if it would be advantageous to generate the imperfection shape without the need of LBA.

Overall, GNLA of shell structures with geometric imperfections are quite robust and easy to perform. It is evident that the designers of the software provided the tools specifically for this purpose. Without geometrical imperfections, the analyses becomes much more difficult and the results much less reliable. This is expected for symmetrical structures loaded by self-weight, but the inaccuracy was also observed in asymmetric loading as well.

Chapter 6

Study of Imperfection

6.1 Summary

Construction tolerances given to contractors offer a wide margin of error, this is done to avoid future litigation should disasters happen. It is the author's intent to integrate this tolerance in the study of the amplitude of imperfection on structural capacity of thin shells. In chapter 3, the applied imperfection has been in the shape of the first buckling mode with a maximum amplitude of $t/2$. This is in accordance with the design philosophy that the first mode is the worst since it is by definition the mode with the lowest load factor.

However, as indicated by numerous studies [15] and in Chapter 5, in certain structures under certain load and support conditions, imperfections in the shape of the higher modes or a combination of modes may be more critical. Furthermore, other studies have attempted to impose random imperfections in an attempt to extract lower load factors through geometrical non-linear analyses.

Koiter's original theory imposes imperfection of global periodic shapes [28], then at a later stage applied his theory to a localized periodic disturbance and obtained the same imperfection characteristics [29].

Arbocz started by varying the modal imperfection amplitude and also the applied load [18]. He then focused on measuring real imperfections, representing them in Fourier series and recording the coefficients. With the idea of categorizing imperfection based on the production method, he proposed to combine this characteristic imperfection with statistical analysis when analysing shell structures [11] [12]. The Fourier coefficients are the basis of an "Imperfection Databank". Furthermore, Arbocz proposed an improved knock-down factor which rewards manufacturers who are able to produce at a higher quality. This technique has only been applied to metallic circular cylindrical shells.

This study proposes four methods of imperfection generation based on the above attempts, and then applies these methods to both the hyperboloid and the cylinder in an attempt to extract an imperfection shape that produces the lowest load factor.

1. The first method proposed is the single modal method, where one buckling mode is imposed as the imperfection. Two variations are proposed. One introduces a noise on the whole buckling shape, and the second flattens out a buckle wave in the buckling shape.

2. The second method superimposes multiple modal shapes before imposing it as the imperfection shape. The superposition is done in two ways. The first assumes equal contribution from the constituting modes, the second assumes random contribution.

3. The third method generates a Gaussian random imperfection shape based on construction tolerance as an input.

4. The fourth method generates a periodic buckling wave imperfection.

Measured imperfection field is not used in any of the methods described, as characteristic manufacturing imperfection is not available for any shapes other than the cylinder, and it is the author's intent to apply these methods to all shapes. Note that the amplitude of imperfection is not varied in this study. Its effect was shown in Chapter 4, and is assumed to have similar or less pronounced effect on other types of structures. This study also proposes a new knock-down factor to measure the effect of the imperfection shapes on the buckling capacity.

Lastly, stress related and loading imperfections are studied.

6.2 Imperfection Methods

6.2.1 k^{th} buckling mode

The buckling mode that has been used thus far is defined here as the k^{th} buckling mode, where k is the modal number. Therefore the imperfection shape can be defined as follows,

$$\delta^{\text{Imp}}(x, y, z) = \frac{C \cdot t}{\delta^k_{\text{max}}} \delta^k(x, y, z) \tag{6.1}$$

where $C \cdot t$ is the maximum amplitude of imperfection expressed as a function of the thickness, δ^k_{max} is the maximum magnitude of the vectorial deflection in the k^{th} buckling mode, and $\delta^k(x, y, z)$ is the component deflection in the k^{th} buckling mode.

With Eq. (6.1), $\delta^{\text{Imp}}_{i,j,k}$ is the field of imperfection that is applied to the initial perfection geometry on a component by component basis. For example, $k = 1, C = 0.5$ would mean to apply imperfection in the shape of the first mode with the maximum resulting amplitude of half of the thickness.

One weakness to this method is that the boundary layer will remain geometrically perfect if ideal pin / fixed support conditions are assumed. To overcome this issue one could either assume swap the pinned condition to finite stiffness springs or to artificially perturb the boundary layer.

Perturbation

Eq. (6.1) is supplemented with an additional noise term to test the effect of a perturbed buckling shape.

$$\delta^{\text{Imp}}(x, y, z) = \frac{C \cdot t}{\delta^k_{\text{max}}} \delta^k(x, y, z) + \text{GDIS}(\mu, \sigma) \tag{6.2}$$

where μ is the mean and σ is the standard deviation. For this study the mean is set to zero, $\mu = 0$, and the standard deviation is set to be one tenth of the thickness, $\sigma = t/10$. For a detailed discussion on using ANSYS GDIS (Random generator using Gaussian Distribution) to generate probabilistic rough surfaces, see Thompson [42].

With this method of perturbation, the geometry of the boundary layers (top and bottom ring) no longer remain perfect, therefore the effect of perturbing the boundary condition can be assessed as well.

Flattening

The buckling modal imperfection is regionally flattened to eliminate the largest buckle. This is done to test the effect of significant asymmetry. It is implemented with a recursive algorithm that starts at the node with the maximum deflection, and propagates depth-first down to the ring of nodes with less-than-limit deflection. The limit is set at a value slightly above zero to terminate the recursion before the end of one buckle is reached, and to ensure that the recursion never reached the neighbouring buckles.

As ANSYS does not allow recursion (or any iteration) past 20 steps, a more restrictive algorithm is developed to eliminate recursion. The algorithm finds the largest nodal displacement, and parses in four directions (up, down, left, right) until the displacements become less than the limit, and set all imperfections within that rectangular area to zero. Evidently, the algorithm only works with rectangular buckles.

Reverse Flattening

To simulate Koiter's theory on "More-or-less" localized periodic disturbance, the above generation function is modified so that only one buckle is preserved. The imperfection field is set to zero except in the vicinity of the largest buckle as identified by the algorithm above. This is similar to Kroplin's local imperfection, though it appears that the localized imperfection used was smaller than the size of a buckle.

6.2.2 Combination of n buckling modes

The hypothesis of modal interaction is tested here where n modal shapes are combined to produce an imperfection shape. The first variation of this method assumes equal contribution from all selected modes and creates an imperfection shape with the same total maximum amplitude of $C \cdot t$.

$$\delta^{\text{Imp}}(x, y, z) = \frac{C \cdot t}{\max \sum_{k=1}^{n} \delta_{i,j,k}^{k}} \sum_{k=1}^{n} \delta^{k}(x, y, z) \tag{6.3}$$

Perturbation

The second variation generates n random weights to be multiplied to each modal shape. This randomizes the contributions of each mode and produces a different imperfection shape at each trial. With this variation, the correlation between modal contribution and relative change in reduction factor can be tested, and the governing modal shape can be identified.

$$\delta^{\text{rand}}(x, y, z) = \sum_{k=1}^{n} A^{k} \delta^{k}(x, y, z) \tag{6.4}$$

where the random weights range from 0 to 1,

$$A^{k} = \text{rand}(0, 1); k \in [1, n] \tag{6.5}$$

and the sum of these weights is also 1

$$\sum_{k=1}^{n} A^{k} = 1 \tag{6.6}$$

then this random shape is normalized to the same maximum imperfection magnitude of $C \cdot t$,

$$\delta^{\text{Imp}}(x, y, z) = \frac{C \cdot t}{\delta_{\max}^{\text{rand}}} \delta^{\text{rand}}(x, y, z) \tag{6.7}$$

Sufficient n

There as many buckling modes as there are DOFs in the system and it would be infeasible to generate combinations of all of them. For a typical shell such as the hyperboloid, one can include those modes whose the load factor is within a certain percentage of the first mode. This approach may not work for shells that are very sensitive to imperfection where the modes are spaced closely together, such as the cylinder. In that case, the first ten modes are extracted and used as the basis of imperfection shapes. The rationale being that the first ten modes encompass all the different types of buckling shapes (i.e. axisymmetric, asymmetric, and so on).

6.2.3 Gaussian random

While imposing buckling modes as imperfection is the standard approach to thin shell buckling problems, there is no guarantee that the above will produce the worst case scenario. Therefore, random imperfections are generated in an attempt to produce lower load factors.

With the exception of the imperfection data generated by cylinder measurements, the designers often have no other reliable imperfection data aside from the construction tolerance provided by the contractor. To simulate geometrical imperfection that may occur at an actual construction site, an simple application is written which generates such a random imperfection with the total deflection of a buckling mode and a maximum construction tolerance as inputs.

In the purpose of this thesis, to ensure the randomly generated imperfections are comparable to a buckling mode, the maximum displacement is also set as $C \cdot t$ (instead of the construction tolerance). To impose further constraints on the random generation, the total magnitude of vector imperfection displacement is set to equal to those of a buckling mode. With these two constraints in mind, an optimization problem is set to solve for a random shape of the imperfection.

Constraint 1 states that the maximum amplitude of random imperfection must not be greater than that of a modal shape

$$\left|\delta_{\max}^{\text{rand}}\right| \leq \left|\delta_{\max}^{m}\right| \tag{6.8}$$

Constraint 2 states that the total absolute amplitude of random imperfection must not be greater than that of a model shape

$$\sum_{i=1}^{n} \left|\delta_{i}^{\text{rand}}\right| \leq \sum_{i=1}^{n} \left|\delta_{i}^{m}\right| \tag{6.9}$$

Parametrized onto a two dimensional surface, constraint 3 limits the change in deflection (or slope) between neighbouring nodes.

$$\left|\delta_{u,v}^{\text{rand}} - \delta_{u+i,v+j}^{\text{rand}}\right| \tag{6.10}$$

where

$$i \in [u-1, u+1], j \in [v-1, v+1] \tag{6.11}$$

Implementation

The author uses ANSYS's native GDIS function to generate the imperfection field with a Gaussian random function. Two calibration constants, C_1, C_2 are introduced in order to optimize the field towards the constraints, though never to satisfy them rigorously. The optimization is done iteratively where C_1 and C_2 are continuously adjusted with each generation of imperfection field until constraints 1 and 2 are within 95 % of the required values. Constant C_1 is introduced

to the standard deviation of the Gaussian random function. This is so that the probability of generating an individual value outside of the constraint (6.8) is sufficiently small.

$$\sigma = C_1 \cdot C \cdot t \tag{6.12}$$

Constant C_2 is introduced to simulate pinching of the distribution of the randomly generated imperfection field. This pinching is done by multiplying the field by a linear function. Figure 6.1 shows one such Gaussian distribution and the linear multiplier function. Note that this linear function is applied to the sample values on the x-axis and not the probabilities on the y-axis. The function is set so that the maximum and the minimum values of the imperfection field remain the same (multiplied by 1), and the closer the values are to 0, the more they are reduced, with the maximum reduction set at C_2. C_2 could also be a negative number to effectively widen the distribution, and increase the total absolute amplitude. A parabolic function could also be implemented, however since the maximum and the minimum amplitude are not necessarily the same, the function may not be centred at zero.

$$\delta_{\mathrm{i}}^{\mathrm{imp}} = \delta_{\mathrm{i}}^{\mathrm{rand}} \cdot f(\delta_i^{\mathrm{rand}}) \tag{6.13}$$

$$f(\delta_i^{\mathrm{rand}}) = \begin{cases} \frac{\delta_i^{\mathrm{rand}}}{C_2(\delta_{\mathrm{min}}^{\mathrm{rand}}} - 1) + 1 & \delta_{\mathrm{i}}^{\mathrm{rand}} \leq 0 \\ \frac{\delta_i^{\mathrm{rand}}}{C_2(\delta_{\mathrm{max}}^{\mathrm{rand}}} - 1) + 1 & \delta_{\mathrm{i}}^{\mathrm{rand}} \geq 0 \end{cases}$$

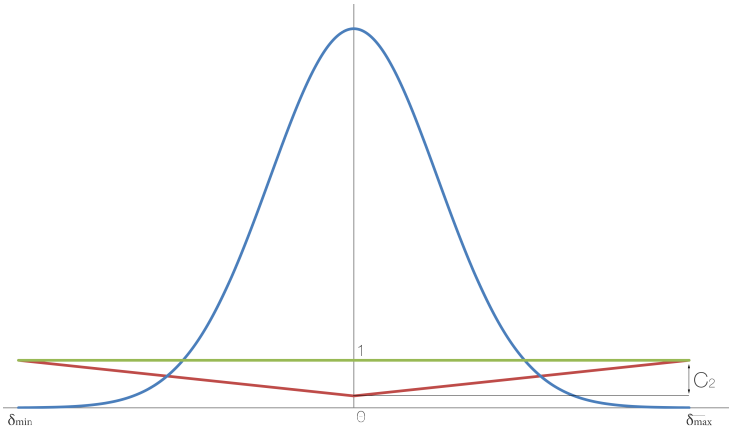

Figure 6.1: Typical g;aussian distribution and the linear multiplier function

The above is applied to each individual coordinate components (x,y,z) separately. This however tended to generate ill-shaped elements for extremely refined meshes. In such cases, the normal to the element surface may be calculated, and the nodes may be perturbed along the normal vector. In all models in this thesis however, no ill-shaped errors occur. Constraint 3 is implemented via the smoothing function native to ANSYS.

6.2.4 Buckling waves

Seeing that the buckling shapes are essentially different super-positions of periodic waves, a function is written that generates an imperfection field based on the number of buckles in u and v directions. This function generates periodic buckling wave shaped imperfections over the whole surface of the structure. Presuming the structure can be parametrized onto a 2-D surface, the algorithm superimposes two sinusoidal functions onto that surface. Kroplin also performed an analysis with sine - imperfection [31].

$$C_{u,v} = A \cdot sin(\frac{m\pi}{L_1}x_u + \phi_1) \cdot sin(\frac{n\pi}{L_2}x_v + \phi_2) \tag{6.14}$$

Note that there is no randomness in this method. In this thesis, no phase shift is added, and the buckling wave parameters are m and n. Should either m or n be zero, then buckles would only exist in one direction. This shape would be similar to a axisymmetric buckling shape.

6.3 New Knock-down factor

The author hypothesizes a new knock-down factor C_{m} which compares the resulting load factor of a geometrically non-linear analysis perturbed by m^{th} imperfection to the same model perturbed by the imperfection in the shape of the first mode. This differs from the traditional knock-down factor (Eq. (2.6)) in that the load factor is no longer compared with the linear buckling load factor. This new factor serves to eliminate the uncertainty around the imperfection sensitivity of a geometry.

$$C_{\mathrm{m}} = \frac{\lambda_{\mathrm{ult},1}}{\lambda_{\mathrm{ult},m}} \tag{6.15}$$

With $\lambda_{\mathrm{ult},1}$ the designer would understand both the imperfection sensitivity, and the real buckling capacity of the design. Should the first buckling mode always governs, then C_{m} would be greater than 1. As an example, should $0.8 \leq C_m \leq 1.2$ then for this particular structure with this particular load case, 0.8 would be the safety factor applied to the load factor produced by the perturbed GNLA (Eq. (6.16)).

$$R = C_{\mathrm{m}}\lambda_{\mathrm{ult},1} \tag{6.16}$$

6.4 Application to cylinder

The methods of imperfection generation proposed above are used on the cylindrical model from Chapter 4. It is hypothesized that these methods cover most of the reasonable imperfection shapes, and therefore the modified knock-down factor obtained can be used to design such a structure. The cylinder is chosen for its extreme imperfection sensitivity. This study shows that the first mode does not govern, and modal combinations are more severe, and so are some random shapes. As was discussed in Chapter 4, displacement-control is assumed for all analyses of the circular cylinder. The model and analysis set-up remains identical.

6.4.1 Method 1

As with previous analyses, first the LBA is performed to obtain sufficient number of buckling modes. Figure 6.2 shows the buckling shape of the first ten modes, and the eigenvalues associated with each. As stated in Chapter 4, though the most shapes are distinct, the eigenvalues remain almost identical. This would suggest that the structure is imperfection sensitive. It is also observed that some modes are axisymmetric in the sense that there are buckling waves primarily in one (vertical) direction (3, 6, 7, and 10) and the rest are asymmetrical.

The LBA result file is duplicated for each subsequent GNLA to ensure that the starting point remains identical. Ten GNLA are performed, each assuming the imperfection one of the first

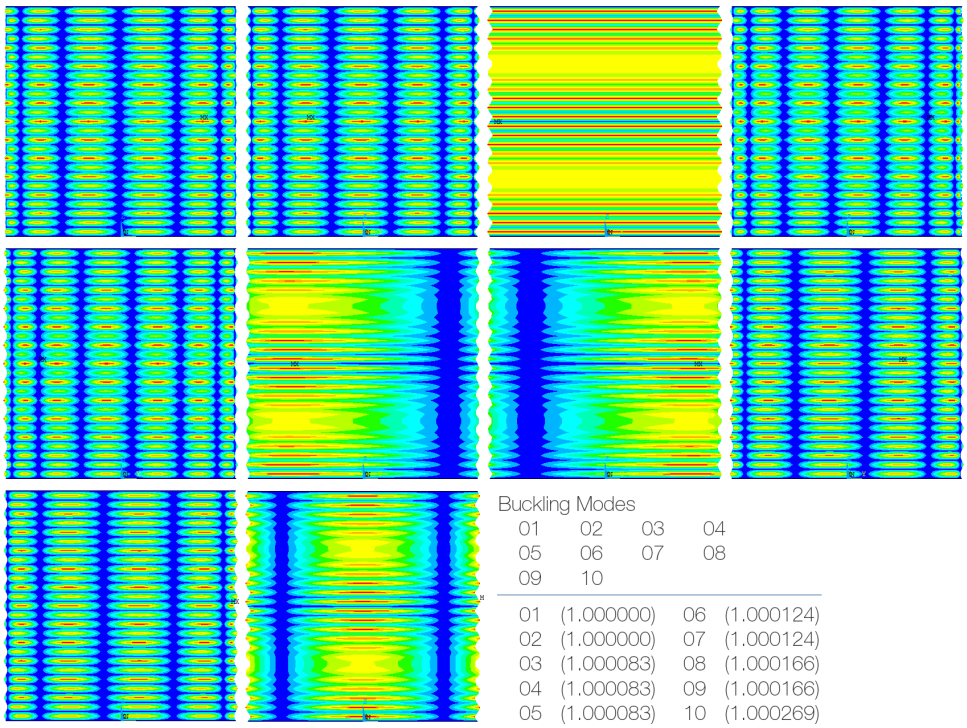

Figure 6.2: First 10 buckling modes of a cylinder

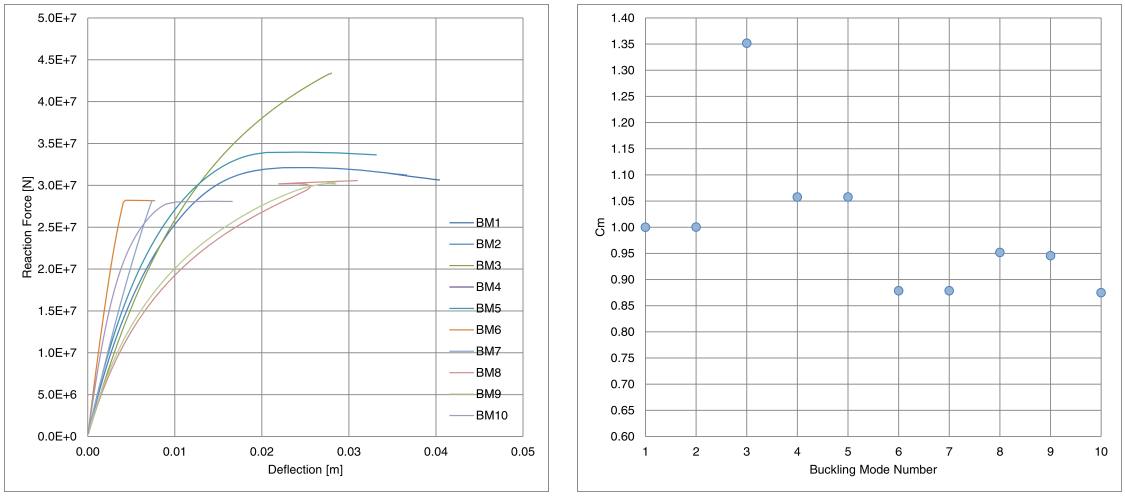

(a) Load displacement curves

(b) C_{m} values

Figure 6.3: Behaviour resulting from modal shaped imperfections

ten modes. The maximum imperfection amplitude is set at $t/2$ for all ten cases. The results are gathered in Figure 6.3a.

Figure 6.3a contains the load displacement curves of all the analyses. The wide scatter of both stiffness and ultimate strength is evident. As was discussed in Chapter 4 already, all trials exhibit a major reduction in capacity when compared to the results of LBA or with the results of GNLA of a geometrically perfect cylinder.

The previously defined modified knock-down factor C_{m} is applied to this series of analysis with the GNLA result from trial 1 as a reference. Trial 1 is the GNLA with first buckling mode as the imperfection. Figure 6.3b plots the C_{m} for each trial.

It is evident that C_m is not monotonically increasing, proving that the first modal imperfection does not generate the largest reduction factor in capacity. Furthermore, the distribution seems to be random, with similar factors for different imperfection shapes. Mode 3 (an axisymmetrical mode) seems to have the least reduction factor, while other axisymmetrical modes (6, 7) govern the reduction.

Method 1 Variation 1

Gaussian noise is added to the modal imperfection shapes with a standard deviation of $\sigma = {}^{t}/_{10}$ and a mean of zero. The same ten trials are performed, but each buckling modal shape is perturbed with Gaussian noise. It is expected that the modal shapes would be the worst imperfection shapes, and any perturbation around the shapes would lessen the effect. This is not the case for cylinders. Several interesting observations can be made with the above analyses.

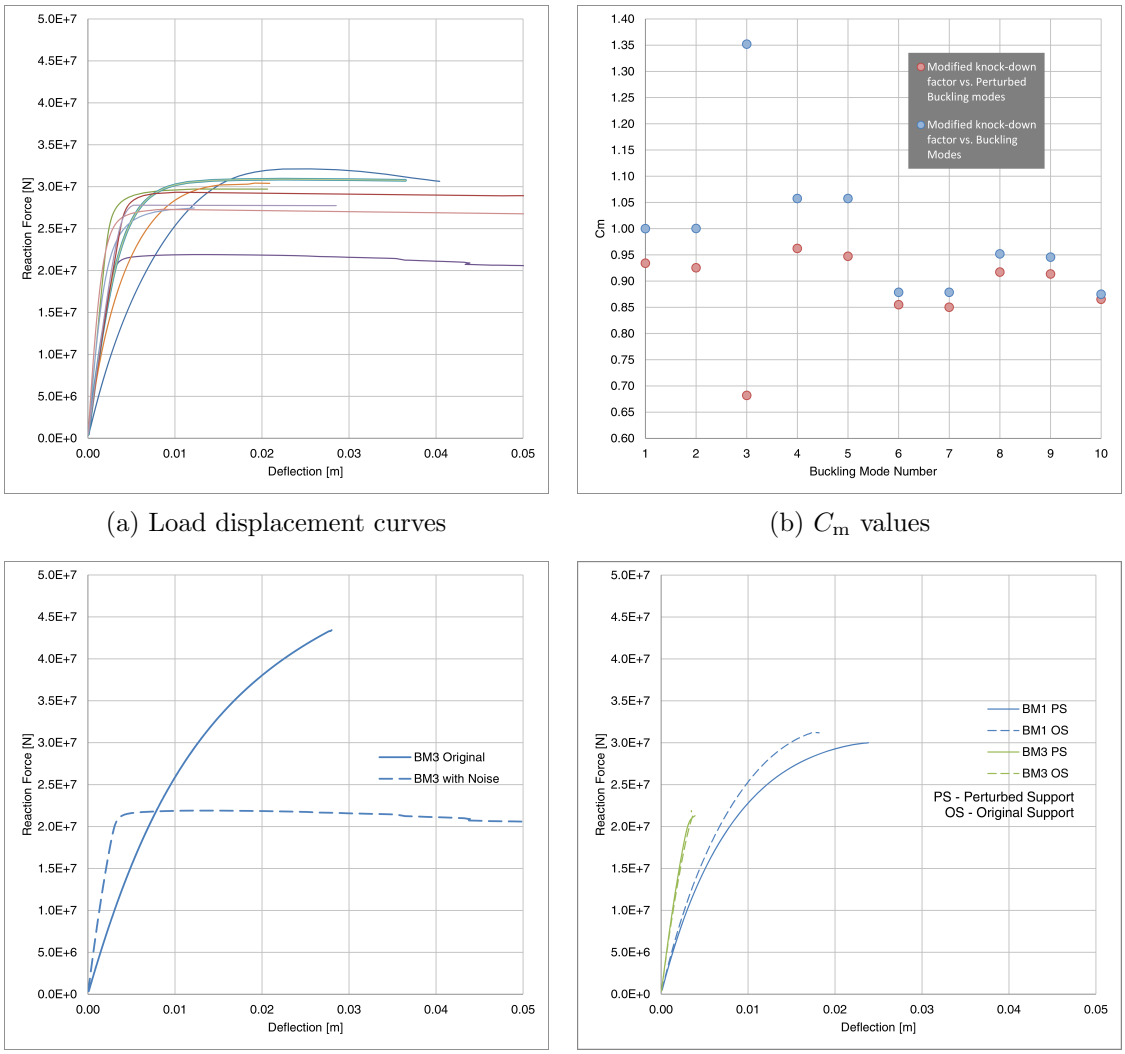

(a) Load displacement curves

(b) C_m values

(c) Effect of Gaussian noise

(d) Original and perturbed boundary

Figure 6.4: Effect of Gaussian noise and perturbing the boundary layer

As Figure 6.4a shows, the post-buckling behaviour is more sustained and ductile. Larger strain is observed for all trial runs.

Figure 6.4b shows the effect of Gaussian noise on C_m. A uniform decrease is observed in all but one trial, where a significant drop is exhibited. The load displacement curves of these two trials

are isolated in Figure 6.4c. This observation would imply that axisymmetrical imperfections may introduce an artificial capacity in the hoop direction to the structure, and prevent buckling in between the ring buckles. By introducing the noise, this artificial capacity is removed. This form of buckling is investigated in more detail in chapter 7.

Lastly, Figure 6.4d shows the effect of boundary layer disturbance. Trials involving imperfection shape 1 and 3 are re-analysed but with the boundary nodes (both top and bottom) unperturbed (by the Gaussian noise). Shape 1 is chosen as a normal case and 3 as an extreme one (in terms of the effect of Gaussian noise). An improvement is observed as expected, but the improvement is not drastic. Therefore, it can be stated that the geometrical perturbation of the boundary layer does not have as large of an impact on the buckling capacity as general geometrical imperfection.

Furthermore, referring to Calladine's initial boundary stress condition [32] where an induced localised initial stress around the support showed a significantly less influence on capacity reduction, it seems that boundary layer does not play an important role on imperfection sensitivity of a thin cylindric shell.

Method 1 Variation 2

Buckle flattening and reverse flattening is only applicable to asymmetric buckling modes, as with axisymmetric modes there is already no buckle in the tangential direction. Furthermore, as the buckles are extremely localized in the cylinder, the mesh is not sufficiently refined for the algorithm to function.

6.4.2 Method 2

6.4.3 Variation 1

Method 2 forms new imperfection shapes by combining the different modal shapes. As with method 1, the resulting imperfection field is scaled so that the maximum amplitude equals to $t/2$. The first attempt is to pair-wise combine neighbouring modes with equal contribution. The results are plotted in Figure 6.5a, where for example, combination of mode 1 and 2 is plotted as buckling mode 1.5. Most combinations result in buckling capacities exactly the average of the results of their two constituents. The exception is around mode 3 as was the case in the previous method. Combination 2 and 3, and combination 3 and 4 resulted in capacities that are more inline with the result from the Gaussian noise method than with the original. This suggests that the modal combination also removes the artificial stiffness introduced by the mode 3 shape.

The buckling shapes of combination 2+3 and 3+4 resulted from GNLA are shown below. Note that in both cases, buckles occur at the equator of the cylinders, and in both tangential and vertical directions.

It is evident that the third mode produces the largest reduction in capacity, therefore the next study combines the third mode with other modes. Figure 6.5b superimposes the C_{m} factors of combination 3+1 to 3+10 on results from method 1. It is evident that when the third mode (an axisymmetric mode) combines with another axisymmetric mode (6, 7, 10), the capacity increases, suggesting that the artificial stiffness is not eliminated. Conversely, when it is combined with an asymmetric mode, the capacity lowers.

6.4.4 Variation 2

Going back to the combinations of 2+3 and 3+4, instead of assuming equal contribution, the weights are varied to assess the impact of each constituting modes. 3 random trials are done with

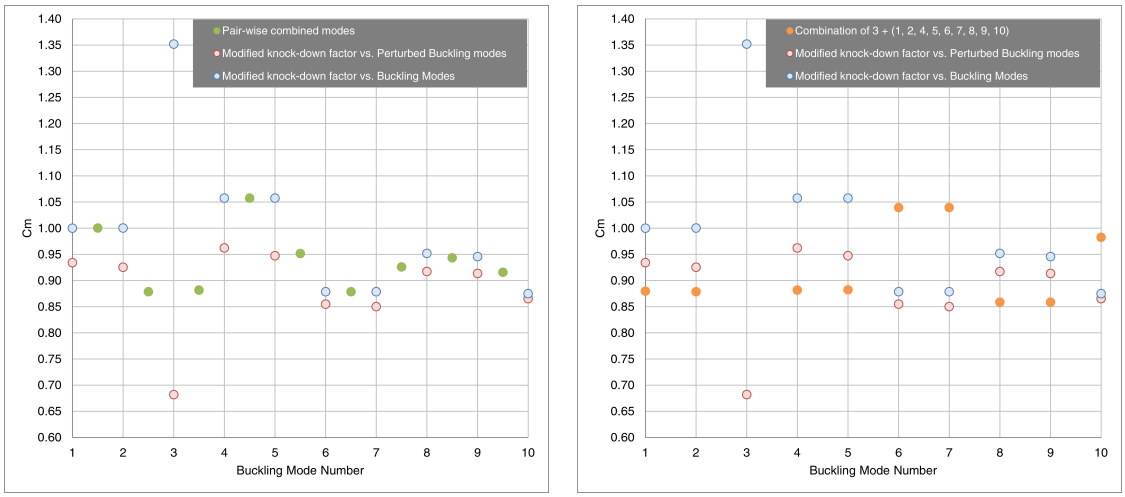

(a) Pair-wise combination (b) Combination with BM3

Figure 6.5: Effect of modal combination

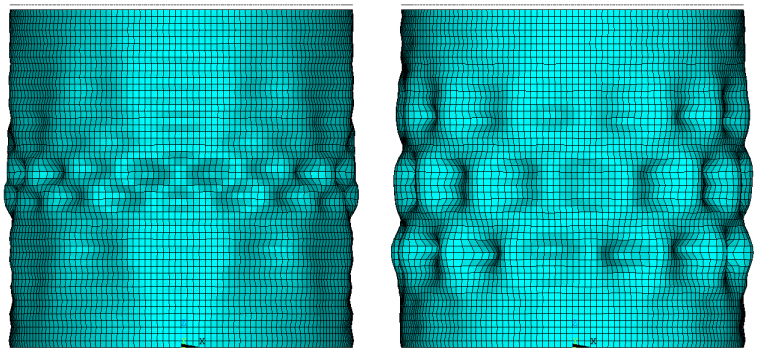

(a) Combination BM2 + BM3 (b) Combination BM3 + BM4

Figure 6.6: Final displacement diagrams resulting from different imperfection shapes

each of the two combinations. By observing figure 6.7, it is clear that as long as an asymmetric mode is present, however minutely, the reduction deviates towards the governing value. Indeed, the Gaussian noise may be considered a minute asymmetric perturbation. Beyond that, the more contribution the axisymmetric mode has, the larger the capacity reduction is.

6.4.5 Method 3

This method generates a Gaussian random field as a geometrical imperfection. In the design phase of an actual project, the only parameter needed is the construction tolerance. This tolerance is used to calculate a standard deviation for the Gaussian distribution. In this thesis, for the sake of comparison, a modal displacement field is used as a reference.

5 GNLA are performed with buckling mode 1 as the reference and 5 more with buckling mode 2, towards a total of 10 simulations. In addition, 2 more GNLA are performed for each buckling mode but doubling the magnitude of total imperfection.

Figures 6.8 compares the C_{m} resulted from random imperfection with those from modal shaped imperfections. It is immediately evident that modal imperfection governs the capacity for buckling mode 1. The magnification lowers the capacity but not by an overwhelming amount. For

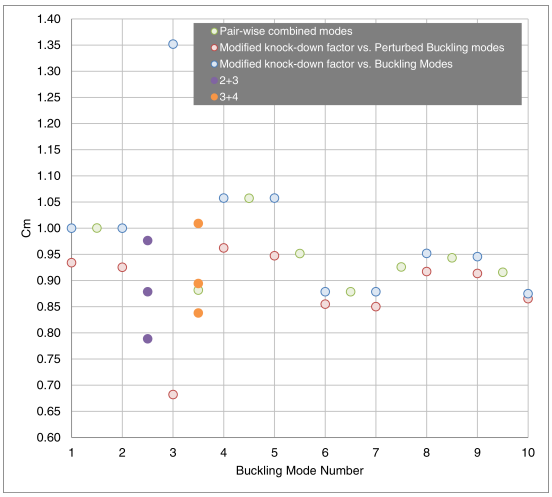

Figure 6.7: Combination of 2+3 and 3+4 with random contribution

BM1	BM2	W1	W2
2	3	0.733593	0.266407
2	3	0.499557	0.500443
2	3	0.287106	0.712894
3	4	0.593494	0.406506
3	4	0.469052	0.530948
3	4	0.191967	0.808033

Table 6.1: Contributing modes, and associated weights

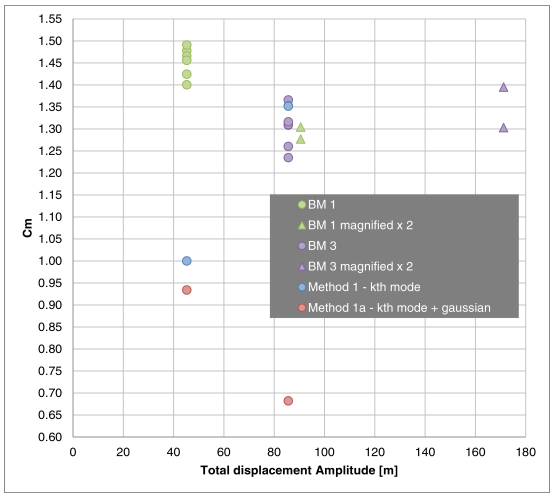

Figure 6.8: Gaussian random imperfection trials

buckling mode 3 as reference however, some trials of the randomly generated imperfection generates a lower capacity value than the unperturbed buckling modal imperfection. Magnification does not have a visible effect.

If we consider buckling mode 3 as an outlier, there seems to be little correlation between the maximum imperfection amplitude or the total imperfection amplitude of an imperfection shape to the structures buckling capacity. Indeed, if the shape is randomly generated, C_{m} remains above 1.2 irrespective of the total displacement amplitude. The shape of the imperfection is the remaining uncertainty that need be investigated.

6.4.6 Method 4

Different permutation of tangential and vertical buckling wave numbers, m and n, are simulated in separate GNLA trials in attempts to extract the governing buckling capacity of the cylinder. m and n range from 0 (i.e. no waves) to 5, 10, and 20, resulting in 64 separate analyses. To reduce the computational effort, several combinations are eliminated for being unrealistic or not representative. Table 6.2 lists the permutations of analyses and the resulting C_{m}.

C_m		m							
		0	1	2	3	4	5	10	20
n	0							1.940	1.760
	1		2.200	2.21	2.117	2.025	2.091	2.114	
	2		2.060	2.167	1.991	2.014	1.980	1.978	
	3		1.986	2.052	1.050	2.003	2.027	1.880	
	4		1.823	2.052	2.019	1.971	1.043	1.578	
	5		1.597	1.907	1.897	1.860	1.640	1.387	
	10	0.990	2.262	1.726	1.726	1.046	1.045	0.870	
	20	0.820	0.850	0.850	0.850	0.890	0.859		0.930

Table 6.2: C_m resulting from wave imperfection of varying m and n

Similar calibration parameters are adopted from Method 3, though C_1 is made redundant since the maximum amplitude of the imperfection field can be precisely set to equal to that of the reference modal shape. Since there is no randomness in this method, no iteration is needed, and C_2 can be calculated for each permutation of m and n so that the total amplitude matches that of the reference modal shape.

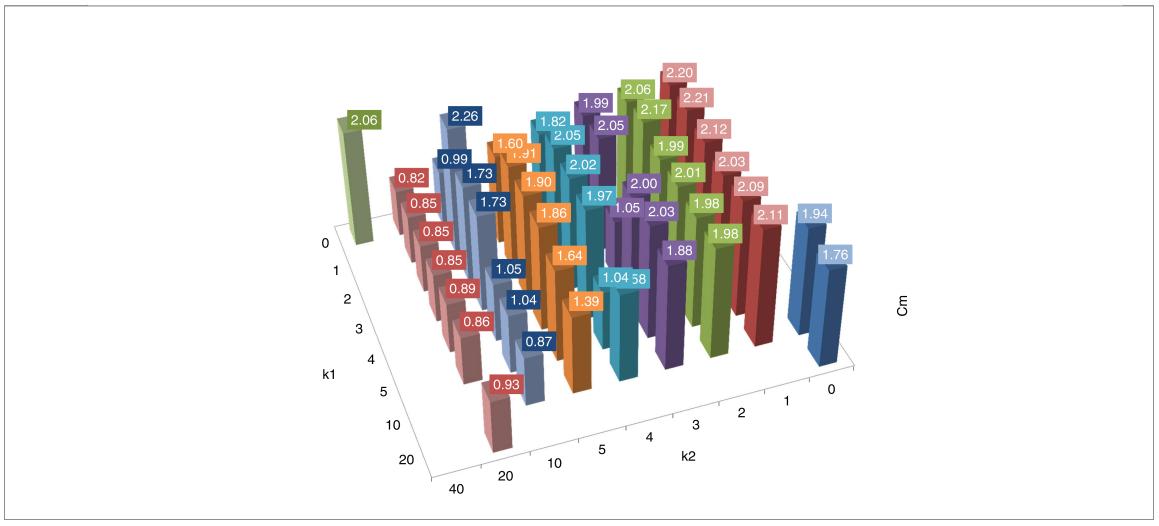

Figure 6.9: Bar graph of C_m of wave imperfection of varying m and n

Figure 6.9 shows the GNLA results from these permutations of buckle wave numbers. It is observed that in general, more buckling waves lead to lower capacities. Buckles in the vertical direction reduces capacity far more than buckles in the tangential direction. With n 20 and $m = 0$, the imperfection shape resembles that of the third buckling mode. However, this imperfection does not exhibit the artificial stiffening behaviour as was the case with the third buckling mode, and the reduction factor is in-line with the result from method 1a (with the Gaussian noise).

6.5 Application to Concrete cooling Tower

The concrete cooling tower is used as an example of a moderately imperfection sensitive structure. Self-weight is applied as the only load case. It is implemented in ANSYS as an gravitational acceleration in the negative global z direction, and as such displacement control is not feasible.

For a detailed description of the geometry and modelling parameters, refer to Chapter 3.

6.5.1 Method 1

The axisymmetrical nature of the structure resulted in mirrored or paired buckling modes from LBA calculations, therefore only the odd modes are extracted for the subsequent analyses. Modes 1, 3, 5, 7, 9, 11 are imposed separately as imperfection shapes onto the original structure. The maximum imperfection magnitude remains $t/2$.

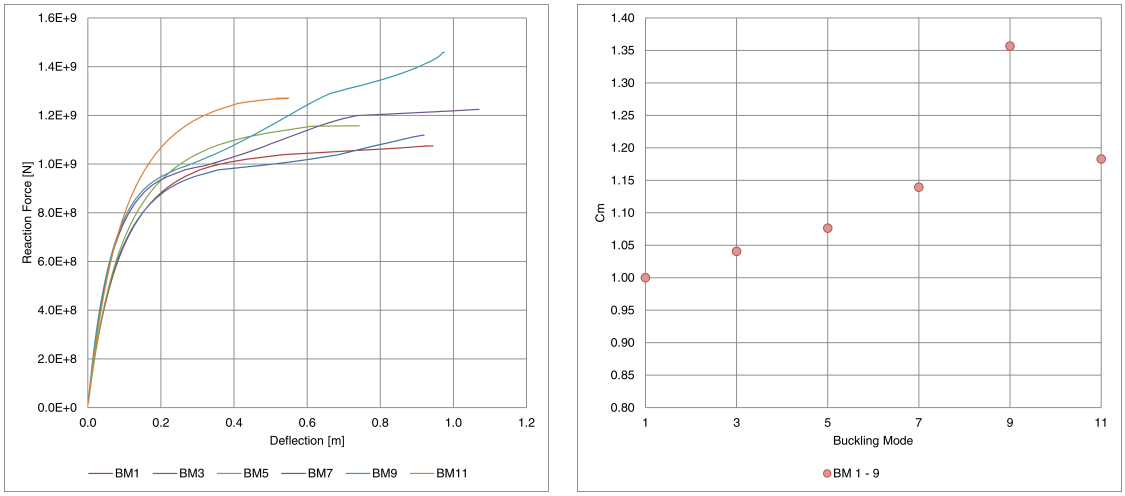

(a) Load displacement curves

(b) C_{m}s

Figure 6.10: Results of modal shaped imperfections

From Figure 6.10b it is evident that C_{m} is greater than 1, and monotonically increasing until mode 11. This would suggest that geometrical imperfection in the first buckling mode governs the capacity.

Method 1 Variation 1

Gaussian noise is introduced to each of the above buckling modal imperfections. GNLA is then performed to obtain the following results.

By combining the modal shapes, figure 6.11a show that the load displacement curves reduce in scatter. C_{m} while still greater than 1, is no longer monotonically increasing. In fact, significant divergence is observed for the higher imperfection modes (7 and 9). To verify that it is the change in geometry due to the noise, and not the slight change in amplitude that is causing the reduction in C_{m} in imperfection model 9, the standard deviation of the Gaussian noise is reduced by a factor of 2, and then 4. The resulting C_{m}s are plotted in 6.11b near the original model 9 value (they should all be aligned vertically in the plot but for clarity, they are shifted slightly to the right). The data points near mode 9 shows that the change in amplitude of noise does not have an effect on the capacity reduction. This agrees with the conclusion from Chapter 4.

Method 1 Variation 2

With the hyperboloid, buckles flattening and reverse flattening is more easily accomplished since they are large and rectangularly defined. From the figure, it is clear that one of the

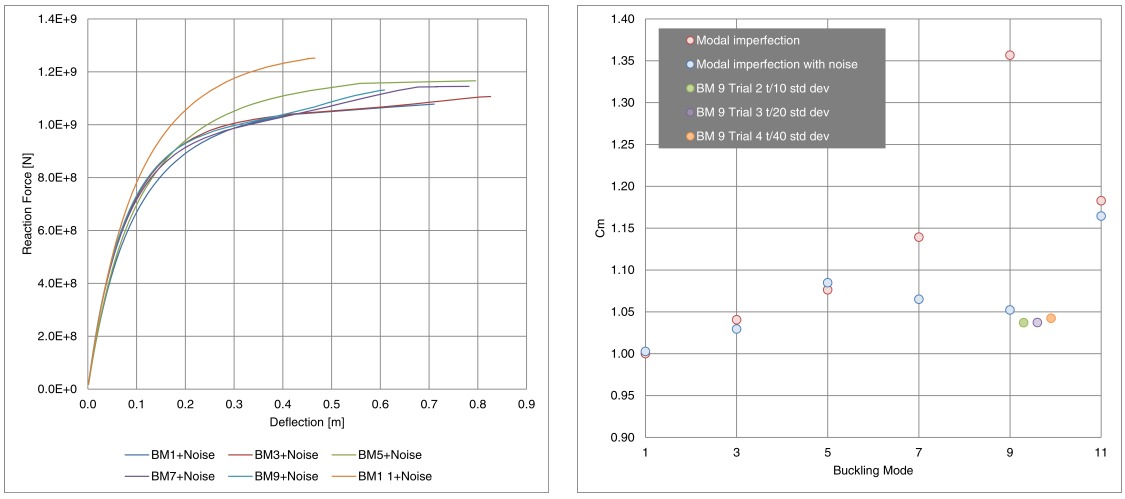

(a) Load displacement curves

(b) C_{m} with noise of different amplitude

Figure 6.11: Effect of noise on imperfection

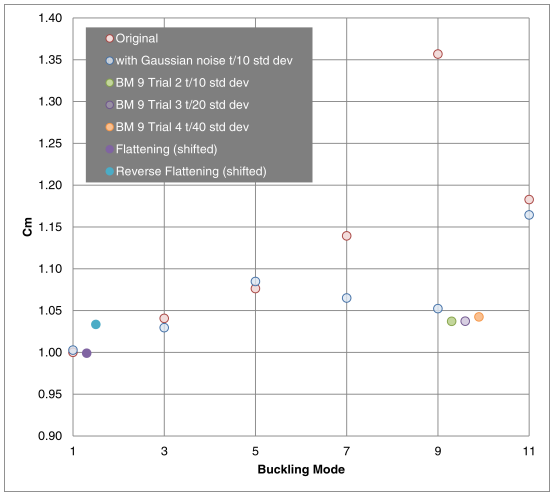

Figure 6.12: Effect of flattening and preserving one buckle

bottom buckles would be effected. The buckle with the largest amplitude (by chance) is an inward buckle, and this is the buckle that is flattened or preserved in the two situations.

From the results plotted in the above figure, it is shown that the elimination of one buckle has no effect in the buckling capacity. The elimination of all but one buckle increases the capacity. Since buckling does occur at the location of the largest buckle, this increase is only slight.

6.5.2 Method 2

6.5.3 Variation 1

Same as the cylinder analyses, pair-wise combinations of modal shapes are imposed as imperfections. Again, only the odd modes are selected for this study, and combinations of 1+3, 3+5, 5+7, 7+9, and 9+11 are used. By combining the modal shapes, the load displacement curves reduce in scatter as well. C_{m} are brought by in-line with the results from the Gaussian noise method. The combination 5+7 seems to have the largest impact on the reduction factor.

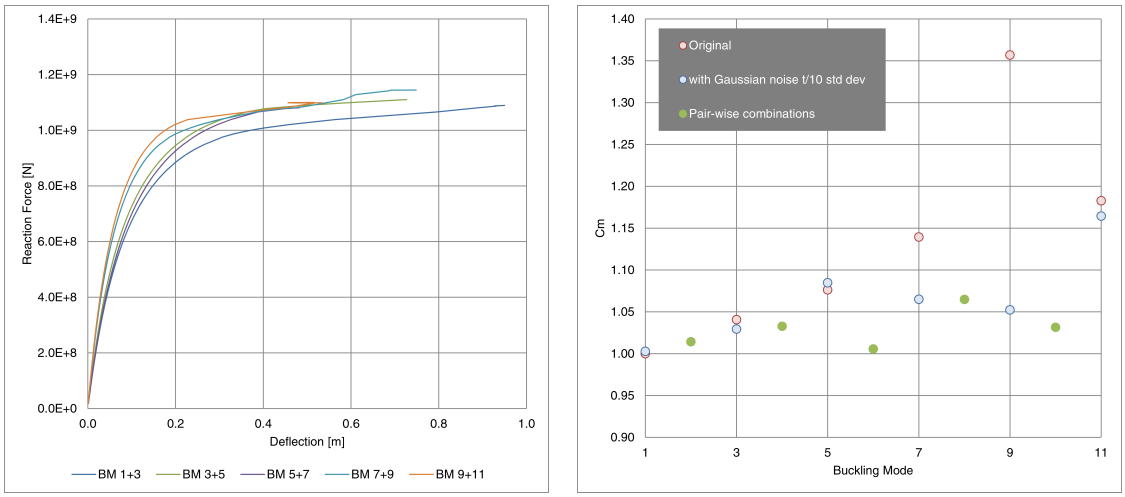

(a) Load displacement curve

(b) C_{m}s

Figure 6.13: Behaviour resulting from imperfection in shapes of combinations of buckling modes

6.5.4 Variation 2

Since combination 5+7 appears to be the most critical, more analyses are run with the contribution of its constituents weighed randomly. Figure 6.14 shows the results from 5 trials, each with different weights assigned.

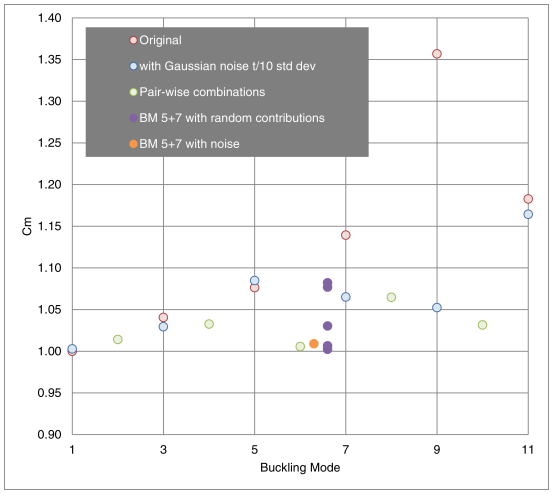

Figure 6.14: C_{m}

BM 5	BM 7	C_{m}
0.922	0.078	1.082
0.765	0.235	1.077
0.566	0.434	1.030
0.306	0.694	1.007
0.488	0.512	1.002

Table 6.3: Contributing modes, and associated weights

The above results would suggest that equal contribution actually produces the worst imperfection shape. Since the reduction factor is still greater than 1, no further analyses are done.

6.5.5 Method 3

Results from the random imperfection trials suggest that neither the maximum imperfection amplitude, nor the total imperfection amplitude govern the buckling capacity of the hyperboloid. In fact, comparing to the modal shapes with the same maximum and total amplitude, the capacity resulting from random imperfection is higher by an average of 30 % (Fig. 6.15b). As

in the case of the cylinder, the parameter remaining is the shape of the imperfection. The load displacement curves (Fig. 6.15a) of all the random trials differ only in their stiffnesses, and not in the final strengths.

By plotting the reduction factor resulting from modal imperfections against total imperfection amplitude however, there seem to be a minimum at amplitude near 300 m. Whether this is an coincidence should be further investigated.

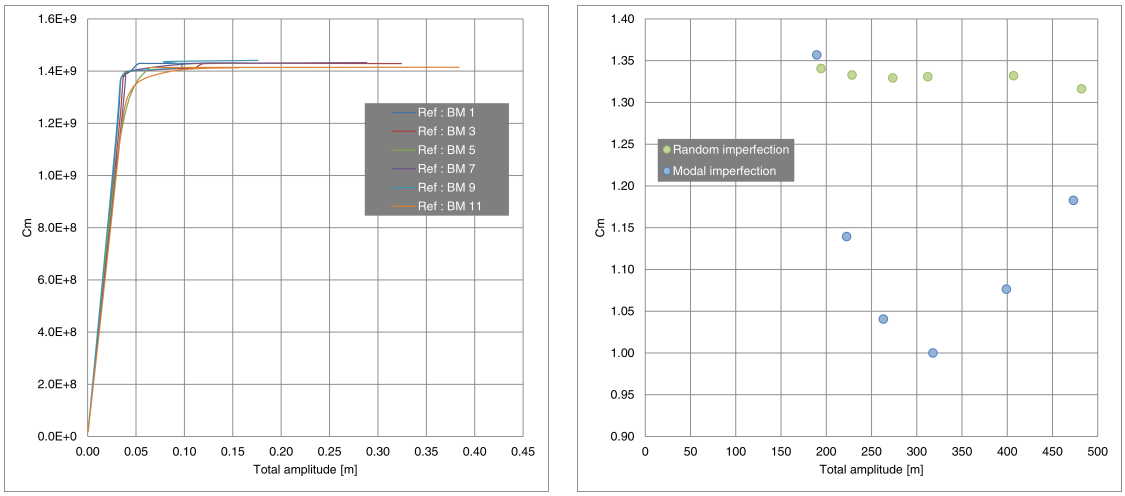

(a) Load displacement curves

(b) C_{m}s

Figure 6.15: Behaviours and results of random imperfection, compared with modal imperfection

6.5.6 Method 4

A similar set of analyses are done with the hyperboloid as the base geometry. Wave shaped imperfections are imposed onto the geometry prior to GNLA. The wave numbers range from 0 to 40 in both m and n directions. The result can be seen in figure 6.16. From the figure, it is clear that imperfection in these shapes have very limited influence on the buckling capacity. The largest reductions occur around $m = 4, 5, 10$ and $n = 3, 4$, these wave numbers correspond roughly to the first modal shape.

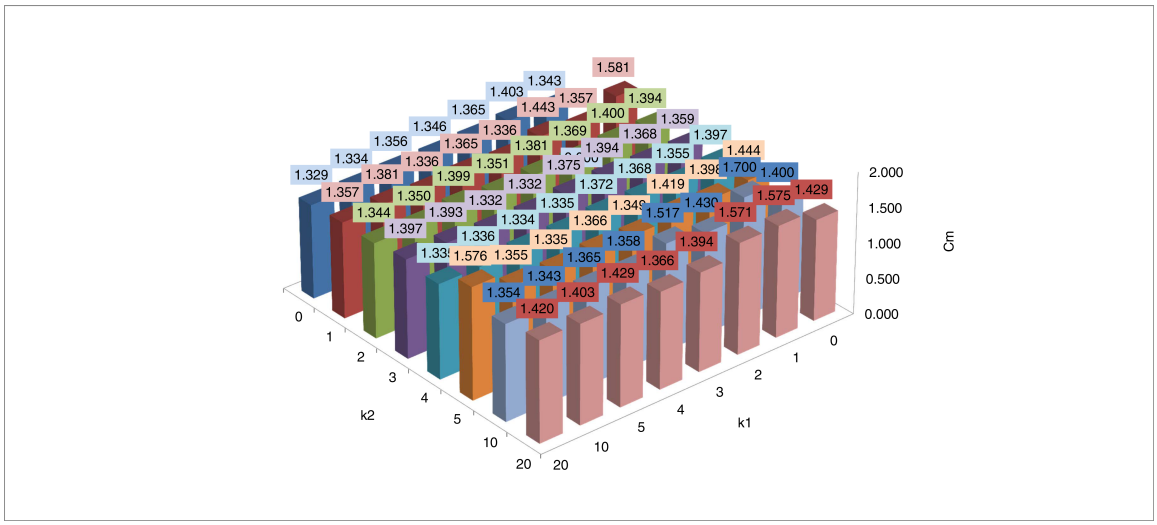

Figure 6.16: C_{m} resulting from wave imperfection of varing m and n

C_{m}		m							
		0	1	2	3	4	5	10	20
n	0	N/A	1.343	1.403	1.365	1.346	1.356	1.334	1.329
	1	1.581	1.357	1.443	1.336	1.365	1.336	1.381	1.357
	2	1.394	1.400	1.369	1.381	1.351	1.399	1.350	1.344
	3	1.359	1.368	1.394	1.375	1.332	1.332	1.393	1.397
	4	1.397	1.355	1.368	1.372	1.335	1.334	1.336	1.335
	5	1.444	1.398	1.419	1.349	1.366	1.335	1.355	1.576
	10	1.400	1.700	1.430	1.517	1.358	1.365	1.343	1.354
	20	1.429	1.575	1.571	1.394	1.366	1.429	1.403	1.420

Table 6.4: Modified knock-down factor resulting from wave imperfection

6.6 Other types of Imperfections

6.6.1 Stress Imperfection

Geometrical imperfection has been the main focus of this thesis. However, as pointed out by Calladine [17], it is impossible for a fabrication to remain stress free when deformed in a double-periodic pattern (since this necessitates a change in Gaussian curvature).

Calladine stated that it is unreasonable to assume a stress free surface when change in Gaussian curvature (by the existence of imperfection) clearly induces stress. Therefore, stress must be present in an imperfect surface, and need to be accounted for. To test the effect of this residual stress, the imperfection is imposed not as a change in nodal coordinates, but as a nodal displacement. As with previous analyses, the first buckling mode is used as the imperfection shape, and the maximum amplitude is set at half the thickness.

The scaled displacement is imposed as a displacement boundary condition on each node to induce an initial stress state directly in GNLA. This displacement load is applied only to the first load step, and removed there after. It is found that as soon as the displacement is removed, the structure "bounces" back to the perfect state, and proceed as if unperturbed. The resulting capacity is identical to the one from GNLA without imperfection. Therefore a second solution is proposed where the initial stress / strain state is obtained from the above displacement boundary conditions using LEA. The resulting stress / strain state is then imposed onto the model prior to the eventual GNLA as an initial condition.

ANSYS does not currently support the imposition of initial stress and strain values on nodes of shell elements using the global coordinate system, therefore the imposition is acted on the elements using each element's local coordinate system. The intent of this section to obtain the geometrical imperfection "equivalent" stress / strain state. Therefore, three different attempts are made, one is to impose only the initial stresses, two, only the initial strains, and three, imposing both stress and strain.

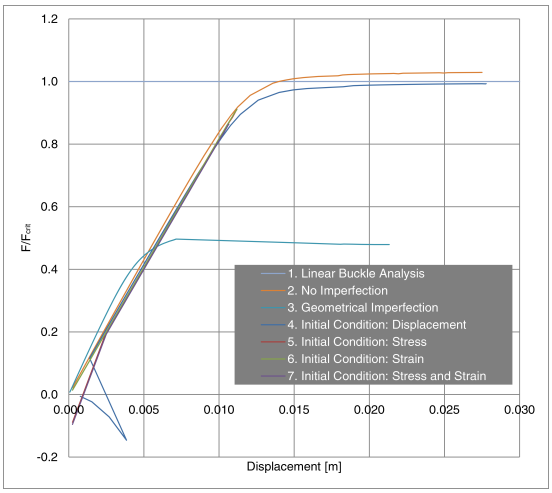

Figure 6.17: Force displacement curves of the different trials with LC3 - geometrical imperfection as reference

	Capacity [N]	C
1	73.34×10^6	1.000
2	75.47×10^6	1.029
3	29.22×10^6	0.398
4	72.83×10^6	0.993
5	77.98×10^6	1.063
6	66.82×10^6	0.911
7	63.34×10^6	0.864

Table 6.5: Knock-down factor resulting from other types of imperfection

From the analyses, it is apparent that initial conditions, be it stress, strain, or displacement, has negligible influence on the final capacity of a thin cylinder in comparison with geometrical imperfection. The initial irregularity in Figure 6.17 at the beginning of the curves is due to there being more upward stress (or displacement) than downward, resulting in a negative reaction force. Beyond the initial portion of the analyses, these initial conditions all resulted in similar

capacity as from the LBA or from the model with no imperfection at all. Furthermore, the force displacement curves from these different initial conditions remain remarkably similar. This proves that the geometrical perturbation has significance beyond the introduction of an initial stress / strain state to the surface. The deformation diagrams are included in Appendix F. This result concurs with Calladine's experimental study on the effect of initial stress imperfection on axially loaded cylindrical shell [32] [49], where the result exhibited less reduction in capacity (ie. buckling occurred at the higher end of the scatter shown in Chapter 4), and without the characteristic scatter exhibited by geometrically imperfect cylinders.

6.6.2 Boundary Layer Imperfection

For a structurally indeterminant structure, change in boundary (such as settlement) induces significant stress. Thus far in this section, the load has always been applied perfectly uniformly to the top ring of the cylinder. However, it is unreasonable to assume that the experimental set-up includes a perfectly flat loading plate, and that the specimen has perfectly flat top and bottom rings. To fully investigate the issue of loading imperfection, an imperfect loading plate should also be included in the FEM model, such that there exists a layer of contact elements in between the plate and the cylinder. To simplify this procedure for the purpose of this study however, it is assumed that the applied displacement varies sinusoidally along the top ring of the cylinder. This loading condition is adapted from DIANA's example manual.[1]

To understand the magnitude of this imperfection, it is helpful to visualize the load as a combination of axial displacement and rotation. The axial displacement is set at $u_z = 0.025$ or $l/400$, and maximum rotation is set to $\phi_z = \pi/3600$, this value ensures the magnitude of the eccentricity does not dominate the behaviour. The total displacement can then be calculated as follows,

$$u_z^{tot}(\theta, 0 \leq LS \leq 1) = u_z + u_z^{\mathrm{e}} \cdot sin(a\theta); a \geq 1 \tag{6.17}$$

Where a determines the number of waves in the tangential direction. The eccentric component can be calculated as follows,

$$u_z^{\mathrm{e}} = R \cdot tan(\phi_z) = R \cdot tan(\frac{\pi}{3600}) = 0.004\,36\,\mathrm{m} \tag{6.18}$$

This loading imperfection is only implemented in the first load step as it is assumed that local imperfections are flattened out after initial contact due to localized plasticity. For all further load steps, the regular loading is specified.

$$u_z^{tot}(\theta, LS > 1) = u_z \tag{6.19}$$

Four different values of a ranging from $1, 5, 10$ to 20 are chosen to assess the effect of initial loading imperfection (Figure 6.19a shows the scheme of the implementation).

From the LBA results (Fig. 6.18), it is observed that the buckling shapes differ greatly. The first mode exhibits complete asymmetric behaviour as there is one dominate applied moment. The modes with higher wave numbers become symmetrical, though the buckles are localized at the point under the troughs of the sinusoidal load. This agrees with Maiboroda's assertion that "an uneven loading leads to localization of the buckling form near the weakest point, the buckling form decreases as one moves away from this point" [34]. The eigenvalues resulting from LBA is plotted against a in figure 6.19b.

[1] DIANA manual - https://support.tnodiana.com/manuals/d95/Diana.html

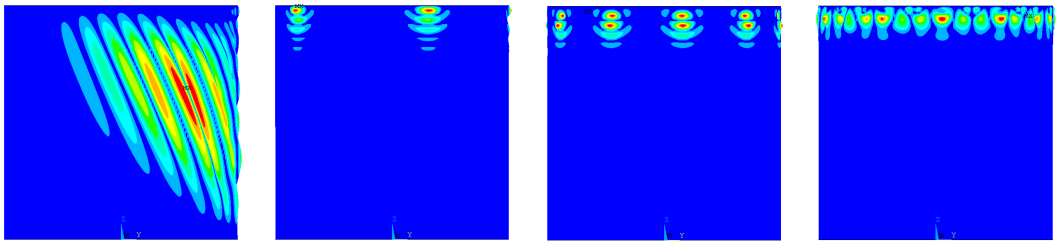

(a) $a = 1$ (b) $a = 5$ (c) $a = 10$ (d) $a = 25$

Figure 6.18: Buckling modes with varying a

From the "knock-down factor - no imperfection" curve of Figure 6.19b, we can conclude that GNLA with no geometric imperfection (only load imperfection) shows no imperfection sensitivity. In fact, the resulting capacity is consistently greater than that of the LBA results. From displacement diagrams it is observed that as the loading increases, the initial loading imperfection becomes insignificant as the displacements "smooth" out. The structure always reverts back to the uniform downward deflection state when the imperfection is removed ($LS \geq 1$). This may be due to the fact that aside from the assumed local plasticity near the troughs of the sinusoidal load pattern, the global behaviour remains elastic prior to onset of buckling.

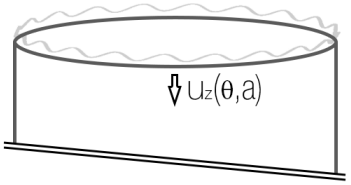

(a) Scheme of imperfect load application

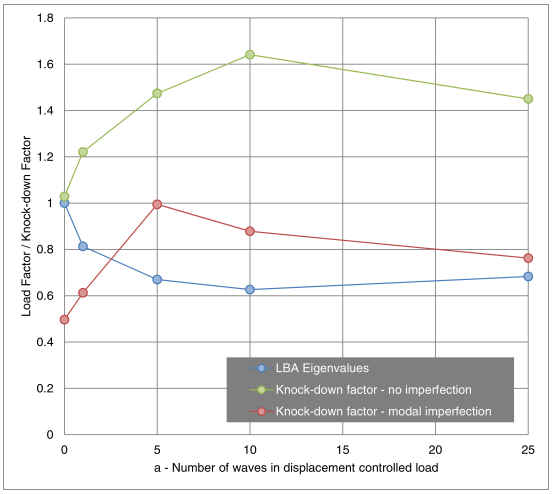

(b) Resulting knock-down factor

Figure 6.19: Results of variable displacement control

If geometrical imperfections (in the buckling shapes shown in Figure 6.18) are imposed in addition to the loading imperfection however, the behaviour becomes drastically different and significant imperfection sensitivity is observed. The resulting capacity is similar to Method one at the beginning of this chapter. It is observed from the deformation diagrams that the deformation caused by the initial load imperfection is still being absorbed, and it is the geometrical imperfection that causes the eventual buckling. The deformation diagrams are included in Appendix F. This shows that as with the previous section, geometrical imperfection has a far larger impact on the buckling capacity of a thin-shell than other types of imperfections.

6.7 Conclusion

This chapter discusses the methods of imperfection generation and categorization. In the absence of characteristic imperfection measurement, a credible random imperfection field can be

generated with the knowledge of tolerance alone. 4 different types of imperfection shapes are discussed, namely modal shaped, combination of modes, Gaussian random, and sinusoidal waves.

A modified knock-down factor is proposed to replace the traditional knock-down factor, and to take advantage of the modern computational capability. C_{m} is defined as the quotient of the shell true ultimate load and the shell ultimate load that follows from a geometrical nonlinear analysis including the first buckling mode imperfection. Should C_{m} be larger than one, then the designer may stop the imperfection analysis after imposing the first buckling mode as the imperfection. The true ultimate load can be computed by a full non-linear analyses including random imperfections. In this project this factor has been determined as 0.8 for axially loaded cylinders and 1 for concrete cooling towers. It is recommended that this factor is determined for many types of thin shell structure.

An exhaustive list of imperfection shapes derived from the 4 types are imposed onto both the cylinder and the cooling tower. It was observed that for a structure with closely spaced eigenvalues, imperfection sensitivity is severe in general. A large knock-down factor can be expected. Furthermore, for such a structure, imperfection in the shape of the first mode may not govern the capacity. Cylinder is an extreme example of such a structure, where imperfection in the shape of higher modes, combinations of mode, or sinusoidal waves may govern.

In particular, attention is applied to the third buckling mode. This mode shows an axisymmetric shape with no buckles in the tangential direction. If it is used as the imperfection shape, a deceptively low knock-down factor is observed. However, should the shape be perturbed by a Gaussian noise, or be combined with an asymmetric shape, the knock-down factor increases significantly to point of governing the behaviour. Therefore, one recommendation is to always impose additional noise should axisymmetric mode emerge. In general, for an axially loaded cylinder a modified knock-down factor of $C_{\mathrm{m}} = 0.8$ should be used.

For a moderately sensitive structure such as the hyperbolic cooling tower, all the above imperfection shapes are similarly applied. However, after many attempts, the first mode still governs the buckling behaviour of the structure.

Lastly, other types of imperfections are applied to the cylinder. The axial load is imposed as a sinusoidal (as opposed to uniform) displacement for the first load step. The number of periods in the sine wave is varied. This resulted in completely different buckling modes as buckles appear localized right underneath the troughs of the wave. However, if load shape constitutes the sole imperfection, the perturbation is absorbed by the structure before buckling occur. The behaviour remains as if there is no imperfection at all. The second attempt involves imposing the imperfection not geometrically, but rather as a stress, a strain or a displacement. Again, no visible change in capacity is observed in all of the cases.

Overall, it is possible to impose randomly shaped imperfections but this requires much effort of the analyst and this is not feasible for engineering design. It is recommended that finite element software is extended so that random imperfections to shell structures can be inserted effortlessly.

Chapter 7

Influence of Surface Curvatures

7.1 Introduction

Weingarten and Seide [45] stated in a 1969 NASA monograph that the buckling strength of a doubly curved shell is influenced by its curvature along with other parameters. Aside from the popular cylindrical shells, doubly curved surfaces are also frequently used in both civil and space applications. Both spheres and hyperboloids have doubly curved surfaces, and almost all free formed surfaces are doubly curved. This chapter focuses on identifying the possible correlations between the curvature of a thin shell surface and its buckling capacity and imperfection sensitivity. The first section introduces different initial curvatures in the vertical direction to the cylindrical model from Chapter 4. By running the same series of analyses, the author proposes relationships between the ratio of curvatures k_{zz}/k_{xx} of a geometry and its buckling shape and capacity. The second section compares the change in Gaussian curvature of a surface as load increases. From the change in Gaussian curvature, an attempt is made to predict the onset of buckling.

7.2 Initial curvatures

To expand on the observation that cylinders are much more susceptible to imperfection than hyperboloids, the cylinder geometry is modified to incorporate curvature in its vertical direction. 37 different models are constructed, each with a different curvature in the z-direction. The equatorial (throat) radius is kept constant at 5 meters while the top and bottom radii vary from 2.32 m to 7.68 m. This is done as oppose to varying the equatorial radius because Zerna stated that such were the experimental set-ups [48].

Similarly to the cooling tower geometry, the radii at each elevation (z-direction) is calculated as follows, though instead of realistic hyperbolic constants, they are set up to simply the geometry.

$$R_{mid} = 5; a \in [-20, 20]; b = 10 \tag{7.1}$$

First the coordinates of the surface of revolution is calculated following a similar hyperboloid formulation,

$$x = a\left(1 - \sqrt{1 - \left(\frac{z - \frac{L}{2}}{b}\right)^2}\right) + R_{\text{mid}} \tag{7.2}$$

The vertical curvature k_{zz} varies along the length of the geometry. To calculate the curvature at any point on a surface, one must find the radius of the tangential circle R that intersect the

point. Using the finite element mesh, three adjacent points on a local axis of a element can be used to find one of the principle curvature $k_{zz} = {}^1/_{R_z}$ along that particular element.

Using point A in figure 5.1 as an example. R_z is calculated by solving a system of three equations with $O(x)$, $O(z)$, and R_z as the unknowns. $O(x)$, $O(z)$ are the distances from the origin of the coordinate system to the origin of the particular circle that intersects the three points, and R_z is the radius of that circle.

$$(x_1 - O(x))^2 + (z_1 - O(z))^2 = R_z^2 \tag{7.3a}$$
$$(x_2 - O(x))^2 + (z_2 - O(z))^2 = R_z^2 \tag{7.3b}$$
$$(x_3 - O(x))^2 + (z_3 - O(z))^2 = R_z^2 \tag{7.3c}$$

Instead of solving the above non-linear equations directly, the following simplification involving trigonometry is used. Referring to Figure 7.1, $m(A)$ and $m(B)$ are slopes of lines A and B respectively. Using these slopes, centre of the circle that intersects these three points are calculated as $O(x)$ and $O(z)$. The radius R_z follows from the Pythagoras theorem. Finally, reciprocate R_z and obtain k_{zz}.

$$m(A) = \frac{z_2 - z_1}{x_2 - x_1} \; ; \; m(B) = \frac{z_3 - z_2}{x_3 - x_2} \tag{7.4a}$$
$$O(x) = \frac{m(A)m(B)(z_3 - z_1) + m(A)(x_2 + x_3) - m(B)(x_1 + x_2)}{2(m(A) - m(B))} \tag{7.4b}$$
$$O(z) = -\frac{1}{m(A)}\left(O(x) - \frac{x_1 + x_2}{2}\right) + \frac{z_1 + z_2}{2} \tag{7.4c}$$
$$R_z = \sqrt{(O(x) - x_2)^2 + (O(z) - z_2)^2} \tag{7.4d}$$
$$k_{zz} = \frac{1}{R_z} \tag{7.4e}$$

The tangential curvature k_{xx} and R_x can be calculated in a similar fashion using three points along the surface tangent, through that is unnecessary as the origin is known to be on the z-axis, and the equatorial radius is set at $R_x = 5$.

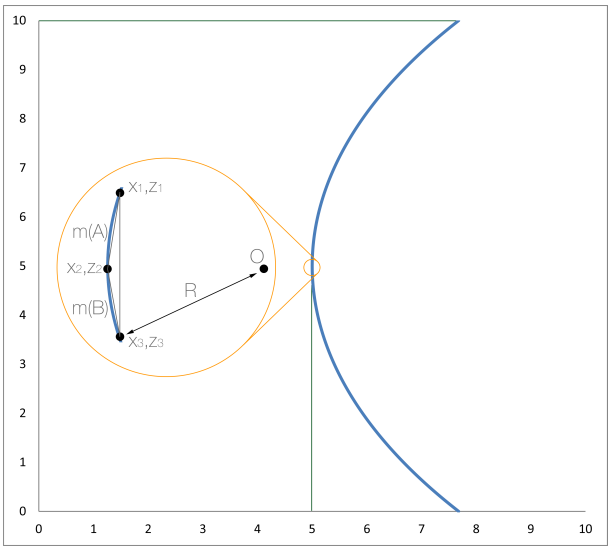

Figure 7.1: Surface and curvature calculation variables

The curvature ratio, ${}^{k_{zz}}/_{k_{xx}}$, is calculated at the mid point of the structure. From the change in a, corresponding change occurs in k_{zz}.

$$a \in [-20, 20]; k_{zz} \in [+1, -1] \tag{7.5}$$

Increments of $\Delta^{k_{zz}}/_{k_{xx}} = 0.05$ is used over the above range except nearing 0 where increasingly smaller changes in curvature are used. The list of curvature ratios used are listed in table 7.1.

Trial	$^{k_{zz}}/_{k_{xx}}$	R_F N	Load Factor	F_{crit} N	F_{ult} N	C
1	1.00	3729661	9.252	34506000	20893000	0.605
2	0.75	5401823	8.457	45684000	26910000	0.589
3	0.50	7865679	7.465	58720000	31370000	0.534
4	0.45	8480845	7.225	61277000	31325000	0.511
5	0.40	9139767	6.971	63715000	31549000	0.495
6	0.35	9841189	6.705	65982000	31838000	0.483
7	0.30	10581566	6.428	68023000	31426000	0.462
8	0.25	11354324	6.146	69784000	30478000	0.437
9	0.20	12149094	5.862	71217000	30337000	0.426
10	0.15	12951065	5.581	72279000	29509000	0.408
11	0.10	13740617	5.308	72938000	27384000	0.375
12	0.05	14493514	5.053	73237000	23902000	0.326
13	0.025	14847596	4.937	73300000	22418000	0.306
14	0.005	15116772	4.850	73319000	21177000	0.289
15	0.0025	15149432	4.838	73291000	35075000	0.479
16	0.0005	15175392	4.819	73132000	36707000	0.502
17	0.00025	15178627	4.817	73108000	36772000	0.503
18	0.00005	15181213	4.814	73087000	36459000	0.499
19	0	15181859	4.814	73081000	36419000	0.498
20	-0.00005	15182505	4.813	73075000	35225000	0.482
21	-0.00025	15185089	4.810	73045000	34277000	0.469
22	-0.0005	15188316	4.807	73006000	33014000	0.452
23	-0.0025	15214051	4.768	72544000	27870000	0.384
24	-0.005	15246003	4.698	71629000	26242000	0.366
25	-0.025	15492555	3.637	56346000	33153000	0.588
26	-0.05	15775993	2.597	40977000	25200000	0.615
27	-0.10	16247255	1.833	29784000	22024000	0.739
28	-0.15	16571272	1.399	23188000	19650000	0.847
29	-0.20	16731157	1.197	20026000	18871000	0.942
30	-0.25	16719867	1.068	17850000	18028000	1.010
31	-0.30	16541129	0.982	16246000	19080000	1.174
32	-0.35	16208688	0.923	14958000	16284000	1.089
33	-0.40	15744123	0.886	13956000	13435000	0.963
34	-0.45	15173832	0.873	13246000	12566000	0.949
35	-0.50	14525880	0.860	12491000	12132000	0.971
36	-0.75	10948374	0.925	10124000	9829000	0.971
37	-1.00	7957466	1.088	8655000	8077000	0.933

Table 7.1: Summary of results

7.2.1 Linear Elastic and buckling analysis

The mesh density in this study is set to be double of the cylinder model in Chapter 4. This is done so that the Gaussian curvature (in the second part of this chapter) can be calculated with a higher resolution. The trade off is much longer calculation time (averaging 4 hours compared to 30 minutes), and much larger hard drive requirement (depending on the number of bisections, each analysis may take up to 20 GB of space).

Following the same procedure laid out in chapter 4, load is applied via displacement controlled steps to the top ring of the cylinder. To ensure sufficiently refined load steps, the step-wise downward displacement is set at $u_z = 0.025\,\mathrm{m}$. The top ring is similarly laterally restrained to prevent in-extensional deformation, and the bottom ring is pinned.

LEA is performed on each of the models to obtain the equivalent reaction forces. This is multiplied to the eigenvalues produced by the buckling analysis to calculate the critical load. Since the eigenvalues from LBA are calculated based on a displacement-controlled load, it must be shown that it can be applied to the reaction force. This was done in Chapter 4. The first buckling mode of the different geometries are recorded in figure 7.2.

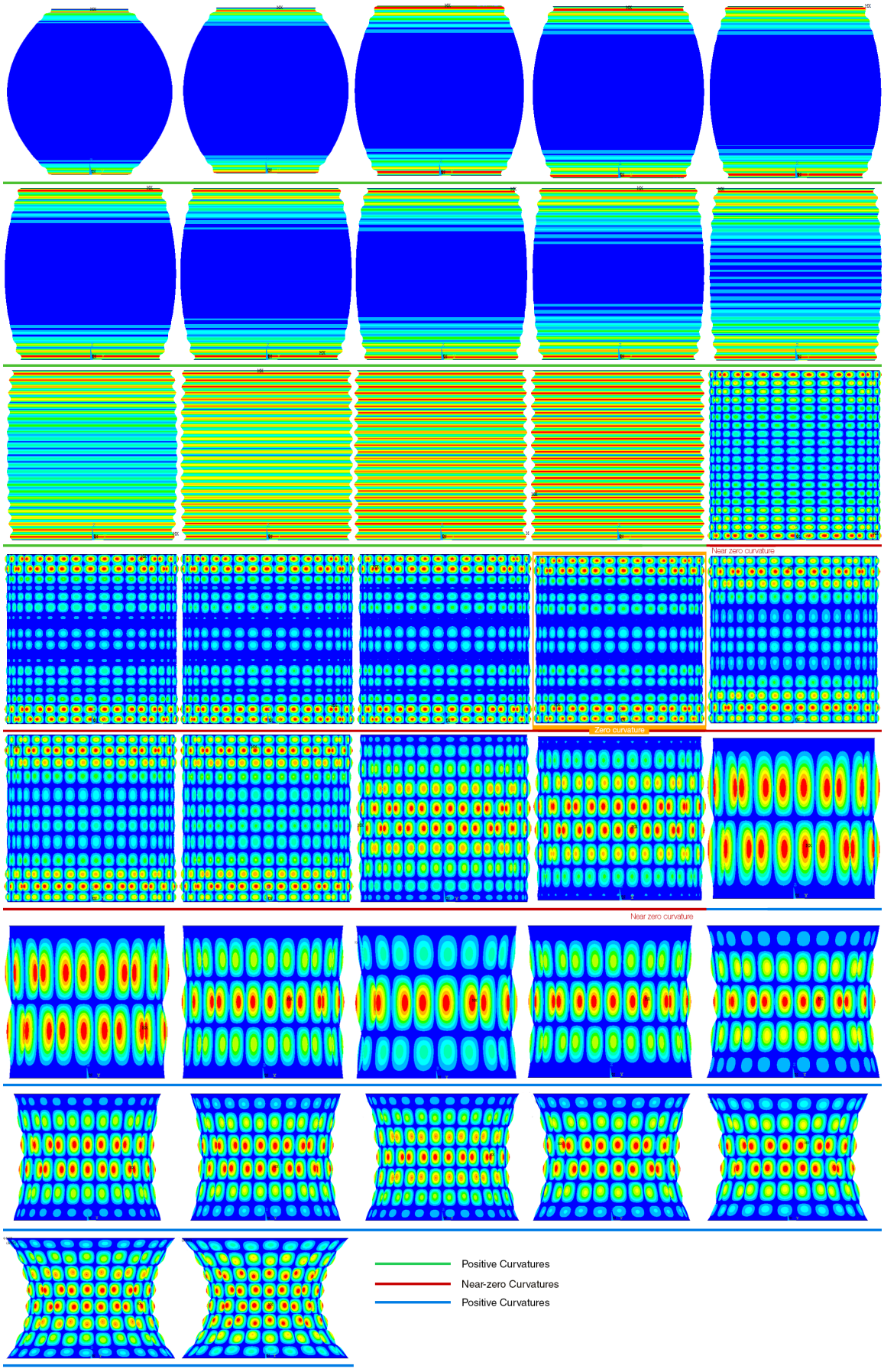

Figure 7.2: First buckling mode of the different geometries (Left then down from 1 to 37)

From the figure above, it is observed that when the geometry is in the positive curvature group, axisymmetric buckling mode is always the dominant mode (buckles only in the vertical direction and none in the tangential). This is in-line Tovstik's assertion that for shells of positive curvature, the deformation occur in lines [43]. As the curvature increases, the ring shaped buckles occur more towards the edge, and become more localized. As the curvature ratio approaches zero ($0 \leq {}^{k_{zz}}/_{k_{xx}} \leq 0.0025$) the axisymmetric modes disappear.

When the curvature ratio is sufficiently negative (${}^{K_{xx}}/_{K_{zz}} \leq -0.005$), buckling modes similar to the ones produced by the hyperbolic cooling tower emerges. A chessboard pattern that spread along the entire neutral surface appear as the deformation shape due to the fact that negative Gaussian curved surfaces have two systems of asymptotic lines. The notion of "sufficiently negative" was also referenced by Tovstik who stated the chessboard pattern emerges assuming that the Gaussian curvature is not small.

In the near-zero group, the behaviour cannot be clearly categorized. The shape of buckles is what Tovstik predicted, deformation pits stretch along the generatrices (vertical lines) of the cylinder [43]. However, it would appear as though LBA cannot distinguish made between the different near-cylindrical geometries: the resulting buckling shapes are similar if not identical, especially on the slightly positive curvature side ($0.0025 > {}^{K_{xx}}/_{K_{zz}} \geq 0$).

More troubling fact is that when compared with the coarse mesh model in Chapter 6, it is observed that with the refined mesh, the axisymmetric (governing) buckling shape does not occur within the first 20 modes. It is possible that the mesh is still not refined sufficiently for the small difference in curvature to change the buckling behaviour, ie. all geometries in the near-zero group are considered cylindrical by the software. Mesh density is of importance with the near-zero models as the buckles are small and numerous, there must be sufficient amount of elements per buckle to represent them accurately. This is not an important issue for hyperboloidal shapes as the buckles are larger, and the influence of mesh density is reduced.

Based on these observations, the analyses are grouped in three categories, negative (${}^{k_{zz}}/_{k_{xx}} \geq 0.005$), near-zero ($-0.005 \leq {}^{k_{zz}}/_{k_{xx}} \leq 0.0025$), and positive (${}^{k_{zz}}/_{k_{xx}} \leq -0.0025$). Based on this grouping, Figure 7.3a shows a plot of reaction forces and buckling load factors, both normalized to the cylinder geometry. Critical forces are calculated as follows,

$$F_{\text{crit}} = \lambda_{\text{crit}} F_{\text{z}} \tag{7.6}$$

The behaviour on the positive curvature side is expected. As the contact surface decreases (top and bottom ring diameters shrink), the stiffness lowers and less force is experienced due to the displacement, and therefore the load factor increases and reaction force decreases. On the negative curvature side, the reaction force increases until ${}^{k_{zz}}/_{k_{xx}} = -0.2$ where it reaches a maximum. On further increase of the curvature, the structure becomes less stiff and the reaction forces decrease. Both the buckling load factors and the critical buckling force decays exponentially on the negative curvature side as the curvature increases.

When zoomed into the range around near-zero curvature, it is observed that the transition is smooth for all three variables, implying that the transition from positive to negative curvature does not have an influence on the structural stiffness.

7.2.2 Imperfection

Imperfection in the shape of the first buckling mode (7.2) is imposed onto the structure. The maximum amplitude is scaled to half of the thickness. Should the modal shape be axisymmetric (ie. all models in the positive curvature group, similar to model 14), addition Gaussian noise is imposed. This is done to extract a realistic knock-down factor as suggested in Chapter 6. Only

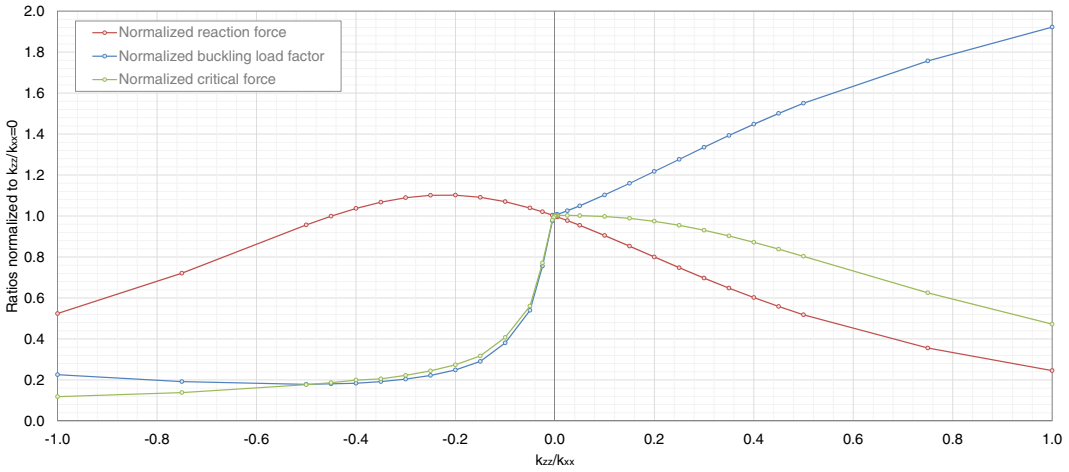

(a) $-1.0 \leq {}^{k_{zz}}/_{k_{xx}} \leq 1.0$

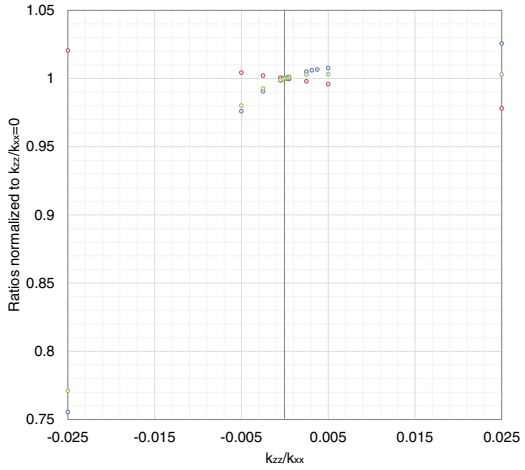

(b) $-0.005 \leq {}^{k_{zz}}/_{k_{xx}} \leq 0.005$

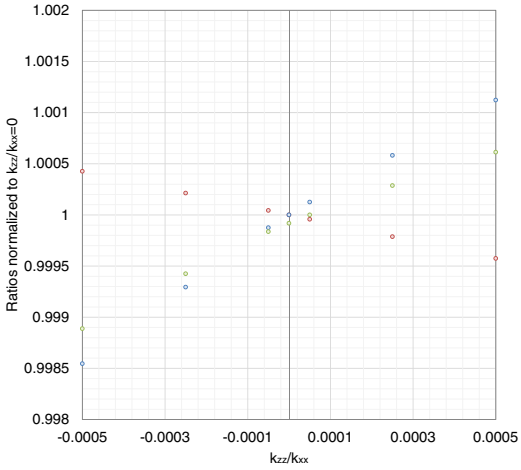

(c) $-0.0005 \leq {}^{k_{zz}}/_{k_{xx}} \leq 0.0005$

Figure 7.3: Eigenvalues, reaction force, and critical buckling force, normalized to the values of the cylinder

the first mode is used in the trials due to time constraint, but as shown in Chapter 6, the first mode may not govern the behaviour. The imperfection imposition is done on a node by node basis, no ill-conditioned elements resulted.

7.2.3 Non-Linear Analysis

GNLA are performed on each of the 37 perturbed FEA models, and the results are collected and grouped in the same three categories as above. The resulting capacity is converted to a knock-down factor. These are shown with different scales in figure 7.4. Figure 7.4a plots F_{ult} from GNLA and F_{crit} from LBA against the curvature ratio. It is evident that the three groups of curvatures behave differently. With the positive curvature geometry, both F_{ult} and F_{crit} follow a predictable pattern. As the stiffness decreases (F_{crit} decreases), the imperfection sensitivity decreases as well (the gap between F_{ult} and F_{crit} decreases). This group is also where the largest knock-down factor occurs; a factor of $\sim {}^{1}/_{3.5}$ results from the model with a curvature ratio of 0.005 (model number 14, the first model where axisymmetric buckling mode emerges). This differs from the notion that cylinder is most imperfection sensitive. However, this result is

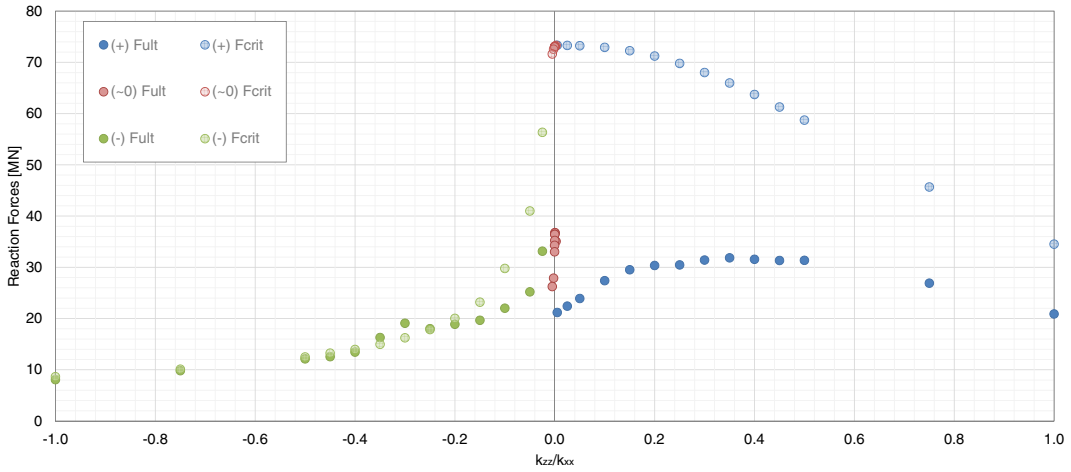

(a) $-1.0 \leq {}^{k_{zz}}/_{k_{xx}} \leq 1.0$

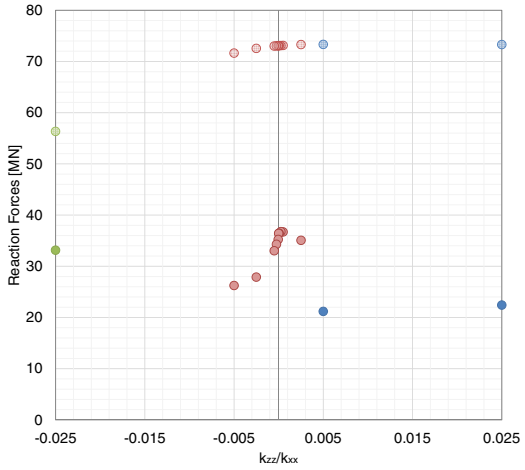

(b) $-0.025 \leq {}^{k_{zz}}/_{k_{xx}} \leq 0.025$

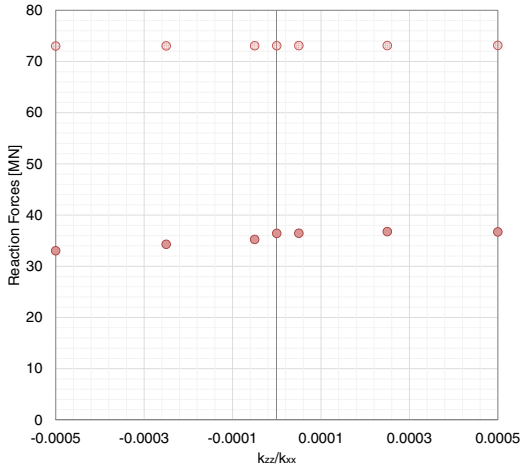

(c) $-0.0005 \leq {}^{k_{zz}}/_{k_{xx}} \leq 0.0005$

Figure 7.4: F_{crit} from LBA and F_{ult} from GNLA

remarkably similar to the analysis done on the cylinder with the third mode as the imperfection in Chapter 6. Similarity exist both in the imperfection shape (axisymmetrical buckles) and in the knock-down factor ($\sim {}^{1}/_{3.4}$).

This is an important observation in several ways. In chapter 6 (the study on a variety of imperfection shapes), the cylinder was constructed with a coarser mesh. It is assumed that a coarser mesh is less accurate than the finer mesh used in this chapter. With the finer mesh in this chapter, the axisymmetric mode does not appear(within the first 20 modes) until there is sufficient positive curvature, ${}^{k_{zz}}/_{k_{xx}} \geq 0.005$. The fact that the axisymmetric mode emerged as a buckling mode at all in the coarse model means that the software was not able to distinguish between curvatures that are less than 0.005. Conversely, assuming that the finer mesh is more accurate, it would be correct to state that coarse meshing adds an additional imperfection term to the FEM model that must be accounted for. However, from chapter 6, two conclusions were drawn,

1. The axisymmetric mode is not the first, but the third mode
2. The axisymmetric imperfection shape resulted in the largest knock-down factor

These conclusions show that the axisymmetric imperfection is desirable, but does not exist in a perfect cylinder if a finer mesh is used. To produce such a shape, either the mesh density must be adjusted (made less refined), or the curvature must be changed. Furthermore, it can be said that mesh density has a large influence on buckling modes, but it is not immediately obvious that a finer mesh is better. As the eigenvalues are very close together, and they are not so accurately represented with a coarse mesh, introducing reducing mesh density may actually be beneficial in obtaining a real capacity. The axisymmetric mode is studied in detail in the next sections.

Shifting the attention to the negative curvature part of the plot. Both F_{ult} and F_{crit} decays exponentially, with F_{crit} decaying at a faster rate. For curvatures ≤ -0.2, the models are practically imperfection insensitive as is the case for the hyperboloid cooling towere analysed in chapter 5.

The near-zero portion of the plot is the most intriguing and complex. From figure 7.4b, there is a clear discontinuity in ultimate buckling capacity F_{ult}, but not in the linear buckling F_{crit}. From figure 7.4c, there appears to be a local maximum between $k_{zz}/k_{xx} = 0$ and 0.0005. In immediate vicinity outside of that range, the capacity decreases. This contradict the notion that a perfect cylinder should result in minimal capacity.

This may be explained by realizing that the difference in curvature between these models are practically invisible to the naked eyes, they may well result from manufacturing imperfections. It is encouraging to see that none of the models in this range produce a worse knock-down factor than $k_{zz}/k_{xx} = +0.005$ (model 14 with the first axisymmetric imperfection). This suggest that a designer may be able to use either a slightly off-perfect cylindrical model or with a coarser mesh to design a cylindrical structure.

Figure 7.5 shows the calculated knock-down factor of the various geometries using the following knock-down factor equation.

$$C = \frac{F_{\text{ult}}}{F_{\text{crit}}} \tag{7.7}$$

The discontinuity at near-zero curvature is clearly visible here as well, where C decreased by approximately 50 % from 0.6 to 0.3, therefore the knock-down factor in the near-zero range is difficult to predict. Fortunately, the behaviour of positive curvature geometry can be described as a monotonically increasing function. Using a polynomial fit with bi-square fit, the following relationship is obtained with coefficient of determination value of 0.99,

$$C = -0.342(\frac{k_{zz}}{k_{xx}})^2 + 0.644\frac{k_{zz}}{k_{xx}} + 0.3 \tag{7.8}$$

k_{xx} is known in our case as the throat radius remains constant. By substituting it with $1/R = 0.2$ we obtain,

$$C = -8.54k_{zz}^2 + 3.22k_{zz} + 0.3 \tag{7.9}$$

Since the largest knock-down factor occurs at $k_{zz}/k_{xx} = 0.005$, it is conservative to assume that this equation is valid from $0 \leq k_{zz}/k_{xx} \leq 1$. In the instance of a perfect cylinder, $k_{zz} = 0$ and $C = 0.3$, which is lower and therefore more significant than any results in the near-zero group. Beyond curvature ratio of one, the geometry transforms into a point-loaded sphere and the behaviour may differ significantly.

Considering the results of the imperfection study in Chapter 6, where imperfection in the shape of the axisymmetric mode governed the capacity, and the observation from this chapter that the axisymmetric mode starts to emerge as the first mode at $k_{zz}/k_{xx} > 0.025$, it can be assumed that for curvatures greater than 0.025, the first mode governs the knock-down factor.

The negative side is more complex due to the loss of stiffness as the curvature becomes more negative. It is reassuring however that C is higher in general, and the geometry becomes

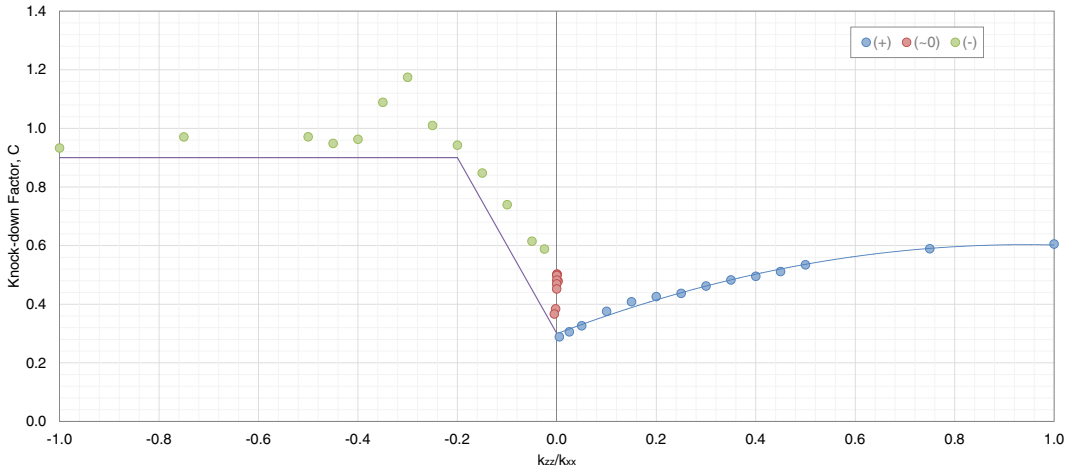

(a) $-1.0 \leq {}^{k_{zz}}/_{k_{xx}} \leq 1.0$

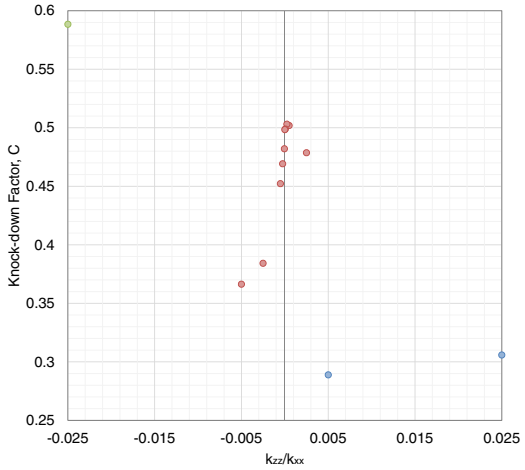

(b) $-0.025 \leq {}^{k_{zz}}/_{k_{xx}} \leq 0.025$

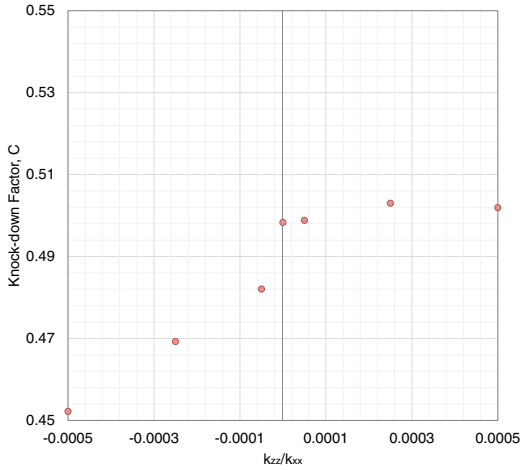

(c) $-0.0005 \leq {}^{k_{zz}}/_{k_{xx}} \leq 0.0005$

Figure 7.5: Knock-down factor of the different geometries

practically imperfection insensitive beyond ${}^{k_{zz}}/_{k_{xx}} < -0.2$. It is not helpful to curve-fit the entire resulting knock-down factors aside from noting the emergence of the festoon shapes. However, if we focus solely on the geometries in between curvatures $0 \leq {}^{k_{zz}}/_{k_{xx}} < 0$, an almost linear fit can be constructed (Eq.(7.10)).

$$C = -3.0{}^{k_{zz}}/_{k_{xx}} + 0.3 \tag{7.10}$$

The reason for this fit ending at the lower bound of the entire graph will become clear in a later section where it is shown that the slight hyperbolic geometry can also result in a knock-down factor of ≈ 0.3. Combining this with the previous observation that the geometry becomes imperfection insensitive beyond ${}^{k_{zz}}/_{k_{xx}} < -0.2$, we obtain the following conclusion,

$$C = \begin{cases} -3.0{}^{k_{zz}}/_{k_{xx}} + 0.3 & \text{if } -0.2 \leq {}^{k_{zz}}/_{k_{xx}} < 0; \\ 0.9 & \text{if } {}^{k_{zz}}/_{k_{xx}} < -0.2. \end{cases} \tag{7.11}$$

From Chapter 6 it can be seen that imperfection in the shape of the first mode of the cooling tower does govern the behaviour. When similar buckling mode starts to emerge in this chapter (ie. ${}^{k_{zz}}/_{k_{xx}} < -0.005$), it can be assumed at the first mode governs the ultimate buckling

capacity. Therefore, only within the near-zero region does it become ambiguous as to the governing imperfection shape. This is investigated further in the following sections.

7.2.4 How cylindrical is cylindrical

As was previously compared, with a finer mesh, the axisymmetric mode does not emerge when the geometry sufficiently resembles a perfect cylinder. This section finds the curvature at which the axisymmetric starts to emerge, but not yet the dominate mode.

Since the axisymmetric mode emerges as the predominate mode at $k_{zz}/k_{xx} = 0.005$ and is completely absent at $k_{zz}/k_{xx} = 0.0025$, a new geometry is created with a curvature ratio that bisects the two above, $k_{zz}/k_{xx} = 0.00375$. By running LBA, results (Figure 7.6a) shows that the predominate model remains the axisymmetric one. Bisection is done again between $k_{zz}/k_{xx} = 0.00375$ and 0.0025 and a new geometry is created at $k_{zz}/k_{xx} = 0.003125$. Running LBA again, Figure 7.6b shows that while the axisymmetric mode still exists, it is no longer the first mode. Note that due to the similarity between these models, the resulting eigenvalues are very similar. It has been mentioned before that the order of the buckling modes is highly dependent on a variety of factors such as mesh density, therefore all parameters except the vertical curvature are kept constant to ensure that this study produces valid result.

This trend that the axisymmetric mode moves forward as curvature increases is alarming since imperfection in that particular modal shape is shown to govern the buckling behaviour. It suggests that the particular mode may move backward (up the modal number) as curvature becomes 0 and therefore may be neglected if only the first modes are extracted.

This shows the benefit of using a coarse mesh as the axisymmetric mode is captured with a coarse model of zero curvature. With a coarse mesh such as the one in Chapter 6, the solver is not able to distinguish it and another geometry with a curvature up to $k_{zz}/k_{xx} = 0.00375$ as the above figure 7.6b suggests, as the resulting buckling modes look identical to Figure 6.2.

7.2.5 Numerical and Analytical Analysis of Axisymmetric Mode

Effect of the axisymmetric imperfection

Upon observing the detrimental effect of the axisymmetric imperfection shape on the positively curved geometries, one wishes to impose it also on the hyperbolic and cylindrical geometries. The obstacle lies in the fact that axisymmetric buckling does not occur in negatively or zero curved surfaces. Therefore, through trickery, the axisymmetric buckling mode is borrowed from the least positively curved surface that still produces such a mode within the first 20, $k_{zz}/k_{xx} = 0.003125$. After performing LBA, the positively curved geometry is modified to a negatively curved one, $k_{zz}/k_{xx} = -0.025$, and then the axisymmetric mode is imposed as imperfection. Note that this hack would only work for geometries with exactly the same number of nodes and nodal arrangements.

After imposing the axisymmetric imperfection, the same GNLA is performed with displacement controlled load steps. Figure 7.7a shows that for a slight hyperbolic structure $k_{zz}/k_{xx} = -0.025$, larger reduction factor can be obtained by imposing an axisymmetric imperfection shape than with the 1st buckling mode. This is especially significant as this imperfection shape would never result from the buckling analysis of a hyperbolic structure, making it unsafe to use only the first mode as the imperfection shape.

The traditional knock-down factor can not be used in this case as there is no corresponding critical force since the imperfection is not a real modal shape. The modified knock-down factor

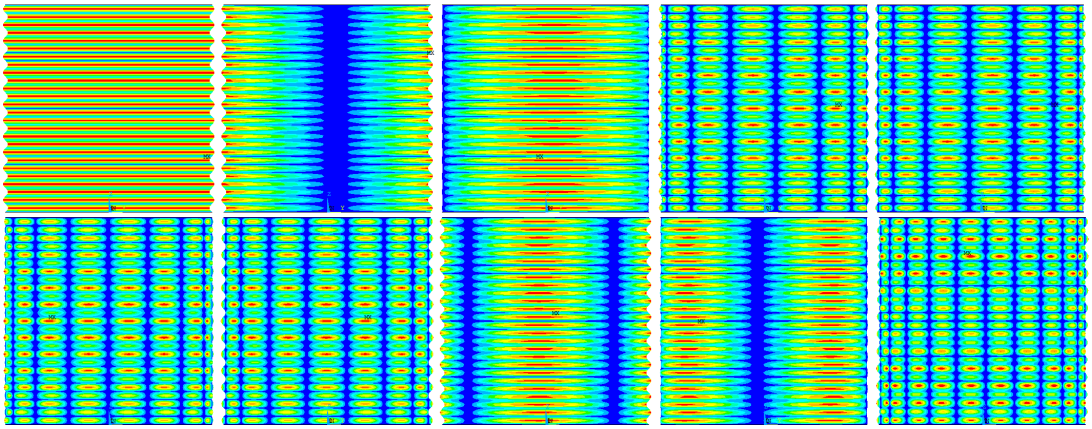

(a) $k_{zz}/k_{xx} = 0.00375$, axisymmetric mode governs

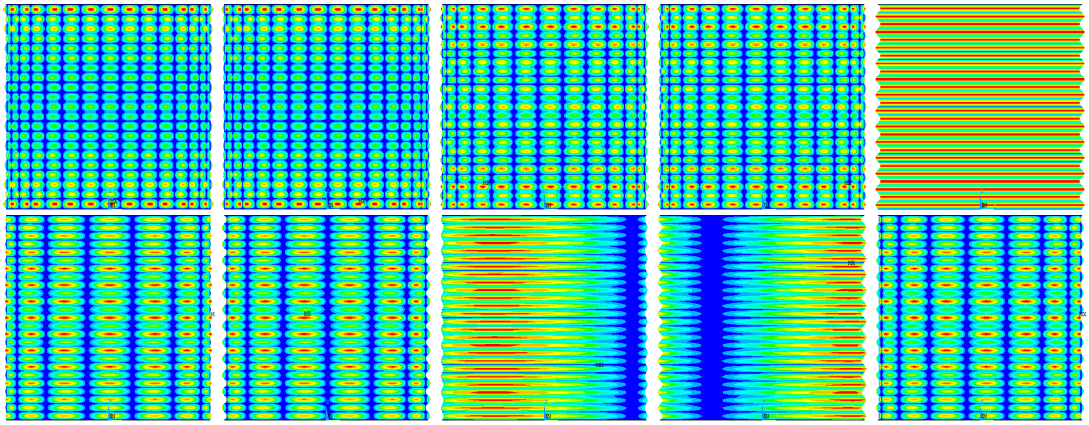

(b) $k_{zz}/k_{xx} = 0.003125$, axisymmetric mode does not govern (similar to the cylinder model in chapter 6)

Figure 7.6: First ten buckling modes of the two different curvatures

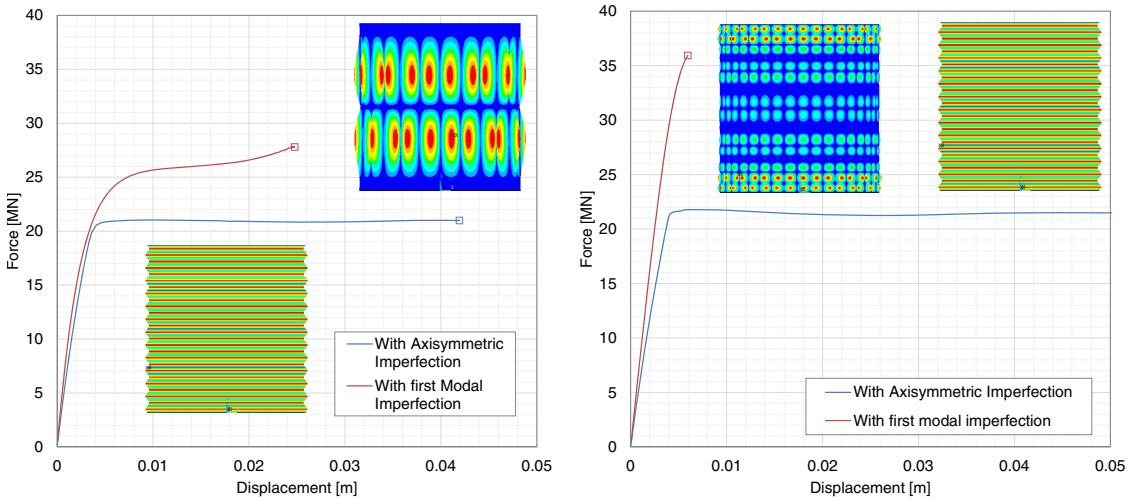

(a) Hyperboloid, $k_{zz}/k_{xx} = -0.025$ (b) Cylinder, $k_{zz}/k_{xx} = 0$

Figure 7.7: Force displacement curves comparison between effect of first modal and axisymmetric imperfections

comes quite handle here as it compares the ultimate capacity with the capacity resulting from

GNLA with the first mode as imperfection.

$$C_{\mathrm{m}} = \frac{F_{\mathrm{ult,axi}}}{F_{\mathrm{ult},1}} = \frac{21040479}{33153000} = 0.635 \tag{7.12}$$

$F_{\mathrm{ult},1}$ and the traditional knock-down factor of the hyperboloid retrieved from Figure 7.5 are $F_{\mathrm{ult},1} = 33\,153\,000\,\mathrm{N}$ and $C = 0.588$ respectively.

The same procedure is applied to the perfect cylinder, ${}^{k_{zz}}/_{k_{xx}} = 0$. This is done because such a buckling mode is not present in a cylindrical model with a fine mesh density (at least within the first 20 modes). The resulting load displacement plot (Fig. 7.7b) shows a significant reduction as well.

Similar knock-down factor can be calculated,

$$C_{\mathrm{m}} = \frac{F_{\mathrm{ult},i}}{F_{\mathrm{ult},1}} = \frac{21787000}{36419000} = 0.598 \tag{7.13}$$

The traditional knock-down factor of the cylinder with the first mode as imperfection is $C = 0.498$.

From these two results, it may be suggested that the initial curvature does not influence the capacity as much as the initial imperfection, at least for geometries in close proximity to a cylinder. With this axisymmetric mode as imperfection, the resulting knock-down factor of the near-cylindrical hyperboloid, the cylinder, and the previously analysed near-cylindrical barrel become remarkably similar.

The failure mode of these two analyses are similar as well (Fig 7.8), both experience three distinct phase of displacement shapes. The axisymmetric shape, the Yoshimura shape (Fig 7.8b, lasting for a brief time), and then a modified Yoshimura pattern with layers of buckles alternating between flattened out or deepened (i.e. the wave length doubled).

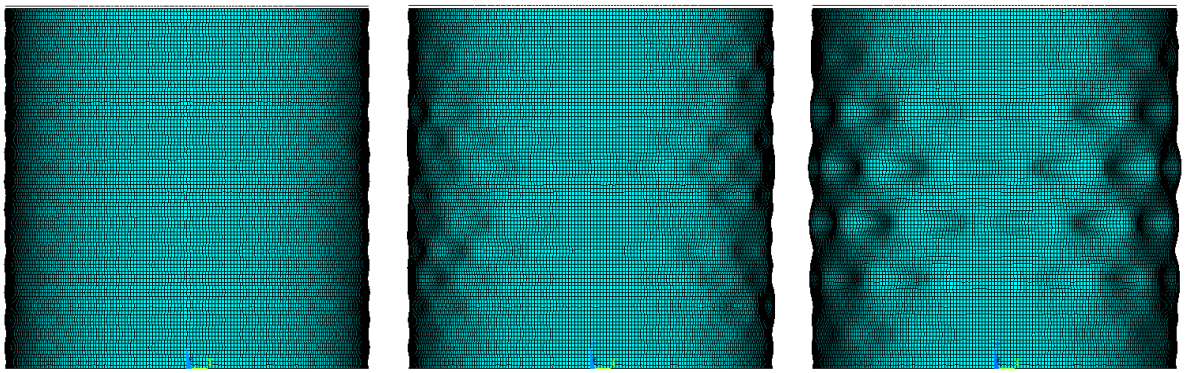

(a) LS170 (b) LS178 (c) LS187

Figure 7.8: Deflected shape near buckling

The same axisymmetric imperfection is applied to another hyperboloid, though with a much larger curvature ${}^{k_{zz}}/_{k_{xx}} = -0.5$. From the results shown in figure 7.9, it was shown that this geometry is not imperfection sensitive if the first buckling mode is applied as the imperfection. The axisymmetric mode is no longer governing as was the case for the near-zero curvatures. This is inline with the expectation that sufficiently negatively curved structures are not imperfection sensitive.

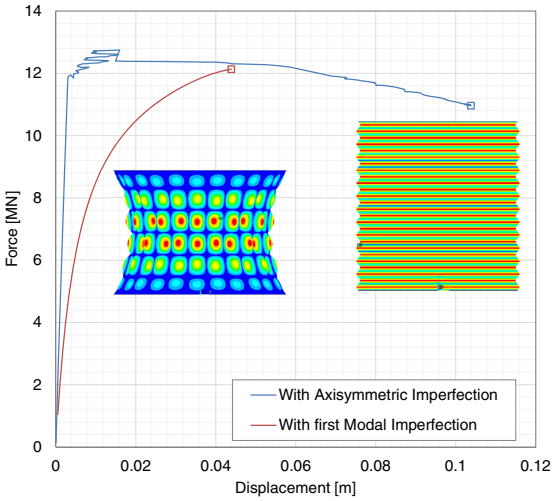

Figure 7.9: Hyperboloid, $k_{zz}/k_{xx} = -0.5$

Prediction of buckling

It is clear from above that the axisymmetric imperfection shape holds significance in the buckling behaviour of thin cylindrical shells. This section classifies this shape, and predicts buckling as a result of this shape. In particular, the author relates the vertical imposed displacement u_z to the circumferential membrane force n_x at the onset of secondary (circumferential) buckling (Fig. 7.8b). The circumferential displacement is used as the dependent variable, and its behaviour is categorized first.

The axisymmetric modal imperfection can be described as a sinusoidal curve with an initial amplitude of $e_i = t/2$, as $t/2$ is set as the maximum imperfection amplitude. Figure 7.10 shows the actual profile of imperfection against a sinusoidal relation described with equation (7.14),

$$x = -e_i sin\left(\frac{m\pi}{L}z\right) + a \tag{7.14}$$

where m is the number of half buckle waves, L is the length of the cylinder, and a is the radius.

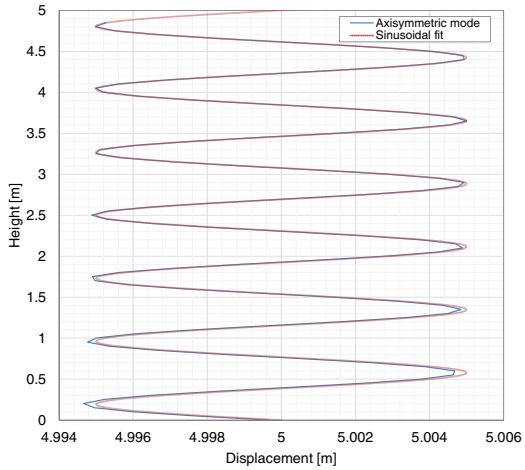

Figure 7.10: Axisymmetric imperfection, and superimposed sinusoidal curve fit (note that only a half of the cylinder is shown)

The number of half waves in the axisymmetric mode is 26, and the wavelength is calculated as $L/m = 0.385\,\text{m}$. This is verified by Calladine who derived equation (7.15).

$$\begin{aligned}\frac{L}{m} &= \pi\left(\frac{a^2h^2}{12(1-\nu^2)}\right)^{\frac{1}{4}} \\ &\approx 1.72\sqrt{ah} \\ &= 0.385\,\text{m}\end{aligned} \tag{7.15}$$

Like compressing an accordion, the amplitude of the sine wave (the horizontal displacement) increases as the axial load increases. The total displacement in the circumferential direction is defined by $e = e_i + \Delta e$.

$$e_i = \frac{t}{2} = 0.0005 \tag{7.16}$$

By plotting the horizontal displacement (Δe) of an inward and an outward buckle against the imposed displacement(u_z) as it increases, one can obtain an almost linear relationship prior to secondary (circumferential) buckling (see the average displacement plot on figure 7.11). Note that in the real system, outward buckles displace more than the inward ones, even though the initial imperfection assumes buckles of equal amplitude. For this study, this asymmetry is ignored, and the buckles are assumed to be equal in lateral displacement, and the numerical value used is the average of the two. This is assumed to be valid as Δe at the onset of buckling is $1/2.5$ of e_i.

$$\Delta e = \frac{\Delta e_{\text{out}} + \Delta e_{\text{in}}}{2} \tag{7.17}$$

Δe, being the horizontal displacement at the extremities of buckles, can be estimated by the pre-buckling displacement of a series of vertical columns supported laterally by distributed by springs (similar to how a wine barrel is constructed). The attempt to construct such a relation is detailed in appendix D, however the end result is asymptotic in shape, and does not match with the near-linear relationship (Fig 7.11) given by FEM without an adjustment factor. It is proposed that the initial axisymmetric imperfection has already pre-buckled the structure, and what is calculated by FEM is the post-buckling behaviour (of the axisymmetric buckling). And it is this post-buckling state that leads to the onset of secondary (circumferential) buckling.

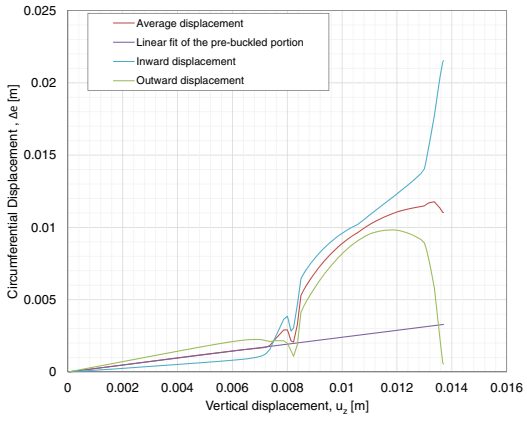

Figure 7.11: Circumferential displacements of an outward, and an inward buckle

An empirical relation between Δe and the imposed vertical displacement based on figure 7.11 is constructed instead (Eq. (7.18)).

$$\Delta e = 0.24 u_z \tag{7.18}$$

Now that Δe can be predicted with a formula, the next step is to relate it to the membrane force in the hoop direction. To predict the onset of asymmetric buckling in between the rings of axisymmetric buckles, the compressive stress in the hoop direction must be calculated. Take a section of an inward buckle, one can construct a free body diagram as in Figure 7.12, where q_1 and q_2 are the membrane stresses at the top and bottom of the section, and P_1 and P_2 are the hoop forces at the top and the bottom ring of the section.

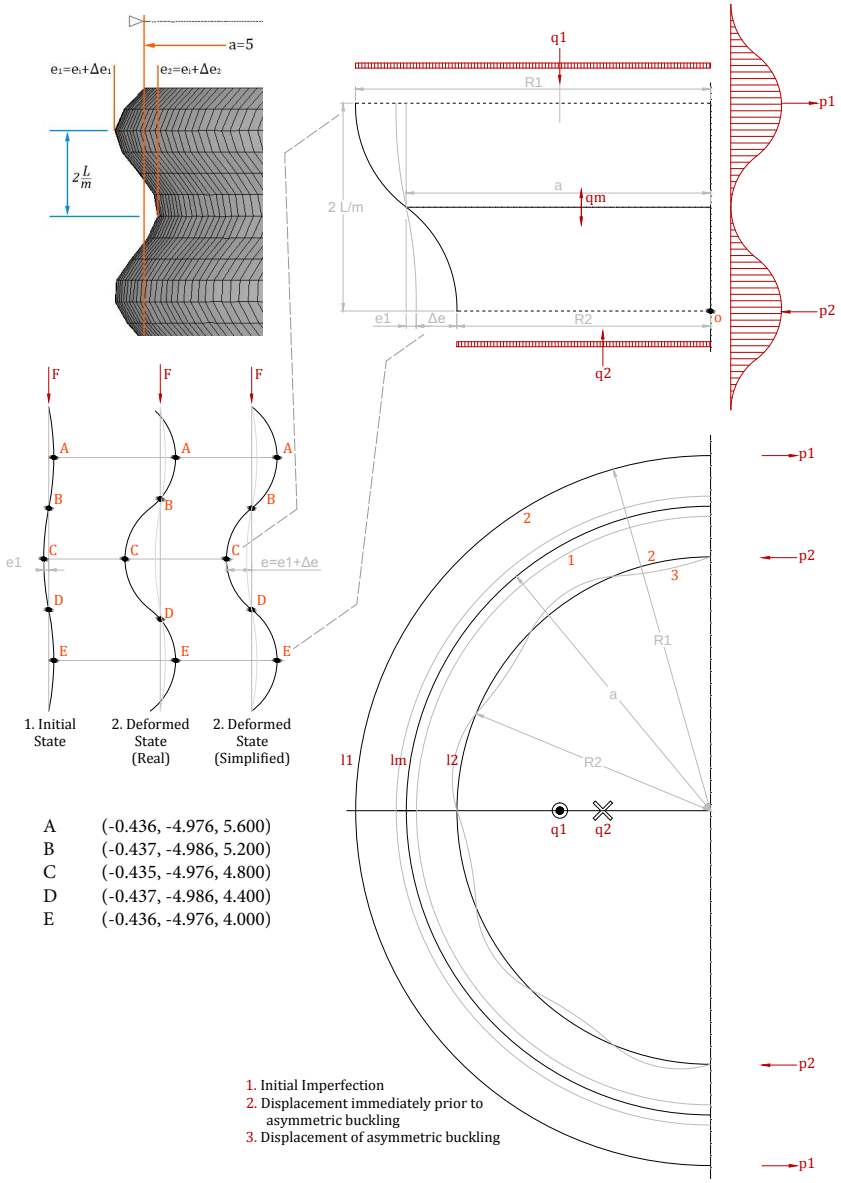

Figure 7.12: Free body diagram of axisymmetric buckling

From equilibrium in the vertical direction,

$$\sum F_y = 0 = h(q_1 l_1) = h(q_2 l_2) \tag{7.19a}$$

$$n_{z,1} l_1 = n_{z,2} l_2 \tag{7.19b}$$

$$l_1 = \pi R_1 \tag{7.19c}$$

$$l_2 = \pi R_2 \tag{7.19d}$$

From equilibrium in the horizontal direction, it is clear that

$$\sum F_x = 0 \tag{7.20a}$$
$$P_1 = P_2 \tag{7.20b}$$

From equilibrium in rotation around point "o", assuming a clock-wise coordinate system,

$$\sum M_A = 0 = -n_{z,1} l_1 \frac{4R_1}{3\pi} + n_{z,2} l_2 \frac{4R_2}{3\pi} + 4P_1 \frac{L}{m} \tag{7.21a}$$
$$P_1 = \frac{1}{3\pi} \frac{m}{L} n_{z,1} l_1 (R_1 - R_2) \tag{7.21b}$$

The centre of gravity of a semicircle is located $^{4R}/_{3\pi}$ from the equator, P_1 is the hoop force of one edge, therefore a factor of 2 is applied. The above relations shall always hold true in all load steps, and all except the radii R_1 and R_2 remain constant as load increases. In particular, the vertical distance $^{L}/_{m}$ remains constant as the transition between axisymmetric and the asymmetric state is brief, and the loading conditions are almost identical. After imposing the imperfection and before loading the eccentricity equals to the initial imperfection amplitude. Going back to finding how the radii change as load increases,

$$R1 = a + e_i + \Delta e \tag{7.22a}$$
$$R2 = a - e_i - \Delta e \tag{7.22b}$$
$$R1 - R2 = 2e_i + 2\Delta e \tag{7.22c}$$

To convert forces P_1 and P_2 to membrane forces, one assumes that the stress distributes sinusoidally over the distance of $2^{L}/_{m}$. Therefore, the peak stress is the amplitude of the sine wave.

$$n_x(z) = \frac{n_x}{2} \left[1 - cos\left(\frac{m\pi}{L} z \right) \right] \tag{7.23}$$

The area under the stress curve is the force

$$P = \int \sigma \, \mathrm{d}A \tag{7.24a}$$
$$= \int_0^{2L/m} n_x \, \mathrm{d}z \tag{7.24b}$$
$$= \frac{1}{2} n_x \left[z - \frac{L}{m\pi} sin\left(\frac{m\pi}{L} z \right) \right] \Bigg|_0^{2L/m} \tag{7.24c}$$
$$= \frac{L}{m} n_x \tag{7.24d}$$

To convert q_1 to the stress at an undisturbed cross section ($R_m = a = 5$), one can make reference to line l_m and stress q_m in figure 7.12.

$$n_{z,1} l_1 = n_{z,m} l_m \tag{7.25a}$$
$$n_{z,1} = \frac{l_m}{l_1} n_{z,m} \tag{7.25b}$$

Now we can construct the relationship between the reaction force and hoop stress,

$$\frac{L}{m}n_x = \frac{1}{3\pi}\frac{m}{L}n_{z,1}l_1(R_1 - R_2) \tag{7.26a}$$

$$n_x = \frac{m}{L}\frac{1}{3\pi}\frac{m}{L}n_{z,m}l_m(2e_i + 2\Delta e) \tag{7.26b}$$

$$= \frac{m^2}{L^2}\frac{1}{3\pi}n_{z,m}l_m(2e_i + 2\Delta e) \tag{7.26c}$$

$$= \frac{m^2}{L^2}\frac{1}{3\pi}n_{z,m}\pi a(h + 2\Delta e) \tag{7.26d}$$

$$= \frac{m^2}{L^2}\frac{ah}{3}n_{z,m}\left(1 + \frac{2\Delta e}{h}\right) \tag{7.26e}$$

The last step is to relate the membrane force $n_{z,m}$ to the imposed displacement u_z. Assuming the axisymmetric imperfection is sufficiently small so that the cylinder behaves as a column in the pre-buckled phase, the following equation can be constructed,

$$\sigma_z \propto E\epsilon \tag{7.27a}$$

$$n_{z,m} = C\frac{Eh}{L}\Delta u_z \tag{7.27b}$$

The factor C is introduced to account for bending due to the imperfection induced eccentricity. By comparing with the FEM result, with $C = 1.5$ the following plot can be obtained (Fig. 7.13). With the critical membrane force equation is as follows,

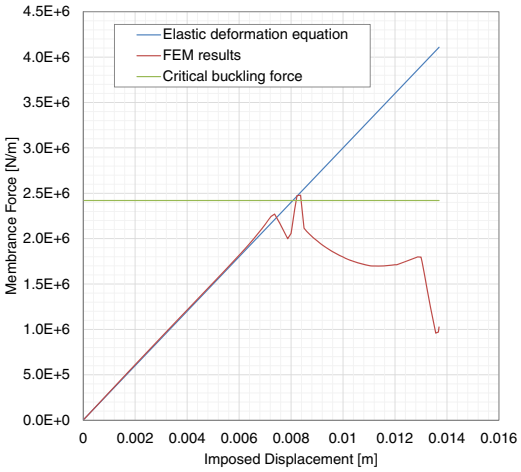

Figure 7.13: Showing the relationship between critical force equation (7.28), FEM result and the elastic deformation fit (7.27)

$$n_{\text{cr}} = \frac{0.605Eh^2}{a} \tag{7.28}$$

Note that the critical force equation without a knock-down factor can predict the critical membrane force in the vertical direction at the onset of buckling quite well. Now substituting this into equation (7.26), we obtain

$$n_x = \frac{m^2}{L^2}\frac{ah}{3}C\frac{Eh}{L}u_z\left(1 + \frac{2\Delta e}{h}\right) \tag{7.29}$$

Now substitute Δe with equation (7.18) we obtain,

$$n_x = \frac{m^2}{L^3}\frac{ah^2}{2}Eu_z\left(1 + \frac{4.8}{h}u_z\right) \tag{7.30}$$

With this equation and the resulting plot on Figure 7.14, it can be seen that while the values between the analytical and the numerical result are similar, the behaviour is not. With FEM, the pre-buckling behaviour is linear, whereas with the equation above, the behaviour is quadratic (with the u_z^2 term).

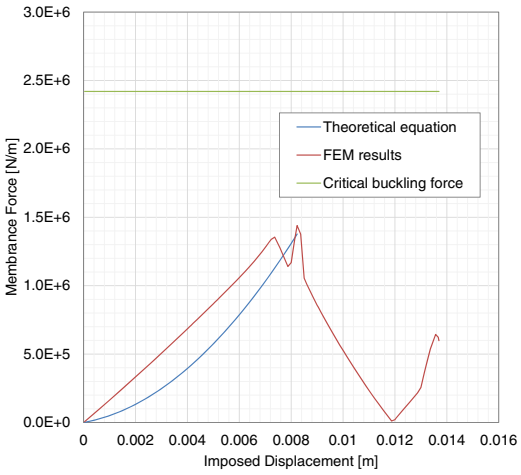

Figure 7.14: Plotting equation (7.30) with FEM results

For reference, the more complete picture of stress development can be observed from the stress plots at the positions of the circumferential buckles (Fig 7.15).

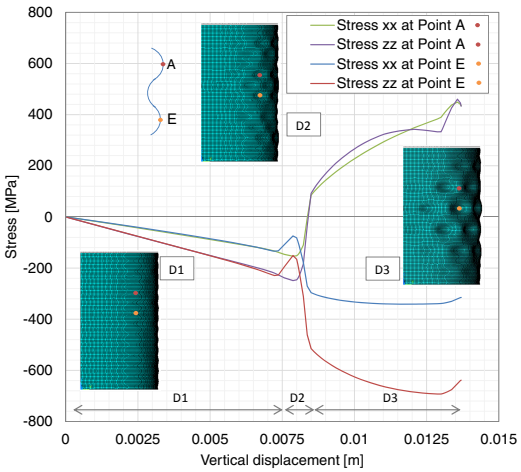

Figure 7.15: Circumferential and vertical stresses verses top displacement load, with different stages of buckling superimposed

7.2.6 Change in eigenvalue

It has been suggested that closely spaced eigenvalues is an indication of imperfection sensitivity. This hypothesis is tested here with the 37 geometries. The first 20 buckling modes of each geometry are calculated (results of LBA is shown in Appendix E) and the difference is defined as the percentage change between the first and the twentieth eigenvalue as stated in Equation (7.31). The usage of the twentieth mode is arbitrary, one could equally use the tenth, or the fiftieth modes.

$$\Delta\lambda_{\text{cr}} = \frac{\lambda_{\text{cr}}^{20} - \lambda_{\text{cr}}^{1}}{\lambda_{\text{cr}}^{1}} \tag{7.31}$$

The resulting change in eigenvalues are plotted with the calculated knock-down factors against the changing initial curvatures in Figure 7.16.

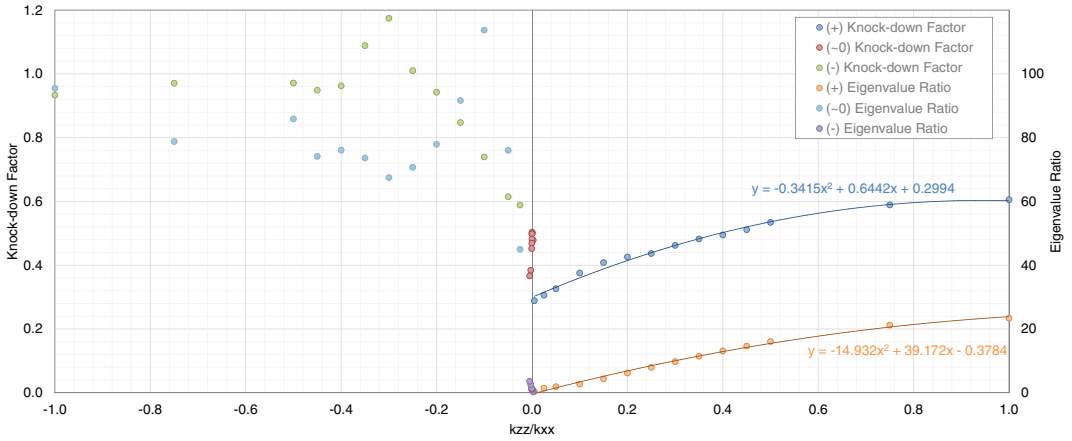

(a) $-1.0 \leq {}^{k_{zz}}/_{k_{xx}} \leq 1.0$

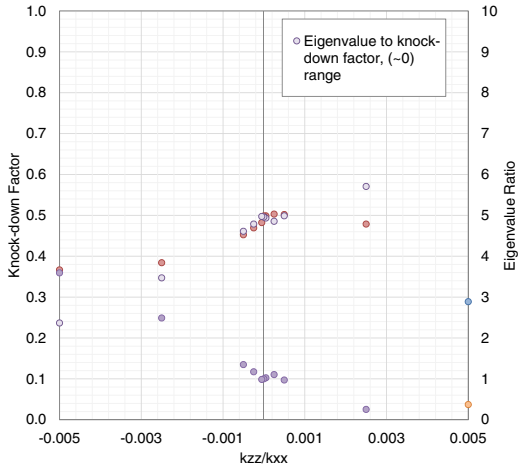

(b) $-0.005 \leq {}^{k_{zz}}/_{k_{xx}} \leq 0.005$

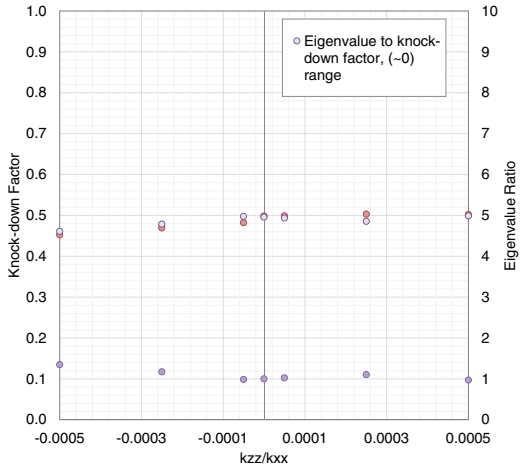

(c) $-0.0005 \leq {}^{k_{zz}}/_{k_{xx}} \leq 0.0005$

Figure 7.16: Change in eigenvalues

The trend is again quite clear for the positive curvature geometries. Graphically speaking it has a strong correlation with the knock-down factor. By using the same curve fit method, one can obtain the following equation to describe the behaviour of the Gaussian curvature.

$$\Delta\lambda_{\text{cr}} = -14.932(\frac{k_{zz}}{k_{xx}})^2 + 39.172\frac{k_{zz}}{k_{xx}} - 0.3784 \tag{7.32}$$

For the near-zero curvature range, as with the knock-down factor, the trend cannot be easily described. However, noting that $\Delta\lambda_{\text{cr}}$ values are similar to the knock-down factors if they were flipped around $C \sim 0.3$, one could construct a rough correlation equation.

$$C = -\frac{\Delta\lambda_{\text{cr}}}{10} + c_1 \tag{7.33}$$

Where, $c_1 = 0.6$ is the mean value of all the knock-down factors and $\Delta\lambda_{\text{cr}}$ values within the near-zero range, plus the knock-down factor at zero curvature. This correlation is plotted in Figure 7.16b and 7.16c.

The shape of negative curvature results also suggests correlations between eigenvalue spacings and ultimate capacities. The festoon shape is also present in the $\Delta\lambda_{\text{cr}}$ values. If we visualize the $\Delta\lambda_{\text{cr}}$ plot stretched in the x direction and compressed in the y direction, so that the peak align with the knock-down factor at $k_{zz}/k_{xx} = -0.3$ then the two plots would look remarkably similar.

This result in itself is an unexpected observation as the spacing of eigenvalues has been used only as an indication of imperfection sensitivity, and not to calculate the actual knock-down factor. However, the above suggest that we may be able to do exactly that, at least for elementary geometries. This correlation deserve study in depth to see whether actual relationship exist.

7.3 Gaussian curvatures

7.3.1 Introduction

It is hypothesized that the imperfection susceptibility of a shell is influenced by its Gaussian curvature. Therefore, structures with positive, negative and zero Gaussian curvatures will be studied in this thesis. From the two principle curvatures, the Gaussian curvature can be calculated using the equation (7.34).

$$K = k_1 k_2 = k_x k_y - k_{xy}^2 \tag{7.34}$$

Figure 7.17 gives a simplistic view of the shapes associated with these curvatures. Note that aside from a few structures, most are designed with a combination of many different curvatures and therefore are more difficult to analyse.

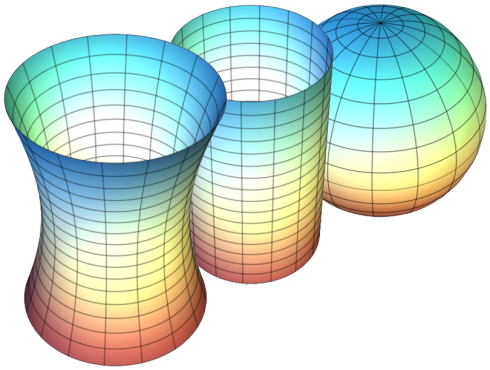

Figure 7.17: Different Gaussian curvatures, from the left: hyperboloid, cylinder, and sphere[1]

This study first details a systematic method to extract Gaussian curvatures of a parametrically rectangular surface mesh. The author then implements this method in ANSYS script as a post-processor to any GNL analyses, so that the change in Gaussian curvature between every load-step can be observed. This tool is used to further investigate the difference in buckling behaviour between the geometry of various curvatures. In particular, attention is paid to the development of buckles, and its relation with change in Gaussian curvature.

7.3.2 Algorithm

ANSYS does not have the native function to compute Gaussian curvature of a surface, therefore a custom calculation macro is written in APDL to calculate the Gaussian curvature at every element. The basis of calculation follows the mathematical theorem which states the Gaussian curvature of a surface in R^3 may be expressed as the quotient of the determinant of the second fundamental form by the determinant of the first. The mathematical limitation of this algorithm is beyond the scope of this thesis[2].

The first fundamental form assumes that the surface is once differentiable and parametrized with u, and v. It then calculates the inner (dot) product of the of the two tangent vectors. If the following is true,

$$K = \frac{\det[\mathrm{II}]}{\det[\mathrm{I}]} = \frac{LN - M^2}{EG - F^2} \tag{7.35}$$

[1] Jhausauer, Gaussian curvature, wikipedia, `http://en.wikipedia.org/wiki/Gaussian_curvature`

[2] Gray, A. The Definition of a Regular Surface in R^n. 12.4 in Modern Differential Geometry of Curves and Surfaces with Mathematica, 2nd ed. Boca Raton, FL: CRC Press, pp. 281-286, 1997.

then E, F, G are the coefficients of the first fundamental form. In a discrete system, the coefficients can be calculated by taking the dot product of the partial derivatives

$$\begin{aligned} \boldsymbol{E} &= \boldsymbol{u} \cdot \boldsymbol{u} && = x_u^2 + y_u^2 + z_u^2 \\ \boldsymbol{F} &= \boldsymbol{u} \cdot \boldsymbol{v} && = x_u \cdot x_v + y_u \cdot y_v + z_u \cdot z_v \\ \boldsymbol{G} &= \boldsymbol{v} \cdot \boldsymbol{v} && = x_v^2 + y_v^2 + z_v^2 \end{aligned} \tag{7.36}$$

where

$$\begin{aligned} \nabla x &= \frac{\delta x}{\delta u} + \frac{\delta x}{\delta v} && = x_u \vec{u} + x_v \vec{v} \\ \nabla y &= \frac{\delta y}{\delta u} + \frac{\delta y}{\delta v} && = y_u \vec{u} + y_v \vec{v} \\ \nabla z &= \frac{\delta z}{\delta u} + \frac{\delta z}{\delta v} && = z_u \vec{u} + z_v \vec{v} \end{aligned} \tag{7.37}$$

and,

$$\begin{aligned} \boldsymbol{u} &= x_u \vec{i} + y_u \vec{j} + z_u \vec{k} \\ \boldsymbol{v} &= x_v \vec{i} + y_v \vec{j} + z_v \vec{k} \end{aligned} \tag{7.38}$$

Then the normal vector to the surface is determined.

$$\begin{aligned} \boldsymbol{m} &= \boldsymbol{u} \times \boldsymbol{v} \\ \boldsymbol{p} &= \sqrt{\boldsymbol{m} \cdot \boldsymbol{m}} \\ \boldsymbol{n} &= \frac{\boldsymbol{m}}{\boldsymbol{p}} \end{aligned} \tag{7.39}$$

Assuming the displacement field is twice differentiable (not a concern when it is a discrete system), the coefficients of the second fundamental form L, M, N can be calculated as follows. First the second derivatives of the displacement is calculated.

$$\begin{aligned} \nabla x_u &= \frac{\delta x_u}{\delta u} + \frac{\delta x_u}{\delta v} && = x_{uu} \vec{u} + x_{uv} \vec{v} \\ \nabla y_u &= \frac{\delta y_u}{\delta u} + \frac{\delta y_u}{\delta v} && = y_{uu} \vec{u} + y_{uv} \vec{v} \\ \nabla z_u &= \frac{\delta z_u}{\delta u} + \frac{\delta z_u}{\delta v} && = z_{uu} \vec{u} + z_{uv} \vec{v} \\ \nabla x_v &= \frac{\delta x_v}{\delta u} + \frac{\delta x_v}{\delta v} && = x_{vu} \vec{u} + x_{vv} \vec{v} \\ \nabla y_v &= \frac{\delta y_v}{\delta u} + \frac{\delta y_v}{\delta v} && = y_{vu} \vec{u} + y_{vv} \vec{v} \\ \nabla z_v &= \frac{\delta z_v}{\delta u} + \frac{\delta z_v}{\delta v} && = z_{vu} \vec{u} + z_{vv} \vec{v} \end{aligned} \tag{7.40}$$

Then

$$\begin{aligned} \boldsymbol{uu} &= x_{uu} \vec{i} + y_{uu} \vec{j} + z_{uu} \vec{k} \\ \boldsymbol{uv} &= x_{uv} \vec{i} + y_{uv} \vec{j} + z_{uv} \vec{k} \\ \boldsymbol{vv} &= x_{vv} \vec{i} + y_{vv} \vec{j} + z_{vv} \vec{k} \end{aligned} \tag{7.41}$$

Finally, the coefficients are calculated,

$$\begin{aligned} \boldsymbol{L} &= \boldsymbol{uu} \cdot \boldsymbol{n} \\ \boldsymbol{M} &= \boldsymbol{uv} \cdot \boldsymbol{n} \\ \boldsymbol{N} &= \boldsymbol{vv} \cdot \boldsymbol{n} \end{aligned} \tag{7.42}$$

7.3.3 Implementation

Most of the script is a direct adaptation of the above algorithm as common operators such as dot and cross product are a part of the built-in library. The coordinates x, y, z are stored in a 2-D matrix with 3 columns which are accepted by the built-in functions. Gradient is calculated according to Matlab's numerical gradient, *gradient*, function (eq (7.43)[3]). The practical (and further restrictive) assumption of the algorithm that it can only be applied to a matrix of coordinates, with each of the two dimensions being greater than 5.

$$A_i = \frac{1}{2}\sum_{i=2}^{N-1} A_{i+1} - A_{i-1} \tag{7.43}$$

Along the top and bottom edges, the gradient is calculated single-sided difference between the value itself and its neighbour. This ensures the resulting matrix size has the same size. The left and right edges are physically connected since the geometry is a surface of revolution, therefore gradient is calculated between the element's adjacent value and the value at the opposite end.

Since it is much easier to refer to neighbouring elements as oppose to neighbouring nodes when using quadratic elements, the input to this macro is assumed to be the centroidal coordinate of each element. Similarly the output is an array of each element's respective Gaussian curvature. A different macro loops through each load step, and imposes the calculated displacements on to each node[4]. Then the centroidal location of the modified elements are obtained and sent to the Gaussian curvature macro. The resultants are imposed as a surface pressure for visualization purposes.

The incremental change in Gaussian curvature is also of interest. After computing the Gaussian curvature for a particular load step, the difference is calculated between it and the Gaussian curvature of the previous load step. This difference is also displayed as a surface pressure for visualization.

$$\Delta K = \frac{K_t - K_{t-1}}{\delta t} \tag{7.44}$$

7.3.4 Application

Since this algorithm is implemented strictly as a post-processor, it can be used on any of the previously analysed models. Four of the above 37 models are chosen, and the resulting Gaussian curvature visually inspected. Then the numerical values are extracted for the models that exhibit clear buckling behaviour.

Geometry 1 $^{k_{zz}}/_{k_{xx}} = -1$

Starting from the hyperbolic side, the Gaussian curvature of model $^{k_{zz}}/_{k_{xx}} = -1$ is calculated and graphically shown in figure 7.18a. This model is representative in two ways. The top ring is large enough that the cantilever action reduces the stiffness of the structure, and the reaction force decreases (see previous fig 7.3a). It is slightly imperfection sensitive, with a knock-down factor of 0.933.

Figure 7.18a shows the effectiveness of plotting the Gaussian curvature and the change in Gaussian curvature. The initial imperfection can be seen from A1, where the maximum imperfections

[3]Gradient, Numerical gradient, MathWorks., http://www.mathworks.nl/help/matlab/ref/gradient.html

[4]This is a problematic step in the procedure, as the displacement must be scaled small enough to not cause ill-definition, and large enough to distinguish itself from the initial imperfection

occur at equator. A2 shows that the largest curvature also exists at the equator, and also that at $t \sim 0$ the global shape determines K, and not the local imperfection. As the imposed displacement increases (point B), both K and ΔK decrease the most at the equator still. Positive K surface starts forming due to the imperfection. At point C and D however, ΔK decreases the most at the edges. This is not clearly evident in the displacement plots C3 and C4. The model diverges slightly after point E, where from E2, and E3 it is evident that the surface is most curved around the edge points.

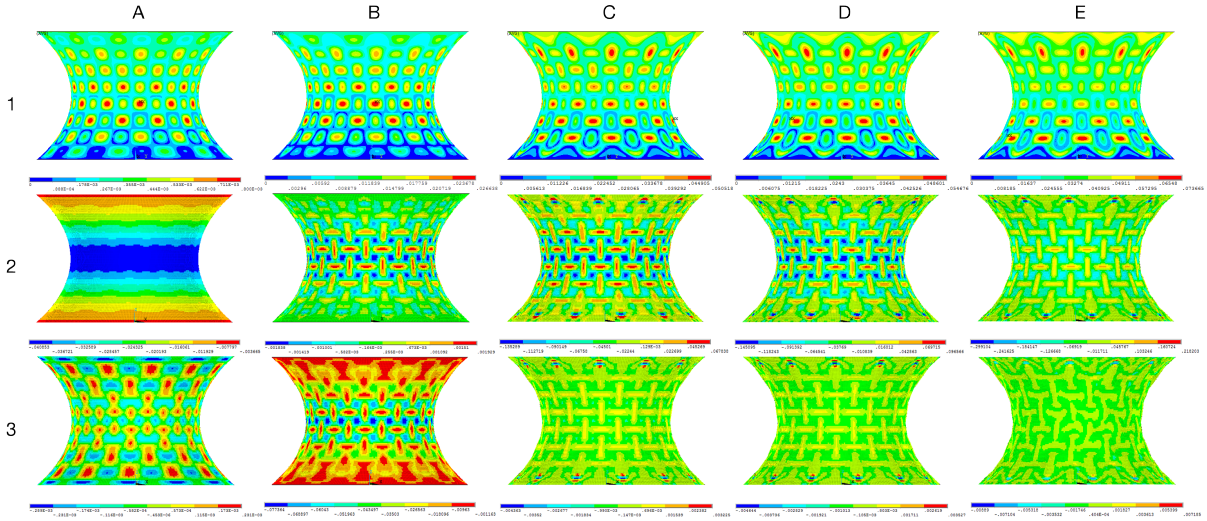

(a) $k_{zz}/k_{xx} = -1.0$; Top - Displacement, middle - K, and bottom - ΔK

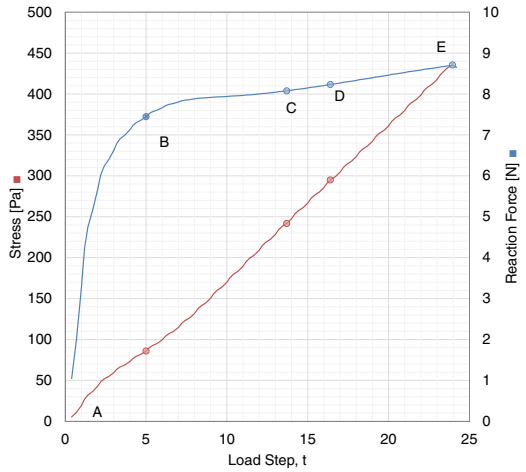

(b) Stress and force vs. load step

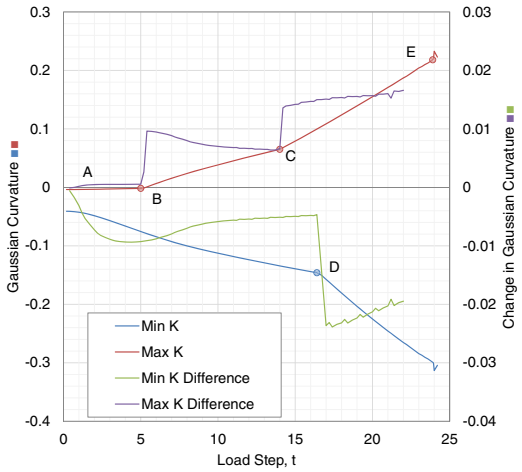

(c) K and ΔK vs. load step

Figure 7.18: Buckling behaviour of geometry with large negative Gaussian curvature

The visual assessment is complimented by plots of K and ΔK vs. load step as show in Figure 7.18b. At $t \sim 0$ it is clear that the initial curvature is largely negative. As load increases, the graph shows that for both maximum and minimum K, the behaviour is largely multi-linear. δK furthers shows that the change in curvature occur in discrete steps and not gradually. From this plot, it is clear where attention should be focused on, and where buckling happens.

Geometry 2 $k_{zz}/k_{xx} = -0.05$

The next geometry is also a hyperboloid, but in this case the buckle happens near the equator of the structure as oppose to at the top and bottom rings. Figure 7.19 shows the same three figures as for the first geometry. A1 shows the shape and the magnitude of the initial imperfection. Column B is where the structure reaches is buckling capacity. Note that there is no significant K or ΔK, as Figure 7.19c shows a flat line at zero for both. Column C shows the structure immediately after buckling. Visually inspecting displacement plot B1 and C1, there is no significant difference aside from the colour change. However the difference is clear between B2 and C2, and B3 and C3. In fact because the curvature changed dramatically from B to C, ΔK at that step is almost equivalent of K (ie. C3 equals to C2), dominating the Gaussian curvature from previous steps. As the load further increases, the buckles become more localized. As shown in Figure 7.19c, load step D and E, step-wise increase of ΔK can be observed.

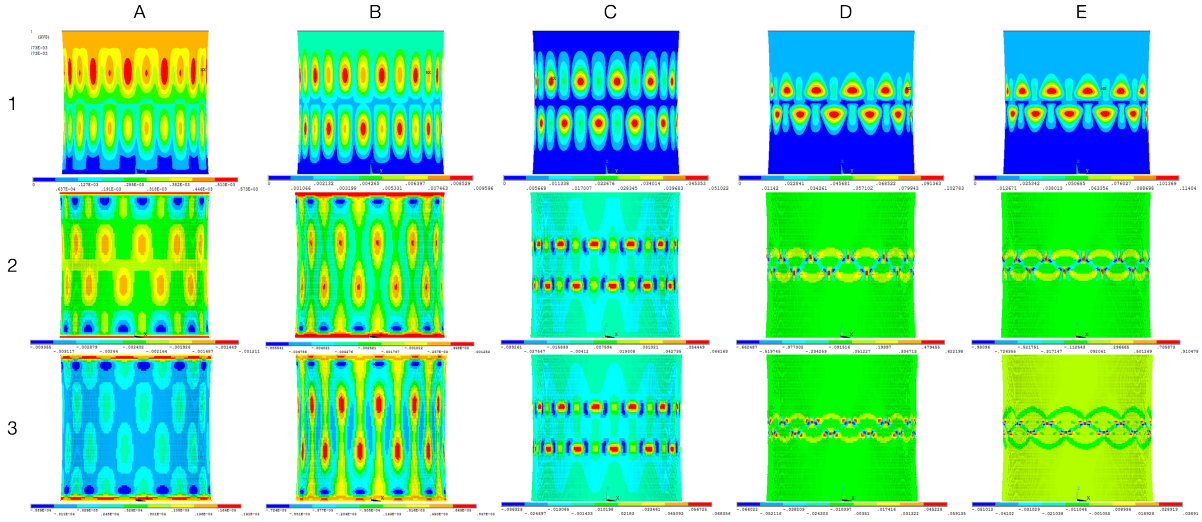

(a) $k_{zz}/k_{xx} = -0.1$; Top - Displacement, middle - K, and bottom - ΔK

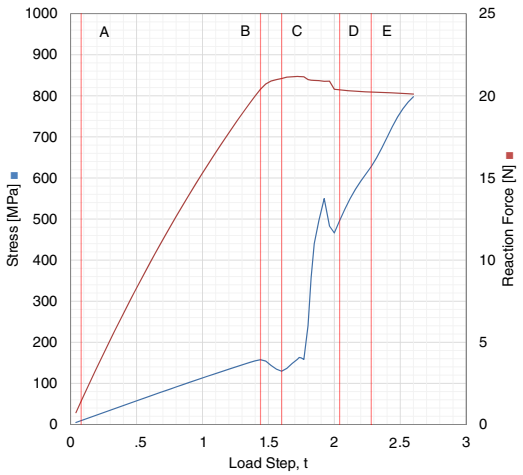

(b) Stress and force vs. load step

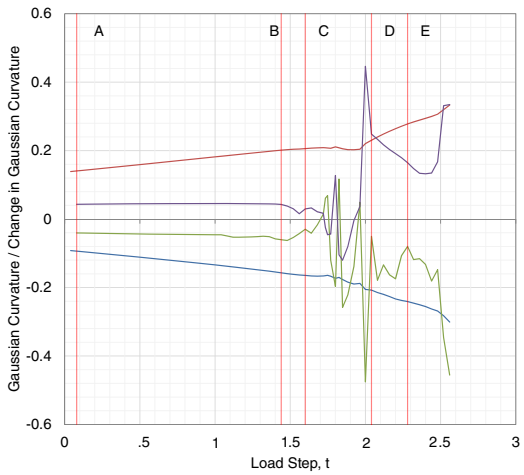

(c) K and ΔK vs. load step

Figure 7.19: Buckling behaviour of geometry with slight negative Gaussian curvature

Geometry 3 $k_{zz}/k_{xx} = 0$

At zero curvature, it is observed that axisymmetric buckling modes do not emerge. Buckles are distributed and small in size. At load step D, the emergence of the second layer of buckles is evident in D3, and develops further in E3. Where as in D1, and D2, the second layer of buckles is scarcely visible. This shows a difference between the initial linear buckling mode and the final buckling mode. This difference may suggest that imperfection in the final shape may reduce the capacity further.

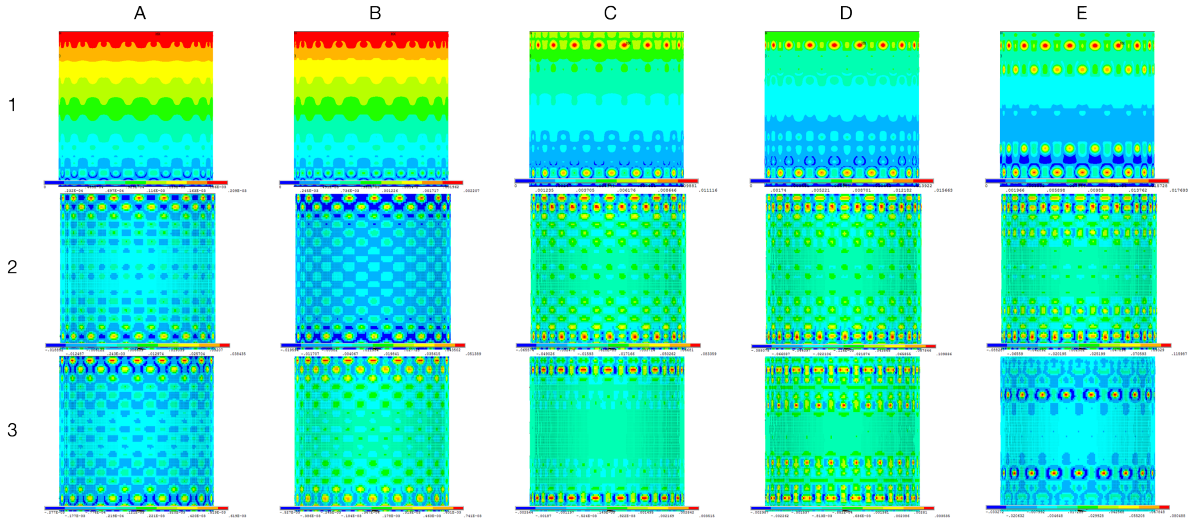

(a) $k_{zz}/k_{xx} = +0.1$; Top - Displacement, middle - K, and bottom - ΔK

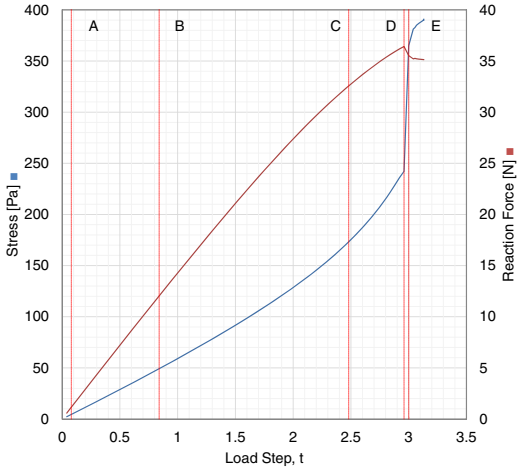

(b) Stress and force vs. load step

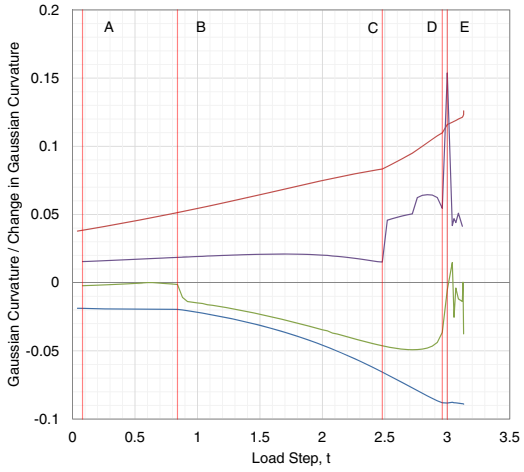

(c) K and ΔK vs. load step

Figure 7.20: Buckling behaviour of geometry with neutral Gaussian curvature

Geometry 4 $k_{zz}/k_{xx} = +0.005$

Next a positive curvature geometry, $k_{zz}/k_{xx} = +0.1$, is analysed. This model resulted in the highest reduction factor out of all the different curvatures analysed in this chapter. Again, Column A of figure 7.21a shows the initial imperfection. Note that the Gaussian noise can be observed here as random specks of local curvature difference. From load step A to B, there is a constant ΔK and a linear increase in K, the structures deforms like an accordion due to the axial load. At point B, slight difference in deformation in the tangential direction starts emerging. This is most obvious in the ΔK plot B3 where the incremental change in Gaussian curvature is no longer symmetrical, but rather wave-like. There appears to be significant asymmetry resulting in a diagonal band. The next load step, C, shows clear buckles forming in C3, at the location of the diagonal band. This is not apparent in either C1 or C2. At D, and E, buckles intensify and become more apparent and localized around the equator. If we focus on the transition between C2 and D2, it is apparent that buckles in the tangential direction form in between the vertical buckles.

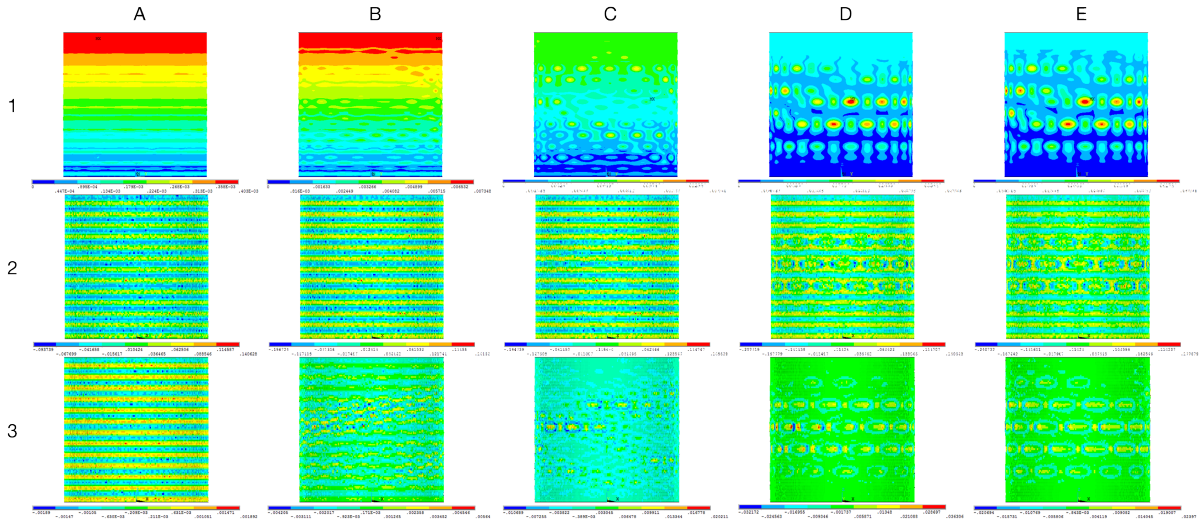

(a) $k_{zz}/k_{xx} = +0.1$; Top - Displacement, middle - K, and bottom - ΔK

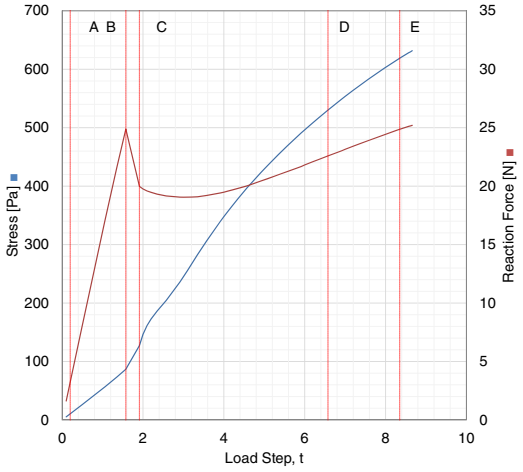

(b) Stress and force vs. load step

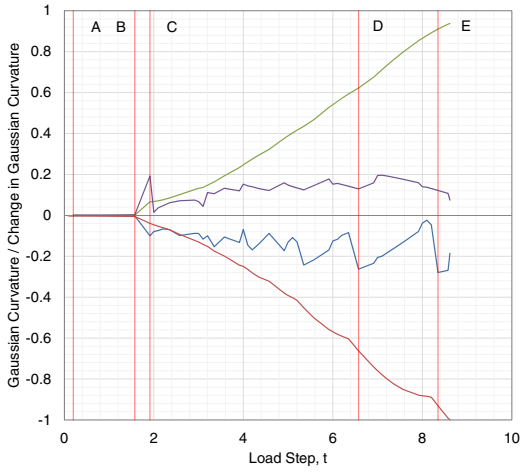

(c) K and ΔK vs. load step

Figure 7.21: Buckling behaviour of geometry with slight positive Gaussian curvature

This observation provides further validation of Koiter's modal interaction theory, where Koiter both qualitatively and quantitatively described the physical behaviour of modal interaction by

considering an axisymmetric buckling mode in Figure 7.22a as the initial imperfection. As axial load increases, the inward-deflecting (concaved) portion of the shell surface also compresses in the hoop direction, this destabilises the shell into a asymmetric (doubly-periodic) mode (Figure 7.22b) at a bifurcation point from the nonlinear prebuckled state.

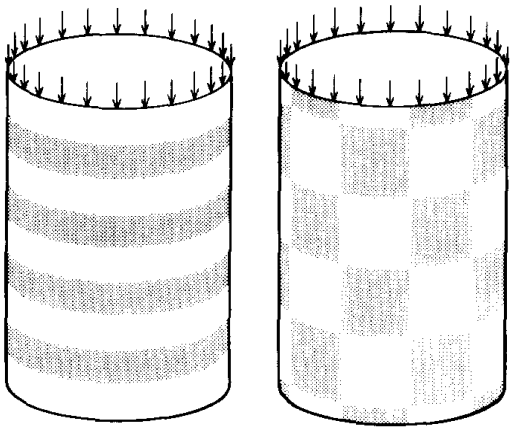

(a) (b)

Figure 7.22: (a) Axisymmetric mode (b) Square mode with matching wavelengths

7.4 Conclusion

The impact of curvature is studied in this chapter. First the cylinder's initial curvature is varied to create multiple hyperbolic and elliptical geometries (37 in total, each with a different curvature). The buckling shapes are calculated for each of the geometries. From the resulting shapes, they are categorized into three curvature groups. The positive group is defined by a governing axisymmetric buckling mode. The negative group is defined by the on set of clear two directional buckles (chessboard). The curvature range in the middle is grouped as near-zero. The remainder of this chapter makes significant use of the above categorization.

From the results of LBA, the critical load factor is plotted against curvature. A clear change in slope at zero curvature is observed in Figure 7.3a. Next GNLA is performed on each of the different geometries. The ultimate capacity is calculated and shown in Figure 7.4a. There exists a clear discontinuity at zero curvature, showing that the transition is an important indication to structural behaviour. When zoomed into the near-zero range (Figure 7.4b), it is noted that this discontinuity does not occur exactly at zero curvature but rather at the transition between near-zero to positive curvature (ie. when axisymmetric mode starts to emerge). The emergence of the axisymmetric mode also results in the largest reduction in capacity as shown in Figure 7.5a.

The behaviour of knock-down factor in the positive curvature range can be accurately predicted from the curvature value alone with a parabolic function. Similarly in the negative curvature range, the prediction can be made with an exponential decay function, albeit with less accuracy. The results in the near-zero range is ambiguous and its the author's recommendation that the function for the positive range be used as well.

After identifying the correlation between curvature and knock-down factor, the relationship between the spacing of eigenvalues and knock-down factor is investigated. By finding the percentage difference in eigenvalue between the 20th and the first mode, equations are proposed that relate the percentage difference and the knock-down factor in both the positive and the near-zero curvature range. The relationship is more complex in the negative curvature range.

Seeing the significant of the transition between near-zero and positive curvature, two more geometries are introduced to extract a non-governing axisymmetric buckling mode (i.e. like what was discovered in Chapter 6). Such is found with $k_{zz}/k_{xx} = 0.003125$. This shows that the axisymmetric mode moves forward as the curvature becomes positive.

Second part of this chapter is devoted to inspecting the change in Gaussian curvature as load increases. Again, geometries are picked from each of the three curvature groups and inspected in detail. In general, buckling can be visualized with the change in Gaussian curvature. As total Gaussian curvature may be dominated by the initial shape, the minute yet significant change may not be readily observable, however the incremental change, when magnified, can predict the onset of drastic change. These changes occur in discrete steps, and not continuously as expected. These discrete steps usually predict the onset of a dramatic change in geometry such as buckling. For the most critical case (with axisymmetric mode as the imperfection), buckling can be predicted by rapid change (spikes) in Gaussian curvature. In that case, buckles in the tangential direction develops in between adjacent rings of buckles in the vertical direction.

Chapter 8

Physical non-linear behaviours

8.1 Introduction

To present a more complete picture on the buckling behaviour of thin shells, physical non-linearities are integrated to the FEA models from the onset of analyses. For the metallic shells, a multi-linear stress strain curve is introduced to represent the elastic and plastic behaviour of steel. The analysis is performed on a number of structures of different curvature from Chapter 7. For the concrete shells, a different type of element (solid element with reinforcement and cracking model) is used to construct the model. This is done on the hyperbolic cooling tower.

This chapter belongs to Part I of the thesis as integrating non-linear material behaviour can be easily done in ANSYS without any scripting, and should be done by structural designers. The procedure is described in detail below. The reason for its placement at the end of Part II is that the author intends to compare the change in Gaussian curvature between an elastic model and an elastic-plastic one.

8.2 Plasticity

This chapter starts by describing the proposed material model, and how ANSYS handles non-linear material behaviour. Then this material model is integrated into the analyses of two structures. For ease of comparison, 2 of the selected geometries in Chapter 7 are reused, their k_{zz}/k_{xx} ratios are -0.05, and $+0.005$ respectively. All aspects of the model and of the analysis procedure remain identical except the introduction of the Multi-linear stress-strain model.

ANSYS provides a large library of plasticity options, out of which the Multilinear Isotropic Hardening (MISO) option is utilized[1]. The stress-strain relationship is defined by 70 line segments starting from $(0, 0)$, the coordinates are listed in Appendix C. The stress-strain curve implemented follows the typical steel behaviour, including the linear elastic portion, the yield plateau and strain hardening. Non-linear Isotropic Hardening may also be used to simplify the relationship.

8.2.1 Stresses

To adequately understand the influence of plasticity, it is worth while to discuss how plastic behaviour is represented in ANSYS. ANSYS conveniently calculates the 3 principal stresses as

[1] Kinematic Hardening should be used should the loading be cyclic

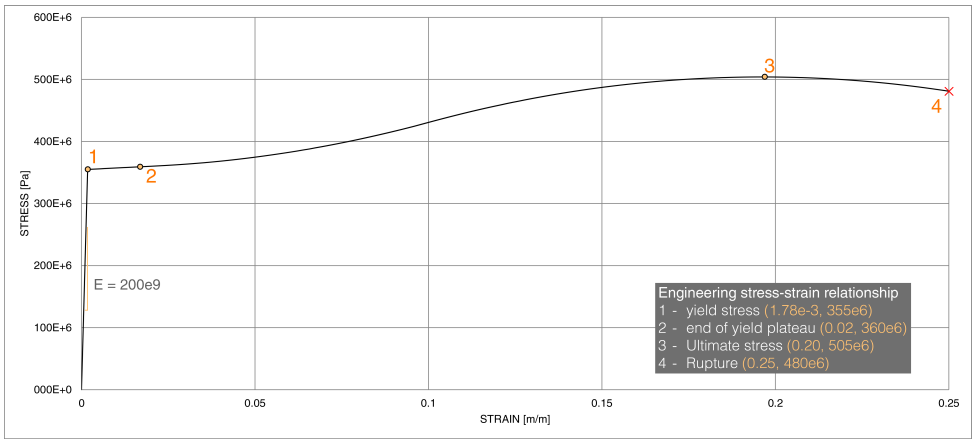

Figure 8.1: Typical stress strain curve for mild steel

well as an equivalent (Von Mises) stress at each corner node. These nodes in actuality represent the four integration nodes of each element. The principal stresses σ_o are calculated as follows,

$$0 = \begin{vmatrix} \sigma_x - \sigma_o & \sigma_{xy} & \sigma_{xz} \\ \sigma_{xy} & \sigma_y - \sigma_o & \sigma_{yz} \\ \sigma_{xz} & \sigma_{yz} & \sigma_z - \sigma_o \end{vmatrix}$$

The equivalent stress is calculated from the principal stresses,

$$\sigma_e = \sqrt{\frac{1}{2}[(\sigma_1 - \sigma_2)^2 + (\sigma_1 - \sigma_3)^2 + (\sigma_2 - \sigma_3)^2]} \tag{8.1}$$

This σ_e can be used to calculate the elastic strain ϵ_e through

$$\sigma_e = E\epsilon_e \tag{8.2}$$

8.2.2 Strains

The principal strains can be calculated in a similar manner,

$$0 = \begin{vmatrix} \epsilon_x - \epsilon_o & \frac{1}{2}\epsilon_{xy} & \frac{1}{2}\epsilon_{xz} \\ \frac{1}{2}\epsilon_{xy} & \epsilon_y - \epsilon_o & \frac{1}{2}\epsilon_{yz} \\ \frac{1}{2}\epsilon_{xz} & \frac{1}{2}\epsilon_{yz} & \epsilon_z - \epsilon_o \end{vmatrix}$$

ANSYS defines the equivalent strain as follows,

$$\epsilon^e = \frac{1}{1+\nu'}\left\{\frac{1}{2}[(\epsilon_1 - \epsilon_2)^2 + (\epsilon_1 - \epsilon_3)^2 + (\epsilon_2 - \epsilon_3)^2]\right\}^{\frac{1}{2}} \tag{8.3}$$

The elastic strain is defined as follows,

$$\epsilon^{\text{el}} = \epsilon - \epsilon^{\text{th}} - \epsilon^{\text{pl}} - \epsilon^{\text{cr}} - \epsilon^{\text{sw}} \tag{8.4}$$

In the case of metal yielding, thermal $^{\text{th}}$, creep $^{\text{cr}}$, and swelling $^{\text{sw}}$ strain vectors are zero. Therefore the total strain is defined as,

$$\epsilon^{\text{tot}} = \epsilon^{\text{el}} + \epsilon^{\text{pl}} \tag{8.5}$$

8.2.3 Yielding and buckling

It is often unclear whether yielding or buckling happens first. This issue is further complicated by the fact that yielding almost always happens immediately after buckling. Using the classical buckling equation for axially loaded cylinders, one could construct a simple stress verses slenderness relation where,

$$\sigma = \begin{cases} f_y & \text{if } \frac{0.605Eh}{a} \geq f_y; \\ \frac{0.605Eh}{a} & \text{otherwise.} \end{cases} \tag{8.6}$$

and,

$$f_y = 355\,\text{MPa} \tag{8.7}$$

This relationship is plotted in figure 8.2. From the plot, it can be assumed that buckling occurs prior to yielding for $a/h = 500$. However, it is also clear from chapter 4 that the critical buckling load equation (8.6) does not reflect the ultimate load capacity of a cylinder, the real curve would be somewhere lower than the buckling curve.

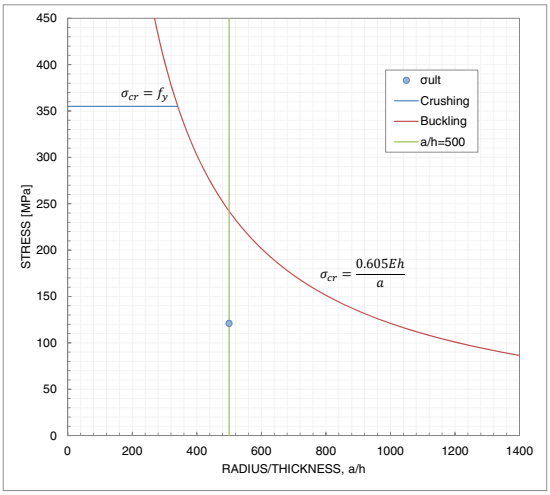

Figure 8.2: Yield and buckling curves

8.2.4 Application to metallic hyperboloid

The first structure detailed here is a hyperboloid with a curvature ratio of $k_{zz}/k_{xx} = -0.05$. The analysis procedure remains identical to that in chapter 7 with the exception of material properties. LEA and LBA are performed on the model, and the resulting load factors remain identical to those from chapter 7. This shows that material non-linearity does not influence linear analyses. The first buckling mode is imposed as the imperfection with a maximum amplitude of $t/2$. Finally a step wise displacement controlled non-linear analysis is performed. The step size is set to be $u_z = 0.001\,\text{m}$.

Structural behaviour is categorized in Figure 8.3. With the first diagram, the stress-strain, and reaction force-strain relationships are plotted for the node with the largest combined displacement. The onset of plasticity is defined as the start of non-zero plastic strain, ϵ^{pl}. The stress strain plot shows that the behaviour remains linear until $f_y = 355 \times 10^6\,\text{Pa}$ at which point yielding occurs. Structural collapse occurs at a strain of approximately $\epsilon \sim 0.014$. Together with Figure 8.3b, it is evident that buckling occurs prior to yielding; buckling occurs at $\epsilon \sim 3.47 \times 10^{-4}$ where as yielding is at $\epsilon \sim 1.77 \times 10^{-3}$.

With compared with the behaviour of the linear model (the orange curve in Fig. 8.3a), it is observed that the material non-linearity eliminated any post-buckling capacity, thereby making

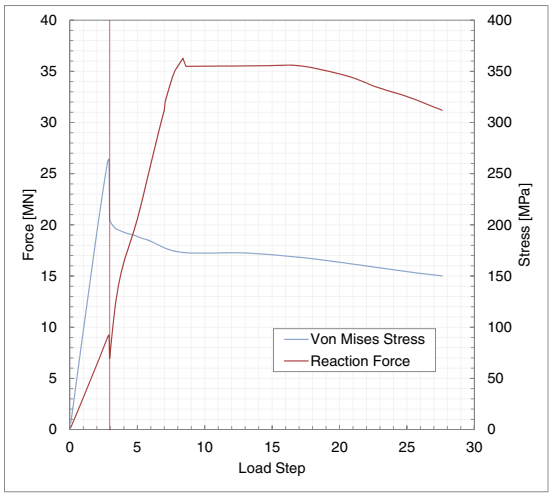

(a) Elastic and post yielding forces and stresses

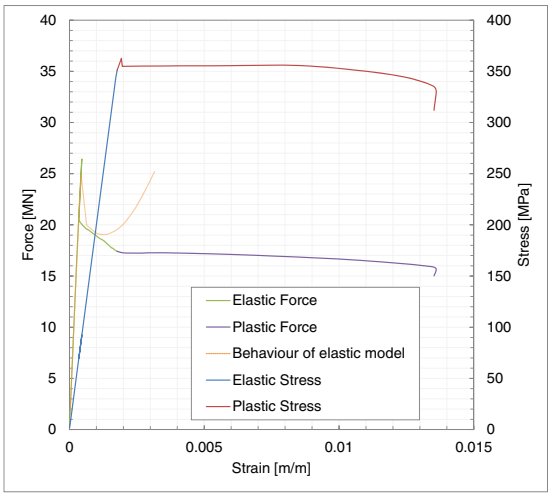

(b) Forces and stresses vs load step

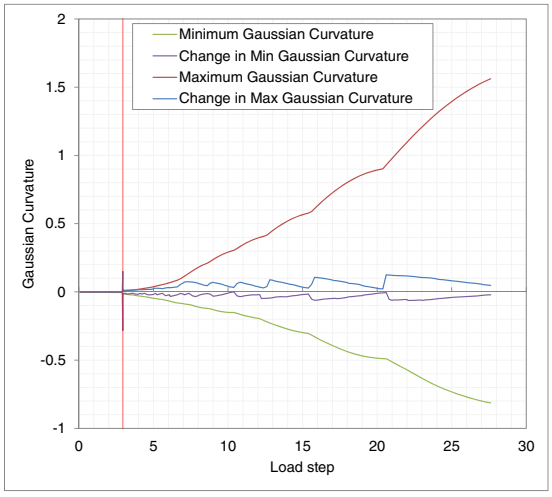

(c) K and ΔK vs load step

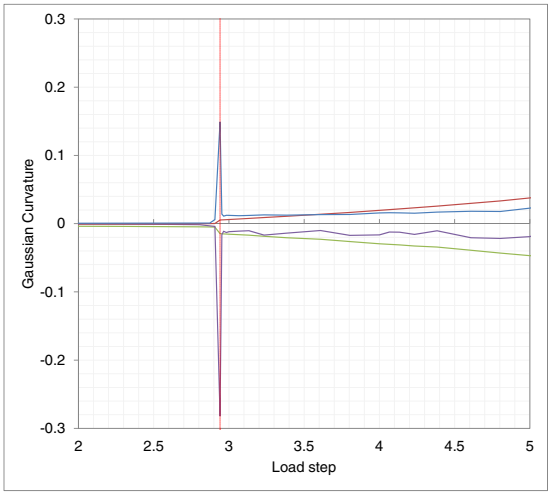

(d) K and ΔK at critical points

Figure 8.3: PGNLA response of $^{k_{zz}}/_{k_{xx}} = -0.05$

this structure imperfection sensitive. This shows that while adding plasticity does not change the buckling behaviour of the structure, it does have a large influence on the post-buckling behaviour. The difference in post-buckling behaviour within the elastic range is caused by the change in the size of sub-steps during loading (the sizes are automatically determined).

Looking at the two lower plots (Fig. 8.3c, 8.3d), the onset of buckling is represented by a spike in ΔK, after which the buckles deepen at discrete intervals. Figure 8.4 visually illustrates the behaviour of the hyperboloid under displacement load.

8.2.5 Application to metallic truncated ellipsoid (barrel)

The next structure detailed here is a barrel with a curvature ratio of $^{k_{zz}}/_{k_{xx}} = +0.005$. As discussed in length in Chapter 7, this geometry resulted in the largest reduction in capacity. Again, the procedure remains identical to that in chapter 7.

Structural behaviour is categorized in Figure 8.5. With the first diagram, the stress-strain, and reaction force-strain relationships are plotted for the node with the largest displacement. The onset of plasticity is defined as the start of non-zero plastic strain, ϵ^{pl}. In figure 8.5b, the stress-strain behaviour remains linear until $f_y = 355 \times 10^6\,\text{Pa}$ at which point yielding occurs.

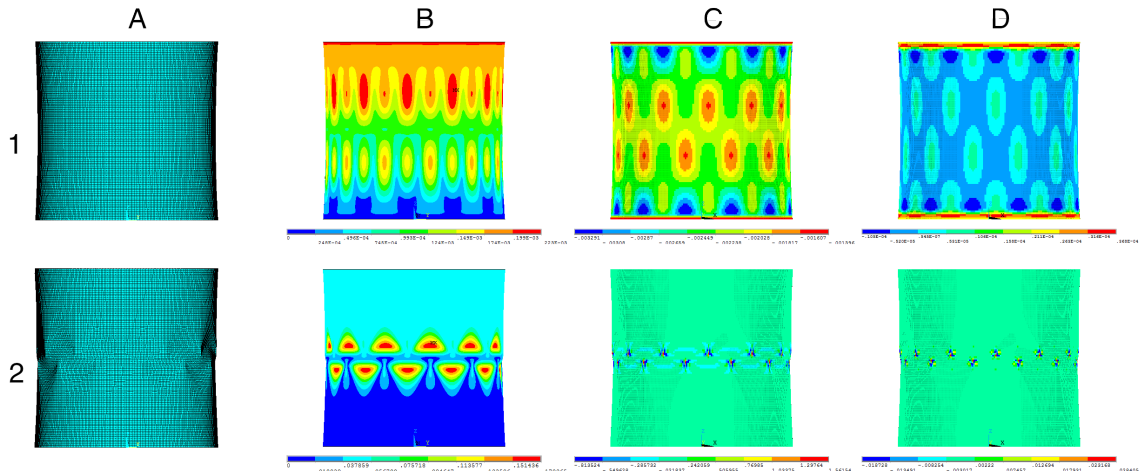

Figure 8.4: Initial (R1) and final state of structure (A), displacement (B), K (C) and ΔK (D)

However from figure 8.5a it becomes evident that stress follows a tri-linear behaviour (blue then red curve), and the first slope changes just prior to ultimate capacity (green curve). This change is preceded slightly by an acceleration in Gaussian curvature growth at around $t \sim 4.5$ (see the green curve in Figure 8.5c). The onset of this growth is caused by the development of asymmetric buckles. Soon after, the ultimate capacity is reached at $t \sim 5.6$ while stress is still in the elastic range, $\epsilon \sim 1.57 \times 10^{-3}$.

8.2.6 Conclusion

Two conclusions can be drawn from this limited study into metallic material non-linearity. In both models, the onset of buckling occurs in the elastic stress range. Therefore, metallic material non-linearity does not have an effect in the calculation of the ultimate buckling capacity. For structures that exhibit significant post-buckling capacity (e.g. the hyperboloid) with a linear material, the introduction of non-linearity eliminates the post-buckling capacity as yielding develops in the buckles, leading to softening and collapse. By including this non-linearity, much more post-buckling behaviour can be calculated as divergence occurs at a much larger displacement (or not at all). In that sense, it is important to include the material non-linearity as a part of a FEM model.

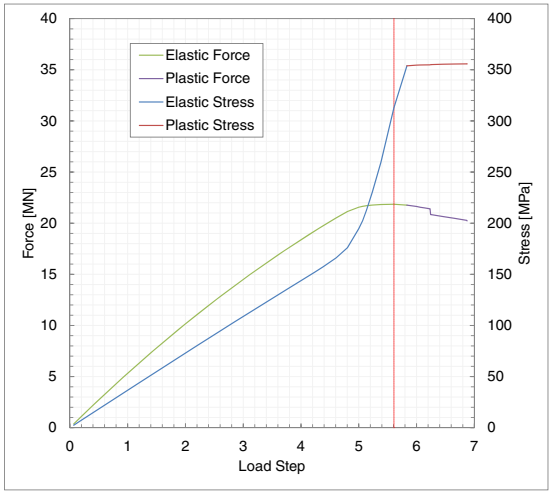

(a) Elastic and post yielding forces and stresses

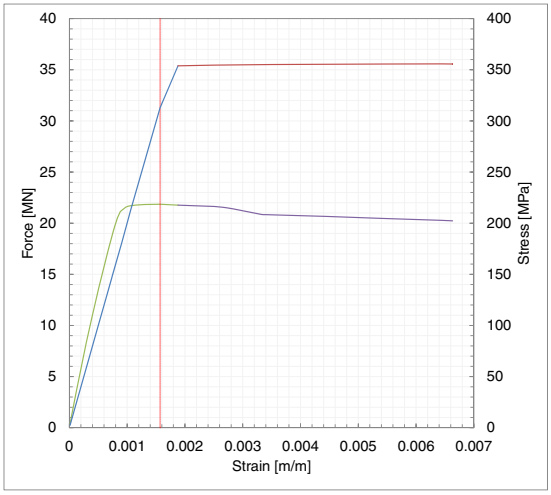

(b) Forces and stresses vs load step

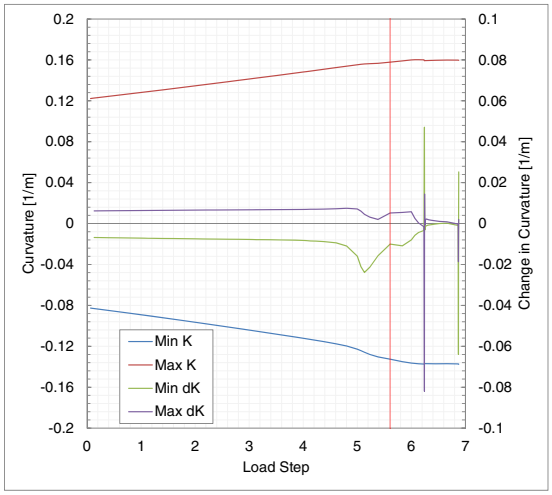

(c) K and ΔK vs load step

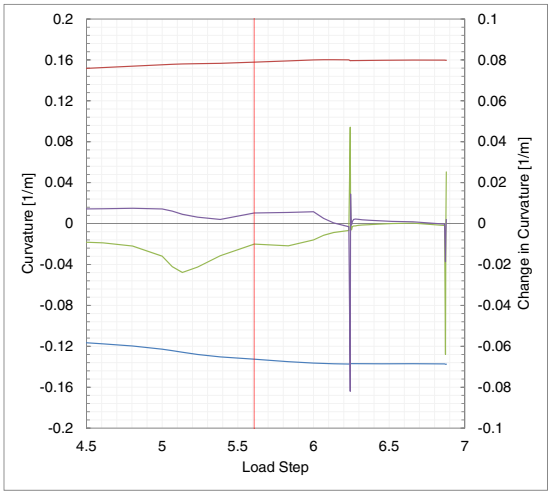

(d) K and ΔK at critical points

Figure 8.5: PGNLA response of $^{k_{zz}}/_{k_{xx}} = +0.005$

8.3 Cracking

To simulate cracking, a reinforced concrete model of the hyperboloid is generated. Instead of using quadratic 2-D elements, linear 3-D elements are used with discrete embedded reinforcement. ANSYS features both a specialized cracking concrete element (SOLID65), and also general brick elements (SOLID185 - 8 nodes, SOLID186 - 20 nodes). Since ANSYS plans to deprecate SOLID65 and dissociate base element formulation from reinforcement element, the 8 node SOLID185 element is used at first.

ANSYS provides several non-linear material models suitable for concrete, Extended Drucker-Prager (EDP) and Microplane being the two current-technology options. EDP includes three yield criteria and corresponding flow potentials to account for the material's internal cohesion and friction. It can be combined with hardening rules (both isotropic and kinematic) to account for yielding behaviour.

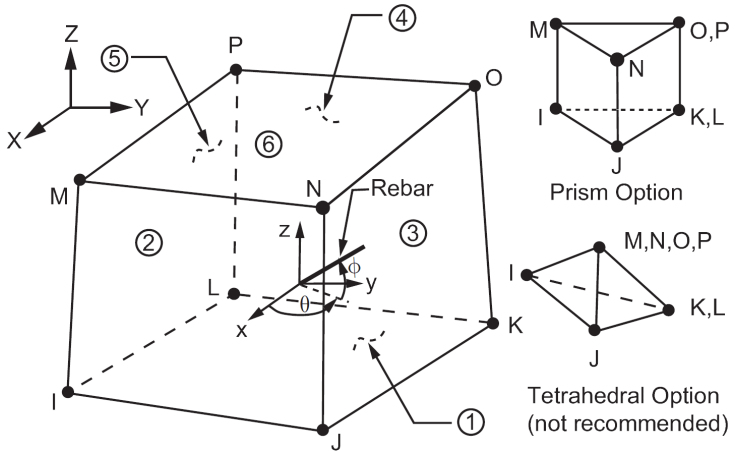

Figure 8.6: ANSYS SOLID65 3-D Reinforced Concrete Solid

However, after initial trials, the author encountered difficulty in inputting the correct parameters for either of the two material models. SOLID65 is used instead, with the associated CONCRETE material model. The parameters of this material model are listed in table 8.1.

Constant	Value	Meaning
1	0.3	Shear transfer coefficients for an open crack.
2	1.0	Shear transfer coefficients for a closed crack.
3	3 MPa	Uniaxial tensile cracking stress.
4	25 MPa	Uniaxial crushing stress.
5	N/A	Biaxial crushing stress .
6	N/A	Ambient hydrostatic stress state for use with constants 7 and 8.
7	N/A	Biaxial crushing stress under ambient hydrostatic stress state.
8	N/A	Uniaxial crushing stress under ambient hydrostatic stress state.
9	N/A	Stiffness multiplier for cracked tensile condition.

Table 8.1: Concrete Material Data

An advantage of SOLID185 is that ANSYS provides the option to automatically impose arbitrary number of discreet reinforcement elements (at any angle) within each base element. The initial model is constructed with one reinforcement bar (REINF194) in each element's three local axes.

Since the results through the thickness direction is of no consequence considering the slenderness ratio, only two layer of solids are used. For SOLID65, the reinforcement must be embedded

manually. This is not a difficult issue in this case as the base model is regularly defined. Reinforcement bars are simulated using linear Timoshenko beam elements, and are placed at the intersection of each brick element. The area of reinforcement is calculated per element. Assuming there is one rebar per element surface, the area of those surfaces are as follows,

$$A_x = l_{\text{elem}} \cdot t = 0.095\,\text{m}^2; A_z = w_{\text{elem}} \cdot t = 0.095\,\text{m}^2 \tag{8.8}$$

Where the subscripts denote the surface normal. LEA calculates the component stresses at each Gauss point, and the area of reinforcement is sized based on these values. It is apparent that under self-weight the only tensile stress is the hoop stress at the top of the hyperboloid.

$$\sigma_x = 0.110\,\text{MPa}; \lambda_{\text{cr}} = 15.373; \sigma_{\text{cr}} = \lambda_{\text{cr}}\sigma_x = 1.715\,\text{MPa} \tag{8.9}$$

Therefore the total force per element surface is,

$$F_x = \sigma_{\text{cr}} \cdot A_x = 163\,\text{kN} \tag{8.10}$$

Assuming the reinforcement has a strength of $f_{\text{rebar}} = 510\,\text{MPa}$, the cross sectional area can be calculated as follows,

$$A_{\text{rebar}} = {}^{F_x}/_{f_{\text{rebar}}} = 320\,\text{mm}^2 \tag{8.11}$$

Therefore one $\phi 20$ bar is used. The reinforcing elements in the z direction cannot be calculated as the stress is always negative, the minimum reinforcement of one $\phi 10$ bar is assumed. The reinforcing elements in the radial (thickness) direction is not effective in this case. Should cross sectional information be necessary and there are more elements through the thickness, then these reinforcing elements can represent the stirrups.

The analysis set-up remains identical to those in other chapters of this thesis. LEA and LBA are performed on the model, and the resulting load factors remain similar to those from chapter 5. The difference in weight is attributed to the added reinforcement. The buckling modes remain identical in shape; the first mode is imposed as the imperfection.

From PGNLA, it is observed that with the concrete material model, cracking drastically reduces the buckling capacity of the hyperboloid (Fig. 8.7). The knock-down factor is reduced from $C = 0.76$ to 0.092. This extreme reduction suggests that with sufficient cracking, the strength of the composite material is much less than that of linear concrete.

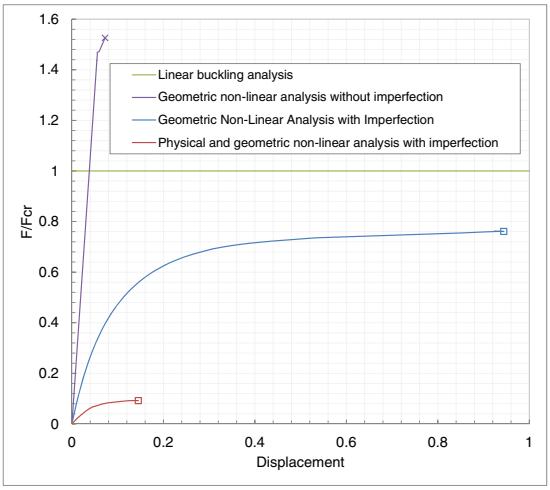

Figure 8.7: Comparison of different non-linearities

By looking at the crack development in detail (Fig 8.8), it is evident that vertical cracks occur at the outward buckles of the initial imperfection shape. This suggests that as the outward

buckle extends in magnitude, the hoop tension causes cracking. At the moment of divergence, the maximum tensile stress in concrete is 3 MPa. The Von Mises stress in the reinforcement is 192 MPa. This further shows that buckling of metallic structures is elastic, and that metal plasticity model is not necessary if the item of interest is the ultimate capacity.

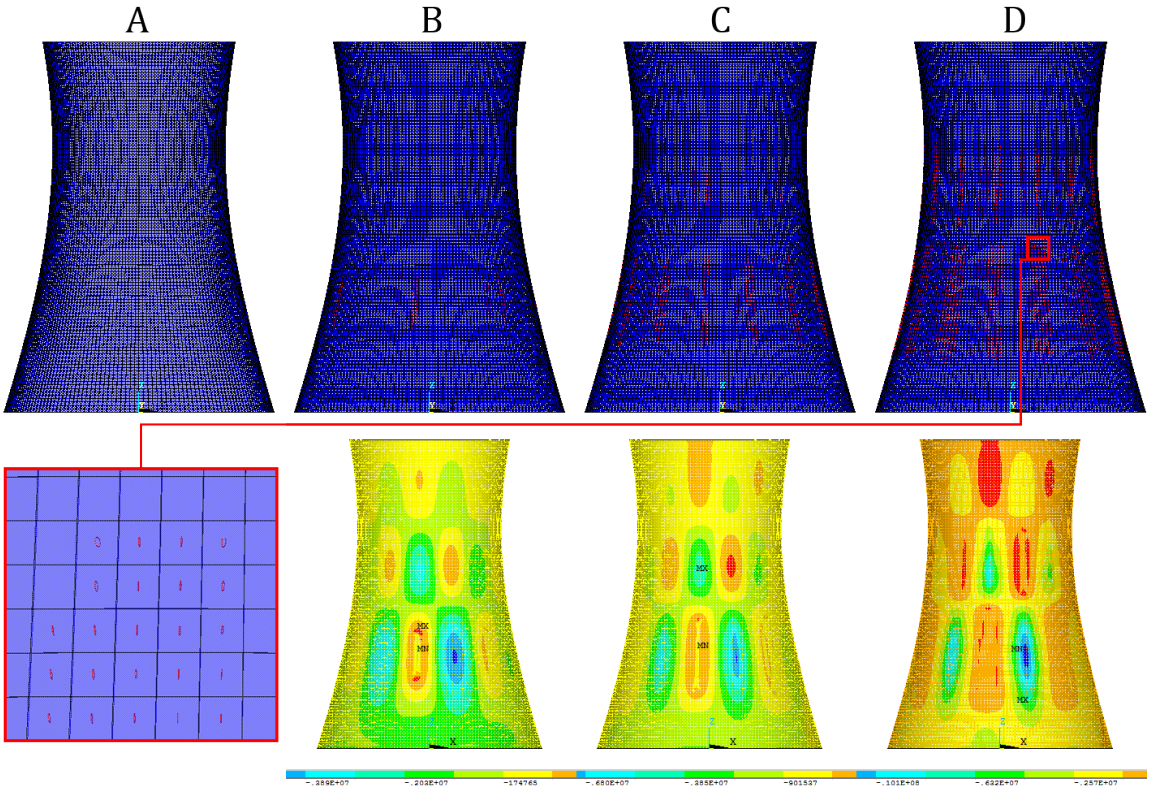

Figure 8.8: Development of cracks, and tangential stress

The crack pattern is very different from the same model without the initial imperfection (Fig 8.9). As both the load and the geometry are axisymmetric, no cracking develops until the top ring develops sufficient hoop tension.

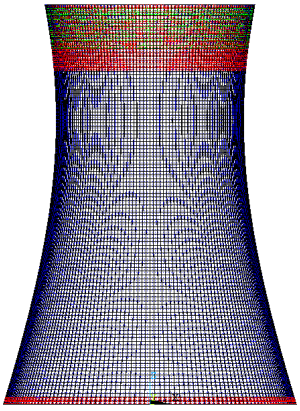

Figure 8.9: Crack pattern of GNLA of the perfect model

Chapter 9

To Infinity... and Beyond

9.1 Part I

9.1.1 Procedure to analyse thin shell structures

This thesis introduces a design procedure for analysing thin-shell structures using commercial finite element method packages. The step-wise procedure is detailed in Chapter 1. The first step is to construct the FEM model and apply the loads and boundary conditions. Linear buckling analysis (LBA) is run to obtain the buckling load factors, λ_{cr}, and the buckling shapes of the structure. Depending on the spacing of these factors, the structure's imperfection sensitivity can be roughly estimated. For a regularly sensitive structure, the first buckling mode is imposed as the geometrical imperfection shape, with the maximum amplitude equalling to that of the construction tolerance (in this thesis, the amplitude is usually set to half of the thickness). A geometrical and physical non linear analysis is then performed on the imperfect geometry to obtain a realistic ultimate capacity of the structure.

9.1.2 Verification of procedure against theoretical and experimental results

Part I of this thesis serves to demonstrate the validity, robustness and effectiveness of the proposed procedure. To that end, the procedure is applied to the well-studied problem of axially compressed cylinder. The results are compared to experimental findings and to Koiter's theoretical work. By varying the slenderness ratio, a/h, of the cylinder while keeping the imperfection shape (i.e. first buckling mode) and amplitude (i.e. $t/2$) constant, ANSYS is able to produce buckling stresses that are within one standard deviation of the mean experimental values up to $a/h = 2500$, beyond which the experiments resulted in lower buckling stress than ANSYS. One can conclude two points from this, one is that ANSYS can reliably simulate buckling behaviour of thin shells, and two, the imperfection shape and amplitude used in these analyses is an adequate representation of real imperfection.

The comparison is made between FEM results and Koiter's asymptotic equation by varying $\bar{\delta}/t$ from 0 (i.e. a perfect cylinder) to 1 (i.e. the amplitude of imperfection equals to its thickness). It is shown that by using the first mode as imperfection, the FEM results match Koiter's equation (with $b = -1$) up to and including $\bar{\delta}/t = 0.6$, beyond which FEM results over estimates the capacity. It can be concluded that with single mode as imperfection, FEM can reproduce theoretical findings by Koiter for small amplitude imperfection.

- General purpose FEM packages can simulate experimental set up and obtain realistic results

- FEM result corroborates with Koiter's asymmetric equation
- The first mode with a maximum amplitude of $t/2$ can be expected in real cylinders

9.1.3 Four case studies

The proposed procedure is then applied to 4 existing structures with realistic load conditions in Chapter 5. The standard design procedure is followed, including a mesh refinement study for each structure. In the geometric non-linear analysis, the load is incremented until buckling occurs. The knock-down factor (Eq. (9.1)) of the various structures and load conditions are summarized in table 9.1.

$$C = \frac{\lambda_{\text{ult}}}{\lambda_{\text{cr}}} \tag{9.1}$$

Structure	Load case	Load factor			Knock-down factor	
		LBA	GNLA	w/ imp	GNLA	w/ imp
Cooling Tower	Self weight	15.73	23.15	11.98	1.472	0.761
	Wind	6.60	7.33	5.54	1.110	0.838
	Self weight + wind	5.76	8.10	6.10	1.406	1.059
Monolithic dome	Wind	22.39	21.20	8.29	0.947	0.370
	Uniform pressure	15.77	15.12	13.75	0.959	0.872
Grain silo	Wind on empty silo	22.53	22.70	17.20	1.007	0.763
	Wind + calm water	22.89	22.50	17.40	0.983	0.760
	Wind + sloshing water	23.31	22.60	17.30	0.970	0.742
Fuselage	Axial compression	3.96	4.95	4.01	1.251	1.012

Table 9.1: Summary of results from the four case studies

From the summary table, several important conclusions can be made,

- GNLA analysis without imperfection can result in un-realistic results, this error is more pronounce in axisymmetric structure with axisymmetric loads
- with imperfection, GNLA results do not exceed LBA results (significantly) even for structures that are not sensitive to imperfection, making GNLA with imperfection universally applicable
- Dome structures experience the largest reduction in capacity of the bunch due to imperfections

9.2 Part II

9.2.1 Imperfection shapes

Part II of this thesis focuses on structures with extreme imperfection sensitivity, and the categorization of such structures. A method for extracting the knock-down factor of extreme imperfection sensitive structures is proposed. The method suggests 4 different categories of imperfection shapes that may be imposed on to the structure. These categories are modal shapes, combinations of modal shapes, random, and superimposed-wave.

A modified knock-down factor C_{m} is proposed to replace the traditional factor when performing an imperfection sensitivity analysis. This new factor is the quotient of the shell true ultimate load and the shell ultimate load that follows from a geometrical non-linear analysis including the first buckling mode imperfection, $\lambda_{\mathrm{ult}}^{1^{\mathrm{st}}\mathrm{Mode}}$. The true ultimate load can be computed by a full non-linear analyses including any imperfection shapes (including the ones mentioned above).

These imperfection shapes are imposed on to the axially loaded cylinder, a classic example of extreme imperfection sensitivity, and on to the cooling tower. It is found that imperfection in the axisymmetric shape with additional Gaussian noise governs with $C_{\mathrm{m}} = 0.68$.

"Random" imperfection does not result in significant reduction in capacity ($C_{\mathrm{m}} > 1$). "Combinations" of modal shapes show that the combination between an axisymmetric mode with a non-axisymmetric one ($[m, n] \in R$) produce a lower reduction factor than combinations between two axisymmetric modes (see Fig. 6.5b).

The cooling tower, being marginally imperfection sensitive, is governed in capacity by imperfection in the shape of the first buckling mode ($C_{\mathrm{m}} > 1$). This further strengthens the procedure proposed in Part I where only the first mode is needed for analysis.

Initial imperfection in loading is also simulated but found to be ineffective as the initial asymmetry is absorbed soon after the load becomes uniform (see Fig. 6.19). Imperfection imposed not as changes in nodal coordinates, but as in initial stresses, strains and boundary conditions are also simulated but found to be similarly ineffective.

9.2.2 Influence of curvature

The significant difference in reduction between the cylindrical and the hyperbolic shape is studied further in Chapter 7 where 37 different geometries of varying curvatures ranging from a barrel to a hyperboloid ($-1 \leq {}^{k_{zz}}/_{k_{xx}} \leq 1$) are generated and analysed. With imperfection in the shape of the first mode, and maximum amplitude set to ${}^{t}/_{2}$, the procedure proposed above is used on each model.

From linear buckling analyses, it is evident that the models can be categorized into three groups based on their initial curvature, ${}^{k_{zz}}/_{k_{xx}}$ and the shape of the first mode (Fig. 7.2).

The resulting knock-down factor also show three distinct patterns of behaviour, in the positive curvature group, the imperfection sensitivity decreases parabolically from $C = 0.289$ with a near-cylindrical geometry (${}^{k_{zz}}/_{k_{xx}} = 0.005$) to 0.605 with a barrel (${}^{k_{zz}}/_{k_{xx}} = 1$). The correlation between the curvature and the knock-down factor is detailed in equation (7.8). $C = 0.289$ also represents the largest knock-down factor of the entire study. This knock-down factor is induced by an axisymmetric imperfection shape, this corroborate with the findings of chapter 6.

The discontinuity in knock-down factor, C, around the zero curvature geometry preludes simple correlations to be constructed, though all Cs in this group are higher than $C = 0.289$, therefore equation (7.8) applies in the near-zero curvature range as well.

In the negative curvature group, the reduction sharply decreases and forms festoons that approaches 1 beyond ${}^{k_{zz}}/_{k_{xx}} \leq -0.2$, meaning that the geometries become insensitive to imperfections. The knock-down factor of negative curvature geometries can also be predicted using Eq. (7.11). Furthermore, post-buckling capacity is observed, making the hyperboloid a class I geometry.

Upon observing the effect of the axisymmetric imperfection, it is imposed on to both the cylinder and a hyperboloid ${}^{k_{zz}}/_{k_{xx}} = -0.05$, and the results can be observed in figure 7.7. It is shown that the axisymmetric imperfection results in a larger reduction than the shapes' 1^{st}buckling mode (for the cylinder, $C = 0.297$, and for the hyperboloid $C = 0.373$). It can be concluded that the design of near-zero curvature geometries (cylindrical shapes) should adopt an axisymmetric imperfection shape.

- Axisymmetric imperfection shape results in the largest knock-down factor for near-cylindrical structures, irrespective the linear buckling behaviour
- The knock-down factor of positive, zero and negative curvature geometries can be calculated from the initial curvature alone
- Negative curvature geometries are less sensitive to imperfection, and becomes insensitive with sufficient curvature

9.2.3 Gaussian curvature

Both cumulative and incremental changes in Gaussian curvature (K and ΔK) are calculated so that the onset of buckling can be observed. K is calculated as the ratio of the determinants of the second and first fundamental forms. In a very negatively curved geometry where initial imperfection covers the entire surface in grid pattern, it can be seen that K follows a multi-linear increase (Fig 7.18b), and points of slope change indicate dramatic changes in the surface, i.e. the formation of buckles. As load increases, the initial imperfection buckles increase in magnitude until the buckles shift and localize to the boundary edges. The shift corresponds to a slope change in Gaussian curvature, and to the start of non-linearity in the load-displacement curve (Fig 7.18).

In the most critical geometry in the positive curvature range (where axisymmetric mode governs), the change in Gaussian curvature remains constant in both positive and negative extremes (the axisymmetric shape becomes more compressed and both convex and concave buckles become more defined as load increases), until asymmetric buckles occur. The point of occurrence can be observed in ΔK as a band of sharp curvature change, and in the end of the linear portion of the load displacement curve (Fig. 7.21). After this point, asymmetric buckles spread through the meridian of the surface. This suggests that the extreme imperfection sensitive nature of cylinders is indeed caused by modal interaction as Koiter suggested, where an axisymmetric mode changes to an asymmetric one at the moment of bifurcation.

- Axisymmetric imperfection shape leads to secondary buckling in the circumferential direction as predicted by Koiter's modal interaction theory
- Incremental change in Gaussian curvature is an accurate indicator of buckling behaviour, though a fine mesh is needed to accurately calculate the numerical values

9.2.4 Physical non-linearities

It has been the assumption that the buckling phenomena above occur within the elastic range. To test the validity of this assumption, a yield model is introduce to the cylindrical imperfect FEM model used in chapter 7. From the result shown in figure 8.3b, it is clear that buckling indeed occur within elastic stress range, $\sigma_{\text{vm}} \approx 250 \times 10^6$ Pa. However, the yield material model eliminates the post-buckling capacity exhibited by the elastic model. With the yield model, the post-buckling behaviour becomes more stable and converges for a larger strain range than with the elastic model.

A concrete cracking model is applied to the imperfect cooling tower FEM geometry, and the result is shown in figure 8.7. From chapter 5, it was found that the knock-down factor without physical non-linearity is $C_{\text{elas}} = 0.76$. This is more than eight times higher than the factor with physical non-linearity, $C_{\text{conc}} = 0.092$. The circumferential cracks occur at the locations of initial imperfection buckle waves. These cracks are entirely absent if the geometry is perfect.

- Elasto-plastic model for metallic structures does not change the ultimate capacity, but does reduce the post-buckling capacity
- Cracking model must be applied for thin concrete shells as the resulting capacity reduces drastically (in combination with initial imperfection)

9.3 Future work

As with all research endeavours, questions are just as frequently generated as answers. This thesis is no exception, several important yet unanswered questions deserve more detailed investigation.

9.3.1 Modal interaction

This thesis has shown that modal interaction does occur in the case of an axisymmetric imperfection transforming into an asymmetric one. Given that this produced the largest reduction in capacity, it would be beneficial to procedure modal interaction in other structures with other imperfection shapes. The dome geometry under external pressure would be an ideal candidate.

9.3.2 Case study on complex doubly curved structures

As the name suggests, structures that are significantly more complex than the ones studied in this thesis may be used as base structures for the proposed procedure. It would be especially interesting to study the imperfection sensitivity of doubly curved structures such as the Rolex Learning Center, and relating its curvature to the buckling capacity.

9.3.3 Post-buckling behaviour

As the reader may have noticed, this thesis focused almost exclusively on the pre-buckling and the buckling behaviour of shells. Koiter himself stated that his post-buckling theory only works in the immediate vicinity of buckling. With ever more robust solving methods such as Ritz method or slow dynamic analysis, it would be interesting to obtain a more complete picture of buckling.

9.3.4 Change in Gaussian curvature

On a more fundamental level, it would be useful to relate the incremental change in Gaussian curvature to the stress state at the element level.

9.3.5 Eigenvalue spacing

It has already been shown that the change in eigenvalue can be correlated to the ultimate capacity of an imperfection sensitive structure (e.g. an axially loaded cylinder). This correlation is done on a numerical level, it would be interesting to formulate a theory that shows this relationship from first principles.

Bibliography

[1] Design Criteria for Tornado and Hurricane Safe Rooms. Technical report, Federal Emergency Management Agency, 2008.

[2] Abaqus Documentation 6.13. Technical report, Dassault Systèmes, Providence, Rhode Island, 2013.

[3] stainless steel liquid tanks. Technical report, Meridian Manufacturing, Inc., Storm Lake, Iowa, 2013.

[4] Sohrabuddin Ahmad, Bruce M. Irons, and O.C. Zienkiewicz. Analysis of thick and thin shell structures by curved finite elements. *International Journal for Numerical Methods in Engineering*, 2(October 1969):419–451, 1970.

[5] AM El Ansary, AA El Damatty, and AO Nassef. Optimum Shape and Design of Cooling Towers. *waset.org*, 9:4–13, 2011.

[6] ANSYS Inc. Command Reference for the Mechanical APDL. In *ANSYS Manual*, volume 15317, pages 1–1920. Canonsburg, PA, 12.0 edition, 2009.

[7] ANSYS Inc. Theory Reference for the Mechanical APDL and Mechanical Applications. In Peter Kohnke, editor, *ANSYS Manual*, volume 3304, pages 32–38, 877–879. Canonsburg, PA, 12.1 edition, 2009.

[8] ANSYS Inc. Structural Mechanics. *ANSYS Manual*, pages 5–12, 2011.

[9] ANSYS Inc. ANSYS Mechanical APDL Element Reference. In *ANSYS Manual*, volume 15317, pages 1377–1390. canonsburg, PA, 14.5 edition, 2012.

[10] J. Arbocz. Past, present and future of shell stability analysis. Technical report, Department of Aerospace Engineering, Delft University of Technology, Delft, 1981.

[11] J. Arbocz and H. Abramovich. The initial imperfection data bank at the Delft University of Technology: Part I. Technical report, Department of Aerospace Engineering, Delft University of Technology, Delft, 1979.

[12] J. Arbocz and J. Ho. Collapse of axially compressed cylindrical shells with random imperfections. *AIAA journal*, 23(December 1991):131–158, 1991.

[13] S.M. Bauer, S.B. Filippov, A.L. Maiboroda, A.L. Smirnov, and I. Yu. Teterin. Buckling of Thin Cylindrical Shells and Shells of Negative Gaussian Curvature. In Remi Vaillancourt and Andrei L. Smirnov, editors, *Asymptotic Methods in Mechanics*, pages 153–161, Providence, Rhode Island, 1993. American Mathematical Society.

[14] D. O. Brush and B. O. Almroth. *Buckling of Bars, Plates and Shells.* McGraw-Hill, Inc., New York, 1975.

[15] B. Budiansky and J.W. Hutchinson. A survey of some buckling problems. *AIAA Journal*, 4(9):1505–1510, 1966.

[16] David Bushnell. Buckling of Shells-Pitfall for Designers. *AIAA Journal*, 19(9):1183–1226, September 1981.

[17] C.R. Calladine. Understanding imperfection-sensitivity in the buckling of thin-walled shells. *Thin-walled structures*, 23:215–235, 1995.

[18] G. Cederbaum and J. Arbocz. Reliability of shells via koiter formulas. *Thin-Walled Structures*, 24(2):173–187, January 1996.

[19] J. Chilton. Heinz Isler's Infinite Spectrum: Form Finding in Design. *Architectural Design*, pages 64–71, 2010.

[20] Fehmi Cirak. Finite Element Formulation for Shells Overview of Shell Finite Elements.

[21] Bruce W.R. Forde and Siegfried F. Stiemer. Improved arc length orthogonality methods for nonlinear finite element analysis. *Computers & Structures*, 27(5):625–630, January 1987.

[22] M.L. Gambhir. *Stability Analysis and Design of Structures.* Springer, Berlin, 2004.

[23] M.W. Hilburger, M.P. Nemeth, and J.H. Starnes. Shell buckling design criteria based on manufacturing imperfection signatures. *AIAA journal*, (May), 2006.

[24] P.C.J. Hoogenboom. CIE4143 Shell Analysis, Theory and Application.

[25] Wilfred H. Horton, Stanley C. Bailey, and Beatrice H. Mcquilkin. An Introduction to Stability. *Stanford University report version of Paper 219 presented at ASTM Annual Meeting, Atlantic City, N.J.*, 115(638), 1966.

[26] Sheldon Imaoka. Analyzing Buckling in ANSYS Workbench Simulation. *ANSYS Advantage*, II(1):41–43, 2008.

[27] T. Karman and H.S. Tsien. The buckling of thin cylindrical shells under axial compression. *Journal of the Aeronautical Sciences*, 8(8):303–312, 1941.

[28] Warner Tjardus Koiter. *The stability of elastic equilibrium.* Dissertation for a degree of doctor in the technical sciences, Techishe Hooge School at Delft, Delft, 1970.

[29] Warner Tjardus Koiter. The influence of more-or-less localised short-wave imperfections on the buckling of circular cylindrical shells under axial compression (in a first approximation). *In Complex Analysis and its Applications*, pages 242–244, 1978.

[30] W.B. Kratzig, Y. Basar, and U. Wittek. Nonlinear Behavior and Elastic Stability of Shells - Theoretical Concepts - Numerical Computations - Results. In E. Ramm, editor, *Buckling of Shells*, pages 19–56, Stuttgart, 1982. Springer.

[31] B.-H. Kroplin. Postbuckling Instability Analysis of Shells Using the Mixed Method. In *Buckling of Shells*, pages 175–199, 1982.

[32] E.R. Lancaster, C.R. Calladine, and S.C. Palmer. Paradoxical buckling behaviour of a thin cylindrical shell under axial compression. *International Journal of Mechanical Sciences*, 42(5):843–865, May 2000.

[33] B. Liu and Y. Huang. The Stable Finite Element Method for Minimization Problems. *Journal of Computational and Theoretical Nanoscience*, 5(7):1251–1254, July 2008.

[34] Aleksandr L. Maiboroda. Buckling of Convex Shells under Nonaxisymmetric Loading. In Remi Vaillancourt and Andrei L. Smirnov, editors, *Asymptotic Methods in Mechanics*, pages 217–225, Providence, Rhode Island, 1993. American Mathematical Society.

[35] P. Mandal and C.R. Calladine. Buckling of thin cylindrical shells under axial compression. *International Journal of Solids and Structures*, 37(33):4509–4525, August 2000.

[36] C. Maraveas and K. Miamis. Shell buckling evaluation of thin-walled steel tanks filled at low liquid level according to current design codes. *Proceedings of the Annual Stability ...*, pages 710–724, 2013.

[37] National Institute for Coastal and Marine Management. Wind climate assessment of the Netherlands, 2005.

[38] E. Ramm and H. Stegmüller. The displacement finite element method in nonlinear buckling analysis of shells. In E. Ramm, editor, *Buckling of Shells*, pages 201–235, Stuttgart, 1982. Springer.

[39] A.T. Sarawit, Y. Kim, M.C.M. Bakker, and T. Peköz. The finite element method for thin-walled members-applications. *Thin-Walled Structures*, 41(2-3):191–206, February 2003.

[40] David B. South. Monolithic Domes. Technical report, Monolithic, Italy, Texas, 2004.

[41] Jin Guang Teng. Buckling of Thin Shells: Recent Advances and Trends. *Applied Mechanics Reviews*, 49(4):263, 1996.

[42] MK Thompson and JM Thompson. Methods for generating probabilistic rough surfaces in ANSYS. *... of the 20th Korea ANSYS User's ...*, 2010.

[43] Petr E. Tovstik and Andrei L. Smirnov. *Asymptotic Methods in the Buckling Theory of Elastic Shells*. World Scientific Publishing Co. Pte. Ltd., Singapore, 1st edition, 2001.

[44] UK Ansys. Structural Mechanics Highlights. Technical report, ANSYS Inc., 2013.

[45] V. I. Wingarten and P. Seide. Buckling of Thin-Walled Doubly Curved Shells. Technical report, Langley Research Center, NASA, Hampton, 1969.

[46] W. Wunderlich, H.J. Rensch, and H. Obrecht. Analysis of Elastic-Plastic Buckling and ImperfectionâĂŤSensitivity of Shells of Revolution. In E. Ramm, editor, *Buckling of shells*, pages 137–174, Stuttgart, 1982. Springer.

[47] Hailan Xu. *Buckling, Postbuckling and Imperfection Sensitivity Analysis of Different Type of Cylindrical Shells by Hui's Postbuckling Method*. Doctor of philosophy, University of New Orleans, 2013.

[48] W. Zerna and I. Mungan. Buckling stresses of shells having negative gaussian curvature. In E. Ramm, editor, *Buckling of Shells*, pages 467–485, Stuttgart, 1982. Springer.

[49] E. Zhu, P. Mandal, and C.R. Calladine. Buckling of thin cylindrical shells: an attempt to resolve a paradox. *International journal of mechanical ...*, 44(202):1583–1601, 2002.

Appendix A

ANSYS APDL scripts

All FEM models used in this thesis were generated, analysed, and processed with APDL scripts. The included scripts are tested to function on ANSYS 15.0 Mechanical APDL. They are not tested on Workbench. The author did his best to optimize the performance of some of the slower-running scripts by using built-in APDL commands, however there is room for further optimization.

The scripts are intended for a structure whose surface can be parametrized onto a rectangular 2-D plane, no generalization is attempted for irregular surfaces. The scripts are user interactive, i.e. they may ask for user inputs. The unit system used is the SI system (metre, kilogram, Pascal, and second). Refer to the excellent ANSYS APDL Command Reference whenever in doubt.

The scripts are visually grouped in Figure A.1. Each block in the flowchart represents one APDL script file. The background colour of each block gives indication as to whether it is a pre-, solver, or post-processing script. The arrows indicates the sequence the scripts should be run.

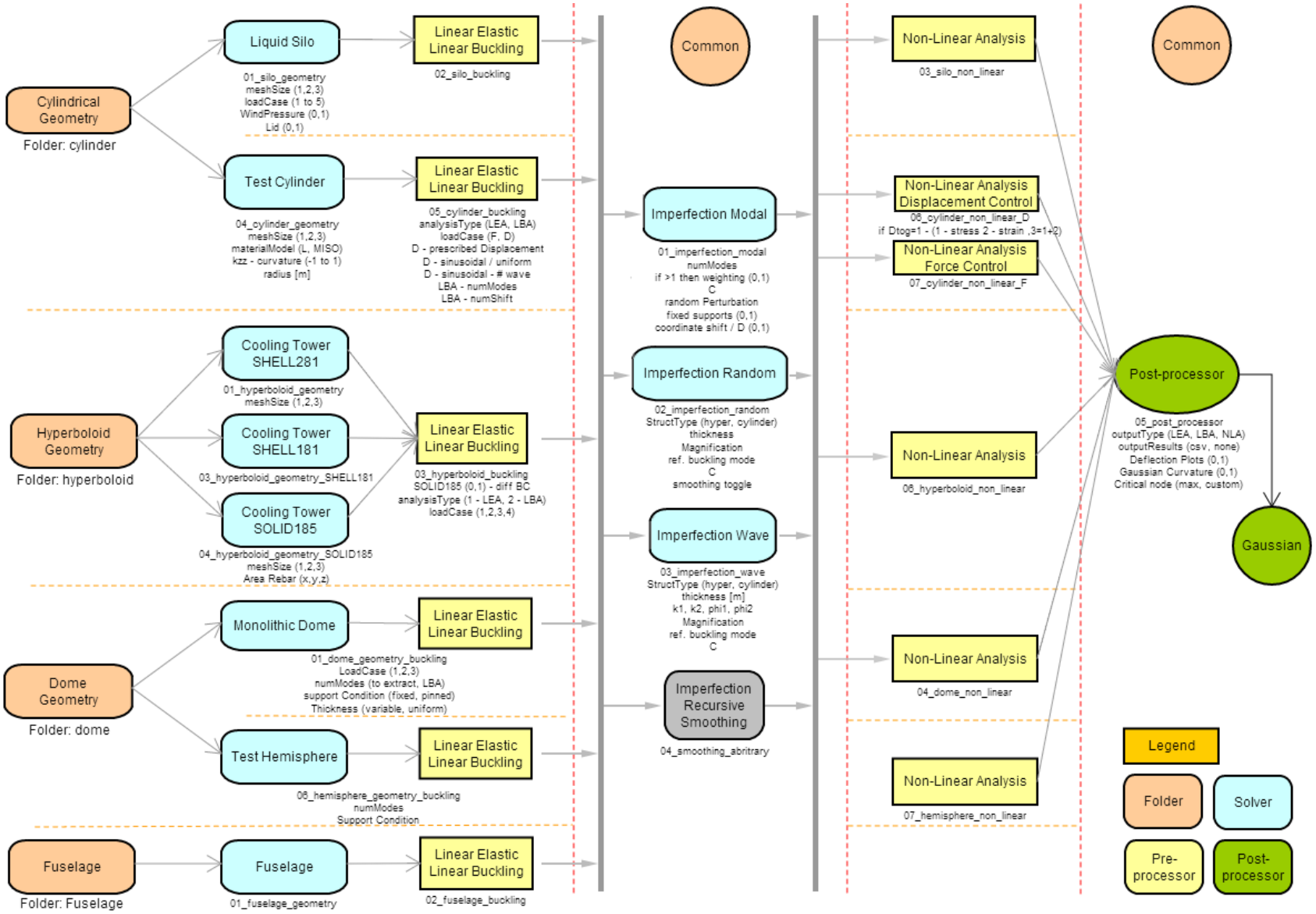

Figure A.1: Mechanical APDL code flowchart

Appendix B

Example procedure and results

Using the cylinder with zero curvature as an example, this section details the procedure that is followed to obtain the results in figure 7.4a. First the geometry of the cylinder if generated. As there is no curvature, 0 is specified in the curvature field. In this study, the mesh density is set to fine. This corresponds to an element size of x by y, and approximately # elements per metre squared. Figure B.1a shows the meshed geometry.

Then the boundary conditions are specified on the model. The nodes on the bottom ring are selected, and pinned condition is imposed on each of them. To prevent in-extensional deformation, the nodes on the top ring are constrained in global x and y directions, ie. they are only allowed to move up and down, and rotate.

The load is applied as a downward displacement of 0.025 m on each of the nodes on the top ring. LEA is performed to obtain the total reaction force. As expected, the displacement field is a pure downward movement, with the top nodes deflection the most. Figure B.1b shows the LEA result.

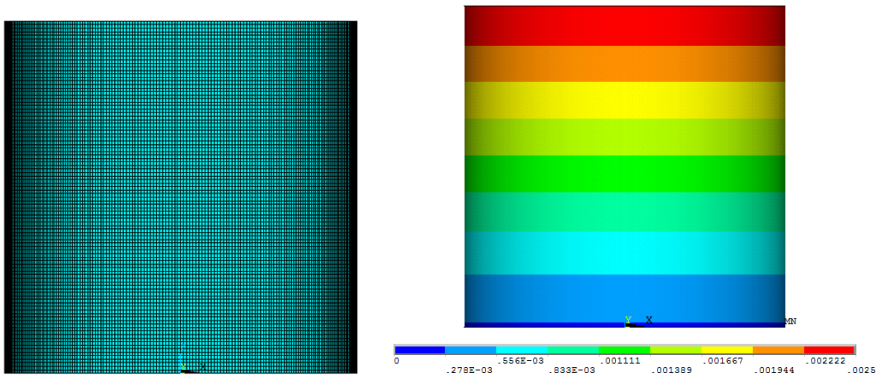

(a) (b)

Figure B.1: (a) Mesh geometry (b) LEA result plot

Next, LBA is performed to extract 20 buckling modes, of which the first one is used as the imperfection shape. Figure B.1b shows the first 20 buckling modes of the cylinder with the associated eigenvalues.

The imperfection is imposed after it is uniformly scaled down so the largest imperfection amplitude equals to half the thickness. Random or wave imperfections are applied in a similar manner. A magnified shape of the imperfection can be seen in the following figure.

After applying the imperfection, large displacement is enabled. With the imposed displacement on the top ring of the structure as load, GNLA is performed on the imperfect geometry. The

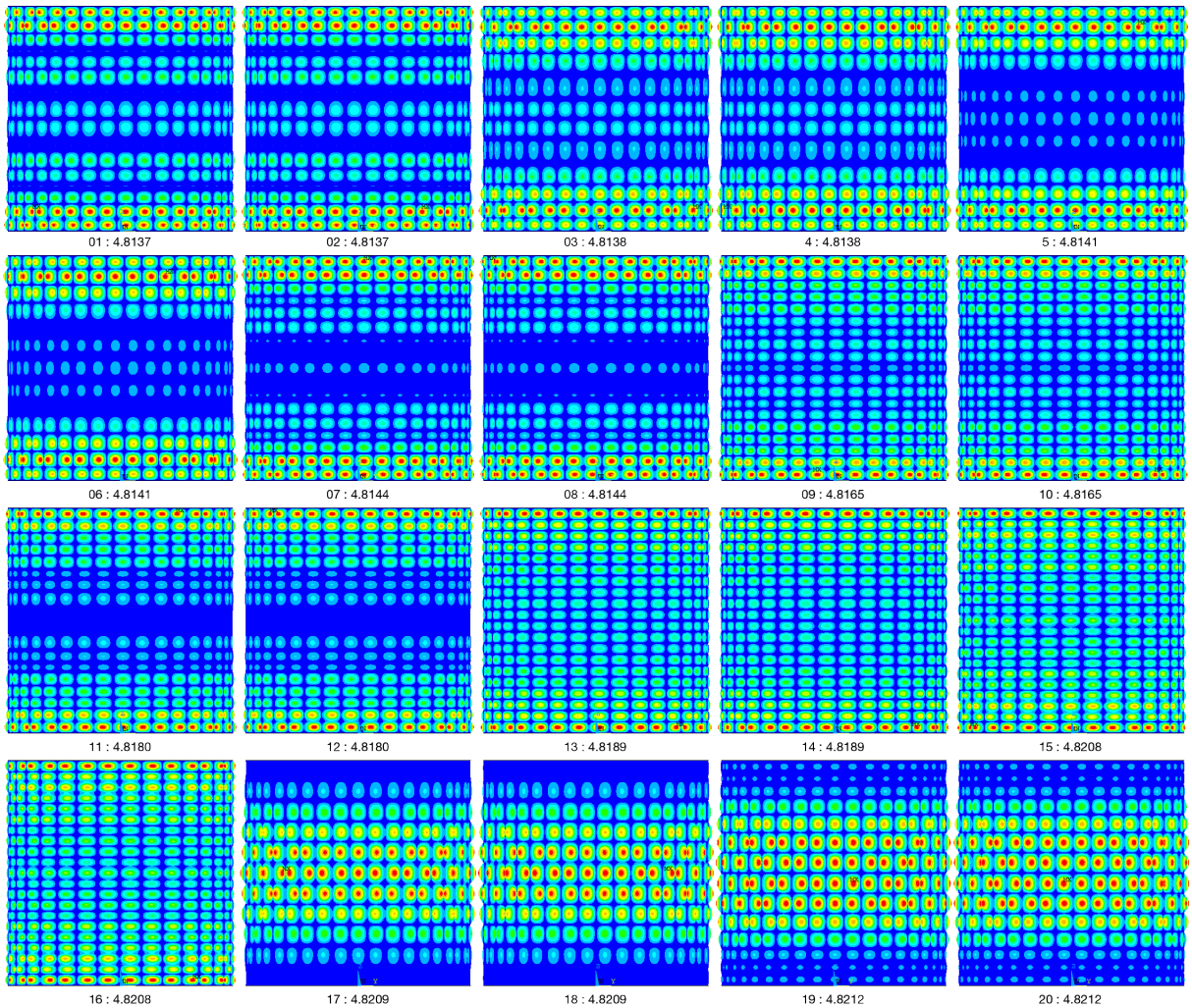

Figure B.2: Buckling modes of the perfect cylinder and their associated load factor

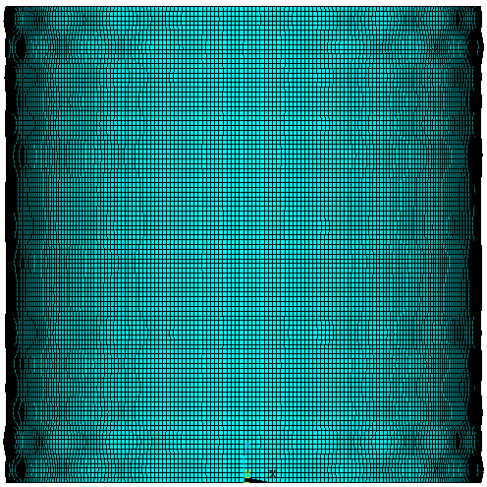

Figure B.3: Imperfect geometry, imperfection magnified 10x

initial load is set to be equal to 0.025 m, and it is doubled in every subsequent load step. The intra-step load profile is ramped (gradual increase) and not stepped. Once the peak capacity is reached, limited post-buckling behaviour is also captured. The structure usually diverges at this point.

Load Step	D_z
	mm
1	0.025
2	0.05
3	0.075
4	0.1
⋮	

Table B.1: Load Steps

Following the analysis, a post-processing script is run. Depending on user input, the script will produce the following. A series of displacement results, each for one sub-step, an spreadsheet with stress, strain, displacement and reaction force, and Gaussian curvatures.

Time Time	Stress Pa	Elastic Strain m m^{-1}	Plastic Strain m m^{-1}	Total Strain m m^{-1}	Displacement m	Reaction N
4.E-02	2259760	1.17E-05	0	1.17E-05	7.42E-05	580807.2
8.E-02	4532071	2.35E-05	0	2.35E-05	1.48E-04	1162057
0.12	6807851	3.53E-05	0	3.53E-05	2.23E-04	1742108
			⋮			

Table B.2: Spreadsheet output

With the Gaussian curvature, another series of images will be produced, with the calculated Gaussian curvature, and change in Gaussian curvature imposed as a fictitious element-normal pressure. In addition to the images, an additional spreadsheet containing the maximum and the minimum Gaussian curvature and change thereof is produced.

$K_{\min}$	$K_{\max}$	$\Delta K_{\min}$	$\Delta K_{\max}$
-1.876304948E-02	3.78E-02	0	0
-1.88521416E-02	3.84E-02	-2.77E-04	6.19E-04
-1.893555015E-02	3.91E-02	-2.84E-04	6.23E-04
-1.901400506E-02	3.97E-02	-2.93E-04	6.29E-04
-1.908718409E-02	4.03E-02	-3.03E-04	6.36E-04
-1.915474832E-02	4.10E-02	-3.14E-04	6.42E-04
	⋮		

Table B.3: Spread sheet output of K and ΔK

Appendix C

Steel Multi-linear Stress Strain Data

Strain (ϵ)	Stress (σ)	Strain (ϵ)	Stress (σ)	Strain (ϵ)	Stress (σ)
$\mathrm{m\,m^{-1}}$	Pa	$\mathrm{m\,m^{-1}}$	Pa	$\mathrm{m\,m^{-1}}$	Pa
0.00000	0	0.08698	4.12E+08	0.17395	5.00E+08
0.00178	3.55E+08	0.08875	4.15E+08	0.17573	5.01E+08
0.00355	3.56E+08	0.09053	4.17E+08	0.17750	5.01E+08
0.00533	3.56E+08	0.09230	4.20E+08	0.17928	5.02E+08
0.00710	3.57E+08	0.09408	4.22E+08	0.18105	5.02E+08
0.00888	3.57E+08	0.09585	4.25E+08	0.18283	5.03E+08
0.01065	3.58E+08	0.09762	4.27E+08	0.18460	5.03E+08
0.01243	3.58E+08	0.09940	4.30E+08	0.18638	5.03E+08
0.01420	3.59E+08	0.10118	4.33E+08	0.18815	5.04E+08
0.01598	3.59E+08	0.10295	4.35E+08	0.18993	5.04E+08
0.01775	3.60E+08	0.10473	4.38E+08	0.19170	5.04E+08
0.01953	3.60E+08	0.10650	4.40E+08	0.19348	5.04E+08
0.02130	3.61E+08	0.10828	4.43E+08	0.19525	5.04E+08
0.02308	3.61E+08	0.11005	4.45E+08	0.19703	5.04E+08
0.02485	3.62E+08	0.11183	4.48E+08	0.19880	5.04E+08
0.02663	3.62E+08	0.11360	4.50E+08	0.20058	5.04E+08
0.02840	3.63E+08	0.11538	4.52E+08	0.20235	5.04E+08
0.03018	3.64E+08	0.11715	4.55E+08	0.20413	5.04E+08
0.03195	3.64E+08	0.11893	4.57E+08	0.20590	5.03E+08
0.03373	3.65E+08	0.12070	4.59E+08	0.20768	5.03E+08
0.03550	3.66E+08	0.12248	4.61E+08	0.20945	5.03E+08
0.03728	3.67E+08	0.12425	4.63E+08	0.21123	5.02E+08
0.03905	3.68E+08	0.12603	4.65E+08	0.21300	5.02E+08
0.04083	3.69E+08	0.12780	4.67E+08	0.21478	5.01E+08
0.04260	3.70E+08	0.12958	4.69E+08	0.21655	5.01E+08
0.04438	3.71E+08	0.13135	4.71E+08	0.21833	5.00E+08
0.04615	3.72E+08	0.13313	4.73E+08	0.22010	5.00E+08
0.04793	3.73E+08	0.13490	4.74E+08	0.22188	4.99E+08
0.04970	3.75E+08	0.13668	4.76E+08	0.22365	4.98E+08
0.05148	3.76E+08	0.13845	4.78E+08	0.22543	4.97E+08
0.05325	3.77E+08	0.14023	4.79E+08	0.22720	4.96E+08
0.05503	3.79E+08	0.14200	4.81E+08	0.22898	4.96E+08
0.05680	3.80E+08	0.14378	4.82E+08	0.23075	4.95E+08
0.05858	3.82E+08	0.14555	4.84E+08	0.23253	4.94E+08
0.06035	3.83E+08	0.14733	4.85E+08	0.23430	4.93E+08
0.06213	3.85E+08	0.14910	4.87E+08	0.23608	4.91E+08
0.06390	3.86E+08	0.15088	4.88E+08	0.23785	4.90E+08
0.06568	3.88E+08	0.15265	4.89E+08	0.23963	4.89E+08
0.06745	3.90E+08	0.15443	4.90E+08	0.24140	4.88E+08
0.06923	3.92E+08	0.15620	4.91E+08	0.24318	4.87E+08
0.07100	3.93E+08	0.15798	4.93E+08	0.24495	4.85E+08
0.07278	3.95E+08	0.15975	4.94E+08	0.24673	4.84E+08
0.07455	3.97E+08	0.16153	4.95E+08	0.24850	4.82E+08
0.07633	3.99E+08	0.16330	4.96E+08	0.25028	4.81E+08
0.07810	4.01E+08	0.16508	4.96E+08		
0.07988	4.03E+08	0.16685	4.97E+08		
0.08165	4.06E+08	0.16863	4.98E+08		
0.08343	4.08E+08	0.17040	4.99E+08		
0.08520	4.10E+08	0.17218	5.00E+08		

Table C.1: steel multi-linear stress strain data used in Chapter 8

Appendix D

Circumferential displacement of the axisymmetric imperfection

This appendix section details the formulation that relates the circumferential displacement to the vertical membrane force of a cylinder with axisymmetric imperfection, the FEM results of the same set-up can be found in chapter 7. Assuming the axisymmetric imperfection shape comprises of a series of hyperboloids and barrels stacked one on top another, one barrel is isolated as a free body. Further assume that this barrel can be represented by a series of columns, then pre-buckling displacement due to an initial imperfection can be calculated with equation (D.1).

$$\Delta e = e_i \left(\frac{n}{n-1} - 1 \right) \tag{D.1a}$$

$$n = \frac{F_{\text{cr}}}{R_F} \tag{D.1b}$$

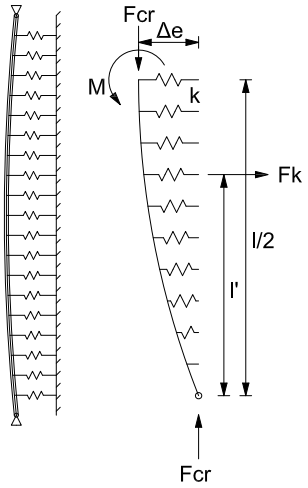

Figure D.1: Laterally spring support column model

F_{cr} could be calculated by consider the shell as a series of distributed spring supported column with pinned ends as suggested by von Kármán (Fig D.1). Solving the differential equation results in equation(D.2) [22].

$$F_{\text{cr}} = \frac{\pi^2 EI}{L_{\text{b}}^2} \left[n^2 + \left(\frac{kL_{\text{b}}^4}{n^2 \pi^4 EI} \right) \right] \tag{D.2}$$

Where I is the second moment of area of the rolled out section of the cylinder, ${}^{l_m h^3}/_{12}$, L_{b} is the length of a buckle, ${}^{2L}/_{m}$ and n is one. The equivalent spring stiffness, k, could be

found by substituting F_{cr} with the maximum reaction force from the FEM analysis. With the maximum reaction force equals to $F_{\text{cr}} = 21.79 \times 10^6\,\text{N}$, k can be found by solving equation (D.2), $k = 217.84\,\text{MPa}$.

k could also be calculated by calculating F_{cr} using Koiter's equation (Eq. (D.3)) without a knock-down factor.

$$F_{\text{cr}} = 0.605\frac{Eh}{a} \tag{D.3}$$

With these two different F_{cr}s, the theoretical displacements are plotted in figure D.2. It is

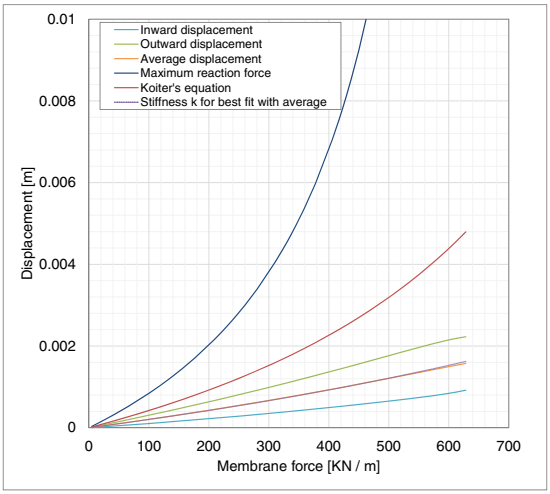

Figure D.2: Average lateral displacement of the buckles, compared to theoretical values

evident that neither adequately represent the actual displacement. Therefore a best-fit stiffness k is calculated in the F_{cr} equation (Eq. (D.2)), $k = 1200\,\text{MPa}$. Continuing equation (D.1), we substitute the above

Looking at figure D.1, one can construct a moment equilibrium around the bottom of the column, and assuming that the top moment M is zero first.

$$\sum M_{\cdot} = F_{\text{cr}}\Delta e - F_{\text{k}}l' = 0 \tag{D.4}$$

The equivalent spring force can be calculated by integrating individual spring over the whole range between 0 and $l/2$. Assuming that the column is deforming parabolically (sinusoidal shape would also work),

$$\begin{aligned} F_k &= \int_0^{\frac{l}{2}} \frac{4\Delta e}{l^2} z(l-z)\,\mathrm{d}z \\ F_k &= \frac{1}{3}\Delta e \cdot l \end{aligned} \tag{D.5}$$

Subtituting F_k back to the equilibrium equation,

$$0 = F_{\text{cr}}\Delta e - \frac{1}{3}\Delta e \cdot l \cdot l' \tag{D.6}$$

The Δe drops out of the equation. This would indicate that the application of force does not change the displacement which is obviously false. This requires further research.

Appendix E

20 Eigenvalues of each 37 models of different curvatures

	Curvature	1	2	3	4	5	6	7	8	9	10	11	12	13	14	15	16	17	18	19	20
1	1	9.2519	9.2724	9.2805	9.2805	9.2881	9.2881	9.3311	9.3311	9.3321	9.3321	9.3970	9.3970	9.3972	9.3972	9.4821	9.4821	9.4821	9.4821	9.5890	9.5890
2	0.75	8.4572	8.4775	8.4805	8.4805	8.4904	8.4904	8.5239	8.5239	8.5261	8.5261	8.5793	8.5793	8.5797	8.5797	8.6495	8.6495	8.6496	8.6496	8.7364	8.7364
3	0.5	7.4654	7.4797	7.4797	7.4806	7.4888	7.4888	7.5091	7.5091	7.5120	7.5120	7.5468	7.5468	7.5475	7.5475	7.5941	7.5941	7.5942	7.5942	7.6522	7.6522
4	0.45	7.2253	7.2376	7.2376	7.2388	7.2460	7.2460	7.2634	7.2634	7.2662	7.2662	7.2968	7.2968	7.2975	7.2975	7.3387	7.3387	7.3388	7.3388	7.3901	7.3901
5	0.4	6.9712	6.9815	6.9815	6.9828	6.9889	6.9889	7.0037	7.0037	7.0062	7.0062	7.0326	7.0326	7.0332	7.0332	7.0689	7.0689	7.0690	7.0690	7.1135	7.1135
6	0.35	6.7047	6.7130	6.7130	6.7144	6.7194	6.7194	6.7315	6.7315	6.7338	6.7338	6.7559	6.7559	6.7565	6.7565	6.7866	6.7866	6.7867	6.7867	6.8244	6.8244
7	0.3	6.4284	6.4350	6.4350	6.4361	6.4401	6.4401	6.4499	6.4499	6.4517	6.4517	6.4698	6.4698	6.4701	6.4701	6.4949	6.4949	6.4949	6.4949	6.5259	6.5259
8	0.25	6.1460	6.1509	6.1509	6.1518	6.1548	6.1548	6.1624	6.1624	6.1637	6.1637	6.1779	6.1779	6.1781	6.1781	6.1976	6.1976	6.1977	6.1977	6.2222	6.2222
9	0.2	5.8619	5.8653	5.8653	5.8661	5.8682	5.8682	5.8737	5.8737	5.8747	5.8747	5.8851	5.8851	5.8853	5.8853	5.8999	5.8999	5.8999	5.8999	5.9181	5.9181
10	0.15	5.5809	5.5832	5.5832	5.5846	5.5861	5.5861	5.5886	5.5886	5.5904	5.5904	5.5963	5.5963	5.5977	5.5977	5.6063	5.6063	5.6077	5.6077	5.6188	5.6188
11	0.1	5.3082	5.3094	5.3094	5.3124	5.3124	5.3148	5.3157	5.3157	5.3169	5.3169	5.3184	5.3184	5.3228	5.3228	5.3228	5.3228	5.3287	5.3287	5.3306	5.3306
12	0.05	5.0531	5.0537	5.0537	5.0550	5.0550	5.0572	5.0572	5.0603	5.0603	5.0646	5.0646	5.0658	5.0662	5.0662	5.0672	5.0672	5.0678	5.0678	5.0680	5.0680
13	0.025	4.9368	4.9371	4.9371	4.9379	4.9379	4.9392	4.9392	4.9411	4.9411	4.9440	4.9440	4.9450	4.9450	4.9455	4.9455	4.9457	4.9457	4.9469	4.9469	4.9478
14	0.005	4.8502	4.8504	4.8504	4.8508	4.8508	4.8510	4.8510	4.8513	4.8513	4.8514	4.8514	4.8522	4.8522	4.8523	4.8523	4.8525	4.8525	4.8525	4.8525	4.8530
15	0.0025	4.8379	4.8379	4.8380	4.8380	4.8380	4.8380	4.8389	4.8389	4.8390	4.8390	4.8394	4.8394	4.8394	4.8394	4.8397	4.8397	4.8397	4.8397	4.8398	4.8398
16	0.0005	4.8191	4.8191	4.8196	4.8196	4.8206	4.8206	4.8208	4.8208	4.8208	4.8208	4.8224	4.8224	4.8227	4.8227	4.8242	4.8242	4.8256	4.8256	4.8264	4.8264
17	0.0003	4.8165	4.8165	4.8170	4.8170	4.8172	4.8172	4.8175	4.8175	4.8187	4.8187	4.8202	4.8202	4.8208	4.8208	4.8225	4.8225	4.8236	4.8236	4.8248	4.8248
18	5E-05	4.8143	4.8143	4.8145	4.8145	4.8148	4.8148	4.8149	4.8149	4.8170	4.8170	4.8184	4.8184	4.8193	4.8193	4.8212	4.8212	4.8218	4.8218	4.8220	4.8220
19	0	4.8137	4.8137	4.8138	4.8138	4.8141	4.8141	4.8144	4.8144	4.8165	4.8165	4.8180	4.8180	4.8189	4.8189	4.8208	4.8208	4.8209	4.8209	4.8212	4.8212
20	-5E-05	4.8131	4.8131	4.8132	4.8132	4.8134	4.8134	4.8138	4.8138	4.8161	4.8161	4.8175	4.8175	4.8185	4.8185	4.8200	4.8200	4.8204	4.8204	4.8205	4.8205
21	-3E-04	4.8103	4.8103	4.8106	4.8106	4.8109	4.8109	4.8117	4.8117	4.8144	4.8144	4.8157	4.8157	4.8164	4.8164	4.8170	4.8170	4.8173	4.8173	4.8191	4.8191
22	-5E-04	4.8067	4.8067	4.8071	4.8071	4.8079	4.8079	4.8090	4.8090	4.8119	4.8119	4.8122	4.8122	4.8134	4.8134	4.8135	4.8135	4.8151	4.8151	4.8168	4.8168
23	-0.003	4.7682	4.7682	4.7688	4.7688	4.7718	4.7718	4.7739	4.7739	4.7739	4.7739	4.7750	4.7750	4.7805	4.7805	4.7819	4.7819	4.7865	4.7865	4.7867	4.7867
24	-0.005	4.6982	4.6982	4.6999	4.6999	4.7012	4.7012	4.7035	4.7035	4.7059	4.7059	4.7074	4.7074	4.7205	4.7205	4.7214	4.7214	4.7228	4.7228	4.7245	4.7245
25	-0.025	3.6370	3.6370	3.6870	3.6870	3.7296	3.7296	3.7753	3.7753	3.7996	3.7996	3.8110	3.8110	3.8234	3.8234	3.8346	3.8346	3.8555	3.8555	3.8919	3.8919
26	-0.05	2.5974	2.5974	2.6709	2.6709	2.7388	2.7388	2.7838	2.7838	2.7899	2.7899	2.8007	2.8007	2.8241	2.8241	2.8345	2.8345	2.8420	2.8420	2.9051	2.9051
27	-0.1	1.8332	1.8332	1.8593	1.8593	1.8649	1.8649	1.8828	1.8828	1.9428	1.9428	1.9685	1.9685	2.0377	2.0377	2.0799	2.0799	2.0930	2.0930	2.1581	2.1581
28	-0.15	1.3993	1.3993	1.4298	1.4298	1.4301	1.4301	1.4441	1.4441	1.4464	1.4464	1.4652	1.4652	1.5020	1.5020	1.5072	1.5072	1.5753	1.5753	1.5991	1.5991
29	-0.2	1.1969	1.1969	1.2077	1.2077	1.2109	1.2109	1.2114	1.2114	1.2433	1.2433	1.2588	1.2588	1.2612	1.2612	1.2631	1.2631	1.3388	1.3388	1.3422	1.3422
30	-0.25	1.0676	1.0676	1.0736	1.0736	1.0757	1.0757	1.0759	1.0759	1.1118	1.1118	1.1139	1.1139	1.1184	1.1184	1.1318	1.1318	1.1806	1.1806	1.1852	1.1852
31	-0.3	0.9821	0.9821	0.9860	0.9860	0.9876	0.9876	0.9936	0.9936	1.0197	1.0197	1.0265	1.0265	1.0274	1.0274	1.0451	1.0451	1.0838	1.0838	1.0854	1.0854
32	-0.35	0.9228	0.9228	0.9264	0.9264	0.9381	0.9381	0.9395	0.9395	0.9647	0.9647	0.9674	0.9674	0.9755	0.9755	0.9776	0.9776	1.0189	1.0189	1.0287	1.0287
33	-0.4	0.8864	0.8864	0.8975	0.8975	0.8991	0.8991	0.9050	0.9050	0.9258	0.9258	0.9275	0.9275	0.9384	0.9384	0.9475	0.9475	0.9848	0.9848	0.9915	0.9915
34	-0.45	0.8730	0.8730	0.8730	0.8730	0.8774	0.8774	0.8879	0.8879	0.8987	0.8987	0.9099	0.9099	0.9199	0.9199	0.9276	0.9276	0.9685	0.9685	0.9738	0.9738
35	-0.5	0.8599	0.8599	0.8666	0.8666	0.8738	0.8738	0.8826	0.8826	0.8908	0.8908	0.9094	0.9094	0.9096	0.9096	0.9123	0.9123	0.9621	0.9621	0.9750	0.9750
36	-0.75	0.9247	0.9247	0.9432	0.9432	0.9492	0.9492	0.9531	0.9531	0.9599	0.9599	0.9659	0.9659	0.9986	0.9986	1.0073	1.0073	1.0258	1.0258	1.0382	1.0382
37	-1	1.0877	1.0877	1.0964	1.0964	1.1090	1.1090	1.1256	1.1256	1.1297	1.1297	1.1567	1.1567	1.1591	1.1591	1.1624	1.1624	1.2206	1.2206	1.2495	1.2495

Table E.1: Models of different curvature and their associated 20 eigenvalues

Appendix F

Other Types of Imperfections

F.1 Initial Conditions Deformation Diagrams

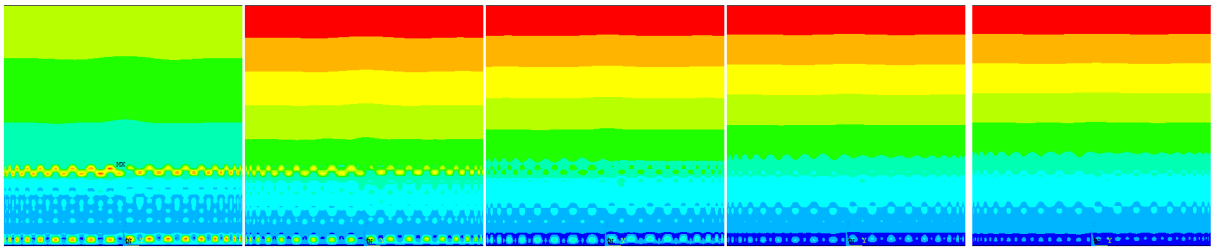

(a)

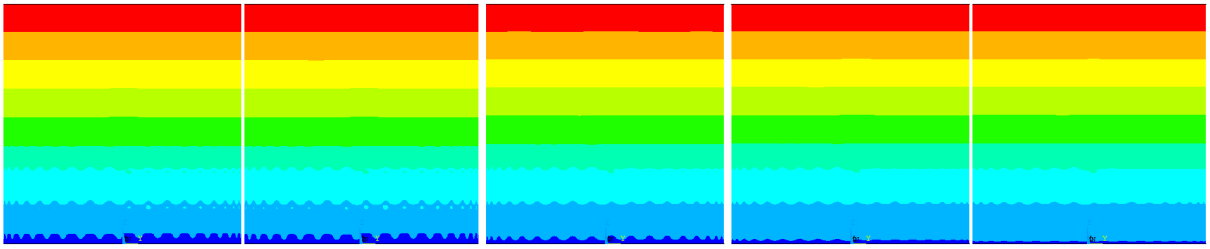

(b)

Figure F.1: (a) Initial stress (b) Initial stress + strain

F.2 Loading Imperfection Deformation Diagrams

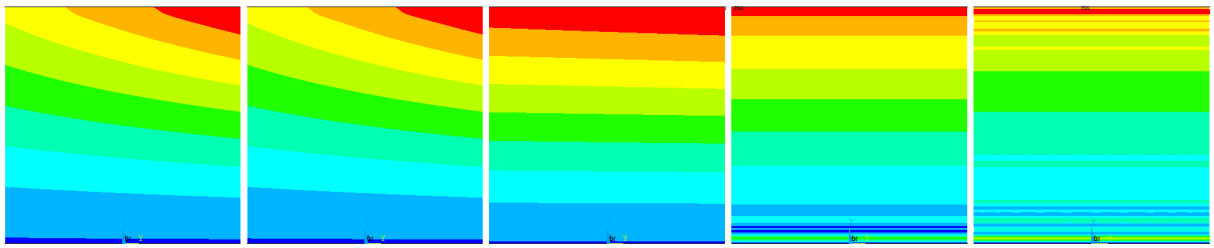

(a)

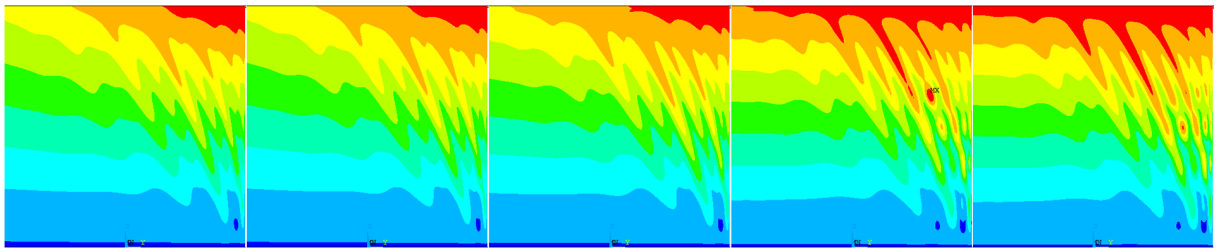

(b)

Figure F.2: a=1 (a) Load imperfection (b) Load + geometrical imperfection

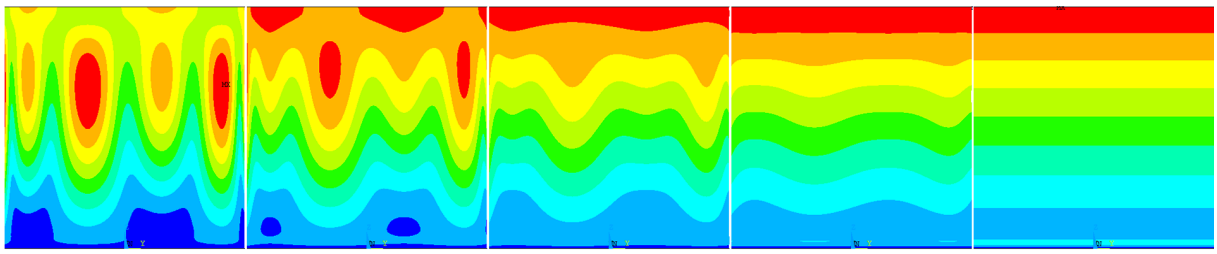

(a)

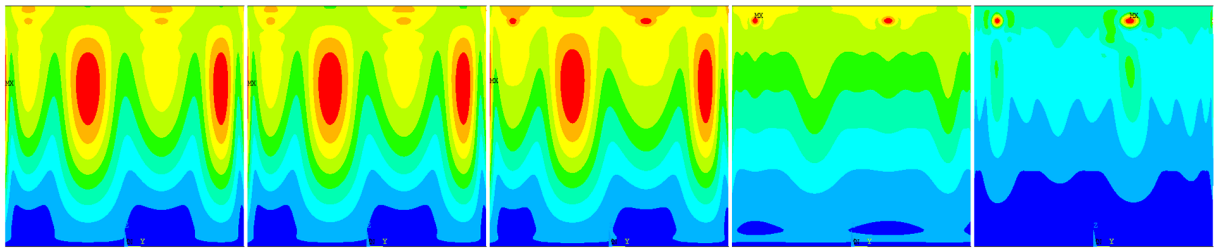

(b)

Figure F.3: a=5 (a) Load imperfection (b) Load + geometrical imperfection

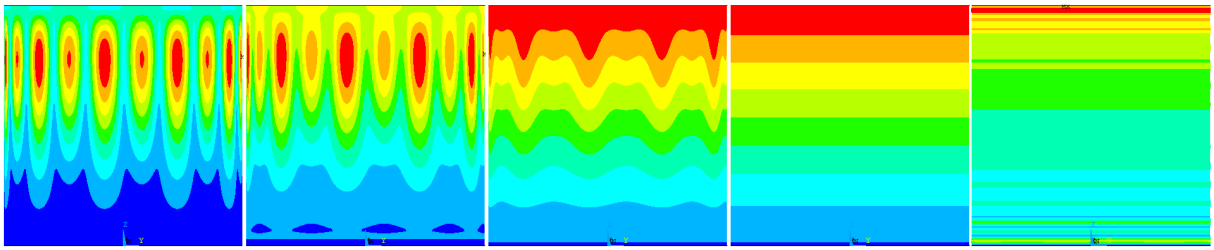

(a)

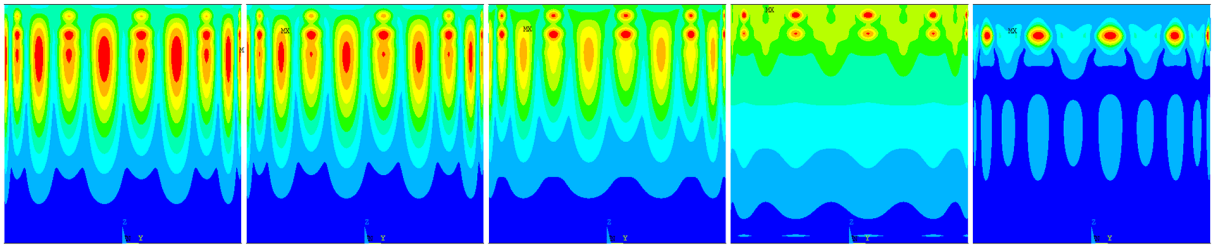

(b)

Figure F.4: a=10 (a) Load imperfection (b) Load + geometrical imperfection

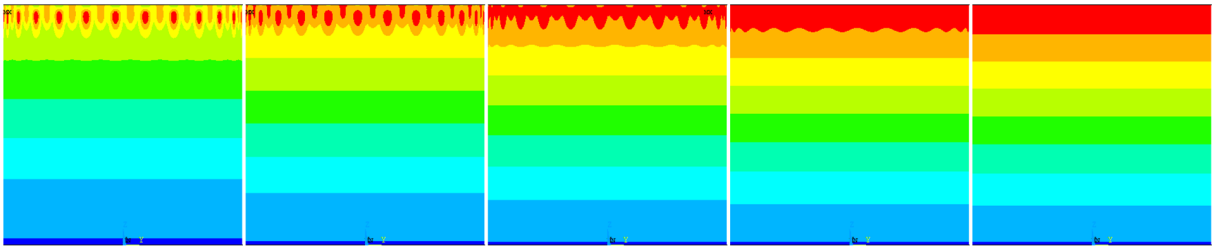

(a)

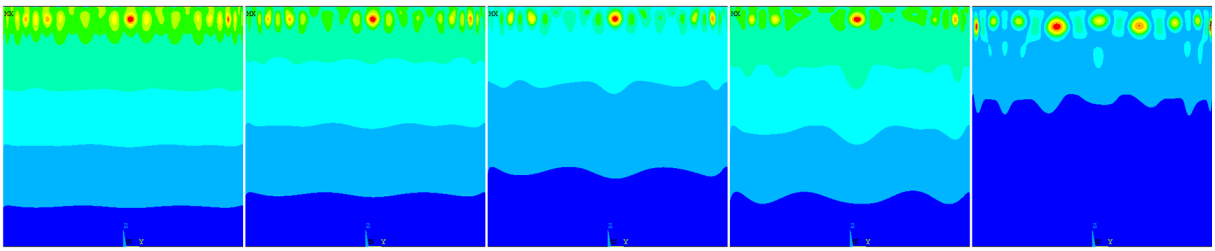

(b)

Figure F.5: a=25(a) Load imperfection (b) Load + geometrical imperfection